In Vitro Cytotoxic and Ultrastructural Effects of Selected Carboxylic Ionophores on Cardiac and Skeletal Myoblasts

By

Danielle Henn

Submitted in partial fulfilment of the requirements for the degree
PhD in Veterinary Science

in the

Department of Paraclinical Sciences
Faculty of Veterinary Science

UNIVERSITY OF PRETORIA

Date
August 2022

UNIVERSITY OF PRETORIA
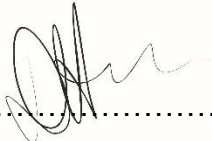**FACULTY OF VETERINARY SCIENCE**

DECLARATION OF ORIGINALITY

Full names of student: Danielle Henn

Student number: 13009410

Declaration:

1. I understand what plagiarism is and am aware of the University's policy in this regard.
2. I declare that this thesis is my own original work. Where other people's work has been used (either from a printed source, Internet or any other source), this has been properly acknowledged and referenced in accordance with departmental requirements.
3. I have not used work previously produced by another student or any other person to hand in as my own.
4. I have not allowed and will not allow anyone to copy my work with the intention of passing it off as his or her own work.

Signature of student: ....

ACKNOWLEDGMENTS

SUMMARY

In Vitro Cytotoxic and Ultrastructural Effects of Selected Carboxylic Ionophores on Cardiac and Skeletal Myoblasts

By

Danielle Henn

Supervisor: Prof. C.J. Botha

Department: Paraclinical Sciences

University: University of Pretoria

Degree: PhD (Veterinary Science)

Carboxylic ionophores are polyether antibiotics that are extensively used in production animals for the control of coccidiosis and to promote growth and feed efficiency. Unfortunately, due to feed mixing errors and extra-label use, cases of ionophore toxicosis occur and primarily affect cardiac and skeletal muscles. Ionophores form dynamically reversible complexes with cations and facilitate their movement across biological membranes, affecting the ion homeostasis of cells and disrupting their normal physiological functions. The aim of the study was to determine the cytotoxicity, subcellular changes and ultrastructural effects caused by the three different antibiotics, monensin, salinomycin and lasalocid on cardiac (H9c2) and skeletal (L6 and C2C12) myoblasts *in vitro*. The cytotoxicity of each ionophore over a 72-h period was determined using the 3-(4,5-dimethylthiazol-2-yl)-2,5-diphenyl tetrazolium bromide (MTT) viability assay. Immunofluorescent and immunocytochemistry techniques were used to investigate the effect of the ionophores on the microfilament and microtubule networks, as well as on the intermediate filaments desmin and synemin. Finally, electron microscopy was used to determine the ultrastructural effects of ionophore exposure. Monensin induced the highest cytotoxicity of the three ionophores, with EC_{50}s in the low nanomolar range after 48 and 72 h exposure, followed by salinomycin and lasalocid. Myoblasts exposed to the different ionophores had similar morphological changes, with cytoplasmic vesicles filling the entire myoblast as well as myoblasts 'rounding off' and detaching from their surroundings. The microfilament and microtubule networks showed minimal to moderate disruption depending on the cell line, ionophore, ionophore concentration and exposure time. Disruption to the intermediate filament network was observed after monensin and salinomycin exposure, resulting in the aggregation of desmin around the nuclei of affected myoblasts. However, the synemin network was the least affected. Ultrastructural changes included the accumulation of electron-lucent vesicles within the cytoplasm, mitochondrial and chromatin condensation as well as myoblasts with apoptotic and necrotic features. In conclusion, of the carboxylic ionophores tested monensin was the most cytotoxic *in vitro*. Furthermore, ionophore exposure resulted in the disruption of the cytoskeletal networks, especially desmin filaments, which could contribute to the myofibrillar degeneration and necrosis seen in the skeletal muscles of animals suffering from ionophore toxicosis. Finally, cytoplasmic vesiculation and mitochondrial condensation was the most prominent ultrastructural changes that occurred as a result of ionophore exposure *in vitro*, with both apoptotic and necrotic myoblasts present.

Keywords: Carboxylic Ionophores, Cytotoxicity, Cytoskeleton, Myoblasts, Ultrastructure

Published:
- Henn, D., Venter, A., Ferreira, G.C., Botha, C.J., 2022. The *In Vitro* Cytotoxic Effects of Ionophore Exposure on Selected Cytoskeletal Proteins of C2C12 Myoblasts. Toxins 14, 447.

Manuscripts In Progress:
- Henn, D., Lensink, A., Botha, C.J., 2022. Ultrastructural changes in cardiac and skeletal myoblasts following *in vitro* exposure to monensin, salinomycin and lasalocid.
– S*ubmitted.*

- Henn, D., Venter, A., Ferreira, G.C., Botha, C.J., 2022. The *In Vitro* Cytotoxic Effects of Carboxylic Ionophores on the Microtubule and Microfilament Networks of H9c2 and L6 Myoblasts.
– *In Preparation*

- Henn, D., Botha, C.J., 2022. Review of the *In Vitro* Cytotoxic Effects of Carboxylic Ionophores.
– *In Preparation*

Table of Content

List of Abbreviations

ABPE	Acute Bovine Pulmonary Oedema and Emphysema
AST	Aspartate Transaminase
ATCC	American Type Culture Collection
ATP	Adenosine 5'-Triphosphate
ATPase	Adenosine Triphosphatase
BSA	Bovine Serum Albumin
Ca^{2+}	Calcium
CPK	Creatine Phosphokinase
DAB	3,3'-Diaminobenzidine
DAPI	4',6-Diamidino-2-Phenylindole
dH_2O	Distilled Water
ddH_2O	Double Distilled Water
DISC	Death Inducing Signalling Complex
DMEM	Dulbecco's Modified Eagle's Medium
DNA	Deoxyribonucleic Acid
DNase	Deoxyribonuclease
$EC_{50}/EC_{50}s$	Half Maximal Effective Concentration(s)
EDTA	Ethylenediaminetetraacetic Acid
EdUTP	5-Ethynyl-2'-Deoxyuridine-5'-Triphosphate
ELISA	Enzyme-Linked Immunosorbent Assay
Em	Emission
EM	Electron Microscope/Microscopy
ER	Endoplasmic Reticulum
EtOH	Ethanol
Ex	Excitation
FBS	Foetal Bovine Serum
H^+	Proton(s)
H-DAB	The Combination of Haematoxylin and Diaminobenzidine
HIER	Heat-Induced Epitope Retrieval
HIV	Human Immunodeficiency Virus
HMDS	1,1,1,3,3,3-Hexamethyldisilazane
JCRB	Japanese Collection of Research Bioresources
K^+	Potassium
LC-MS	Liquid Chromatography/Mass Spectrometry
$LD_{50}/LD_{50}s$	Half Maximal Lethal Dose(s)

LDH	Lactate Dehydrogenase
LMN	Lower Motor Neuron
NCCD	Nomenclature Committee on Cell Death
MeOH	Methanol
Mg^{2+}	Magnesium
MPT	Mitochondrial Permeability Transition
MTT	3-(4,5-Dimethylthiazol-2-yl)-2,5-Diphenyltetrazolium Bromide
MW	Molecular Weight
n	Number of Biological Repeats
Na^+	Sodium
NHE	Sodium/Proton Exchanger
OsO_4	Osmium Tetroxide
PBS	Phosphate Buffered Saline
PI3K	Phosphoinositide 3-Kinase
PKA	Protein Kinase A
PSF	Point Spread Function
RER	Rough Endoplasmic Reticulum
RIPA	Radioimmunoprecipitation Assay
RNA	Ribonucleic Acid
ROI	Region of Interest
ROS	Reactive Oxygen Species
SDS	Sodium Dodecyl Sulphate
SEM	Scanning Electron Microscopy
StEM	Standard Error of the Mean
TdT	Terminal Deoxynucleotidyl Transferase
TEM	Transmission Electron Microscopy
TLC	Thin layer Chromatography
TNF	Tumour Necrosis Factor
TUNEL	Terminal Deoxynucleotidyl Transferase-dUTP Nick End Labelling
UPR	Unfolded Protein Response

List of Figures

List of Tables

Chapter 1: Introduction

1.1 A Brief Introduction to Carboxylic Ionophore Antibiotics

Carboxylic ionophore antibiotics are lipid-soluble cation transporters, initially used for the control of coccidiosis in poultry (Novilla, 2018). Subsequently their use as feed additives for the promotion of growth and feed efficiency in cattle was discovered, prompting their wide use within the livestock industry. Carboxylic ionophore antibiotics, however, are toxic to animals in high doses and many cases of ionophore toxicosis have been reported, mainly as a result of extra-label use and feed mixing errors. The severity of ionophore toxicosis is dependent on both the species and dose. Clinical signs often include, but are not limited to, feed refusal, anorexia, diarrhoea, depression, tachyarrhythmias, dyspnoea, weakness, ataxia and recumbency (Bastianello and Fourie, 1996; Dowling, 1992; Gruys et al., 2001; Gy et al., 2020; Hall, 2000; Novilla, 2018). Ionophore toxicosis primarily target the cardiac and skeletal muscles of affected animals but have also been shown to cause neuromuscular disorders in cats and dogs (Bosch et al., 2018; Pakozdy et al., 2010; Segev et al., 2004). Cardiac and skeletal muscle lesions consist of degeneration and necrosis of the myofibers, as well as attempts at repair and a variable inflammatory component (Confer et al., 1983; Mollenhauer et al., 1981; Van Vleet and Ferrans, 1984a, b). Unfortunately, lesions are not pathognomonic and take time to develop, often being absent in animals that die shortly after ionophore exposure. To date, treatments for ionophore intoxication are mainly supportive and symptomatic as there is no known antidote.

The mechanism of action of carboxylic ionophore antibiotics pertain to their ability to ferry cations across biological membranes down their concentration gradient, resulting in the disruption of cellular ion homeostasis (Novilla, 2018; Pressman et al., 1967; Pressman, 1976). Both muscle and nervous tissue are highly dependent on ion fluxes in order to function. Various cellular processes are subject to the precise regulation of the ion homeostasis (Abdul Kadir et al., 2018; Blackiston et al., 2009; Danese et al., 2017; Urrego et al., 2014). The ensuing downstream effects of exposure to toxic ionophore concentrations include calcium (Ca^{2+}) overload, the production of reactive oxygen species (ROS), alteration of intracellular pH and the

disruption of the mitochondrial membrane potential (Mollenhauer et al., 1990; Novilla, 2018; Przygodzki et al., 2005). Monensin, salinomycin and lasalocid are of the most well-known ionophores with a proclivity towards sodium (Na^+), potassium (K^+) and Ca^{2+}, respectively (Novilla, 2018). These three ionophores are often involved in cases of ionophore intoxication and used in studies for their effects *in vitro* (Ashrafihelan et al., 2014; Decloedt et al., 2012; Kiełbasiński et al., 2020; Kim et al., 2017a; Novilla, 2018; Pakozdy et al., 2010; Zavala et al., 2011).

1.2 Problem Statement

Ionophores are important prophylactic feed additives in production animals. However, due to various reasons, such as feed mixing errors, dosage miscalculations, feeding to an unintended species, drug incompatibilities and extra-label use, ionophore toxicity still occurs and mainly affect the cardiac and skeletal muscles of affected animals.

1.3 Benefits Arising with These Studies

The purpose of this study was to increase understanding of the effects of toxic concentrations of carboxylic ionophore antibiotics on skeletal and cardiac myoblasts, by investigating the cytotoxicity and ultrastructural effects on myoblasts *in vitro*. In addition to enhancing knowledge on a class of compound so widely used in the livestock industry, this project also aimed to contribute academic knowledge with specific regard to the effect of ionophore exposure on important cytoskeletal filaments. Furthermore, as the majority of the experimental studies conducted on ionophores, especially regarding veterinary science, is quite dated, this study will contribute more recent views to this particular field.

1.4 Aims and Objectives

The overall aim of this study was to investigate the cytotoxicity, subcellular effects and ultrastructural changes caused by three different carboxylic ionophore antibiotics i.e., monensin, salinomycin and lasalocid, on cardiac and skeletal myoblasts *in vitro*. The focus was on determining the effects of the ionophores on specific cytoskeletal proteins, as their disruption contributes to cardiac and skeletal muscle lesions seen

in affected animals. Additionally, more detailed analysis on the effect ionophores have on cell and organelle ultrastructure was performed using electron microscopy, as there is a lack of literature available on this subject and most of the relevant literature is dated.

The specific objectives were:

- to provide a comprehensive review of the effects of carboxylic ionophore antibiotics *in vivo* and *in vitro*,
- to determine the half maximal effective concentration (EC_{50}) and cytotoxic effects of monensin, salinomycin and lasalocid on cardiac (H9c2) and skeletal (L6 and C2C12) myoblasts after 24, 48 and 72 h exposure,
- to differentiate the H9c2, L6 and C2C12 myoblasts to form myotubes,
- to determine the proportion of L6 myoblasts with DNA fragmentation as a result of ionophore exposure,
- to investigate the effects of monensin, salinomycin and lasalocid on the microtubule and microfilament networks of H9c2, L6 and C2C12 myoblasts,
- to evaluate the effects of monensin, salinomycin and lasalocid on the intermediate filament proteins, desmin and synemin, of C2C12 myoblasts,
- to examine the ultrastructural changes induced by monensin, salinomycin and lasalocid on H9c2 and L6 myoblasts using transmission electron microscopy (TEM) and
- to assess the ultrastructural effects of monensin, salinomycin and lasalocid on the surface of H9c2 and L6 myoblasts using scanning electron microscopy (SEM).

Chapter 2: Literature Review

2.1 Background

Carboxylic ionophore antibiotics are polyether compounds with a broad range of activity and are widely used in the livestock industry (Anderson, 2008; Novilla, 2018). As indicated by the name, iono*phores* (Greek: *phoros* - meaning bearer/bearing) form dynamically reversible, lipid-soluble complexes with cations that allow for the transfer of ions across biological membranes (Pressman et al., 1967). To this end they have also been known as "complexones" (Ovchinnikov et al., 1974). The first three carboxylic ionophore antibiotics, referred to as X-206, X-464 (nigericin) and X-537A (lasalocid), were isolated and purified from *Streptomyces* species in 1951 (Berger et al., 1951), with many more having since been discovered. In addition, some synthetic compounds, such as crown ethers (Pedersen, 1967) and cryptands (Lehn and Sauvage, 1971), have likewise been identified to have similar ion-bearing properties. Ionophores can be divided into two major subclasses, these being neutral ionophore antibiotics and carboxylic ionophore antibiotics (Novilla, 2018; Pressman, 1976). Neutral ionophore antibiotics form highly toxic, charged complexes with ions and are capable of perturbing both biological membranes and the action potential of cells. In contrast, carboxylic ionophore antibiotics form zwitterionic complexes with cations which promote electrically neutral ion transfer via diffusion. Structurally, all carboxylic ionophore antibiotics have a linear backbone that consist of oxygen-containing heterocyclic rings (**Figure 2.1 a**-**c**). The oxygen groups in the structure allow for cation ligation. Carboxylic ionophore antibiotics are cyclised by hydrogen bonding between the carboxyl group at one terminal of the molecule and one or more hydroxyl groups at the opposite terminal (**Figure 2.1 d**). The carboxylic ionophore antibiotics, thus, create a hydrophilic interior and hydrophobic exterior that enable the molecule to cross the plasma membrane (Pressman, 1976).
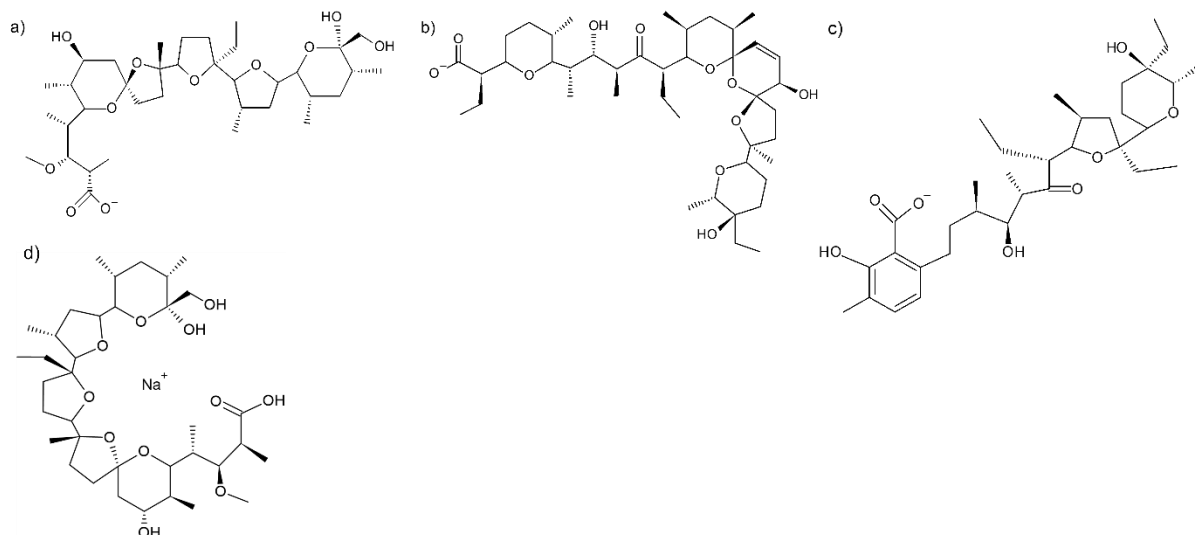
Figure 2.1 Chemical structures of the carboxylic ionophores: monensin (a), salinomycin (b) and lasalocid (c) as well as an example of monensin as a cyclic structure (d).

Compared to neutral ionophore antibiotics, carboxylic ionophore antibiotics (subsequently referred to as 'ionophores') are less harmful for animals, thus many are used as feed additives for cattle and poultry (Novilla, 2018). However, in the event of toxicosis following ionophore overdosage, striated muscle cells are primarily affected due to the resulting high intracellular Ca^{2+} concentration and the extreme movement of ions (Anderson, 2008). Clinical signs are thus accordingly associated mainly with skeletal muscle and myocardial dysfunction (Novilla, 1992). Due to their ability as ion carriers, ionophores alter the normal ion concentration gradients of cells. This results in ion imbalances across cell membranes, changes in intracellular pH, Ca^{2+} overload, lipid peroxidation and disruption of cellular membranes (Novilla, 2018).

2.2 Ionophores in the Livestock Industry

2.2.1 Benefits of Commercial Ionophores

Ionophores are used in the broiler and cattle industry to curb coccidiosis and to promote growth and feed efficiency (Goodrich et al., 1984; Marques and Cooke, 2021; Perry et al., 1976; Weppelman et al., 1977). In feedlot cattle, ionophores assist with maintaining the balance of the rumen microbial population, which translates into a more efficient feed conversion rate during periods of high-volume concentrate feeding (Anderson, 2008; Goodrich et al., 1984; Perry et al., 1976). This in turn allows for greater economic gain for meat producers. The commercially used

ionophores have different ion proclivities (Pressman and Fahim, 1982), often described as being either monovalent or divalent, and are marketed under several names (**Table 2.1**).

Additional benefits resulting from the incorporation of ionophores into cattle rations include the reduction of bloat, ruminal lactic acidosis, subclinical ketosis and acute bovine pulmonary oedema and emphysema (ABPE or fog fever) (Duffield et al., 2002; Goodrich et al., 1984; Nocerini et al., 1985). Monensin, lasalocid and laidlomycin cause increased propionate levels and decreased acetate and butyrate levels in the rumen (Nocerini et al., 1985; Perry et al., 1976; Richardson et al., 1976; Spires and Algeo, 1983). It is, however, unfortunate that despite the relative safety of the ionophores as well as their many advantages, cases of ionophore poisoning still do occur.

Table 2.1 A list of ionophores currently used in livestock and poultry production systems throughout the world.

Ionophore	Example of Trade Names	Ion Proclivity
Laidlomycin	Cattlyst	Monovalent
Lasalocid	Avatec, Bovatec, Taurotec	Divalent
Maduramicin	Cygro	
Monensin	Aniban, Ancoban, Coban, Coxidin, Ecox, Logoban, Monotec, Poulcox, Rumecox, Rumensin	Monovalent
Narasin	Maxiban, Monteban	Monovalent
Salinomycin	Aviax, Bio-cox, Ceva Salinomycin, Coxiban, Coxistat, Procoxacin, Saccox, Salecox, Salinopharm, Vibracox	Monovalent
Semduramicin	Aviax	

2.2.2 Mechanism of Action

Ionophores are capable of transporting cations across lipid membranes, influencing the ion homeostasis of the cell (Pressman et al., 1967; Pressman, 1976). The transport of ions can be between the extra- and intracellular spaces of the cell, as well as between the extra- and intra-organelle spaces. By binding a cation, the weak organic acid ionophore becomes lipid soluble and can then transport an ion across a membrane down its concentration gradient. Subsequently, the ionophore binds

another cation e.g., protons (H^+), to re-cross the membrane. The ion transporting ability of ionophores results in a net imbalance of Na^+, K^+, Ca^{2+}, and H^+. Failure to maintain ion homeostasis causes an increase in the osmotic gradient and eventually leads to cell swelling i.e., oncosis, which in turn results in damaged organelles and cell death (Mehlhorn et al., 1983; Smith et al., 1981). Overall, ionophores cause ion imbalances, changes in the intracellular pH and disrupts cellular membranes (Novilla, 2018) (**Figure 2.2**). Monensin preferably forms cation complexes with Na^+. If monensin binds to Na^+ outside the cell, the ionophore is capable of carrying the ion across the plasma membrane to the inside of the cell. Subsequently, the sudden increase in the intracellular Na^+ concentration is counterbalanced by a slow efflux of K^+ ions, as well as an initial efflux of H^+. The efflux of H^+ may result in intracellular alkalosis. Additionally, the rise in the intracellular Na^+ concentration causes an increase in the intracellular Ca^{2+} concentration owing to the indirect inhibition of the Na^+/Ca^{2+}-exchanger. Other ionophores such as salinomycin preferably complex with K^+. The K^+ efflux is countered by an initial H^+ influx, which in turn, lead to the acidification of the intracellular environment. Lasalocid is considered a divalent ionophore that preferentially forms complexes with divalent ions, namely Ca^{2+} and magnesium (Mg^{2+}). It transports Ca^{2+} ions directly into the cell through the plasma membrane. Lasalocid also has the ability to complex and transport catecholamines (Shen and Patel, 1977). Catecholamines and toxic oxidation products cause an influx of Ca^{2+} ions and the formation of free radicals, which leads to myocardial necrosis. Thus, toxic concentrations of ionophores cause Ca^{2+} overload in several ways. The increase of intracellular Na^+, results in the subsequent increase of intracellular Ca^{2+}. Mitochondria act as a buffer by sequestering the excess Ca^{2+} from the cytoplasm via Ca^{2+}-pumps, a process that requires energy. Consequently, the buffering capacity of the mitochondria is exhausted causing mitochondrial damage, resulting in a disruption of oxidative phosphorylation and an ultimate depletion of energy resources (Wrogemann and Pena, 1976). Without energy, the cell cannot pump Ca^{2+} out of the cytoplasm resulting in the accumulation of intracellular Ca^{2+}. Intracellular Ca^{2+} concentrations are further increased by the release of catecholamines and their degradation products (Jiang and Downing, 1990; Novilla, 2018; Reichenbach and Benditt, 1970). The elevated Ca^{2+} levels then result in the activation of various proteases and phospholipases, initiating various degradative processes such as the disassembly of myofilaments and membrane damage

(Boehmerle and Endres, 2011; Sandercock and Mitchell, 2004). According to Osweiler (1996) ionophores interfere with K^+ transport across mitochondrial membranes inhibiting adenosine triphosphate (ATP) hydrolysis and disrupting energy production. Additionally, exposure of rat neonatal cardiac myocytes to the Ca^{2+} ionophore A23187 (calcimycin) resulted in the production of ROS and a delayed decrease in the mitochondrial membrane potential (Przygodzki et al., 2005). Ionophores are also lipophilic with detergent properties and can cause disruption and damage to the plasma membrane through lipid peroxidation, consequently increasing the Ca^{2+} influx (Novilla, 2018). Eventually this leads to cell death. Membrane lipid peroxidation is caused when free radicals interact with the double bonds of unsaturated fatty acids that compromise the membrane phospholipids. Consequently, the impairment of ion channels and membrane transport proteins further disrupts ion homeostasis. One cause of channel and transporter disruption is direct oxidation of these proteins by free radicals. Alternatively, evidence suggests that the production of lipid hydroperoxides and aldehydes of various carbon-chain lengths during membrane lipid peroxidation also plays a role in inhibiting their function (Mattson, 1998). Monensin and narasin decrease adenosine triphosphatase (ATPase) activity (Wong et al., 1977), while salinomycin and lasalocid induces pH dependent inhibition of both coupled and uncoupled ATP hydrolysis (Estrada-O et al., 1974; Mitani et al., 1976). Ionophores alter pH through the transportation of H^+ across biological membranes. Monensin affects cellular transportation by shifting the pH and the function of acidic intracellular compartments i.e., endosomes, the Golgi apparatus and lysosomes (Grinde, 1983; Mahtal et al., 2020; Mollenhauer et al., 1990). Additionally, as a result of the disturbed ion gradients and subsequent osmotic uptake of water, these compartments swell. Late processing events in the Golgi apparatus, such as proteolytic cleavage and terminal glycosylation, are inhibited by monensin, however many of the incompletely processed molecules are still secreted by alternative pathways. Monensin does not appear to inhibit the internalisation of endosomes, but the degradation of internalised ligands may be prevented. Ionophores affect the internal environment of lysosomes, increasing their pH and subsequently inhibiting the complete degradation of cellular material (Grinde, 1983; Mahtal et al., 2020; Mollenhauer et al., 1990).
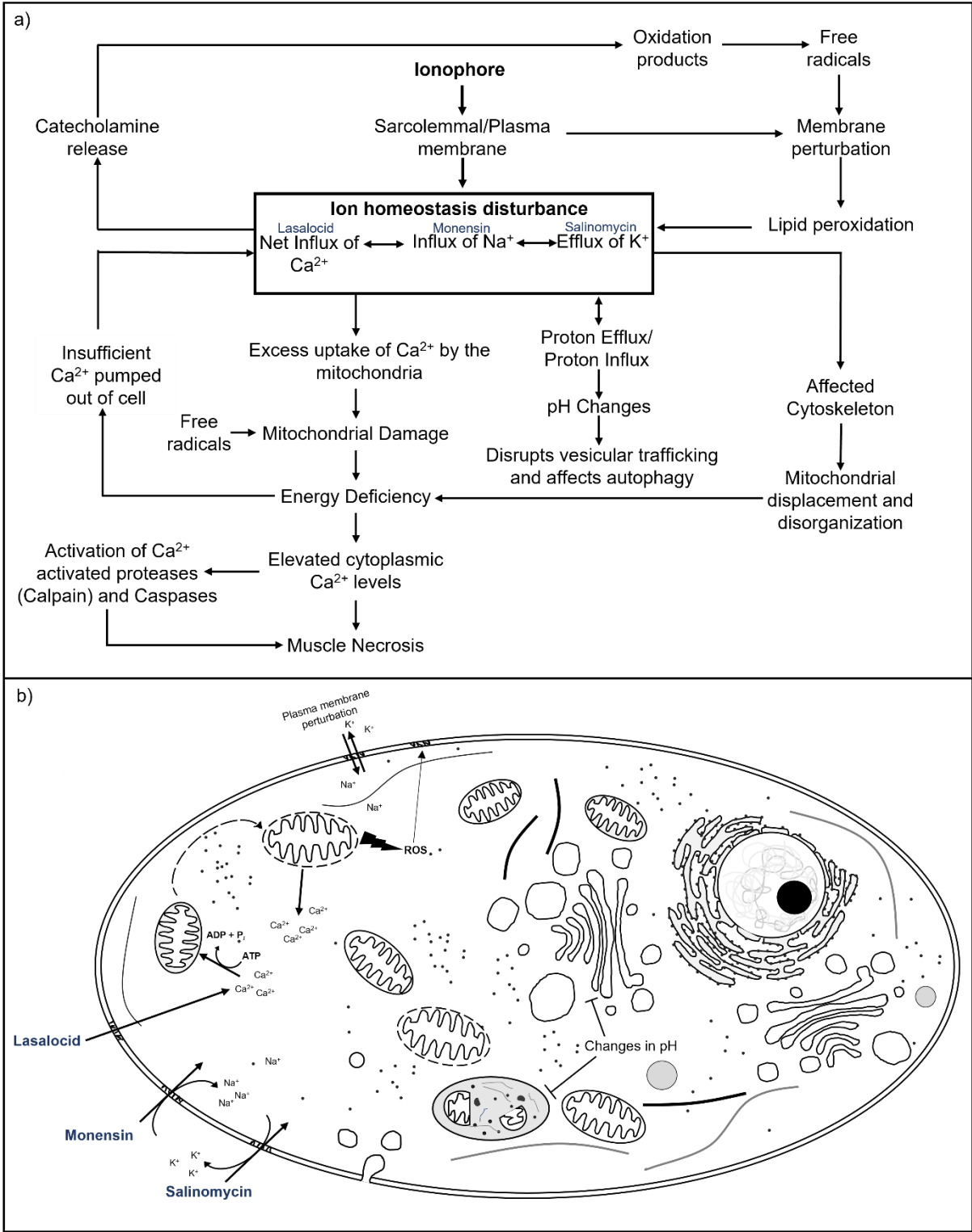
Figure 2.2 A diagram illustrating the possible mode of action of monensin, salinomycin and lasalocid (adapted from Novilla, 1992) (a) and the intracellular systems affected by the ionophores (b).

2.2.3 Ionophore Toxicosis

Ionophore toxicosis occurs in both target and non-target species, often as the result of miscalculations or mixing errors during feed preparation; the accidental ingestion of premix concentrates, or feed intended for a specific species fed to a more susceptible species. Additionally, extra-label use may result in adverse effects and drug incompatibilities which can enhance ionophore toxicity, such as with tiamulin that interferes with the metabolic degradation of ionophores in the liver (Carpenter et al., 2005; Geor and Robinson, 1985). It is believed that tiamulin forms a stable metabolic intermediate complex with cytochrome P450 inhibiting oxidative drug metabolism, thus resulting in slower elimination of the ionophore from the body (Witkamp et al., 1995). During large-scale feed production there exists the possibility of cross-contamination of feed additives, such as coccidiostats, from previous batches which may aid the development of antimicrobial resistance as well as result in the exposure of non-target species and subsequent adverse health effects (Hazards et al., 2021; O'Mahony et al., 2012). Thus, in certain countries legislation was introduced dealing with the maximum level of cross-contamination of feed additives allowed as a result of unavoidable carry over as well as the maximum residue limits for veterinary medicinal products in foodstuffs from animal origin. In South Africa, for example, the latter is regulated by Section 15 (1) of the Foodstuffs, Cosmetics and Disinfectants Act No. 54 (1972) of the South African Government (The Ministry of Health SA, 1977). Various analytical methods can be used to determine the levels of antibiotics in feed and animal tissues, as discussed below. Among the non-target species, horses are the most susceptible, but cases of poisoning in other species such as cats, dogs, humans and rabbits have been described (Bosch et al., 2018; Gy et al., 2020; Matsuoka et al., 1996; Pakozdy et al., 2010; Salles et al., 1994; Segev et al., 2004; Story and Doube, 2004). Most cases of accidental ionophore toxicosis involve monensin and salinomycin, however, poisoning with lasalocid, maduramicin and narasin have also been reported. The relative half-maximal lethal dosages (LD_{50}s) of monensin, salinomycin and lasalocid for different species are tabulated (**Table 2.2**).

Table 2.2 The acute oral LD_{50} of monensin, salinomycin and lasalocid for different species reported in mg/kg.

Species	Monensin	Salinomycin	Lasalocid
Cattle	26.4	-	50-150
Chicken	200	44.3	71.5
Horses	2-3	0.6	21.5
Mice	70-96	57.4	100-146
Rats	28.6-40.1	47.6-48.9	122->130
Sheep	11.9	-	75-350
Swine	16.7	-	30-50

Data referenced from Anderson, 2008; Gad et al., 1985; Galitzer et al., 1986; Hall, 2000; Hanson et al., 1981; Novilla, 2018; Potter et al., 1984; Todd et al., 1984.

2.2.4 Clinical signs, Diagnosis and Treatment

Animals suffering from ionophore toxicosis exhibit various clinical signs including feed refusal or anorexia, diarrhoea, depression, hypoactivity, dyspnoea, weakness, ataxia and recumbency (Bastianello and Fourie, 1996; Dowling, 1992; Gonzalez et al., 2005; Gruys et al., 2001; Gy et al., 2020; Hall, 2000; Matsuoka et al., 1996; Nel and Van der Walt, 1988; Oruc et al., 2011). On auscultation of the heart, tachycardia and cardiac arrhythmias are present (Aleman et al., 2007; Bastianello and Fourie, 1996; Decloedt et al., 2012; Fourie et al., 1991; Galitzer et al., 1986; Muylle et al., 1981; Nel and Van der Walt, 1988; Oruc et al., 2011; Shlosberg et al., 1997). Ionophore toxicity is dose and species dependent and, although most of these signs are a constant manifestation of ionophore intoxication, some variation in the appearance of clinical signs do occur. In horses, for example, signs of colic are observed (Gy et al., 2020; Nel and Van der Walt, 1988). With ionophore toxicosis, the cardiac and skeletal muscles are primarily affected, however, in both cats and dogs ionophore intoxication often manifests as a neuromuscular disorder. There has been several reports of cats and dogs suffering from ionophore toxicosis due to accidental ingestion or the presence of ionophores in commercial pet food (Bosch et al., 2018; Pakozdy et al., 2010; Segev et al., 2004; Van der Linde-Sipman et al., 1999). Affected animals suffered from lower motor neuron (LMN) dysfunction with paresis and paralysis often starting in the hind limbs before rapidly progressing to the forelimbs. Peripheral neuropathy was confirmed in some of the cases. Additional signs included dyspnoea and high body temperatures.

Unfortunately, the clinical signs and gross lesions of ionophore toxicity are not pathognomonic, thus six criteria should be considered before a diagnosis of ionophore intoxication can be confirmed (Novilla, 2018):

- History of feed-related problems in a herd or flock
- Clinical signs and clinical pathology manifested during the episode
- Gross post-mortem lesions
- Histopathological findings
- Exclusion of differential diagnoses such as nutritional (e.g., vitamin E and selenium deficiency), infectious diseases (e.g., bovine respiratory disease complex [shipping fever]), and other intoxications (e.g., botulism and cardiac glycoside-containing plants)
- Laboratory analysis of feed

When ionophore toxicosis is suspected, the first course of action is replacing the incriminated feed. At present there is no known antidote or treatment for ionophore intoxication and therapeutic interventions are mostly symptomatic and supportive. Activated charcoal, vitamin E/selenium injections and electrolyte and fluid therapy may be beneficial (Bosch et al., 2018; Novilla, 2018; Pakozdy et al., 2010; Segev et al., 2004; Van Vleet et al., 1983). It is theorised that both vitamin E and selenium help by stabilising the lipid membrane and protecting it from peroxidation (Tappel, 1980). The prognosis is guarded for any animal that has suspected myocardial damage (Gy et al., 2020; Hall, 2000). Even if the animal survives the initial acute phase of poisoning, the risk of potential long-term cardiac problems still exists. These problems include exercise intolerance, poor performance, congestive heart failure (evidenced by dyspnoea, hyperpnoea and ventral subcutaneous oedema), reduced lifespan and finally death (Aleman et al., 2007; Decloedt et al., 2012; Fourie et al., 1991; Gy et al., 2020; Muylle et al., 1981).
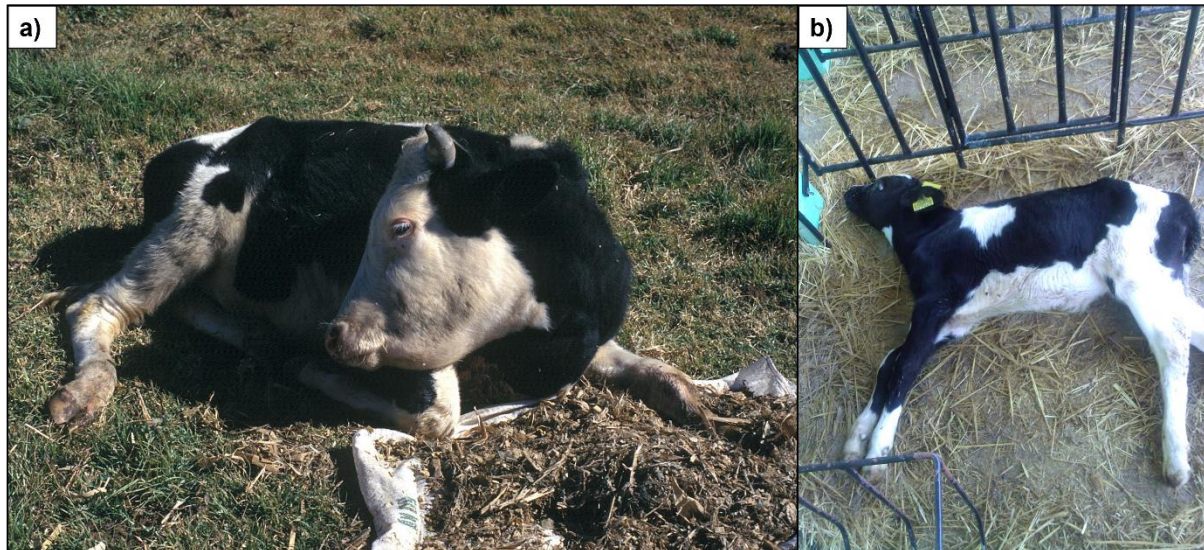
Figure 2.3 An ox suffering from subacute/chronic ionophore toxicosis with submandibular oedema suggestive of congestive heart failure (a). A calf suffering from acute ionophore toxicosis, laying in lateral recumbency (b). Photographs provided by Drs Fourie and Last to Prof CJ Botha, Department of Paraclinical Science, Faculty of Veterinary Sciences, University of Pretoria.

2.2.5 Clinical Pathology

Clinical pathological changes can be used for monitoring groups of animals, but changes may be absent in an individual due to the high degree of intraspecies variability. The absence of any abnormal finding does not exclude the possibility of poisoning, as animals may exhibit normal serum chemistry for a week or longer after ionophore ingestion and it is possible for the changes to occur less than 24 h before the animal dies (Hall, 2003). Clinical pathological changes observed with ionophore toxicosis are attributed to dehydration, electrolyte changes and muscle damage. Notably an elevation of serum aspartate transaminase (AST), creatine phosphokinase (CPK) and lactate dehydrogenase (LDH) concentrations are commonly observed. Serum concentrations of Ca^{2+} and K^+ are reduced (**Table 2.3**). An increase in the cardiac troponin concentration of the serum is indicative of myocardial damage; and this is often seen in horses (Decloedt et al., 2012). During ionophore toxicosis an increase in urine volume may be observed, with the accompanying decrease of urine osmolality. The specific gravity and the levels of glucose, protein and myoglobin in the urine increase, while the pH decrease (Galitzer et al., 1986; Plumlee et al., 1995). Caution is needed when interpreting any clinical pathological alterations, due to the high level of variability and sporadic occurrence of these changes.

Table 2.3 Possible clinical pathological changes caused by ionophores.

Blood Biochemistry	
Increase	**Decrease**
Alkaline phosphatase	Ca^{2+}
Aspartate transaminase	Na^+
Bilirubin	K^+
Blood urea nitrogen	
Cardiac troponin	
Creatinine	
Creatine phosphokinase	
Lactate dehydrogenase	
Nitrogen	
Total serum protein	
Haematology	
Increase	**Decrease**
Haematocrit	
Leukocytes	
Total platelets	

Data referenced from Aleman et al., 2007; Bosch et al., 2018; Britzi et al., 2017; Fourie et al., 1991; Galitzer., 1986; Geor and Robinson, 1985; Gruys et al., 2001; Matsuoka et al., 1996; Muylle et al., 1981; Nel et al., 1988; Shlosberg et al., 1997; Story and Doube, 2004.

2.2.6 Necropsy

As with clinical signs, gross lesions associated with ionophore toxicosis vary from species-to-species and between individuals. It is not rare for lesions to be totally absent in animals that died shortly after exposure to a lethal ionophore dose since lesions require time to develop. Therefore, lesions are more likely to appear in animals that survived a few days or longer after exposure. Gross lesions are typically found on the cardiac muscle of horses (Decloedt et al., 2012; Gruys et al., 2001), the skeletal muscles of sheep, pigs and dogs (Miskimins and Neiger, 1996), and with equal prevalence on both cardiac and skeletal muscle lesions in cattle and poultry (Novilla, 2018). Post-mortem examination of animals that succumbed to ionophore poisoning often reveal haemorrhages and pale areas in the cardiac (**Figure 2.4 a & c**) and skeletal muscles (Britzi et al., 2017; Van Vleet and Ferrans, 1984a). Other

notable findings include pulmonary oedema, hydropericardium, hydrothorax, ascites (**Figure 2.4 a & b**), subcutaneous oedema (**Figure 2.4 d**), gastroenteritis and congestion of the liver (Geor and Robinson, 1985; Gruys et al., 2001; Muylle et al., 1981; Shlosberg et al., 1997). Myoglobinuria, as evidenced by reddish-brown urine, is often observed in dogs, pigs and sheep as skeletal muscle lesions can be quite severe (Miskimins and Neiger, 1996; Plumlee et al., 1995; Van Vleet and Ferrans, 1984a; Wilson, 1980).
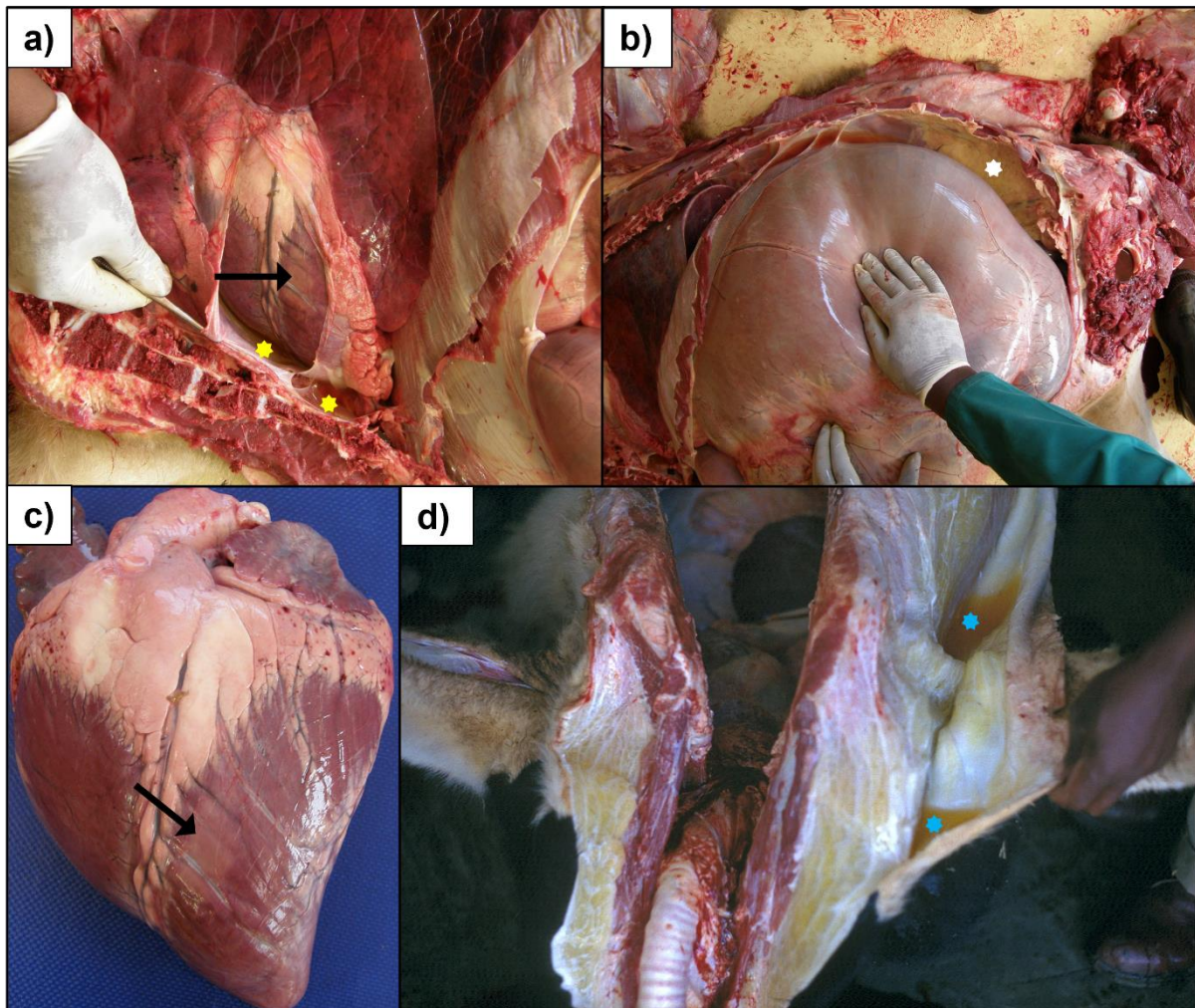
Figure 2.4 Necropsy findings in animals affected by ionophore toxicosis. There is an irregular area of pallor (black arrow) on the epicardial surface of the left ventricle (a and c). Notice the hydropericardium (a, yellow stars). Ascites (blood-stained watery effusion in the abdominal cavity) (b, white star) and subcutaneous oedema (d, blue stars) probably due to cardiac failure present in the affected animal. Photographs provided by Drs Fourie and Last to Prof CJ Botha, Department of Paraclinical Science, Faculty of Veterinary Science, University of Pretoria.

2.2.7 Histopathological Findings

Due to the ionophore's ability of perturbing ion homeostasis, excitable tissues such as muscle and nerves are more severely affected by ionophore poisoning.

Microscopical analysis of affected muscle demonstrates multifocal degeneration, loss of cross-striation, infiltration of inflammatory cells, necrosis and repair of muscle fibres with fibrous connective tissue (Ashrafihelan et al., 2014; Britzi et al., 2017; Carpenter et al., 2005; Decloedt et al., 2012; Gruys et al., 2001; Miskimins and Neiger, 1996; Muylle et al., 1981; Shlosberg et al., 1997). **Figure 2.5** depicts the diaphragm of a Bonsmara heifer that suffered from suspected monensin intoxication*. Single and groups of myofibers showed hyper-eosinophilic swelling (**black arrows**), loss of architectural structure with early myolysis and nuclear pyknosis, intracellular oedema (**black arrowhead**) and subendomysial oedema (**black stars**). Findings are variable, depending on dosage and time of exposure. With time, skeletal muscle fibres can regenerate, and the lesions disappear.

Repair of cardiac muscle takes place in the form of myocardial fibrosis. Secondary lesions as a result of congestive heart failure may be present and include pulmonary oedema, fluid accumulation in the body cavities, and liver and kidney necrosis, among others. **Figure 2.6** shows sections of the heart of a Bonsmara bull that died as a result of monensin intoxication*. The heart had single and groups of myofibers with hyper-eosinophilic swelling (**black arrows**), increased granularity in the cytoplasm due to mitochondrial swelling (**yellow arrows**), loss of architectural structure, myolysis and nuclear pyknosis.

In addition to their well-known effects on the cardiac and skeletal muscles of animals, ionophores have been associated with neurotoxic effects, especially in cats and dogs (as mentioned above). As with cardiac and skeletal muscles, findings may vary depending on the time of exposure, the dosage and the species affected. Reports indicate swelling, fragmentation and loss of axons in the peripheral nerves of affected animals (Decloedt et al., 2012; Pakozdy et al., 2010; Van der Linde-Sipman et al., 1999). Destruction of myelin sheaths, with the formation of digestion chambers and swollen Schwann cells filled with foamy macrophages were also noted.

*The diagnosis was based on a combination of epidemiological data, clinical examination, clinical signs, pathological results and toxicological analysis.
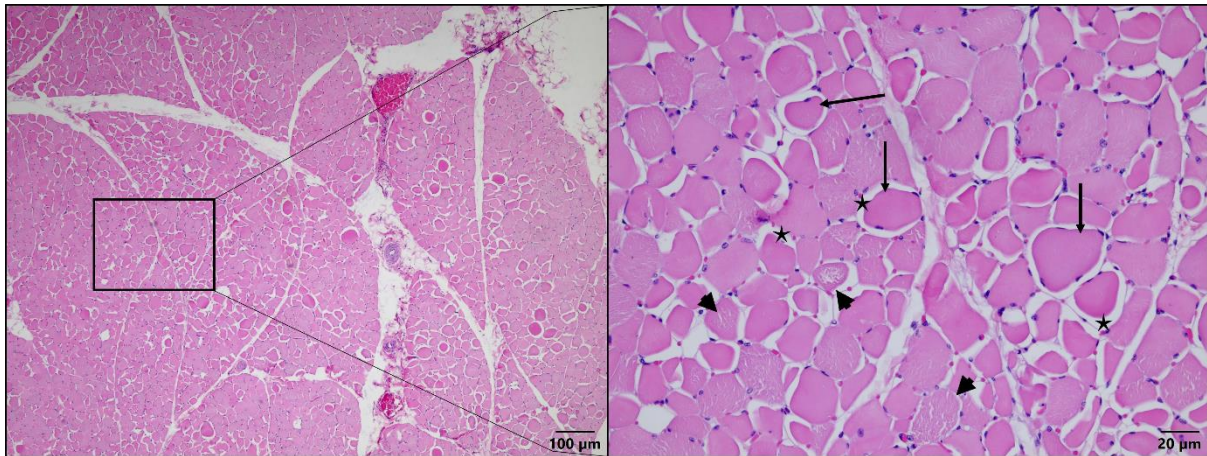
Figure 2.5 An H&E-stained cross section of the diaphragm of a Bonsmara heifer suffering from ionophore intoxication*. The black arrows indicate hyper-eosinophilic swelling suggesting acute necrosis. The black arrow heads and black stars indicate intracellular oedema and subendomysial oedema, respectively. Photographs provided by the Pathology Section, Department of Paraclinical Sciences, Faculty of Veterinary Science, University of Pretoria.
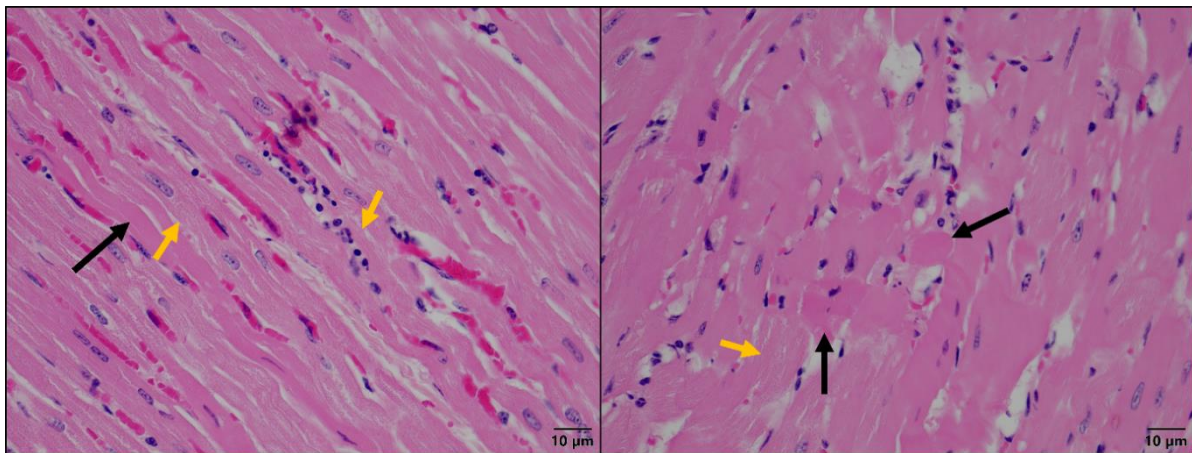
Figure 2.6 Longitudinal (left) and cross (right) H&E-stained sections of the heart of a Bonsmara bull that died due to ionophore (monensin) intoxication*. Swelling of single and groups of myofibers with increased eosinophilia (black arrows), as well as increased granularity in the cytoplasm (yellow arrows) were observed. Additionally, a loss of architectural structure, cytoplasmic lysis and nuclear pyknosis were visible. Photographs provided by the Pathology Section, Department of Paraclinical Sciences, Faculty of Veterinary Science, University of Pretoria.

2.2.8 Laboratory Analysis

To confirm a diagnosis of ionophore intoxication, analysis for the presence and quantity of ionophores in the feed and tissue is crucial. Diagnostic laboratories and manufacturers provide this service (Hall, 2000). However, identifying ionophores in the animal tissue is problematic and only proves that the animal was exposed to ionophores and does not indicate that such exposure was necessarily the cause of mortality. There have been several studies reporting on the fate of ionophores following oral administration in various species, including cattle and poultry (Diaz et

17

al., 2018; Donoho, 1984; Novilla, 2018). Ionophores are rapidly absorbed and metabolised in the liver, before being excreted in bile and do not accumulate in tissues of orally dosed animals when fed according to the recommended dosages (Diaz et al., 2018; Donoho, 1984). However, ionophores can accumulate in tissues, especially the liver, after exposure to toxic doses (Decloedt et al., 2012; Diaz et al., 2018; Shimshoni et al., 2014).

In South Africa, a thin layer chromatography (TLC) screening is first performed before the concentration of the specific ionophore in the feed sample is determined. Simple TLC is a fast, accurate and low-cost technique to ascertain the presence of ionophores in feed samples (Haag et al., 2011; Owles, 1984). The concentration of ionophores, i.e. monensin, salinomycin and narasin, in the feed can then be quantified using a calorimetric method (Golab et al., 1973). There are several other methods for ionophore analysis. A direct competitive enzyme-linked immunosorbent assay (ELISA) can be used, entailing the recognition of the ionophores present in a sample by antibodies. The ionophore-antibody complex is then bound by a secondary antibody immobilised to a microtiter plate. A substrate is added to generate a colour signal and the signal intensity can be used to estimate the quantity of ionophore present in the sample when compared to a standard. More sophisticated methods such as the high performance TLC method described by Bertini *et al.* (2003), liquid chromatography/tandem mass spectrometry (LC-MS/MS) (Abafe et al., 2020; Britzi et al., 2017; Ebel et al., 2004; Vudathala and Murphy, 2012) or reverse phase LC with fluorescent detection (Oruc et al., 2011), can be used to determine the presence of ionophores in feeds and tissues with greater accuracy.

2.3 Ionophores and their Application in Human Diseases

Ionophores are well known in the veterinary field due to their prophylactic use in production animals, however, it should be noted that evidence for their practical application in the treatment of human diseases have also been elucidated. Ionophores have shown antibacterial, antifungal, antiparasitic, antiviral and anticancer activities. In fact, salinomycin and its derivatives have been described as a "magic bullet" due to their "multimodal" mechanism of action (Antoszczak and

Huczyński, 2019). For example, salinomycin and its semi-synthetic derivatives showed excellent inhibitory activity against methicillin-resistant *Staphylococcus aureus* and *Staphylococcus epidermidis* (Sulik et al., 2020). Monensin inhibited the growth of *Candida albicans* by disrupting the function of the fungal vacuole (Tournu et al., 2017). Weete et al., (1988) reported monensin's ability to inhibit the growth and sterol production of four fungi i.e., *Achlya bisexualis, Hypomyces chlorinus*, *Neurospora crassa* and *Taphrina deformans*. Monovalent ionophores displayed potent antimalarial effects both *in vitro* and *in vivo* (Adovelande and Schrével, 1996). Both the asexual and sexual stages of *Plasmodium falciparum* are susceptible to ionophores, while the ookinete development and oocyst formation in the mosquito midgut are also inhibited (D'Alessandro et al., 2015). The antimalarial and transmission blocking activity of ionophores indicate that they could be repurposed in the fight against malaria. A few reports have indicated ionophores as potential antiviral agents. Ionophores inhibit human immunodeficiency virus (HIV) replication in human T-lymphoblastoid (H9) cells (Nakamura et al., 1992). As previously mentioned, ionophores affect the pH of various intracellular compartments, which influences virus assembly. Salinomycin disrupted the acidification of the endosomal-lysosomal compartments inhibiting influenza virus infection (Jang et al., 2018). Ionophores have demonstrated potential as anticancer agents and chemosensitizers (Kaushik et al., 2018). Compared to paclitaxel, a commonly used anticancer drug, salinomycin was at least 100-fold more effective against cancer stem cells (Gupta et al., 2009). Salinomycin also has potent anticancer effects against multidrug resistant cancers (Manmuan et al., 2017; Zhou et al., 2015) and can overcome drug resistance by inhibiting the transporters responsible for the efflux of anticancer drugs from cancer cells (Hermawan et al., 2016; Kim et al., 2015).

2.4 Ionophores and their Intracellular Effects

2.4.1 Ultrastructural Pathology of Tissues and Cells Affected by Ionophore Poisoning

Several studies have focused on describing the ultrastructural effects of monensin toxicosis on cardiac and skeletal myocytes. In general, ionophore poisoning results in mitochondrial swelling, sarcoplasmic vacuolisation, disrupted contractile material, infiltration of macrophages and necrosis (Confer et al., 1983; Mollenhauer et al.,

1981; Van Vleet and Ferrans, 1984a, b). Mitochondria are primarily affected with ultrastructural changes such as swelling, disrupted cristae and flocculent densities that can be observed as early as day one post exposure (Van Vleet and Ferrans, 1984a, b). Van Vleet and Ferrans (1984a) described the alterations of skeletal muscle ultrastructure with acute monensin poisoning in swine. Two patterns of skeletal muscle necrosis with selectivity towards Type I (slow twitch oxidative) fibres were reported. The first pattern included disruption of the fibre contractile apparatus, forming dense and filamentous bundles, scattered within the external lamina; swollen mitochondria with flocculent matrix densities and pyknotic nuclei. The second necrotic pattern showed uniformly dense fibres with undisrupted sarcoplasm. Swift resolution of the fibre necrosis occurred by infiltration of macrophages and the subsequent phagocytosis of the sarcoplasmic debris. Regeneration was initiated almost immediately by the activation of satellite cells to form presumptive myoblasts and resulted in the complete restoration of muscle damage. Furthermore, changes of swine atrial myocardium after monensin toxicosis was also described (Van Vleet and Ferrans, 1984b). Myocytes degenerated and died via necrosis, followed by extensive macrophage infiltration and phagocytosis of all sarcoplasmic debris. Necrotic cells had disrupted contractile material with hypercontraction bands and an accumulation of matrical densities. Sublethal damage was described as moderate to marked myofibrillar lysis and sarcoplasmic vacuolisation. Other descriptions of the ultrastructural alterations caused by monensin toxicosis include studies by Mollenhauer et al. (1981) and Confer et al. (1983) which focused on ponies and sheep, respectively. Briefly, mitochondrial swelling and lipidosis was observed in the myocardial tissues of the ponies 28 to 72 h after exposure to 4 mg monensin/kg (body weight) (Mollenhauer et al., 1981). The hepatocytes had increased numbers of smooth endoplasmic reticulum (ER), lipid droplets, peroxisomes and vacuoles bounded by fibrous material. Ultrastructural changes in sheep exposed to monensin included early and severe mitochondrial swelling, lipid accumulation, myofibrillar alterations, necrosis and macrophage infiltration (Confer et al., 1983). The regeneration of myocytes via myoblast proliferation occurred as early as day four after the initial exposure.

In vitro exposure of tissue slices and cells to ionophores resulted in slightly different ultrastructural alterations. In contrast to the mitochondrial swelling seen in the tissues

of animals exposed to ionophores, the mitochondria of cells *in vitro* are often condensed (Mollenhauer et al., 1990; Paddock and Albrecht-Buehler, 1986). Additionally, distension of the Golgi apparatus and excessive vacuolation of the cytoplasm occurs with electron-lucent vesicles distributed throughout the cells (Mollenhauer et al., 1990; Vladutiu, 1984).

2.4.2 The Cytoskeleton

Cytoskeletal Components

The eukaryotic cytoskeleton is an interconnected network, mainly composed of actin filaments (microfilaments), microtubules and intermediate filaments. These three components act together, alongside various other proteins, to lend structural support to cells, organise and transport cellular content, as well as enable cells to alter their shape during movement (Fletcher and Mullins, 2010; Hohmann and Dehghani, 2019).

Microfilaments are composed of homodimeric actin molecules that are continuously polymerised and depolymerised in response to various intra- and extracellular signals. Microfilaments are less rigid compared to microtubules, but can form highly organised, stiff structures in the presence of a high concentration of crosslinkers (Fletcher and Mullins, 2010). An increase in the organisation and length of the microfilament network is associated with cell stiffness and immobilisation. In contrast, shorter and extensively branched microfilaments are found in connection to cellular movement, for instance at the leading edge of moving cells (Fletcher and Mullins, 2010; Insall and Machesky, 2009; Paddock and Albrecht-Buehler, 1986). Microfilaments are involved in various cellular processes such as chemotaxis, cell-to-cell communication, cell motility, change in cell shape and endocytosis (Fletcher and Mullins, 2010).

Microtubules are stiff polymer filaments consisting of α- and β-tubulin dimers that wind together to form a hollow cylinder around 24 nm wide. These filaments have the ability to change between two polymerisation states i.e., stably growing and rapidly shrinking, which allows them to quickly reorganise in response to various signals (Mitchison and Kirschner, 1984). Microtubules are perhaps most well known for their involvement during mitosis in separating chromosomes, but they are also involved in cell motility and cell signalling events (Binarová and Tuszynski, 2019; Fletcher and

Mullins, 2010; Hohmann and Dehghani, 2019). Furthermore, in cancer cells some tubulin isotypes are overexpressed and localised in the nucleus, while other isotypes exhibit bioenergetic functions through the regulation of mitochondrial ion channels (Binarová and Tuszynski, 2019). Previous studies have demonstrated that *in vitro* microtubule polymerisation requires Mg^{2+} ions, while high concentrations of Na^+, K^+ and Ca^{2+} inhibited microtubule formation (Olmsted and Borisy, 1975).

Both microfilaments and microtubules are considered polar and play a critical role in membrane trafficking. They generate force that help move cargo and provide "tracks" for the long-range delivery of cargo.

Intermediate filaments are a class of related proteins that are not as rigid as either microfilaments or microtubules, however, they are not polarised and are thus unable to support the directional movement of motor proteins (Fletcher and Mullins, 2010). Additionally, unlike microfilaments and microtubules that are composed of a single type of protein i.e., actin and tubulin, intermediate filaments are composed of a variety of proteins depending on the cell type, differentiation status and cellular location (Hohmann and Dehghani, 2019). More than 50 intermediate filament proteins have been classified into five different types (Type I-V) based on the similarities between their amino acid sequences. Intermediate filaments play a structural role in cells and assists with the internal organisation as well as provide a scaffold for the integration of other cytoskeletal components (Fletcher and Mullins, 2010; Hohmann and Dehghani, 2019; Paulin and Li, 2004).

Together microfilaments, microtubules and intermediate filaments are linked to form a network that can transmit compressive and tensile stresses, as well as sense the mechanical microenvironment (Janmey and McCulloch, 2007).

Muscle Cytoskeleton

In muscles, the cytoskeletal network, alongside ATP and Ca^{2+} is responsible for contraction. Myoblasts are mononucleated precursor cells of muscle fibres. During differentiation the myoblasts fuse to form multinucleated fibres, with further differentiation being associated with the formation of cross-striation and contractibility (Yaffe, 1968). The sarcomere is the most basic contractile unit of the muscle and consists of actin (thin) and myosin (thick) filaments (**Figure 2.7**).
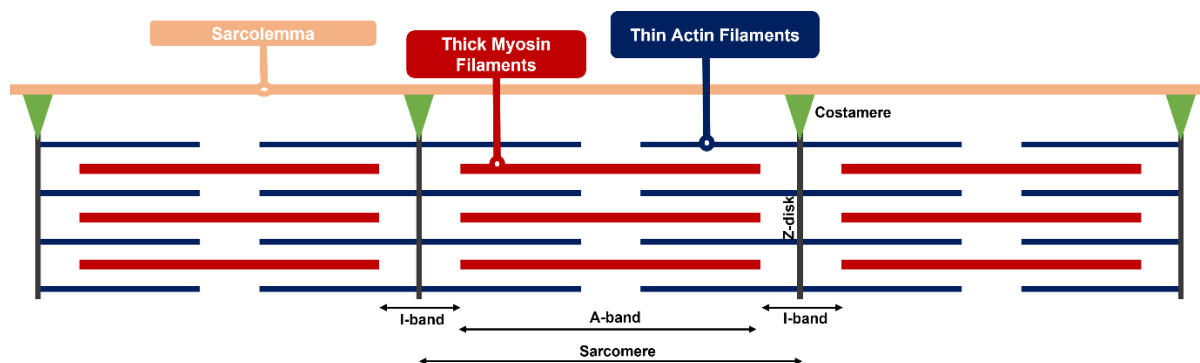
Figure 2.7 A schematic diagram of a sarcomere. The sarcomere is defined as the region between the two Z-disks. Each sarcomere consists of a thick (myosin) filament and two halves of the thin (actin) filaments.

Myocytes contain, in addition to actin and myosin, various intermediate filament proteins such as cytokeratins, desmin, lamins, nestin, syncoilin, synemin and vimentin (Carlsson and Thornell, 2001). Of these, desmin is an intermediate filament protein specific to muscle. It is one of the first muscle-specific proteins that emerges during myogenesis, with lower concentrations in replicating myoblasts and satellite cells, and higher concentrations in differentiated myotubes (Paulin and Li, 2004). Desmin is found primarily in the Z-disk of striated muscle and is critical in maintaining the muscle cytoarchitecture. The intermediate filament forms an extra-sarcomeric scaffold that binds the contractile machinery to the sub-sarcolemmal cytoskeleton, the nuclei, and other organelles (Agnetti et al., 2021; Capetanaki et al., 2007; Costa et al., 2004; Mermelstein et al., 2005; Paulin and Li, 2004). Desmin also regulates the location of mitochondria in the cytoplasm of myocytes and thus affects their respiratory ability (Capetanaki, 2002; Dayal et al., 2020; Kuznetsov et al., 2020; Milner et al., 2000).

Desmin, alongside other intermediate filaments, such as synemin (also known as desmuslin), paranemin and syncoilin, connect the Z-disk to the costameres at the sarcolemma and may assist in the organisation of the myofibrils (O'Neill et al., 2002). Costameres are supramolecular structures consisting of two major protein complexes i.e., the dystrophin-glycoprotein complex and the integrin-vinculin-talin complex. They assist in the assembly and stabilisation of the sarcomere as well as function to link the sarcomeres to the extracellular matrix, allowing the transmission of mechanical forces (Jaka et al., 2015). Synemin co-polymerises with desmin at the Z-disk in both cardiac and skeletal muscle, assists with structural support and connects desmin to the extracellular environment (Lund et al., 2012; Mizuno et al.,

2004; Mizuno et al., 2001). Additionally, synemin functions in various signalling pathways including the protein kinase A (PKA) and phosphoinositide 3-kinase (PI3K)-Akt signalling pathways (Pitre et al., 2012; Russell et al., 2006).

The role of microtubules within myocytes, specifically in context of the contractile apparatus, is not well-known. Detyrosinated microtubules, are associated with desmin at the Z-disk and form springs alongside of the sarcomere, conferring resistance during contraction and regulating mechano-transduction (Robison et al., 2016; Robison and Prosser, 2017). Additionally, they function as a mechanical link between the sarcomeric cytoskeleton and the non-sarcomeric cytoskeleton.

2.4.3 Effects of Ionophores on the Cytoskeleton

The cytoskeleton of cells can be indirectly affected during ionophore toxicosis. Monensin affects the microfilaments in mouse fibroblasts (3T3 cell line) causing the nuclei of 20% of cells with circular nuclei to rotate, while the distribution of microtubules and intermediate filaments remained unaffected (Paddock and Albrecht-Buehler, 1986). Salinomycin affected the microfilaments of certain cancer cells. Sun et al. (2017) reported that salinomycin increased the formation of microfilaments in liver cancer stem cells, increasing the strength of the cytoskeleton and subsequently inhibiting the migration and invasion of these cells. In another study, salinomycin inhibited the migration of pancreatic cancer cells by disrupting actin stress fibres (Schenk et al., 2015). Lasalocid was used in a study that highlighted the role of Ca^{2+} and H^+ in actin polymerisation and membrane fusion in the acrosomal reaction of *Echinoderm* sperm (Tilney et al., 1978). Ionophores can induce the acrosomal reaction by elevating the intracellular pH, which is accomplished by the efflux of H^+ as a result of the influx of other ions transported by the ionophores. The elevated pH in turn is responsible for actin polymerisation. Lasalocid and calcimycin decreased the amount of axonal microtubules and inhibited rapid axonal transport in frog sciatic nerves, possibly as a result of the increased intracellular Ca^{2+} (Kanje et al., 1981).

Ionophores, thus, affect the cytoskeleton of cells via their downstream effects which results in further alteration of the cells.

2.5 Ionophores in *In Vitro* Experimentation

2.5.1 *In Vitro* Cytotoxicity

Although *in vivo* studies are an invaluable tool in toxicity research, the use of animal models when other models are available and feasible, is an ethical concern (Curzer et al., 2016). *In vitro* cell culture models are an ideal substitute for live animals, especially when the research focuses on a compound's effects on specific cells or organelles. The term '*in vitro*' means 'within the glass' and refers to experiments conducted in a controlled environment. *In vitro* studies fall short of *in vivo* studies when it comes to investigating the pharmacokinetics of absorption, distribution, metabolism, and excretion of compounds (Freshney, 2001). However, *in vitro* studies have the advantage of simplification, convenience and reproducibility with experiments focusing on more detailed analysis than what would be possible if the focus were on the whole organism. Additionally, the set-up and analysis of these experiments are relatively straightforward. Cell culture studies reduce the interplay between several types of cells, the extracellular matrix, and the rest of the organism to only focus on one type of cell in a controlled environment. Immortalisation of cell lines allow for the continuous subculturing of these cells; however, care should be taken as genetic instability combined with selection pressure can cause cells to lose some of the characteristics or completely diverge from the original cell type.

In vitro cytotoxicity and viability assays were developed to determine the toxicity of a compound and are the first step in confirming a toxin's mechanism of action. The 3-(4,5-dimethylthiazol-2-yl)-2,5-diphenyltetrazolium bromide (MTT) assay, first described by Mosmann et al. (1983), is one of the most used assays to determine cytotoxicity. The assay relies on the mitochondrial enzymes of viable cells to reduce the yellow MTT salt into an insoluble, purple formazan product. Cell viability is thus proportional to absorbance i.e., there is a direct relationship between increasing absorbance values and increasing number of viable cells. The MTT assay is less sensitive compared to other fluorescent or luminescent assays, and due to the formation of crystals and addition of organic solvents, toxic to cells (Aslantürk, 2018). The assay is thus limited to an end-point assay and no further experiments can be performed after completion of the assay. However, despite its limitations it is a relatively simple assay and is well known as the gold standard for cytotoxicity testing.

2.5.2 Mechanisms of Cell Death

A compound can be considered cytotoxic if it alters cellular morphology, negatively affects cell surface attachment, cellular growth and proliferation or cause cell death and disintegration (Horvath, 1980). According to the Nomenclature Committee on Cell Death (NCCD), a cell is dead only when the cell has lost the integrity of its plasma membrane, completely fragmented into apoptotic bodies or was phagocytosed by adjacent cells (Kroemer et al., 2009). Cell death is often classified based on morphological criteria into three groups i.e., apoptosis, autophagy and necrosis (**Figure 2.8**). Historically this was denoted as type I, type II and type III cell death, respectively. However, it has become apparent that the classic method of categorising cell death can often be oversimplified and inaccurate (Galluzzi et al., 2012b; Kroemer et al., 2009; Kroemer and Levine, 2008). Cell death differs between the *in vitro* and *in vivo* environment. Autophagic cell death rarely affects single cells *in vivo*, and cells undergoing autophagy are usually phagocytosed by neighbouring cells (Baehrecke, 2002; Clarke, 1990). Necrosis can be an alternate way of programmed cell death with important functions, including the induction of a proinflammatory response (Edinger and Thompson, 2004). Additionally, other modes of cell death such as pyroptosis and autolysis with specific morphological and molecular characteristics have also been reported (Fink and Cookson, 2005; Galluzzi et al., 2018; Liu et al., 2013). Still, the original classification of cell death combined with the detailed direction of molecular techniques assist in elucidating the various potential pathways causing cell death.
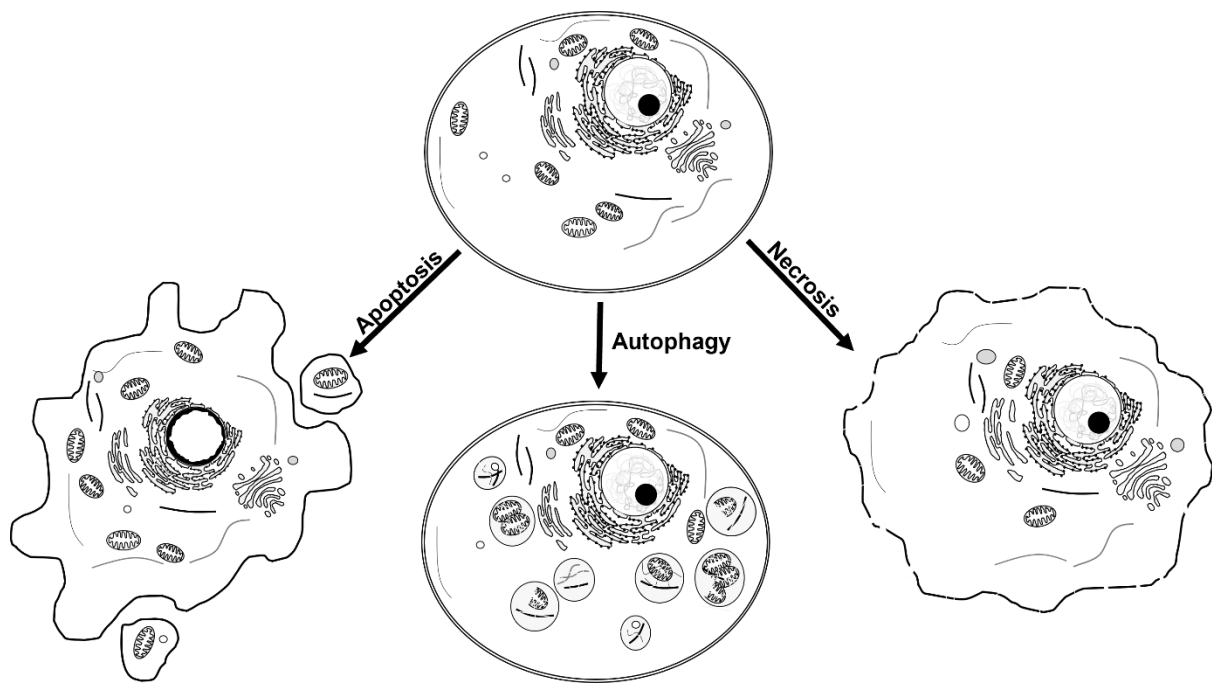
Figure 2.8 The morphology of cells undergoing apoptosis, autophagy and necrosis. Historically, the mechanism of cell death has been classified based on the morphological features that manifest during the cell death process.

Apoptosis

Apoptosis, also known as programmed cell death, is a highly regulated, energy dependent form of cell death. It plays a critical role in various physiological processes including embryogenesis, regulation of cell population and the removal of damaged cells (Elmore, 2007; Horvitz, 1994; Norbury and Hickson, 2001; Renehan et al., 2001). Irregular or dysfunctional apoptosis can bring about a variety of pathological conditions such as auto-immune disease, neurological degeneration, developmental defects and cancer (Elmore, 2007).

Morphologically, apoptosis can be identified using either light or electron microscopy based on an apoptotic cell's characteristic appearance (Burattini and Falcieri, 2013; Kerr et al., 1972). The cells shrink with both the nucleus and the cytoplasm condensing and the cell appearing round or oval with closely packed cytoplasmic organelles. Nuclear condensation occurs, with the nuclear material condensing either peripherally under the nuclear membrane (chromatin margination) or as uniformly dense nuclei. This is followed by nuclear fragmentation (karyorrhexis) and plasma membrane blebbing. The cell then disperses into apoptotic bodies, consisting of closely packed organelles, with or without nuclear material, encircled by an intact plasma membrane and is finally engulfed by neighbouring phagocytic cells.

In cell cultures, where phagocytic cells are absent, these apoptotic bodies undergo secondary necrosis (Berghe et al., 2010; Elmore, 2007).

Apoptosis is induced by either an extrinsic (death receptor) or an intrinsic (mitochondrial) pathway, both of which converge in an executioner pathway. The extrinsic pathway is initiated through transmembrane receptor-mediated interaction. A group of receptors from the tumour necrosis factor (TNF) receptor superfamily contains cytoplasmic 'death domains' that, upon binding with a ligand on the surface of the cell, transmit a death signal (Ashkenazi and Dixit, 1998; Smith et al., 1994). The death receptor recruits and binds an adapter protein with the corresponding death domain, which associates with procaspase-8 via the dimerization of the death effector domains. A death inducing signalling complex (DISC) is formed, resulting in the autocatalysis, and subsequent activation of caspase-8 (Kischkel et al., 1995). The activation of caspase-8 leads to the executioner pathway.

The intrinsic pathway includes a diverse range of non-receptor mediated stimuli that can act in either a positive or negative fashion to generate intracellular signals (Elmore, 2007). The signals generated by the various stimuli act on the inner mitochondrial membrane, opening a mitochondrial permeability transition (MPT) pore. The MPT pore results in the loss of mitochondrial membrane potential, resulting in the release of various pro-apoptotic proteins such as cytochrome C (Raff, 1998). Cytochrome C binds to Apaf1 and procaspase-9, forming a complex known as an 'apoptosome' (Saelens et al., 2004). The formation of the apoptosome causes the activation of caspase-9 and triggers the executioner pathway. Mitochondrial membrane permeability is regulated by members of the Bcl-2 protein family that can either be pro-apoptotic or anti-apoptotic (Saelens et al., 2004).

Both the extrinsic and intrinsic apoptosis pathways convene at the executioner pathway. During the executioner pathway execution caspases (e.g., caspase-3) are activated, which results in the cross-linking of proteins, the degradation of nuclear and cytoskeletal proteins, cleavage of deoxyribonucleic acids (DNA), formation of apoptotic bodies and the externalisation of phosphatidyl serine on the plasma membrane by which neighbouring phagocytic cells can recognise and engulf the apoptotic bodies (Elmore, 2007; Galluzzi et al., 2018). *In vivo,* apoptosis causes a

reduced inflammatory response, as the cell does not release its constituents into the surrounding environment.

Apoptosis can be determined based on a cells' morphological, biochemical and molecular characteristics using various methods. As mentioned before, electron microscopy can be used to inspect cells for the classical features of apoptosis. Additionally, apoptotic cells can be identified using techniques measuring caspase activation, phosphatidyl serine externalisation and DNA fragmentation. The terminal deoxynucleotidyl transferase-dUTP nick end labelling (TUNEL) assay, developed in 1992, is a widely used assay to detect fragmented DNA (Gavrieli et al., 1992). The fragmentation of DNA is a hallmark, as well as the ultimate determinate of apoptosis.

It should be noted that apoptosis is a natural process, and low levels of apoptosis can be expected in healthy tissues as apoptosis commonly occurs during normal development, aging and as a homeostatic mechanism to maintain cell populations in tissues (Baehrecke, 2002; Elmore, 2007).

Autophagy

Autophagic cell death is morphologically characterised as cell death accompanied by the extensive autophagic vacuolisation of the cytoplasm, but without any chromatin condensation (Kroemer et al., 2009). During macro-autophagy (subsequently referred to as autophagy) cellular material is sequestered in the autophagosome, a double membraned structure (Lane et al., 2013). The autophagosome fuses with lysosomes forming an autolysosome, a single membraned structure containing degrading cellular material and organelles.

The term 'autophagic cell death' is often used incorrectly to describe cells that die *with* autophagy as opposed to cells that die *due* to autophagy (Kroemer and Levine, 2008). Autophagy is a physiological process that assist with cell survival during periods of starvation, growth factor deprivation and other stress conditions. It helps maintain energy homeostasis, recycles nutrients and degrades toxic cellular content. High levels of autophagy in apoptotic and necrotic cells are considered a 'self-clearance' mechanism and is essential for the removal of dead cells (Qu et al., 2007).

Autophagy can be clearly identified using transmission electron microscopy (TEM); however, molecular techniques are required to determine whether the cells die via

the autophagic death pathway. A cell can be defined as dying due to autophagy when genetic manipulation of at least two different autophagic genes/regulators such as AMBRA1, ATG5, ATG12 or beclin1 inhibits cell death (Galluzzi et al., 2018; Galluzzi et al., 2012b).

Necrosis

Cells undergoing necrosis are morphologically defined by oncosis; swelling organelles such as the ER, Golgi apparatus and mitochondria; permeabilization of the plasma membrane; and finally the loss of cellular content (Burattini and Falcieri, 2013; Kroemer et al., 2009). *In vivo*, necrosis is often associated with an inflammatory response due to cell content leaking into the surrounding tissues. Necrosis causes several other pathogenic processes including production of ROS, ATP depletion, Ca^{2+} overload, the perinuclear clustering of organelles, activation of non-apoptotic proteases and lysosomal rupture (Golstein and Kroemer, 2007). Historically, necrosis was considered to be an accidental, uncontrollable form of cell death. However, more recent evidence indicated that the necrotic process is regulated by various signal transduction pathways and catabolic processes (programmed necrosis) (Festjens et al., 2006; Golstein and Kroemer, 2007).

As with apoptosis, necrosis can be identified through studying the cells' morphological features using electron microscopy. Biochemically, necrosis is defined as cell death lacking both apoptotic and autophagic markers (Kroemer et al., 2009). Additionally, assays determining the plasma membrane integrity of cells, such as the lactate dehydrogenase (LDH) assay or propidium iodide dye, can be used to identify necrotic cells.

Caveats, Limitations and Other Forms of Cell Death

Although categorising cell death into apoptosis, autophagy or necrosis is straightforward, such assumptions may be flawed. Cells within the same population can experience different types of cell death and even within a cell multiple cell death pathways can be active at once (Ankarcrona et al., 1995; Kostin et al., 2003; Leist et al., 1997). Often the type of cell death i.e., programmed death pathway or necrosis is dependent on the magnitude of the insult received (Bonfoco et al., 1995; Dypbukt et al., 1994; Fischer et al., 2000; Zysk et al., 2000).

Apoptosis is often seen as synonymous with programmed cell death, however there are other types of programmed or regulated cell death mechanisms such as pyroptosis, entosis and anoikis (Kroemer et al., 2009). Pyroptosis is a pro-inflammatory form of programmed cell death, initially identified in bacteria-infected macrophages and is dependent on caspase-1 (Brennan and Cookson, 2000). Entosis occurs when one cell engulfs another live cell in its surroundings, which then dies within the phagosome (Mormone et al., 2006; Overholtzer et al., 2007). Anoikis is molecularly similar to apoptosis, but induced by the loss of attachment between a cell and substrate or neighbouring cells (Grossmann, 2002).

The term necrosis, which describes the degradation after cell death, is seen by a few as an improper term to use for a mechanism of cell death (Elmore, 2007). Oncosis is used to define the process that leads to necrosis with cell swelling and karyolysis, and thus the terms "oncotic necrosis" and "oncotic cell death" is recommended by some (Levin et al., 1999; Majno and Joris, 1995). However, these terms are not widely used.

2.5.3 *In Vitro* Cytotoxicity with the focus on Ionophores

Various *in vitro* studies have been conducted determining the effects of ionophores on cells and the mechanisms by which they induce cytotoxicity and cell death. The EC_{50}s of monensin, salinomycin and lasalocid on several cell lines are tabulated (**Table 2.4**).

Silybin, a cell membrane stabiliser, permeability regulator and antioxidant, reduced the cytotoxicity of monensin, salinomycin and lasalocid on hepatoma on skeletal muscle cell lines (Cybulski et al., 2015; Radko et al., 2011, 2013a, b). The authors reported that exposure to the ionophores affected cell metabolism and protein synthesis, as well as disrupted the integrity of cell membranes. Radko et al. (2013a, b) concluded that the plasma membrane of rat skeletal muscle myoblasts (L6 cell line) is damaged due to salinomycin and lasalocid toxicity before mitochondrial function is affected. In contrast, monensin had a greater effect on mitochondrial activity. In murine dorsal root ganglia, salinomycin resulted in the activation of calpain, which induced caspase-mediated apoptosis (Boehmerle and Endres, 2011).

Cancer cells are relatively susceptible to ionophores, and many have EC_{50}s in the low micromolar to nanomolar range after 48 h exposure. Monensin, salinomycin and

lasalocid have all previously been shown to inhibit proliferation and induce apoptosis in various cancers and cancer stem cells e.g. breast cancer, endometrial cancer, hepatocellular cancer, ovarian cancer and prostate cancer cells as well as in osteosarcoma and lymphoblasts cell lines (Iljin et al., 2009; Kaushik et al., 2018; Ketola et al., 2010; Kiełbasiński et al., 2020; Kim et al., 2017a; Kim et al., 2017b; Kim et al., 2016; Lu et al., 2011; Park et al., 2003; Park et al., 2002; Tyagi and Patro, 2019). Oxidative stress due to the production of ROS and alteration of the mitochondrial membrane potential have been reported as mediators for apoptotic cell death (Ketola et al., 2010; Kim et al., 2017a; Kim et al., 2016) as well as programmed necrosis (Qin et al., 2015). Exposure to ionophores also resulted in autophagy. Various studies noted the cytoprotective effects of autophagy and that inhibition of autophagy resulted in enhanced apoptosis (Kim et al., 2017a; Kim et al., 2017b; Kim et al., 2016). Monensin and lasalocid affect autophagy by either increasing the number of autophagic vesicles or lowering their degradation ability (Grinde, 1983; Mahtal et al., 2020; Mollenhauer et al., 1990). Lavine and Arrizabalaga (2012) reported that monensin kills *Toxoplasma gondii* by inducing autophagy in the parasite.

In addition to apoptosis and autophagy, Souza et al. (2005) reported that monensin induced necrosis in cultured murine fibroblasts (L929 cell line), possibly due to early mitochondrial damage. Salinomycin caused both apoptosis and programmed necrosis in glioma cells (U87MG, U251MG and EFC-2 cell line), with the latter contributing to the majority of cell death (Qin et al., 2015).

Table 2.4 EC_{50}s obtained for monensin, salinomycin and lasalocid in different cell lines.

Cell Line	Ionophore	Exposure Time	$EC_{50} \pm$ SEM (µM)	REF
FaO [a]	Lasalocid	24 h	4.9 ± 0.57	1
HepG2 [a]	Monensin	24 h	6.7 ± 1.8	
	Salinomycin	24 h	13.9 ± 1.7	2
	Lasalocid	24 h	4.8 ± 1.20	
LMH [a]	Monensin	24 h	0.8 ± 0.2	
	Salinomycin	24 h	27.1 ± 6.9	3,4
	Lasalocid	24 h	7.0 ± 0.54	
L6 cells [b]	Monensin	24 h	58.3 ± 11.5	3,4
	Salinomycin	24 h	156.3 ± 16.1	
	Lasalocid	24 h	14.0 ± 1.08	
Ishikawa [c]	Salinomycin	24 h	~1	5
VCaP [d]	Monensin	48 h	0.039 ± 0.019	6
LNCaP [d]	Monensin	48 h	0.090 ± 0.037	6
DuCaP [d]	Monensin	48 h	0.009 ± 0.002	6
RWPE-1 [e]	Monensin	48 h	>10	6
EP156T [e]	Monensin	48 h	>1	6
CLL [f]	Salinomycin	48 h	0.23	7
U2OS [g]	Salinomycin	48 h	~5	8
MCF7 [h]	Salinomycin	48 h	8.6 ± 1.2	9
MCF7[DDP][h]	Salinomycin	48 h	13.8 ± 0.8	9
CA46, Molt-4, Raji, Ramos, CCRFCEM, CEM-C15 and CEM-CM 3 [i]	Monensin	72 h	<0.5	10

[a] Hepatocellular carcinoma cell lines; [b] Rat skeletal muscle cell line; [c] Endometrial cancer cell line; [d] Prostate epithelial carcinoma cell lines; [e] Prostate epithelial cell lines; [f] Chronic lymphocytic leukaemia; [g] Bone osteosarcoma cell line; [h] Breast cancer cell lines; [i] Lymphoblast cell lines.

References: [1]Radko et al., 2011; [2]Radko et al., 2013a; [3]Radko et al., 2013b; [4]Cybulski et al., 2015; [5]Kielbasinski et al. 2020; [6]Iljin et al., 2009; [7]Lu et al., 2011; [8]Kim et al., 2016; [9]Tyagi and Patro, 2019; [10]Park et al., 2002

2.6 Ion Homeostasis in Mammalian Cells

Ionophores primarily target cellular ion homeostasis, an essential process for cell survival. Maintaining the balance of both intra and extracellular ion concentrations is critical for the preservation of membrane potential and cell shape as well as the proper functioning of several intracellular pathways (Abdul Kadir et al., 2018). The plasma membrane is a lipid bilayer that consists of two layers of lipid molecules with hydrophilic heads facing outwards and hydrophobic tails facing inwards. The structure of the membrane ensures that it is largely impermeable to various ions, small hydrophilic molecules, and ribonucleic acid (RNA). To aid the movement of ions across the membrane, cells thus rely on facilitated diffusion and active transport (**Figure 2.9**). Facilitated diffusion involves the movement of ions through channels down their concentration gradients. These channels are gated and based on cellular signals, can be either opened or closed. Some types of gated channels include ligand gated and voltage gated channels. In contrast, active transport requires energy to transport the ions against their concentration gradients. Some well-known examples of active transporters include the Na^+/K^+-ATPase (Clausen and Poulsen, 2013) and the Na^+/Ca^{2+}-exchanger (Reeves, 1998).
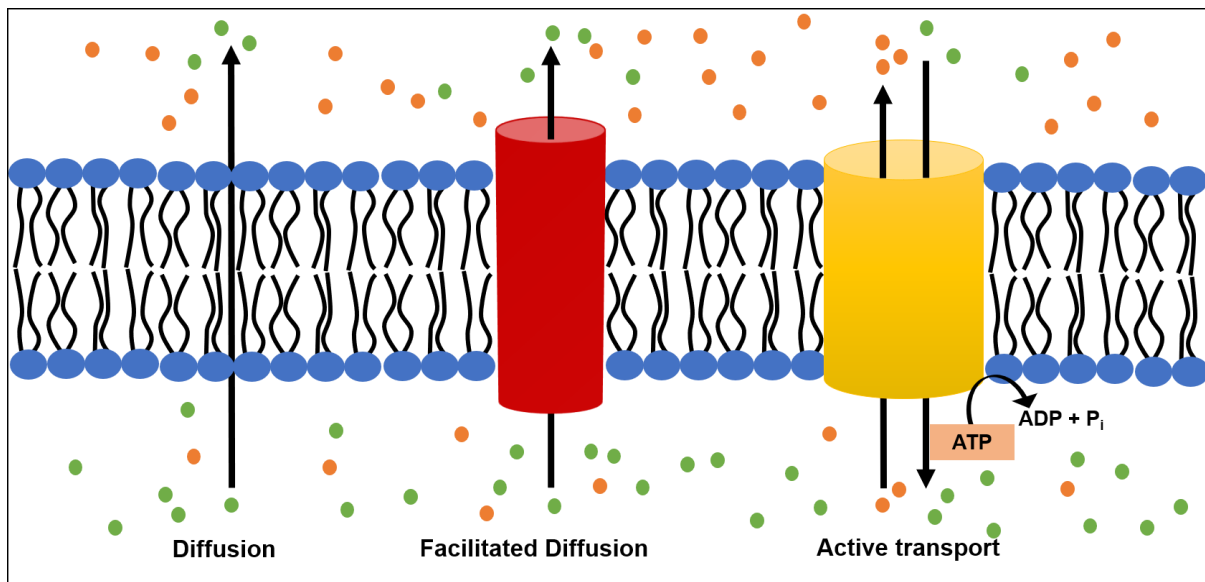
Figure 2.9 A diagram illustrating diffusion, facilitated diffusion and active transport.

Under physiological conditions, cells maintain high intracellular K^+ concentrations, low intracellular Na^+ concentrations and sequester Ca^{2+} within organelles such as the ER/sarcoplasmic reticulum, mitochondria, and nucleus (**Table 2.5**).

Table 2.5 Typical ion concentrations within a mammalian cell.

Ion	Concentration (mM)
Na^+	10
K^+	100
Ca^{2+}	0.1 to 0.01 free

Note that the exact concentration depends on the type of cell as well as physiological and environmental conditions and can change up to one order of magnitude. (Milo and Phillips, 2015)

2.6.1 Sodium (Na^+)

Intracellular Na^+ is maintained at low concentrations in mammalian cells (**Table 2.5**) by different ion pumps and channels. The Na^+/K^+-ATPase is responsible for the transport of three Na^+ ions to the outside and two K^+ ions to the inside of the cell at the expense of chemical energy derived from ATP. The movement of Na^+ against its concentration gradient, alongside that of the movement of K^+, is used to establish the electrochemical gradient of the cell. The electrochemical gradient is then used to drive various secondary transporters for the transmembrane carriage of organic and inorganic solutes. Disruptions in the Na^+ homeostasis results in the disruption of the Ca^{2+} homeostasis, due to the inhibition of the Na^+/Ca^{2+}-exchanger that exchanges extracellular Na^+ with intracellular Ca^{2+} (Reeves, 1998). Sodium flux also plays a role in programmed cell death and is necessary for cell shrinkage during apoptosis (Bortner and Cidlowski, 2003). Additionally, extracellular enzymes generally use Na^+ as cofactors to lower the energy requirement of binding with other molecules (Page and Di Cera, 2006).

2.6.2 Potassium (K^+)

Potassium is present at relatively high concentrations within the cytoplasm (**Table 2.5**) and, with Na^+, is responsible for generating and maintaining the electrochemical gradient of the cell. The two-pore domain K^+ channels (Braun, 2012) and inward-rectifier K^+ channels (Adrian et al., 1970) facilitate a small, constant outward leak of K^+ ions making the plasma membrane somewhat more permeable to K^+ in comparison to Na^+. This steady efflux of positively charged ions results in the polarisation of the plasma membrane. This happens until the chemical driving force of the ion gradient is equalled by the force of the electric field and a resting potential

is reached. According to the Goldman equation, a modified Nernst equation, a cell's resting membrane potential relies on the ion gradients and their membrane permeabilities (Clausen and Poulsen, 2013; Goldman, 1943).

$$V_m = \frac{RT}{F} \ln \frac{P_k[K^+]_o + P_{Na}[Na^+]_o + P_{Cl}[Cl^-]_i}{P_k[K^+]_i + P_{Na}[Na^+]_i + P_{Cl}[Cl^-]_o}$$

Where V_m is the membrane potential, R is the gas constant, T is the temperature, F is the Faraday number and P_x is the membrane permeability to that ion.

The plasma membrane is more permeable to K^+, therefore the resting potential of the cell will be approximate to the equilibrium potential of the K^+ ions. This results in a membrane potential ranging between -50 mV to -90 mV in most cells (Clausen and Poulsen, 2013). The plasma membrane potential is critical in cell cycle progression, with depolarisation of the membrane associated with inhibition at the G_1/S-phase transition, while conversely essential to the G_2/M-phase transition (Blackiston et al., 2009; Urrego et al., 2014). Previous research demonstrated that depolarisation of the plasma membrane through K^+ channel inhibition resulted in decreased proliferation (Blackiston et al., 2009; Freedman et al., 1992; Urrego et al., 2014; Wilson and Chiu, 1993). Additionally, K^+ concentration and K^+ flux is essential in various other cellular functions and pathways. A decrease in intracellular K^+ is necessary for the activation of the apoptotic machinery (Bortner and Cidlowski, 2003). Furthermore, in contrast to Na^+, K^+ ions are generally used by intracellular enzymes as cofactors (Page and Di Cera, 2006).

2.6.3 Calcium (Ca^{2+})

Free Ca^{2+} occurs only in low concentrations within the cell cytoplasm (**Table 2.5**). The majority of Ca^{2+} is stored within organelles such as the ER and mitochondria. The main method of Ca^{2+} entry into and exit out of the cell is through Ca^{2+} channels and the Na^+/Ca^{2+}-exchanger, respectively (Reeves, 1998). Calcium flux, resulting from the release of and restoration of Ca^{2+} ions from their stores, drive various cellular processes e.g., contraction of muscle fibres and activation of Ca^{2+} dependent proteases. If, due to insult or injury to the cell, the Ca^{2+} homeostasis is disrupted, and the cell cannot re-establish homeostasis, it leads to cell death. Calcium overload is a consequence of the imbalance of Ca^{2+} homeostasis. In the event of an abnormal increase in the influx of Ca^{2+}, mitochondria expend energy in order to maintain ion

homeostasis (Wrogemann and Pena, 1976). They do this by sequestering the excess Ca^{2+} ions within the mitochondrial matrix. If homeostasis is not re-established, the individual mitochondria are overloaded with Ca^{2+} which in turn, causes an irreversible lapse in oxidative phosphorylation. When oxidative phosphorylation is disrupted, ATP generation is halted, and the cells will have a shortage of energy. With inadequate energy available for transporting Ca^{2+} out of the cell, mitochondrial Ca^{2+} overloading will accelerate until the mitochondria will no longer be able to sequester Ca^{2+} and may even leak Ca^{2+}. The end result is an increased concentration of Ca^{2+} within the cytoplasm, which eventually leads to cell death. Both apoptosis and necrosis are associated with an increase in intracellular Ca^{2+} (Danese et al., 2017). Increased intracellular Ca^{2+} causes the activation of Ca^{2+}-specific proteases such as calpains and certain caspases. Calpains degrade various substrates including cytoskeletal proteins such as desmin and dystrophin, kinases, proteases and membrane receptors. The activation of mitochondrial calpain can result in the release of the apoptosis-inducing factor, which subsequently triggers a caspase-independent form of cell death (Norberg et al., 2008). In contrast, activation of cytoplasmic calpain can result in cellular damage that leads to necrosis and the cleavage of caspase-12, which activates downstream caspases (Nakagawa and Yuan, 2000). Salinomycin was shown to result in calpain and cytochrome-c mediated cell death due to an increase in intracellular Ca^{2+} (Boehmerle and Endres, 2011).

Perturbations in the ER Ca^{2+} homeostasis will disrupt ER function, leading to the accumulation of unfolded and misfolded proteins in the ER lumen. This in turns triggers the unfolded protein response (UPR), whereby overall protein synthesis is halted until enough chaperones can be generated to deal with the unfolded proteins and restore cellular homeostasis (Varadarajan et al., 2013). If the extent of stress is overwhelming apoptosis is triggered. Another way the ER deals with stress is by reorganising the ER membranes resulting in the clustering and redistribution of ER membrane proteins together with impaired ER function and transport.

2.6.4 Protons (H$^+$)

Cellular pH is generated from H^+ that dissociate from organic acids, e.g., lactic acid (lactate$^-$/H^+) and pyruvic acid (pyruvate$^-$/H^+). Under normal physiological conditions intracellular pH generally falls between 7.0 and 7.4, however, this varies between

tissues. The pH of skeletal muscle, for example, is slightly more acidic. Different cellular organelles also have different pH spanning from 4.5 to 8.0. Lysosomes have low pH and are required to maintain their own ion homeostasis. Disruption in lysosomal ion homeostasis affect the degradation of various cellular components and vesicle trafficking, etc. To maintain physiological pH, cells rely on buffering systems such as the bicarbonate-carbonate, the phosphoric acid and the protein binding systems, as well as several transporters responsible for the removal of H^+ from the cytosol (Aoi and Marunaka, 2014). The sodium-proton exchanger (NHE) plays an important role in the maintenance of intracellular pH by exchanging intracellular H^+ for extracellular Na^+ using the chemical gradient between intra- and extracellular Na^+ concentrations (Aoi and Marunaka, 2014). Additionally, the NHE has two structural functions i.e. anchoring actin filaments and scaffolding signalling complexes (Meima et al., 2007).

2.7 Summary

In summary, ionophores are antibiotics marketed as feed additives in the production animal industry for the promotion of growth feed efficiency as well as for the control of coccidiosis. However, extra-label use or ingestion of concentrations that exceed safety levels result in ionophore toxicosis, which primarily affects the cardiac and skeletal muscles of animals. This is presented by various clinical signs such as weakness, tachycardia and dyspnoea, as well as lesions that appear after sub-acute and chronic ionophore intoxication. Ionophores bind to cations and transport them across biological membranes, primarily resulting in the disruption of ion homeostasis. As ion homeostasis is critical for cellular function, its disruption leads to various downstream effects including alteration of cellular pH, disruption of the mitochondrial membrane potential, production of reactive oxygen species and inhibition of cellular transport. If the toxicity overwhelms the cells' ability to restore balance, it leads to cell death which can occur via different cell death pathways such as apoptosis or necrosis.

Chapter 3: *In Vitro* Cytotoxicity of Monensin, Salinomycin and Lasalocid on Cardiac and Skeletal Myoblasts

3.1 Introduction

The use of ionophores in the production animal industry is advantageous due to their selective toxicity against bacteria and protozoan parasites, combined with their safety margins in approved domestic animals (Hall, 2000; Mehlhorn et al., 1983; Novilla, 2018). However, when animals ingest a dose that exceed these safety margins, ionophore toxicosis occurs. Cardiac and skeletal muscle, as well as nervous tissue, are especially vulnerable to the damage caused by ionophores while the degree of susceptibility varies between species (Bosch et al., 2018; Confer et al., 1983; Novilla, 1992; Pakozdy et al., 2010; Segev et al., 2004; Van Vleet and Ferrans, 1984a, b). The estimated LD_{50}s of various commercially available ionophores, as well as their adverse effects in different animal species have been determined (**Chapter 2**, **Table 2.2**).

Ionophores disrupt the ion homeostasis of the cell by complexing with cations and transporting them across biological membranes. Monensin and salinomycin are monovalent cation transporters with a proclivity towards Na^+ and K^+, respectively. In contrast, lasalocid, a divalent cation carrier, is able to transport Ca^{2+}. Toxic ionophore concentrations can overwhelm the cells' ability to maintain ion balance and, consequently, compromise various cellular pathways. These include mitochondrial respiration, cellular transportation and protein degradation (Estrada-O et al., 1974; Grinde, 1983; Mahtal et al., 2020; Mitani et al., 1976; Mollenhauer et al., 1990; Wong et al., 1977). In addition, ionophores disrupt the plasma membrane, cause oxidative stress, perturb intracellular pH, and can trigger excessive autophagy (Ketola et al., 2010; Kim et al., 2017a; Kim et al., 2016; Mollenhauer et al., 1990; Przygodzki et al., 2005). The end result is cell cycle arrest, cell death via a programmed cell death pathway (i.e., apoptosis) or necrosis.

In this chapter the cytotoxicity of monensin, salinomycin and lasalocid on rat cardiac (H9c2), rat skeletal (L6) and mouse skeletal (C2C12) myoblasts was evaluated. The H9c2 and L6 cell lines are derived from rat left ventricle (Kimes and Brandt, 1976) and rat thigh muscle (Yaffe, 1968), respectively. The L6 cell line retained many

metabolic and morphological characteristics of skeletal muscle and is a good alternative to live animals for myotoxicity testing. The C2C12 cell line is a subclone (produced by H. Blau et al. 1985) of the mouse myoblast cell line established by Yaffe and Saxel (1977). The C2C12 cell line was included in this study, in addition to the H9c2 and L6 cell lines, since the antibodies available for desmin and synemin staining (referred to in **Chapter 4**) did not react with the rat cell lines. Therefore, the C2C12 cell line enabled us to investigate the effects of the ionophores on these intermediate filament networks (**Chapter 4**, *vide infra*). In addition to determining the cytotoxicity of the ionophores, the effect of monensin, salinomycin and lasalocid on mitochondrial localisation and DNA fragmentation was determined via fluorescent microscopy.

3.2 Materials and Methods

3.2.1 Culturing of Cardiac and Skeletal Muscle Myoblasts

The cell lines used during the course of this study include both rat cardiac (H9c2) and skeletal muscle (L6) cell lines, as well as a mouse skeletal muscle (C2C12) cell line (**Figure 3.1** and **Table 3.1**).
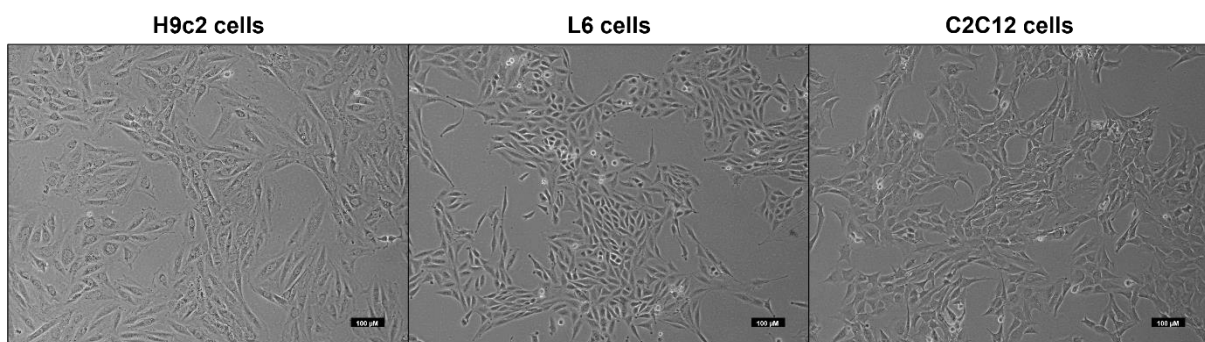
Figure 3.1 Rat cardiac (H9c2), skeletal muscle (L6) and mouse skeletal muscle (C2C12) cell lines under normal culture conditions. Scale bar = 100 µm.

All three cell lines were cultured in Dulbecco's Modified Eagle's Medium (DMEM) (PAN Biotech) supplemented with 100 U penicillin/ml and 100 U streptomycin/ml (Lonza), as well as 10% foetal bovine serum (FBS) (Gibco). The myoblasts were incubated at 37 °C in a humidified atmosphere with 5% CO_2, and periodically sub-cultured to prevent the cultures from reaching confluency.

Table 3.1 Information pertaining to the cell lines used during the course of this study.

Cell Line	Species	Tissue	Source	Reference
H9c2	*Rattus norvegicus*, rat	Heart/myocardium	ATCC	H9c2(2-1) (ATCC® CRL-1446™)
L6	*Rattus norvegicus*, rat	Skeletal muscle	JCRB	L6 (JCRB9081)
C2C12	*Mus musculus*, mouse	Skeletal muscle	ATCC	(ATCC® CRL-1772™)

ATCC - American Type Culture Collection
JCRB - Japanese Collection of Research Bioresources Cell Bank

3.2.2 Cytotoxicity Studies

Growth Curves

Before commencing with the cytotoxicity assays, growth curves for the H9c2, L6 and C2C12 cell lines were evaluated. Growth curves were necessary in order to determine the most appropriate number of myoblasts per well, over a 72 h-period, for each cell line. The myoblasts were seeded into a 96-well microplate, with the medium being changed after 24 h, and then incubated for 24, 48 and 72 h. The absorbance of the myoblasts was determined using an MTT viability assay (as described below).

Stock Solutions

Monensin sodium (MW: 692.85 g/mol), salinomycin sodium (MW: 772.98 g/mol) and lasalocid A sodium (MW: 612.77 g/mol) were obtained from Dr Ehrenstorfer™. The purity of these ionophores as indicated on the certificate of analysis were 98.4%, 78.8% and 96.8% respectively. Salinomycin (TRC Canada), with a higher percentage purity (95%) was later purchased. Stock solutions were prepared by dissolving the ionophores in methanol (MeOH) up to a concentration of 40 mM. It was decided upon using MeOH as a solvent, since it allowed for easy solubilisation of the ionophores.

MTT viability assay

For the cytotoxicity studies, 100 000 H9c2 myoblasts/ml, 25 000 L6 myoblasts/ml and 10 000 C2C12 myoblasts/ml, the optimum number of myoblasts to conduct

exposure studies over 72h as determined by the growth curves, were seeded into a 96-well plate. All myoblasts were allowed 24 h to stabilise and to adhere to the well surface.

Subsequently, the myoblasts were exposed to serial dilutions of monensin, salinomycin and lasalocid for 24, 48 and 72 h using 0.1% MeOH as solvent. The percentage solvent per well was kept constant throughout the serial dilutions. Each study included a blank with wells containing complete DMEM media, a negative control with normal healthy myoblasts, a solvent control with myoblasts incubated with the solvent in the medium, and a positive control with myoblasts exposed to 20 µM doxorubicin hydrochloride (Pfizer).

The salinomycin used throughout the project had a purity of 78.8%. To determine whether the percentage purity would have a significant impact on the cytotoxicity, C2C12 myoblasts were exposed to both 78.8% and 95% pure salinomycin. The concentrations used were 0.01, 0.1, 1, 5 and 10 µM salinomycin and the myoblasts were exposed for 24, 48 and 72 h.

Cytotoxicity assays on the differentiated C2C12 myotubes, generated as described below, were executed with the myoblasts being exposed to 0.1, 1 and 10 µM of the ionophores over a 72-h period.

The cytotoxicity of the ionophores were determined using a modified MTT viability assay as previously described by Mosmann et al. (1983). Post-exposure, the plates were washed with phosphate buffered saline (PBS) (Sigma-Aldrich), followed by the addition of 200 µl complete media and 20 µl (5 mg/ml in PBS) MTT (Sigma-Aldrich) per well. The plates were incubated for 2 h at 37 °C in the dark. Following incubation, the medium was removed, 100 µl dimethyl sulfoxide (DMSO) was added to each well and the plates were gently shaken for 5 min. The absorbance and background absorbance were measured at 570 and 630 nm respectively, using a Synergy HT BioTek microplate reader (BIO-TEK Instruments, Winooski, VT, USA). After subtracting the background absorbance (630 nm) from the absorbance at 570 nm for each well, the viability of the myoblasts was expressed as a percentage of the solvent control as follows:

$$\% \, Cell \, Survival = \frac{Average \, Ab \, Replicates - Average \, Ab \, Media}{Average \, (Average \, Ab \, Solvent \, Control - Average \, Ab \, Media)} \, x \, 100$$

Ab - Absorbance

All experiments were done in triplicate and had at least three biological repetitions.

3.2.3 Statistical Analysis

The results of the cytotoxicity assays were analysed in Microsoft Office Excel 365 and Graph Pad Prism (Version 9.2.0). The percentage cell survival for each replicate corresponding to an ionophore concentration was averaged and the standard deviation was calculated.

The EC_{50}s of all experiments were calculated using a noncomputational method first described by Alexander et al. (1999). The method allows for the calculation of the EC_{50}, provided that the EC_{50} is located upon a linear portion of the curve, without the need for computational curve-fitting programs using the equation shown in **Figure 3.2**. Since the EC_{50}s initially calculated were in log form, the antilog for each had to be calculated to determine the EC_{50} in micromolar concentration. The average EC_{50}s with the standard error of the mean (StEM) was reported.

$$EC_{50} = C - \frac{[(A - 50\%)(C - D)]}{A - B}$$

$$EC_{50} = C - \frac{[(A - 50\%)(x)]}{y}$$
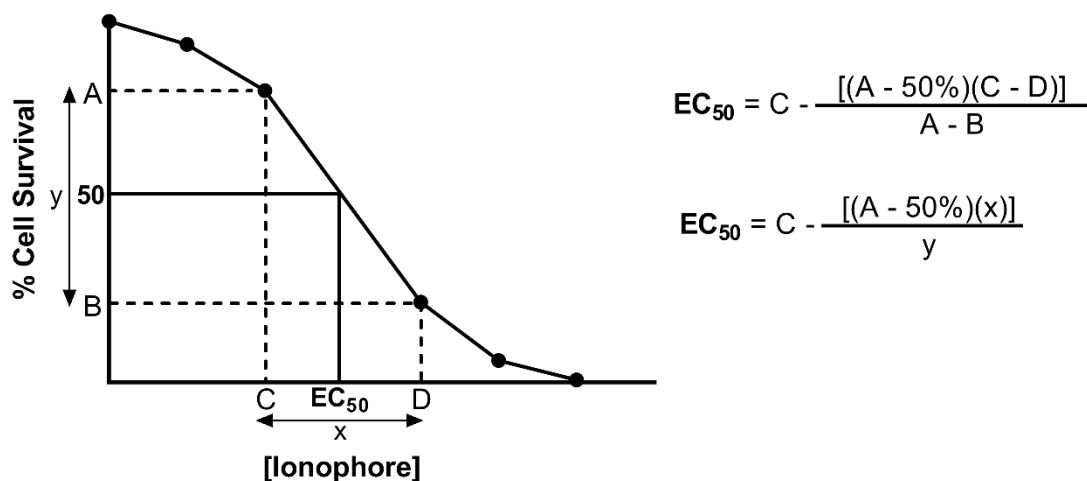
Figure 3.2 Hypothetical dose-response curve showing the technique described by Alexander et al. (1999) as well as the equation used to calculate the EC_{50}. A and B represents the nearest actual recorded responses on either side of 50% cell survival, while C and D represents the corresponding drug concentration used. The difference between A and B is represented by y and the difference between C and D is represented by x.

The significant differences between the transformed EC_{50}s were determined using analysis of variance (ANOVA), followed by the Tukey's multiple comparison test.

43

However, significant differences between cell lines were not compared, as the number and growth rate of the myoblasts used differed. Data was checked for normal distribution and homoscedasticity using a Shapiro-Wilk normality test and a Brown-Forsythe test, respectively.

3.2.4 Cardiac and Skeletal Muscle Myoblast Differentiation

In addition to culturing the undifferentiated myoblasts, it was attempted to differentiate all three cell lines into myotubes.

Briefly, H9c2 myoblasts were seeded into a 96-well plate at a concentration of 150 000 myoblasts/ml. The myoblasts were incubated for eleven days in medium supplemented with 1 to 2% of either FBS or horse serum (HS) (Lonza) as well as 0.01 and 1 μM retinoic acid (Sigma-Aldrich). The medium was changed daily. Further experiments using 100 000, 150 000 and 200 000 myoblasts/ml in 1 to 2% FBS with retinoic acid, were also performed.

L6 and C2C12 myoblasts were differentiated using media supplemented with 5% HS. The myoblasts were seeded into a 96-well plate at 50 000 myoblasts/ml and incubated for seven days, changing the medium every other day.

3.2.5 Light Microscopical Analysis of Myoblast and Myotube Morphology after Ionophore Exposure

All three cell lines were exposed to 0.1 μM monensin, salinomycin and lasalocid over a period of 72 h. Additionally, the C2C12 myotubes were exposed to 1 μM of the above three ionophores for 48 h. The alterations in cellular morphology after ionophore exposure were examined with a phase contrast lens using a Nikon ECLIPSE TS100 inverted microscope (Tokyo, Japan).

3.2.6 Mitochondrial Localisation after Exposure to the Ionophores for 48 h using MitoTracker Green FM

The mitochondria of L6 myoblasts were stained using MitoTracker Green FM (Invitrogen). L6 myoblasts were cultured in a 24-well plate (25 000 myoblasts/ml) containing 10 mm round coverslips and exposed to 0.1 μM monensin, salinomycin and lasalocid for 48 h. The medium was then decanted, and the myoblasts washed with 1% FBS (in PBS) for 5 min. A 1 mM MitoTracker stock solution was prepared in DMSO and stored at -20 °C. All myoblasts were exposed to 0.4 μM MitoTracker (in FBS-free media) and incubated for 45 min at 37 °C in a humidified atmosphere with

5% CO_2. The myoblasts were counterstained with 4',6-diamidino-2-phenylindole (DAPI). A 1 mg/ml DAPI stock solution was made using ddH_2O, aliquoted and stored at -20 °C. The wells were washed once with PBS and then incubated with 500 µl DAPI stain in FBS-free medium for 15 min in the incubator. Following the removal of excess DAPI with three successive PBS washes, the coverslip with the live myoblasts was mounted on a glass slide and viewed using an Olympus BX63 microscope at the Electron Microscopy (EM) unit of the Department of Anatomy and Physiology, Faculty of Veterinary Science, University of Pretoria. The excitation and emission wavelengths of MitoTracker Green FM and of DAPI are 490/516 nm and 340/488 nm, respectively.

The images captured were deconvoluted using Fiji ImageJ as stated below (Schindelin et al., 2012). A theoretical Point Spread Function (PSF) was generated using Diffraction PSF 3D plugin by B. Dougherty (2005), assuming the PSF arises only from diffraction. The PSF was then used with the Iterative Deconvolve 3D plugin for deconvolution of the 2D images (Dougherty, 2005). The PSF was normalised, the maximum number of iterations was set to the recommended 100 and the iteration was terminated if the mean delta was less than 0.01 as recommended.

3.2.7 Percentage DNA Fragmentation in L6 myoblasts after 48 h Ionophore Exposure

A Click-iT PLUS TUNEL assay (Invitrogen) was used to determine the percentage myoblasts with DNA fragmentation after ionophore exposure. L6 myoblasts were seeded (100 000 myoblasts/ml) onto a sterile 10 mm round coverslips in a 24-well plate and cultured for 24 h. The myoblasts were exposed to either 0.1 or 1 µM monensin, salinomycin and lasalocid for 48 h. A negative and solvent control (0.1% MeOH) was added to the experiment, in addition to a 'No Fluorescence' control. The 'No Fluorescence' control was not incubated with the Supermix, as described below, to ensure non-specific fluorescence did not interfere with interpreting the results. After exposure, the medium was removed, followed by fixing the myoblasts with 70% ethanol (EtOH) for 15 min at room temperature. The fixative was removed, and the myoblasts were permeabilised with 0.25% Triton™ X-100 in PBS for 20 min, followed by two washing steps with ddH_2O.

A 100 µl terminal deoxynucleotidyl transferase (TdT) reaction buffer was added to each well and incubated for 10 min at 37 °C. The buffer was removed, and the myoblasts were incubated with 50 µl TdT reaction mixture, which contains TdT reaction buffer, 5-ethynyl-2'-deoxyuridine-5'-triphosphate (EdUTP) and TdT enzyme, for 1 h at 37 °C. The myoblasts were washed twice for 5 min using 3% bovine serum albumin (BSA) in PBS. Subsequently, the myoblasts were incubated with 50 µl Click-iT Plus TUNEL reaction cocktail for 30 min at 37 °C. The reaction cocktail contained Click-iT Plus TUNEL Supermix (1x Click-iT Plus TUNEL reaction buffer, copper protectant and Alexa Fluor^{TM} 488 picolyl azide dye) and 10x Click-iT Plus TUNEL reaction buffer additive. The myoblasts were washed with 3% BSA for 5 min. The nuclei were counterstained with DAPI. A 500 µl DAPI working solution (1.3 µg/ml in ddH$_2$O) was added to each well, followed by a 15 min incubation step at 37 °C. To remove any excess DAPI, the myoblasts were washed three times for 5 min each with PBS.

Finally, the coverslips were mounted on microscope slides, with ProLong^{TM} gold anti-fade reagent (Molecular Probes) and sealed using clear nail polish. The myoblasts were viewed using an Olympus BX63F microscope and exposure time was kept constant for each slide in the same experiment. The images were combined using Fiji ImageJ and analysed using QuPath (version 0.3.0). The percentage myoblasts with DNA fragmentation were determined by dividing the number of TUNEL-positive nuclei by the total number of nuclei detected by DAPI and multiplying with 100. A minimum of 3000 nuclei per slide were counted and the experiment was repeated twice.

3.3 Results

3.3.1 Growth Curves

The growth curves were established to determine the number of myoblasts per well needed to maintain the myoblasts in the log-phase of the cell growth cycle throughout the 72 h-period, without cell death by depletion of resources or accumulation of waste products. The growth curves for the H9c2, L6 and C2C12 cell lines are depicted in **Figure 3.3.**
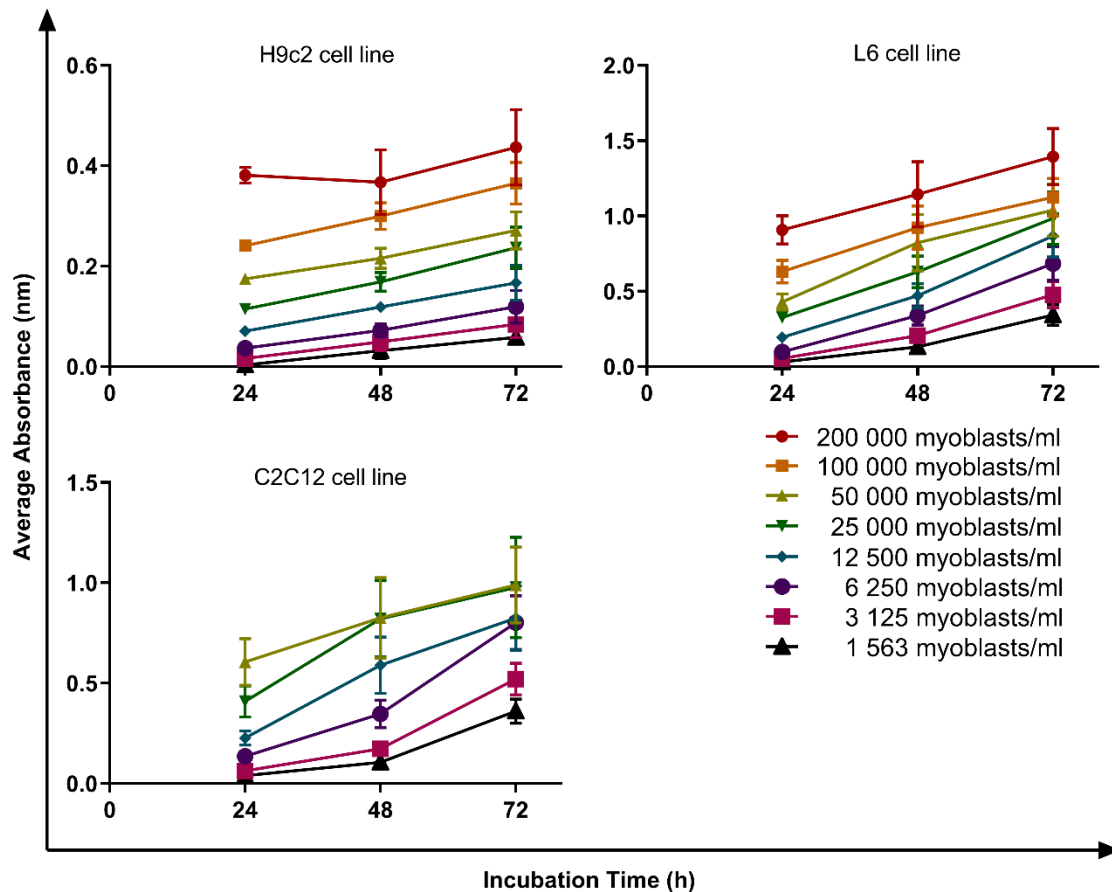
Figure 3.3 The growth curves of H9c2, L6 and C2C12 cell lines over 24, 48 and 72 h. The average absorbance for each cell concentration ± the StEM is indicated (n=4).

It was decided to use 100 000 H9c2 myoblasts/ml (R^2 = 0.999), 25 000 L6 myoblasts/ml (R^2 = 0.998) and 10 000 C2C12 myoblasts/ml. The R^2 values for each line were determined through linear regression from 24 h to 72 h using the means of each replicate. The number of C2C12 myoblasts were decided based on the fact that 10 000 myoblasts/ml was situated between 6 250 myoblasts/ml, where the myoblasts were still in the lag-phase of growth between 24 and 48 h, and 12 500 myoblasts/ml, where the myoblasts started reaching the stationary phase between 48 and 72 h. Additionally, in this laboratory 6 250 C2C12 myoblasts/cm^2 (in a 0.8 cm^2 well) were used for previous experiments (Botha et al., 2019), which translates to 2 000 myoblasts per 0.32 cm^2-well, i.e. 10 000 myoblasts/ml. Of the three cell lines, the C2C12 cell line grew the fastest, followed by the L6 cell line. The H9c2 cell line had the slowest growth.

3.3.2 Cytotoxicity of the Ionophores on Cardiac and Skeletal Myoblasts

The cytotoxicity of monensin, salinomycin and lasalocid on H9c2, L6 and C2C12 cell lines were determined using the MTT viability assay. **Figure 3.4** illustrates the log dose-response curves of the three cell lines when exposed to the different ionophores for 24 (blue), 48 (red) and 72 h (green). A two-way ANOVA, followed by the Tukey's multiple comparison tests were used to detect any significant differences between the transformed EC_{50}s of the different ionophores on the three cell lines at 24, 48 and 72 h exposure. The EC_{50}s are presented in **Table 3.2**.

Exposing the cell lines to the ionophores resulted in a dose-dependent cytotoxic response, with cell viability decreasing concomitantly with increasing concentrations of monensin, salinomycin and lasalocid. The cytotoxicity was also time-dependent, with the percentage cell survival at 24 h being greater compared to after 48 and 72 h exposure. Interestingly, salinomycin exposure resulted in a non-monotonic dose response curve when added to the cardiac myoblasts for 48 and 72 h (**Figure 3.4 b**). The cell survival increased to above 50% at around 20 µM salinomycin. Lasalocid exposure also caused a slight increase in the H9c2 myoblast survival at higher concentrations, though the increase was not significant (**Figure 3.4 c**).

Of the three ionophores, monensin was the most cytotoxic, with the only exception being at 24 h in L6 myoblast. In this case, lasalocid had the highest cytotoxicity. Monensin was followed by salinomycin in its ability to reduce cell survival. Lasalocid was the least cytotoxic of the ionophores tested, except in the instance mentioned above. Exposure of H9c2 myoblasts to the ionophores for both 48 and 72 h resulted in significant differences between the EC_{50}s of the ionophores at those exposure times ($p < 0.01$). Similarly, for L6 and C2C12 myoblasts, the EC_{50}s between the ionophores differed at both 48 and 72 h exposure ($p < 0.001$), with an exception between salinomycin and lasalocid ($p > 0.05$).

In L6 ($p < 0.001$) and C2C12 ($p < 0.01$) myoblasts, the EC_{50}s of both salinomycin and lasalocid were significantly higher at 24 h exposure, compared to 48 and 72 h exposure. However, the cytotoxicity was similar between 48 and 72 h in most cases ($p > 0.05$).
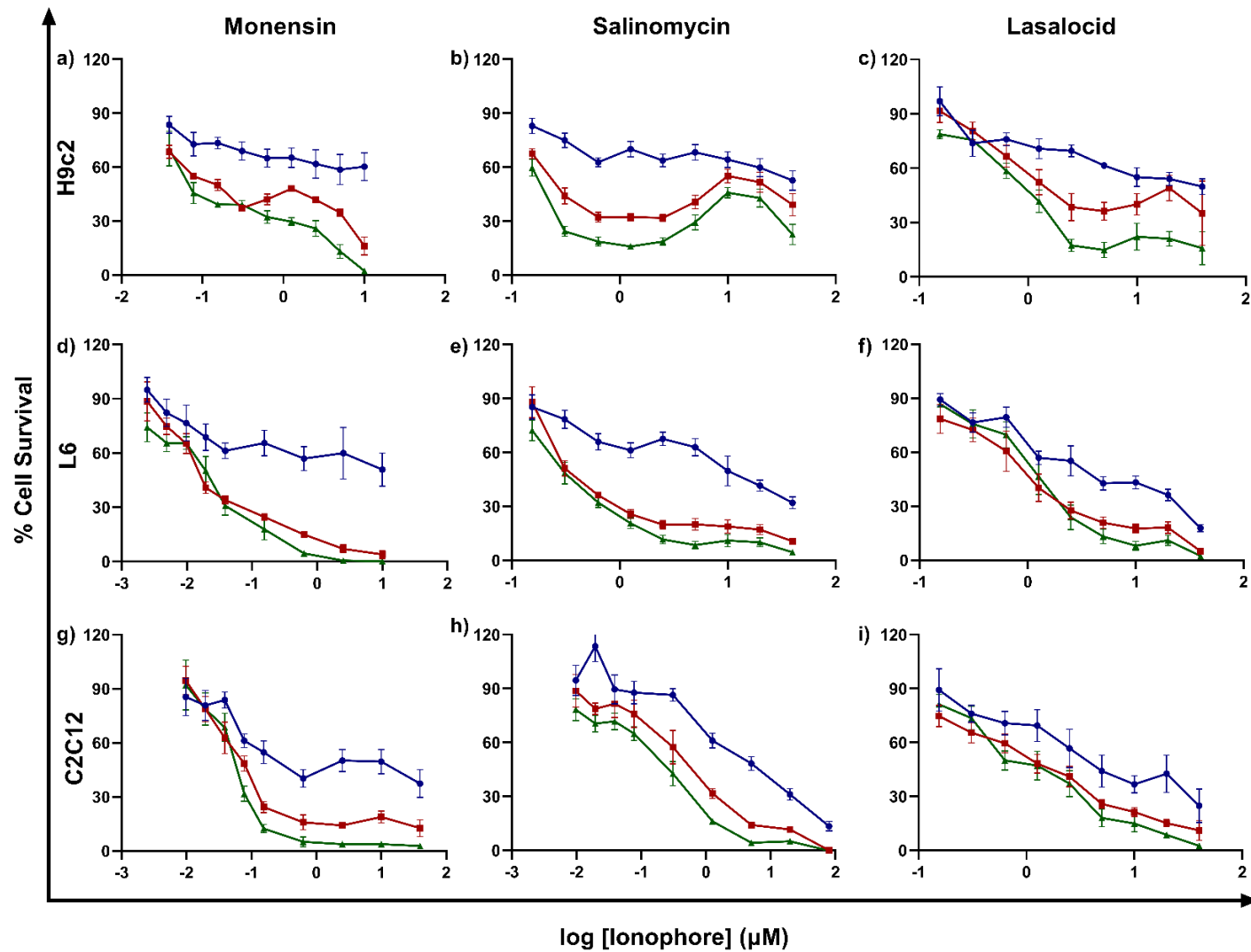
Figure 3.4 Log-dose response curves generated by using the mean percentage cell survival ± StEM vs the log of the concentration of the different ionophores (in μM). (Legend -●- 24 h, -■- 48 h, -▲- 72 h).

Table 3.2 The EC$_{50}$s (µM) ± StEM of the ionophores exposed to three cell lines for 24, 48 and 72 h.

		Monensin	Salinomycin	Lasalocid
H9c2 myoblasts	**24 h**	>10 (n=4)	>40 (n=5)	~40 (95% CI:41.3-58.5)* (n=4)
	48 h	0.15 ± 0.03[a] (n=3)	0.27 ± 0.02[b] (n=4)	1.53 ± 0.57[c] (n=4)
	72 h	0.07 ± 0.02[a] (n=3)	0.22 ± 0.04[b] (n=5)	0.94 ± 0.14[c] (n=4)
L6 myoblasts	**24 h**	>10 (n=4)	12.29 ± 2.59[d] (n=5)	2.98 ± 0.92[d] (n=4)
	48 h	0.006 ± 0.001[a] (n=4)	0.33 ± 0.04[b,e] (n=5)	0.96 ± 0.24[b,e] (n=5)
	72 h	0.011 ± 0.003[a] (n=4)	0.31 ± 0.05[b,e] (n=5)	1.28 ± 0.2[b,e] (n=5)
C2C12 myoblasts	**24 h**	†	4.04 ± 1.01[d] (n=5)	8.68 ± 5.38[d] (n=4)
	48 h	0.04 ± 0.01[a] (n=5)	0.45 ± 0.13[b,e] (n=5)	1.38 ± 0.54[b,e] (n=4)
	72 h	0.02 ± 0.01[a] (n=5)	0.26 ± 0.06[b,e] (n=5)	1.46 ± 0.59[b,e] (n=4)

n = number of biological repeats.

*The 95% confidence interval (95% CI) of cell survival for the concentration shown.

† The EC$_{50}$ falls between 0.15 and 10 µM (n=5).

There are significant differences between [a vs b vs c] (horizontal columns) and between [d vs e] (vertical columns).

3.3.3 Cytotoxicity Comparison Between Salinomycin of Different Purities

The purity of the salinomycin used during the course of this study was 78.8% as indicated on the certificate of analysis. To determine whether the purity would have any impact on the cytotoxicity, C2C12 myoblasts were exposed to two different purity grades (78.8% and 95%) at different concentrations (**Figure 3.5**). The significant differences ($p < 0.05$) between the percentage cell survival at each concentration, for the different salinomycin purity grades were calculated using a two-way ANOVA. There was no significant difference between cytotoxic effects caused by the different salinomycin purity grades, except for when myoblasts were exposed to 0.01 µM salinomycin at 72 h ($p = 0.006$). At 48 and 72 h, the cell survival of C2C12 myoblasts exposed to both 0.1 and 0.01 µM salinomycin (95% purity) surpassed that of the solvent control (**Figure 3.5 b & c**), but was not significantly different from that of the 78.8% purity grade salinomycin.
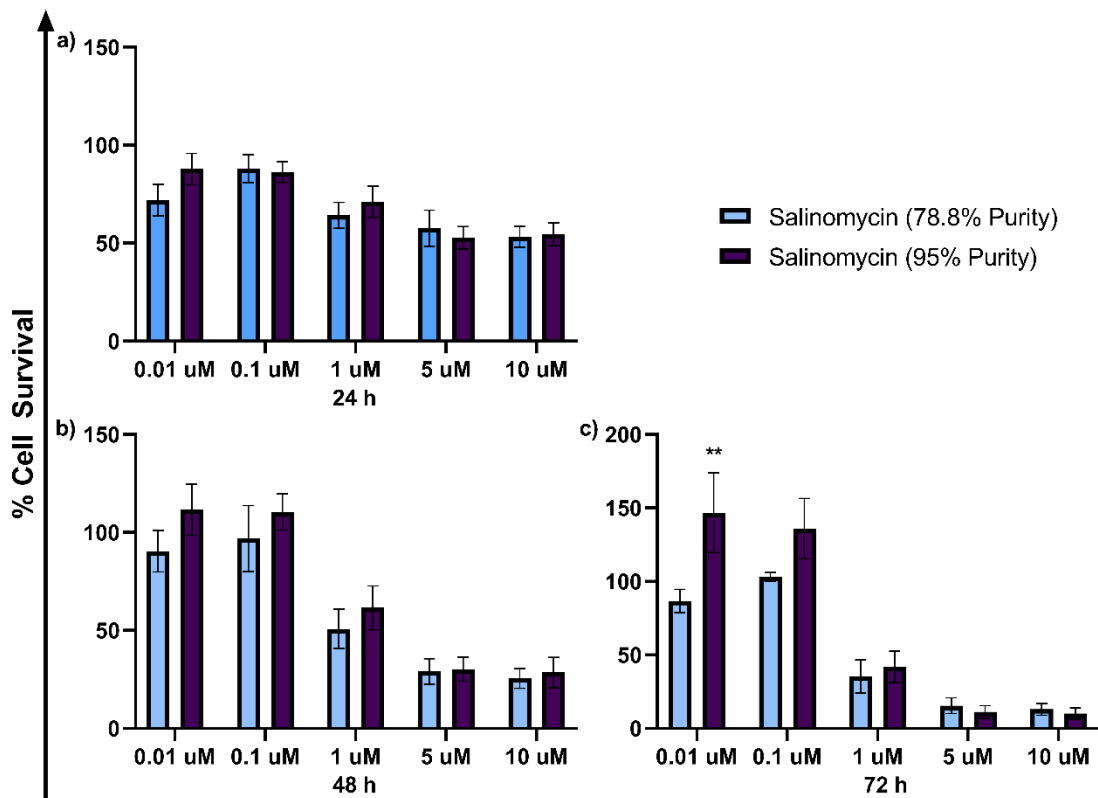
Figure 3.5 Comparison between the cytotoxic effect of different purity grades of salinomycin over 24, 48 and 72 h on C2C12 myoblast survival. Average cell survival ± StEM (n = 5). Significant difference ($p < 0.01$) indicated by **.

3.3.4 Differentiation of Cardiac and Skeletal Muscle Myoblasts

The cardiac and skeletal muscle cell lines were cultured under reduced serum concentrations in order to produce differentiated myotubes. Of the three cell lines, only C2C12 myoblasts could be reliably differentiated, as determined by visual observation, and were thus used for further cytotoxicity studies. A brief description of the differentiation results follows.

Various attempts were made to differentiate the H9c2 cell line, however dependable results could not be obtained. **Figure 3.6** shows H9c2 myoblasts during normal culture, as well as at day eight of the differentiation attempt with media containing 2% FBS and 1 µM retinoic acid. No marked difference could be seen in differentiation state of the myoblasts, however with longer incubation times the number of dead myoblasts and amount of cell debris increased. Similarly, no obvious differentiation was seen for the H9c2 myoblasts cultured in media containing 1 to 2% of either FBS or HS, with different retinoic acid concentrations up to eleven days of culturing.
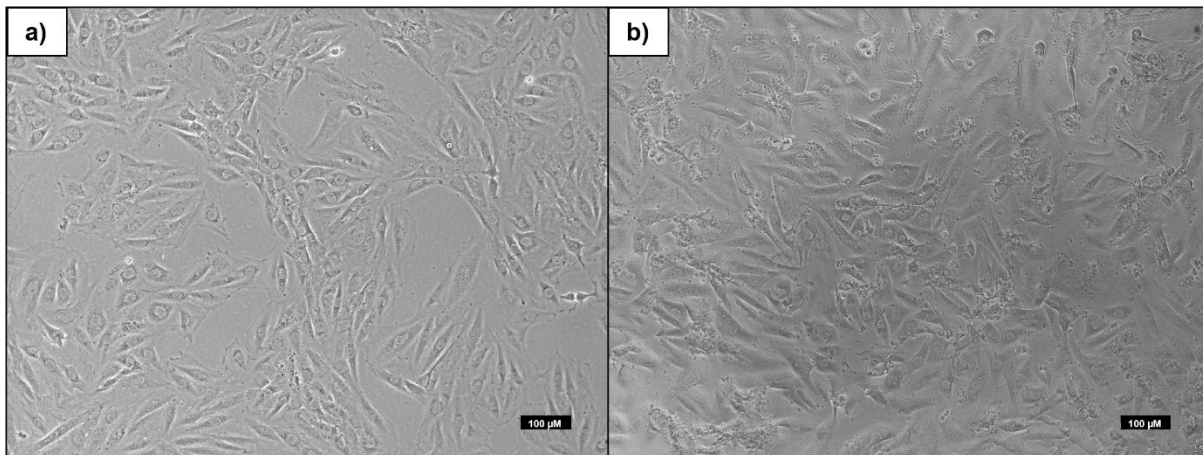
Figure 3.6 H9c2 myoblasts in complete DMEM (a) and H9c2 myoblasts at day 8 of differentiation using 2% FBS and 1 µM retinoic acid (b). Scale bar = 100 µM.

The L6 myoblasts were not as difficult to differentiate compared to the H9c2 myoblasts (**Figure 3.7**), however the number of dead myoblasts and cell debris increased with incubation time. The wells also became severely overgrown during the course of differentiation. Reducing the serum concentrations further resulted in increased death among the myoblasts. During cytotoxicity studies the myotubes were easily lost, detaching from the well surface and thus impacted the consistency of the results.
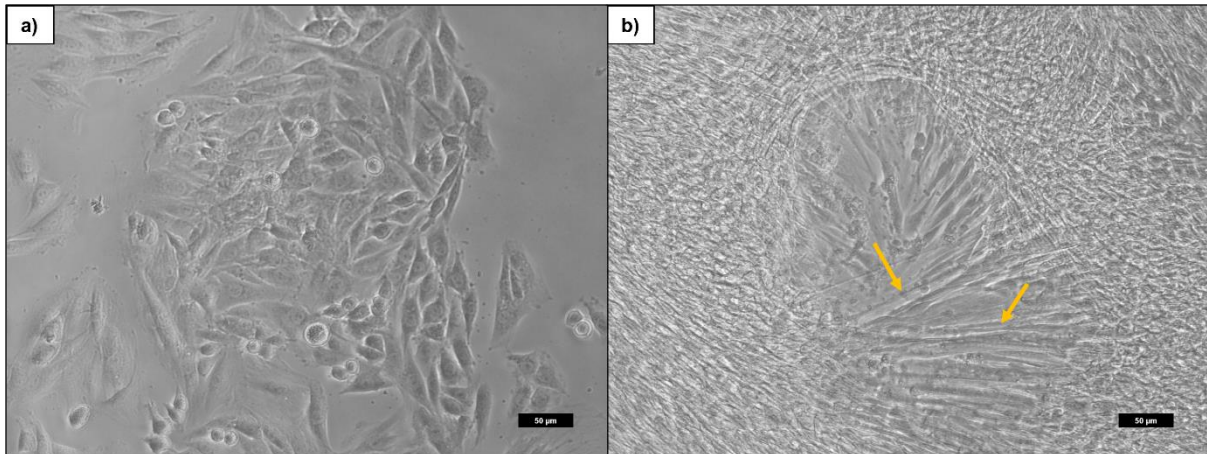
Figure 3.7 L6 myoblasts in complete DMEM (a) and differentiated L6 myotubes in medium containing 5% HS (b). Yellow arrows indicate differentiated myotubes. Scale bar = 50 µm.

C2C12 myoblasts were the most consistent in their ability to differentiate. Visualisation under the light microscope revealed long tubes with multiple nuclei (**Figure 3.8**, **yellow arrows**). A few undifferentiated myoblasts remained, however when cultured for an extended period of time in 5% HS medium the myotubes began to lose their viability.
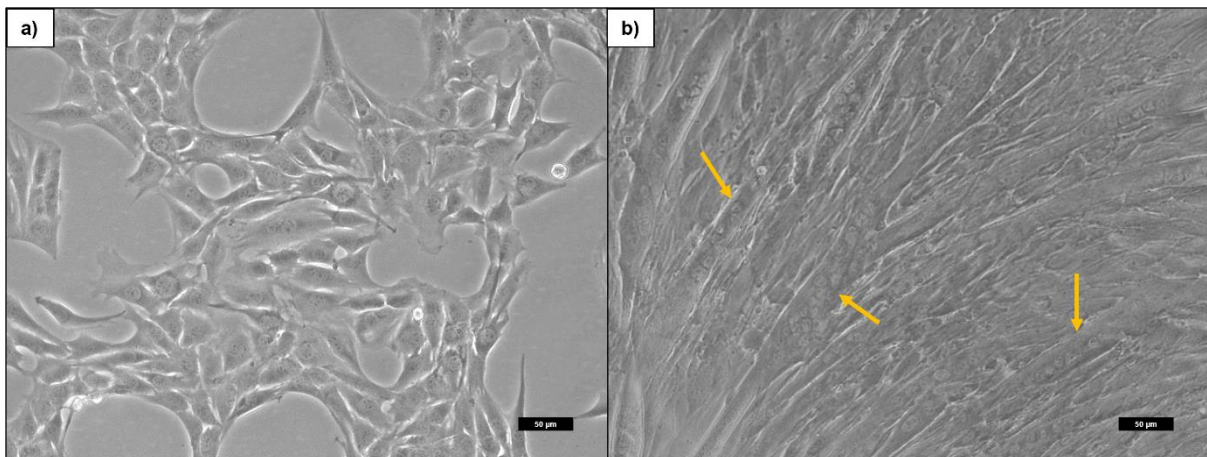
Figure 3.8 C2C12 myoblasts in complete DMEM (a) and differentiated C2C12 myotubes in medium containing 5% HS (b). Yellow arrows indicate differentiated myotubes. Scale bar = 50 µm.

3.3.5 Cytotoxicity of Ionophores on Differentiated C2C12 Myotubes

C2C12 myoblasts were differentiated into myotubes and then exposed to 0.1, 1 and 10 µM monensin, salinomycin and lasalocid for 24, 48 and 72 h (**Figure 3.9**). Compared to the undifferentiated myoblasts, the myotubes were more resistant towards ionophore cytotoxicity. Monensin continued to be the most cytotoxic of the three ionophores investigated, however, cell survival only fell to below 50% after 72 h exposure to 10 µM monensin. Both salinomycin and lasalocid exposure did not

result in cell survival decreasing below 50%, however salinomycin had a slightly greater toxic effect on the myotubes compared to lasalocid. The cell survival increased past that of the solvent control after the myotubes were exposed to 0.1 µM salinomycin as well as 0.1 and 1 µM lasalocid.
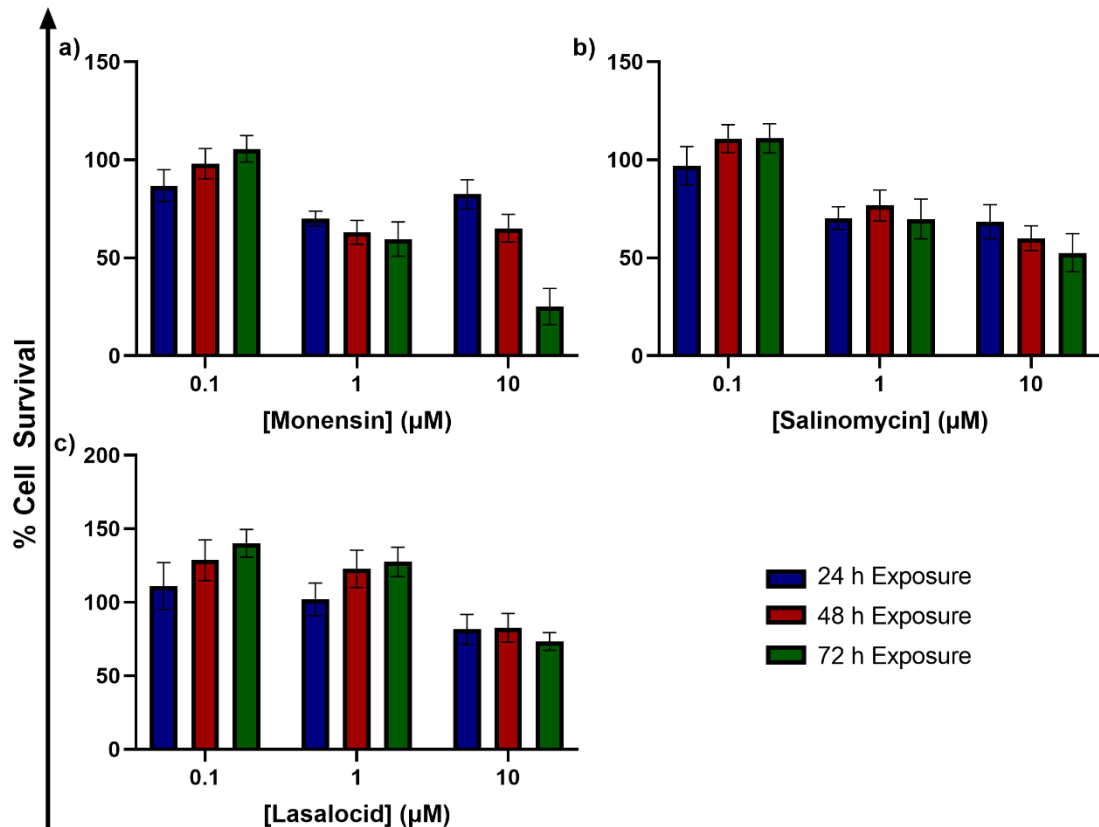
Figure 3.9 Cytotoxicity of ionophores on differentiated C2C12 myotubes. Average cell survival ± StEM (n= 5).

3.3.6 Morphological Alterations of Cardiac and Skeletal Myoblasts, as well as C2C12 Myotubes, due to Ionophore Toxicity

Cardiac and Skeletal Myoblasts

All three cell lines underwent similar morphological alterations when exposed to the ionophores, with the degree of alteration dependent on the ionophore, the concentration of the ionophore, and the exposure time. **Figure 3.10** shows H9c2, L6 and C2C12 myoblasts exposed to 0.1 µM monensin for 24, 48 and 72 h. Myoblasts exposed to low concentrations of monensin and/or exposed for a shorter period, showed no or minor changes between the morphology of exposed myoblasts and the negative control. The first sign of ionophore cytotoxicity appeared as early at 24 h post-exposure. Vesicles appeared within the cytoplasm in the perinuclear region

(**Figure 3.10**, **black arrows**). With higher concentrations and longer exposure periods the vesicles increased both in number and size, eventually filling the cytoplasm. Finally, the myoblasts detached and became spherical, with some appearing to shrink (**Figure 3.10**, **red arrows**). At longer exposure times with higher ionophore concentration cellular debris could be seen floating in the media. Exposure to both salinomycin and lasalocid resulted in similar alterations, however to a lesser extent (not shown).
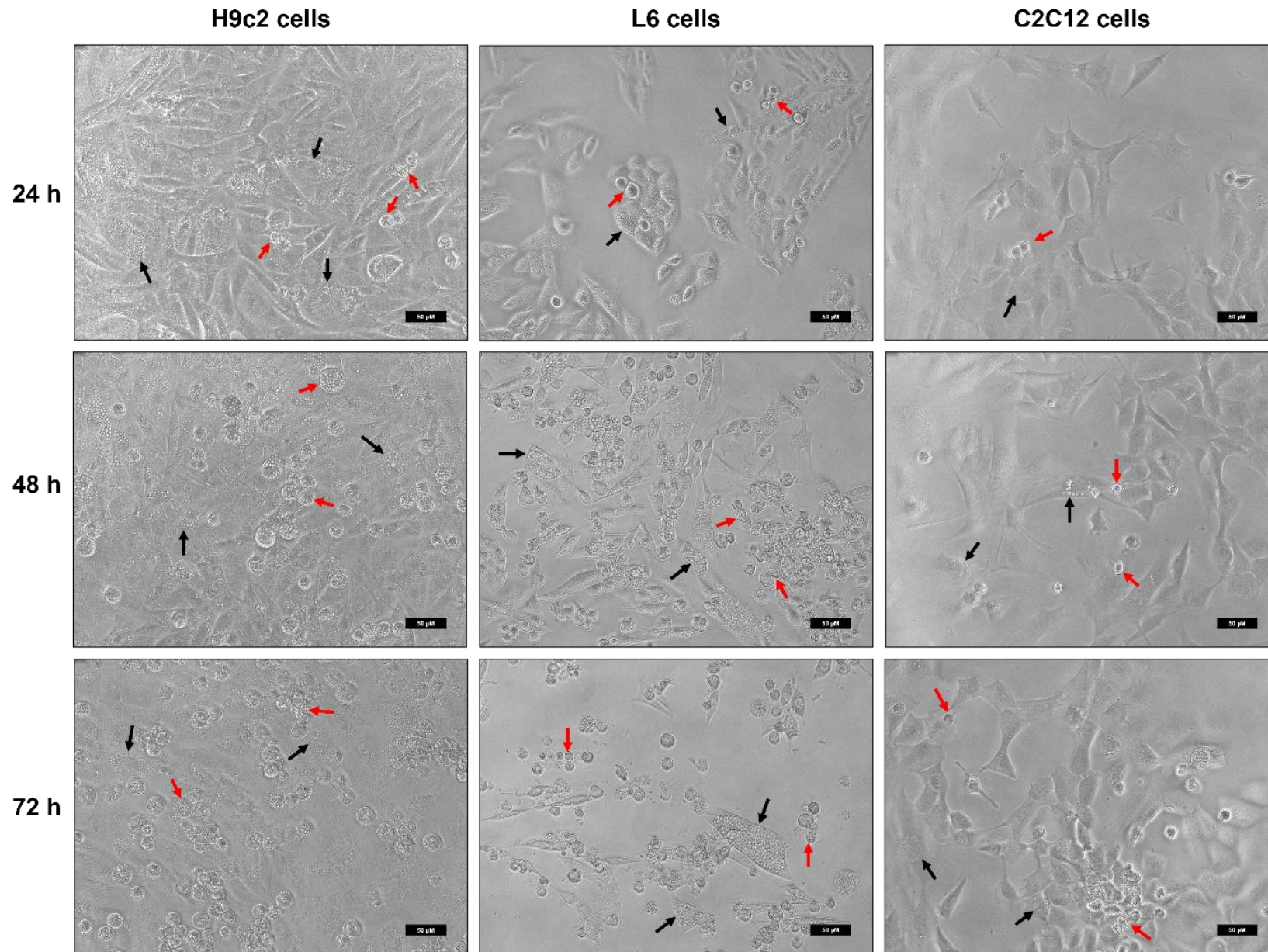
Figure 3.10 H9c2, L6 and C2C12 myoblasts exposed to 0.1 μM monensin. The black arrows indicate myoblasts that have accumulated vesicles within their cytoplasm. The red arrows show spherical myoblasts detached from their surroundings. Scale bar = 50 μm.

Differentiated C2C12 Myotubes

After incubating the myoblasts with media containing 5% HS for a couple of days, the individual C2C12 myoblasts adhered and fused to one another to form long myotubes containing multiple nuclei (**Figure 3.11 a**).

As with the undifferentiated myoblasts, the first visible sign of cytotoxicity was the increasing number of vesicles present within the cytoplasm (**Figure 3.11**, **black arrows**). With increased exposure periods and/or a higher concentration of ionophores, the myotubes swelled and became wider in the middle and tapered towards the ends.
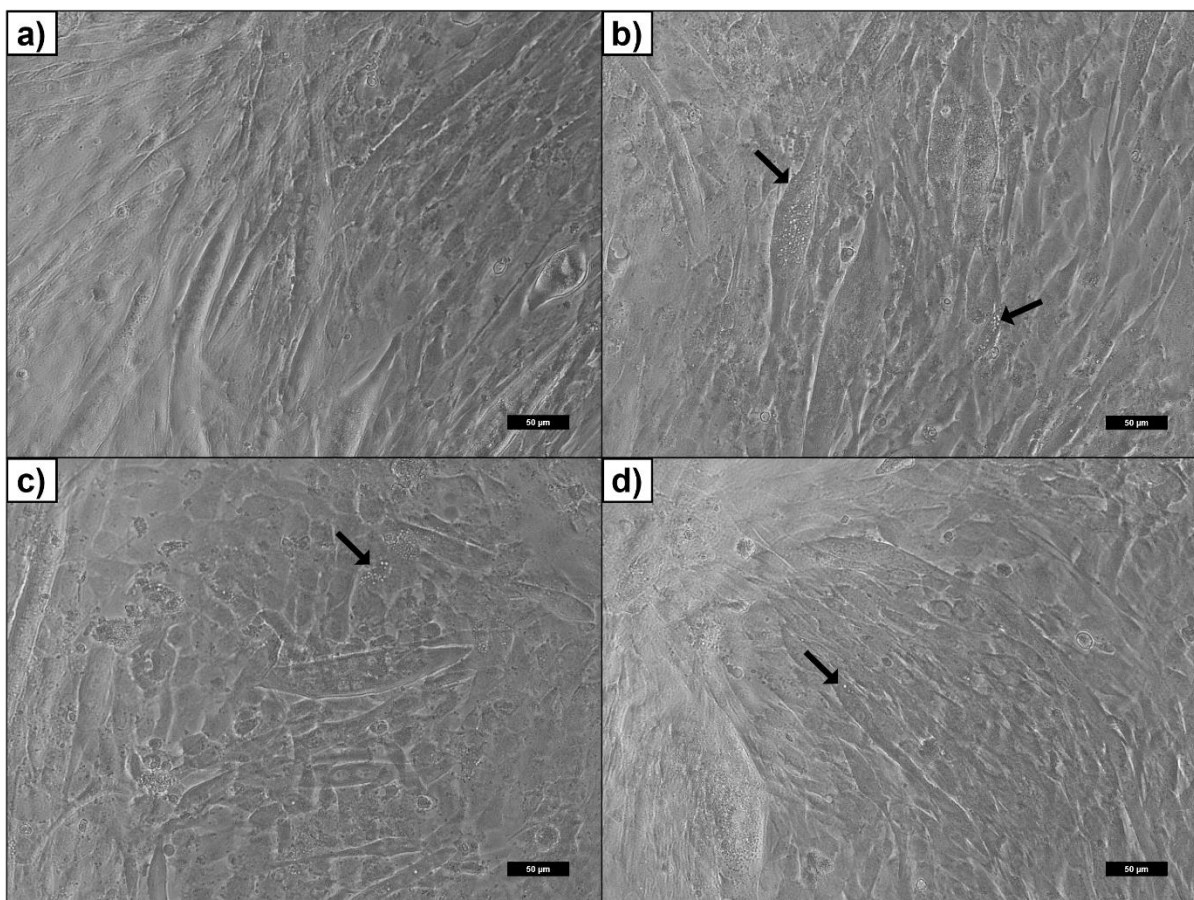
Figure 3.11 Differentiated C2C12 myotubes in complete medium (a), exposed to 1 µM monensin (b), salinomycin (c) and lasalocid (d) for 48 h. Black arrows indicate vesicles accumulated in the cytoplasm. Scale bar = 50 µm.

3.3.7 The Effect of the Ionophores on the Mitochondria of L6 Myoblasts after 48 h Exposure

The mitochondria of L6 myoblasts, stained with MitoTracker Green FM after exposure to 0.1 µM monensin, salinomycin and lasalocid for 48 h, were discernible (**Figure 3.12**). Counterstaining with DAPI confirmed the position of the nucleus.

After image acquisition, the images were deconvoluted to remove the distortions present in the images due to out-of-focus light. Myoblasts from the solvent control appear to have distinct branching mitochondrial networks, diffused across the entire myoblast. After exposure to monensin, the myoblasts were rounder, and the staining of the mitochondria were less specific. On closer view, the mitochondrial network appeared disorganised and disrupted, instead of as fine network-like branches. Salinomycin resulted in a similar lack of distinction between the network-like branches, however to a lesser degree compared to monensin. The distribution of mitochondria of myoblasts exposed to lasalocid were closer to that of the solvent control, however with some myoblasts showing disrupted mitochondrial networks.
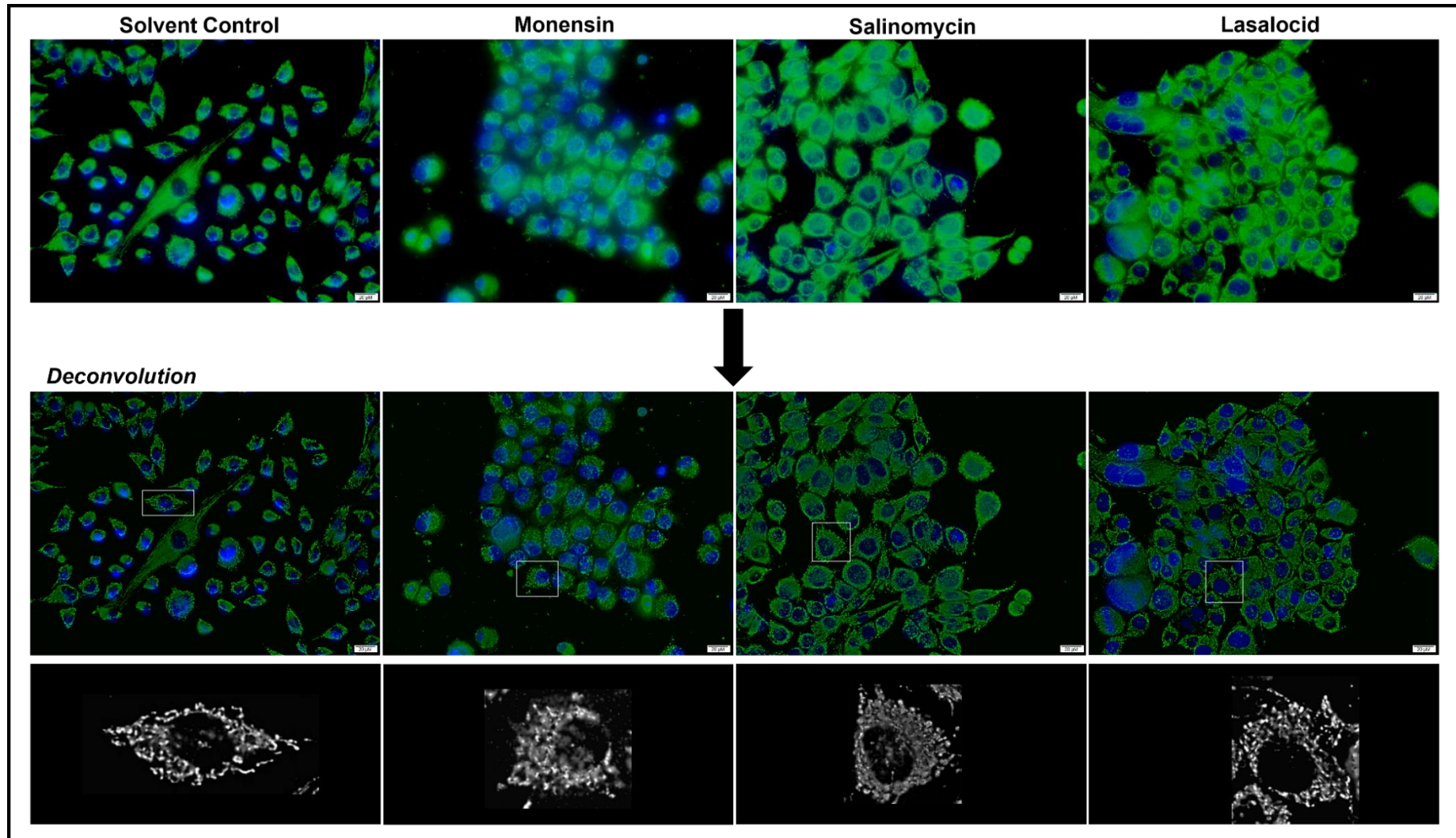
Figure 3.12 The effect of 0.1 μM monensin, salinomycin and lasalocid on the mitochondria of L6 myoblasts after 48 h exposure. The myoblasts were stained with MitoTracker Green FM and DAPI. Deconvolution was used to remove the out-of-focus light from the images. Scale bar = 20 μM.

3.3.8 The Percentage DNA Fragmentation in L6 Myoblasts after Exposure to the Ionophores for 48 h

With the TUNEL assay, DAPI stained the nuclei of the myoblasts blue, while nuclei with DNA fragmentation stained green. In the 'No Fluorescence' control, only nuclei labelled with DAPI were visible (**Figure 3.13**, **No Fluorescence**), thus confirming the absence of non-specific fluorescence. Both the negative and solvent controls only had 0.1% of all nuclei stain positive for DNA fragmentation (**Figure 3.13**, **Negative Control** and **Solvent Control**).
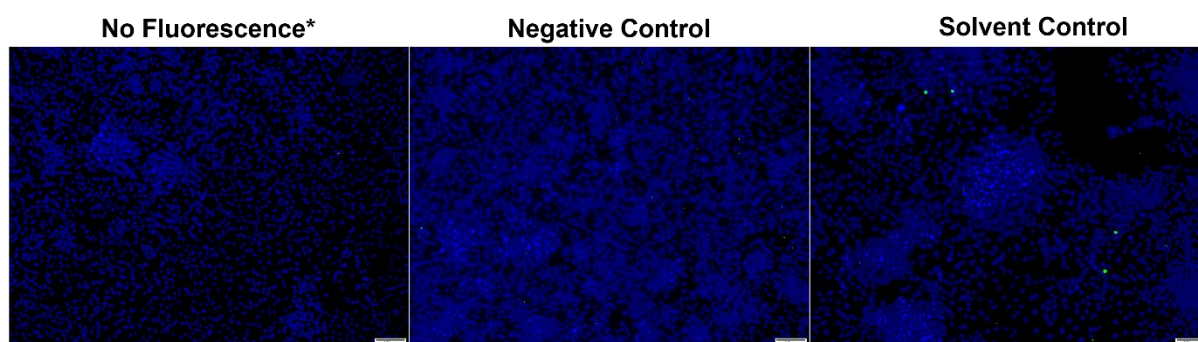
Figure 3.13 The Click-iT PLUS TUNEL assay was performed to investigate the percentage L6 myoblasts with DNA fragmentation. The myoblasts were counterstained with DAPI. The 'No Fluorescence control' was only stained with DAPI. The negative and solvent control had myoblasts incubated in complete medium and complete medium containing 0.1% MeOH, respectively. Nuclei stained blue and TUNEL positive nuclei stained green. Scale bar = 100 µm.

After 48 h ionophore exposure, the number of myoblasts per slide were greatly reduced compared to the controls, especially at higher ionophore concentrations (**Figure 3.14**). The percentage nuclei with DNA fragmentation also increased with higher ionophore concentrations. Exposing the myoblasts to 0.1 µM monensin, salinomycin and lasalocid for 48 h resulted in 4.7, 0.7 and 0.2% of nuclei having DNA fragmentation, respectively. These percentages increased to 11.4, 4.5 and 9.3% after exposure to 1 µM of the respective ionophores. Of the three ionophores, monensin caused the most nuclei to undergo DNA fragmentation.
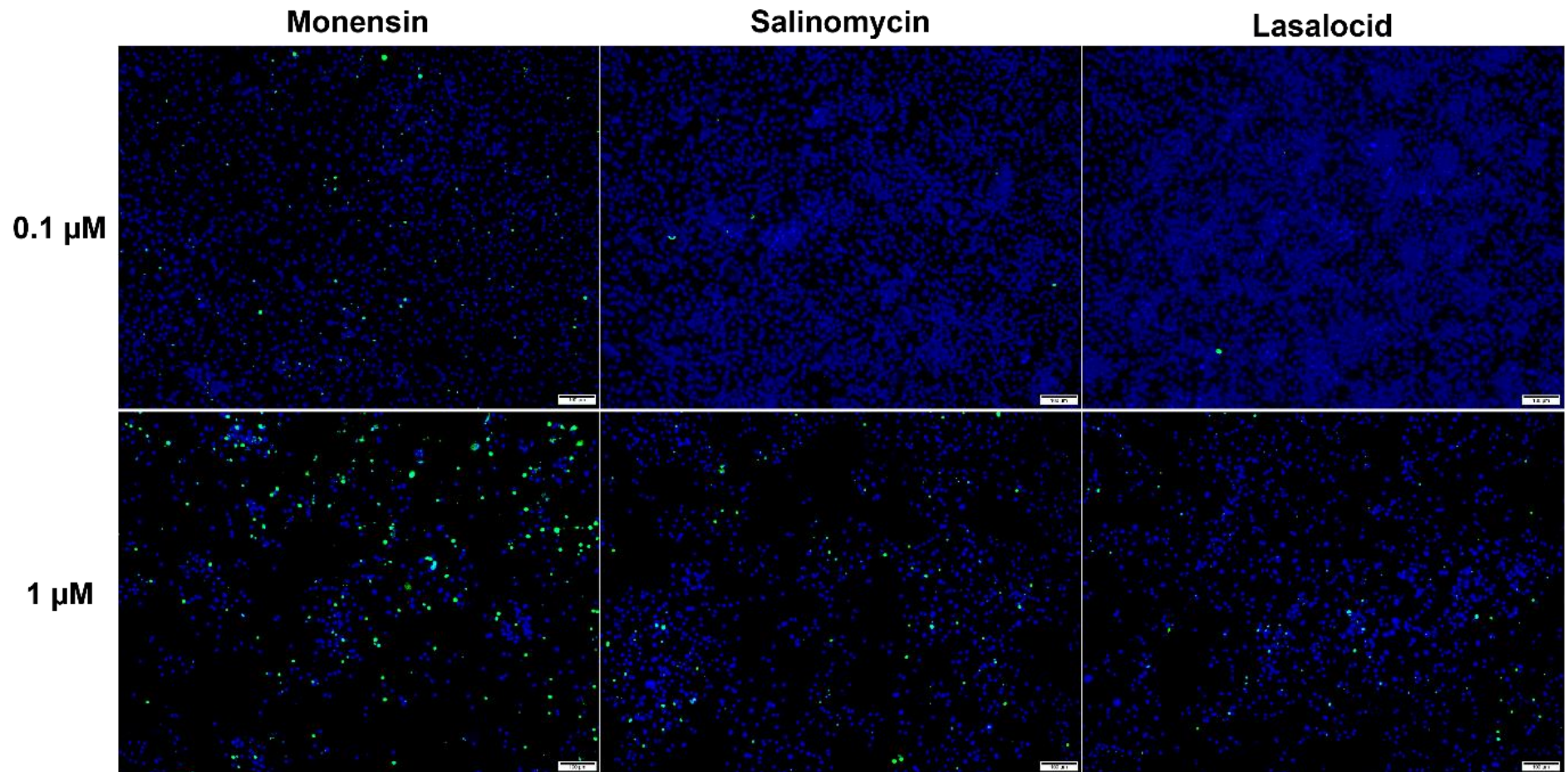
Figure 3.14 The Click-iT PLUS TUNEL assay was performed to investigate the percentage L6 myoblasts with DNA fragmentation after exposure to either 0.1 or 1 µM monensin, salinomycin and lasalocid for 48 h. Nuclei stained blue and TUNEL positive nuclei stained green. Scale bar = 100 µm.

3.4 Discussion

The *in vitro* cytotoxicity of a compound is influenced by various factors such as the organ of origin, species and differentiation status of the cell, the number of cells, nutrients, growth factors, serum concentration and pH in/of the medium and the addition of other drugs that inhibit or accelerate certain cellular pathways (Bagaméry et al., 2021; Hahn and Shiu, 1983; Jablonská et al., 2021; Meingassner et al., 1979). In this chapter the cytotoxicity of three carboxylic ionophores i.e., monensin, salinomycin and lasalocid, were investigated in H9c2, L6 and C2C12 myoblasts as well as in differentiated C2C12 myotubes using the MTT viability assay. The MTT assay reflects the metabolism of viable cells and is dependent on the ability of mitochondrial and cytosolic enzymes to reduce the MTT salt into a purple formazan product (Mosmann, 1983).

Of the three ionophores tested monensin had the greatest cytotoxicity, followed by salinomycin and finally, lasalocid. This corresponds to LD_{50} data obtained from other studies (**Chapter 2**, **Table 2.2**) with a few exceptions (Anderson, 2008; Gad et al., 1985; Galitzer et al., 1986; Hall, 2000; Hanson et al., 1981; Novilla, 2018; Potter et al., 1984; Todd et al., 1984). In all species except for rats, salinomycin has the lowest LD_{50} values recorded. Lasalocid has the highest LD_{50} values recorded, except in chickens. When comparing the susceptibility of the species toward ionophore toxicity, chickens, mice and rats are the most resistant, while horses are the most susceptible having LD_{50} values as low as 0.6 mg/kg. Based on the LD_{50} data, rats are most susceptible to monensin (28.6-40.1 mg/kg), followed by salinomycin (47.6-48.9 mg/kg) and are the least susceptible to lasalocid (122- >130 mg/kg). The H9c2 and L6 cell lines are derived from rat cardiac and skeletal muscles, respectively, and the results corresponds to the LD_{50} data. Mice, however, are more susceptible to salinomycin (57.4 mg/kg) compared to monensin (70-96 mg/kg), but lasalocid (100-146 mg/kg) is still the least toxic. This discrepancy between the EC_{50} data of this study and LD_{50} data could be explained by pharmacokinetic differences *in vivo* including the absorption, distribution, metabolism and excretion of the compound (Freshney, 2001). For example, *in vivo* ionophore toxicity is dependent upon their absorption rate from the gastro-intestinal tract as well as their distribution throughout the organism. Ionophores are rapidly metabolised in the liver to less toxic metabolites and subsequently excreted in bile, thus curtailing their toxic effect

(Novilla, 2018). Additionally, ionophores can result in the release of catecholamines, which in turn affect Ca^{2+} overload and muscle necrosis (Shen and Patel, 1977). *In vitro* experiments have the advantage of simplicity and reproducibility, however, with these advantages comes the exclusion of complex interactions that occur within an organism. During the cytotoxicity experiments, ionophores are directly added to the cells, thus circumventing the toxicokinetic processes. This influence their toxicity and result in the differences seen between *in vivo* and *in vitro* data.

In addition, when evaluating the EC_{50} data, at 24 h the myoblasts were more resistant towards the cytotoxic effect induced by the ionophores and EC_{50}s were higher when compared to 48 and 72 h exposure. *In vivo*, after ingestion ionophores are metabolised in the liver and subsequently excreted in bile, removing the toxin from circulation (Donoho, 1984). However, in cases where ionophores are not efficiently metabolised, such as in the presence of tiamulin, tissues are exposed to ionophores for longer periods which results in increased toxicity (Carpenter et al., 2005; Geor and Robinson, 1985; Witkamp et al., 1995). This is in agreement with the EC_{50} results seen in this study, where longer exposure periods resulted in increased toxicity.

The difficulty experienced when determining the EC_{50} of monensin on C2C12 myoblasts at 24 h was due to the slope of the log-dose response curve. Between 0.25 and 10 µM the cytotoxicity plot remained close to 50% cell survival. Interestingly, at 24 h exposure, lasalocid was the most cytotoxic to L6 myoblasts of the three ionophores. This corresponds to EC_{50} data obtained by Radko et al. (2013b) and Cybulski et al. (2015), who reported that lasalocid was more cytotoxic for L6 myoblasts at 24 h exposure, compared to monensin and salinomycin (see **Chapter 2**, **Table 2.4**). Their EC_{50}s (monensin - 58.3 ± 11.5; salinomycin - 156.3 ± 16.1; lasalocid - 14.0 ± 1.08 µM) were greater in comparison to this study, however, they initially seeded 250 000 L6 cells/ml. As the current study ran over a period of 72 h instead of only 24 h, fewer myoblasts (25 000 L6 myoblasts/ml) were seeded to maintain a log cell growth phase for the duration of the study. Since ionophores are capable of transporting one cation at a time across a biological membrane, the same concentration would have a greater effect on fewer myoblasts. With more myoblasts, the ionophores will distribute more diffusely between myoblasts and the impact on the ion homeostasis of a cell would be less.

Monensin and salinomycin had EC_{50}s in the nanomolar range after 48 and 72 h exposure for all three cell lines. Lasalocid had the highest EC_{50}, it being around the low micromolar range. As mentioned before, exposure to the ionophores resulted in non-monotonic dose-response curves in some instances. The cell survival for H9c2 myoblasts increased at around 10 µM after 48 and 72 h exposure to salinomycin. Lasalocid also caused a slight increase in cardiac myoblasts survival at around 20 µM, though the increase was not significant ($p > 0.05$). A non-monotonic dose-response curve refers to a dose-response curve that shows directional slope changes within the range of concentrations tested. Typical non-monotonic curves can form either a bell or a U-shape. Various examples of non-monotonic dose-responses have previously been reported in literature, such as with endocrine disrupting chemicals (Lagarde et al., 2015). Since a compound might influence a cell or organism's metabolism in a dose-dependent manner, it could potentially result in some cellular pathways being either activated or inhibited at different doses, affecting viability. Alternative reasons for the occurrence of a non-monotonic dose-response curve include, but are not limited to, receptor desensitisation or negative feedback (Lagarde et al., 2015).

The purity of the salinomycin used in this study was 78.8%, however this did not seem to have an impact on cytotoxicity as there was no significant difference when compared to salinomycin with a 95% purity. The only significant difference between the two purity grades was after 72 h exposure (**Figure 3.5**). The 95% purity grade salinomycin promoted myoblasts proliferation at low concentrations, increasing the percentage cell viability past that of the solvent control.

The effect ionophores have on ion homeostasis, indirectly influences various other cellular pathways. Potassium and Na^+ concentrations affect intracellular Ca^{2+}, control cell volume, regulate programmed cell death and play an important role in generating and maintaining the membrane potential of cells (Bortner and Cidlowski, 2003; Kay, 2017). Ion concentrations and membrane potential influence cell cycle progression and can inhibit proliferation (Blackiston et al., 2009; Urrego et al., 2014). Myocytes and neurons with a hyperpolarised membrane potential generally have a diminished degree of mitotic activity compared to cells with a lower membrane potential. For example, the depolarisation of chick spinal cord neurons using ouabain, a Na^+/K^+-ATPase inhibitor, induced DNA synthesis and mitosis (Cone Jr and Cone, 1976;

Stillwell et al., 1973). If ionophore exposure results in the depolarisation of the plasma membrane, ionophores could potentially increase cell proliferation. However there has also been numerous reports where ionophores inhibit proliferation of cancer cells by inducing cell cycle arrest (Iljin et al., 2009; Ketola et al., 2010; Park et al., 2003; Park et al., 2002; Tyagi and Patro, 2019).

Although many cytotoxicity studies are conducted on undifferentiated cells due to ease of work, differentiated cells have a greater resemblance towards the organ of origin and could thus arguably be a better representation of actual cytotoxic effects. Attempts to differentiate H9c2, L6 and C2C12 myoblasts were met with variable success, with the differentiation of the H9c2 cell line presenting the biggest challenge. The addition of retinoic acid to medium with a reduced serum concentration, prevents myogenic trans-differentiation and promotes differentiation towards a more cardiac-like phenotype (Branco et al., 2015; Ménard et al., 1999). Various concentrations of retinoic acid in combination with low concentrations of either FBS or HS were used to differentiate H9c2 myoblasts but was met with little success. Pattern et al. (2017) concluded that the H9c2 cell line might be resistant towards differentiation after two separate laboratories failed to create a robust protocol to establish a homogeneous differentiated population. The history (passage number) of the cell line and the handling of retinoic acid were indicated as factors that could contribute towards this resistance. Failure to induce differentiation in this study might be related to the lowest passage number available in our laboratory i.e., 18. Retinoic acid is also light sensitive, hydrophobic and has a half-life of around 3.5 to 6 h in culture, therefore special care should be taken when handling it (Redfern and Todd, 1988; Williams and Napoli, 1985). Both the L6 and C2C12 cell lines were less resistant towards differentiation and cultures incubated with medium containing 5% HS resulted in long tubular cells with multiple nuclei (**Figure 3.7** and **Figure 3.8**). However, some non-differentiated myoblasts remained, and longer incubation resulted in an increase of dead myoblasts and cellular debris, rather than a more homogeneous differentiated myotube population. An additional complication was the ability of the differentiated myotubes to adhere to the surface of the well into which they were seeded. L6 myoblasts tended to detach during the cytotoxicity assays, resulting in variation between the replicates of the results obtained. C2C12 myoblasts demonstrated a greater ability to adhere to the surface, hence, the

differentiated C2C12 myotubes were selected for comparative cytotoxicity studies with the ionophores. Differentiated C2C12 myotubes were less susceptible to ionophore toxicity compared to undifferentiated myoblasts. This might be due to the increased number of myoblasts needed to achieve differentiation. The same concentration of an ionophore would have greater effect on fewer myoblasts. As with the undifferentiated myoblasts, monensin had the greatest cytotoxicity. In the case of future differentiation studies, the differentiation status of the myoblasts should also be confirmed using cardiac and skeletal muscle specific markers such as troponin and cardiac and skeletal subtype-specific L-type Ca^{2+} channels (as discussed further in **Chapter 6**).

The morphology of the cardiac and skeletal myoblasts exposed to monensin, salinomycin and lasalocid was investigated using phase contrast light microscopy. Clear vesicles first appeared near the nuclei of the myoblasts, possibly arising from a disrupted osmotic balance as well as dilated Golgi apparatus and other organelles such as ER. As the exposure time and ionophore concentrations increased, the number of vesicles increased eventually filling the cytoplasm as shown in **Figure 3.10** (**black arrows**). Ionophores inhibit cellular transportation at the Golgi apparatus, with the resultant accumulation of vesicles within the cytoplasm (Mollenhauer et al., 1990). As the Golgi apparatus is usually located within the perinuclear region (**Chapter 5**, *vide infra*), this could explain why the vesicles are first seen within this region. Additionally, the osmotic gradient of the cell increases after ionophore exposure, for which the cell needs to expend energy in order to maintain homeostasis. When the energy is depleted, the organelles swell due to an influx of water (Mehlhorn et al., 1983; Smith et al., 1981). Autophagy is a mechanism by which the cell can regulate cellular energy metabolism by recycling cellular components. The process has a cytoprotective effect and its inhibition after exposure to the ionophores results in enhanced apoptosis (Kim et al., 2017a; Kim et al., 2017b; Kim et al., 2016). Autophagy is, however, dependent on pH to degrade cellular content, while ionophores are known to disrupt intracellular pH (Mollenhauer et al., 1990). Monensin and lasalocid induce autophagy by either increasing the number of autophagic vesicles or by lowering their degradation ability (Grinde, 1983; Mahtal et al., 2020; Mollenhauer et al., 1990). Therefore, a few of the vesicles visible with light microscopy could presumably be autophagic vesicles, which can be

confirmed using TEM (see **Chapter 5**). In addition to the appearance of cytoplasmic vesicles, the myoblasts become rounded, and detached from both the neighbouring myoblasts and the surface (**Figure 3.10**, **red arrows**). Some myoblasts appear to shrink, possibly suggesting apoptosis. At later stages of exposure and at higher ionophore concentrations, myoblast debris could be seen indicating that the plasma membrane integrity was compromised, and the myoblast underwent necrosis. Notably, in the case of *in vitro* apoptosis, cells will eventually undergo secondary necrosis as there are no processes to remove apoptotic bodies (Berghe et al., 2010; Elmore, 2007). Only the morphological alterations occurring after exposure to monensin is presented in **Figure 3.10**; however, both salinomycin and lasalocid had similar effects, but with less severity. **Figure 3.11** shows the morphological alterations occurring in differentiated C2C12 myotubes after 48 h exposure to 1 μM monensin, salinomycin and lasalocid. Similar to the myoblasts, the myotubes had vesicles appearing in their cytoplasm after ionophore exposure. The centre of the myotube would swell, while the ends remained tapered (**Figure 3.11 b**). Vesicles were dispersed throughout the cytoplasm with increased concentrations and exposure times. The myotubes would become spherical and start to detach from the surface.

An additional pathway by which ionophores induce cytotoxicity is by damaging mitochondria and disrupting oxidative phosphorylation (Wrogemann and Pena, 1976). Fluorescent microscopy was used to investigate the effect of the ionophores on the mitochondria of L6 myoblasts (**Figure 3.12**). As fluorescent images, especially at higher magnification, are often blurry due to scattered light the images were deconvoluted to remove blur generated by light diffusion. The resulting images were dimmer, but with a clearer indication of the myoblasts' mitochondrial networks. Ionophore exposure affected the mitochondria of the myoblasts as expected, with monensin having the greatest impact on mitochondrial morphology. Monensin exposure resulted in the total disruption of the mitochondrial network, with the individual mitochondria appearing less distinct. The mitochondria were also concentrated close the nucleus, which can be explained by the rounding-off of the myoblasts as previously seen in **Figure 3.10** (**red arrows**). As 0.1 μM is much greater than the EC_{50} determined for monensin at 48 h it is not surprising to find that the mitochondrial network in most of the myoblasts appeared damaged. The same

phenomenon can be seen in L6 myoblasts exposed to both salinomycin and lasalocid, but to a lesser degree. It should be noted that the MitoTracker Green FM dye localises in mitochondria irrespective of their mitochondrial membrane potential, therefore the dye does not indicate the functional ability of the mitochondria. In **Chapter 5**, a closer look is taken at the ultrastructural changes that occur in mitochondria after ionophore exposure. Further possible quantitative analysis of the effects of ionophore exposure on the mitochondrial network is discussed in **Chapter 6**.

Ionophores damage mitochondria through Ca^{2+} overload, production of ROS and the subsequent alteration of the mitochondrial membrane potential (Przygodzki et al., 2005; Wrogemann and Pena, 1976). Mitochondria are key components in various cell death pathways and the loss of mitochondrial membrane potential can lead to apoptosis (Galluzzi et al., 2012a; Kroemer et al., 2009). There have been numerous reports of ionophores inducing cell death through the production of ROS (Ketola et al., 2010; Kiełbasiński et al., 2020; Kim et al., 2017a; Kim et al., 2017b; Kim et al., 2016; Qin et al., 2015). Additionally, various cell death mechanisms are dependent on intracellular Ca^{2+} levels (Kroemer et al., 2009). Lasalocid directly interferes with Ca^{2+} homeostasis by transporting Ca^{2+} through cellular membranes (Novilla, 2018). Both monensin and salinomycin likewise, indirectly result in increased intracellular Ca^{2+} by firstly affecting the Na^+ and K^+ ion homeostasis (Novilla, 2018). Increased cytoplasmic Ca^{2+} in turn activates various proteases such as calpains and caspases that induce apoptosis (Danese et al., 2017). ATP depletion, in contrast, is linked to necrosis, as programmed cell death requires energy to proceed (Golstein and Kroemer, 2007; Nicotera and Melino, 2004).

A TUNEL assay was performed to determine whether ionophore exposure resulted in increased DNA fragmentation, an early indicator of apoptosis. Both the negative and solvent controls had a minimal number of myoblasts stained positive (**Figure 3.13**), while myoblast exposed to the different ionophore, especially monensin, had a higher percentage of nuclei with DNA fragmentation. These results imply that toxic ionophore concentrations induce apoptosis in some of the affected myoblasts. However, the number of myoblasts per slide decreased after ionophore exposure and some apoptotic myoblasts could have already detached at the time of the experiment. Additionally, it should be noted that, in some cases, necrotic cells can

also exhibit DNA fragmentation (de Torres et al., 1997; Fink and Cookson, 2005; Zheng et al., 1997). Therefore, whether ionophores cause apoptosis was further investigated as discussed in **Chapter 5**, *vide infra*, using the ultrastructural changes that occurred in the myoblasts after ionophore exposure.

In conclusion, the results reported in this Chapter indicated that, of the three ionophores tested, monensin was the most cytotoxic, followed by salinomycin and lasalocid. Ionophore exposure resulted in the excessive vesiculation of the myoblast cytoplasm as well as disruption of the mitochondrial network. Finally, ionophore exposure resulted in an increase in the percentage myoblasts with DNA fragmentation, possibly indicating an increased tendency towards apoptosis among affected myoblasts.

Chapter 4: The *In vitro* Effect of Monensin, Salinomycin and Lasalocid on Certain Cytoskeletal Proteins and Filaments of Cardiac and Skeletal Myoblasts

4.1 Introduction

Cardiac and skeletal muscles are the primary targets of ionophore toxicosis, with lesions often evident one to two weeks following ingestion. The distribution and severity of the muscle lesions are dependent on time and dosage. Morphologically, the effects on cardiac and skeletal muscle fibres include degeneration, necrosis and repair. A variable inflammatory reaction is occasionally present with macrophages infiltrated between necrotic tissues (Confer et al., 1983; Van Vleet and Ferrans, 1984a, b). Myofibrillar degeneration is generally accompanied by swollen mitochondria, vacuolisation and disruption of the contractile filaments (Confer et al., 1983; Van Vleet and Ferrans, 1984a, b). In swine fed toxic doses of monensin, atrial myocytes underwent contraction band necrosis, likely due to Ca^{2+} overload (Van Vleet and Ferrans, 1984b). The contractile apparatus in myofibers consists of distinct cytoskeletal elements and proteins that enable muscles to contract in response to intracellular Ca^{2+} flux. Actin and myosin are the principal components of thin and thick filaments, respectively and form part of the sarcomere. Furthermore, intermediate filaments such as desmin and synemin are located at the Z-disk and play an essential role in structural support (Mizuno et al., 2001). The microtubule network does not form a direct part in the sarcomere; however, studies suggest that microtubules in combination with desmin mechanically couple the sarcomere to the non-sarcomeric cytoskeleton (Robison et al., 2016). Ionophores can affect the cytoskeleton directly through their alteration of the ion homeostasis or indirectly via their downstream effects e.g., shifting the intracellular pH or activation of various proteases (Kanje et al., 1981; Paddock and Albrecht-Buehler, 1986; Schenk et al., 2015; Tilney et al., 1978).

In this chapter, immunofluorescent and immunocytochemical methods were utilised to determine whether monensin, salinomycin and lasalocid exposure would have an effect on certain cytoskeletal proteins and filaments of cultured H9c2, L6 and C2C12 myoblasts.

4.2 Materials and Methods

4.2.1 Immunofluorescent Staining of Actin & β-Tubulin

The H9c2 (100 000 myoblasts/ml), L6 (25 000 myoblast/ml) and C2C12 (10 000 myoblasts/ml) cell lines were seeded into a 24-well plate containing sterile 10 mm round coverslips and allowed 24 h to adhere to the surface of the coverslip. All three cell lines were exposed to 0.1 and 1 µM monensin, salinomycin and lasalocid for 24, 48 and 72 h. The negative and solvent controls consisted of myoblasts incubated in complete DMEM medium and complete DMEM medium containing 0.1% MeOH, respectively. Cytochalasin D (Sigma-Aldrich) and vinblastine sulphate (Sigma-Aldrich) were used as positive controls since they disrupt the microfilament (Shoji et al., 2012) and microtubule networks (Laisne et al., 2021), respectively. The myoblasts in the positive control were exposed to either 12 µM cytochalasin D for 15 min or 5 µM vinblastine sulphate for an hour at 37 °C prior to fixation.

The myoblasts were washed with PBS for 5 min while being gently shaken using a microplate shaker, followed by fixation using 100% acetone (Merck) for 10 min at -20 °C. The acetone was discarded, and the PBS wash step repeated twice for 5 min each. To stain actin 1 µg/ml phalloidin-fluorescein isothiocyanate (FITC) (Sigma-Aldrich), prepared in PBS, was added to each well and incubated for 30 min at 37 °C. To stain β-tubulin, the myoblasts were incubated with 1% BSA (Biowest) for 30 min at 37 °C in PBS to block all nonspecific binding sites, followed by incubation with 1 µg/ml monoclonal anti-β-tubulin-Cy3 (1:100 in PBS) for 1 h at 37 °C. The myoblasts were rinsed three times with PBS, after which the nuclei were stained with 1.3 µg/ml DAPI (in ddH$_2$O) for 15 min at 37 °C. To remove the excess stain, the myoblasts were washed three times with PBS for 5 min each. Finally, the coverslips were mounted on microscope glass slides using Prolong^{TM} Gold antifade reagent (Molecular Probes) and sealed with clear nail polish to prevent drying of the sample. All slides were viewed with an Olympus BX63 Fluorescent microscope using the filters described in **Table 4.1**.

Table 4.1 The filters used with the Olympus BX63 fluorescent microscope to analyse the immunofluorescent staining of actin and β-tubulin in cardiac and skeletal myoblasts.

	Excitation (nm)	Emission (nm)	BX3 Fluorescent filter cube used
DAPI	359	461	U-FUNA Excitation Filter BP 360-370 Emission Filter BA 420-460
Phalloidin-FITC	496	517	U-FBNA Excitation Filter BP 470-495 Emission Filter BP 510-550
Anti-β-Tubulin-Cy3	550	570	U-FYW Excitation Filter BP 540-585 Emission Filter LP600

The fluorescent images were merged using Fiji – ImageJ image processing package. The images were deconvoluted using the Diffraction PSF 3D and Iterative Deconvolve 3D plugins as previously described in **Chapter 3**. The region of interest (ROI), indicated on the right of **Figures 4.1** to **4.12** were kept in grayscale and magnified from the corresponding image to better indicate the microfilament or microtubule networks of selected myoblasts.

4.2.2 Immunocytochemical Staining of Desmin and Synemin in C2C12 Myoblasts

C2C12 myoblasts were cultured in complete DMEM, seeded into an 8-well chamber slide (10 000 myoblasts/ml) and allowed 24 h to adhere to the surface. On the day of exposure, the myoblasts in each well were exposed to 1 µM monensin, salinomycin and lasalocid for 24, 48 and 72 h. The controls used during this study included a negative control, a solvent control (0.1% MeOH) and two positive controls i.e., 1 mM glyoxal (Sigma-Aldrich) added on the day of exposure as well as 20 µM cytochalasin D (Sigma-Aldrich) added 30 min before fixation. Exposure to glyoxal, an advanced glycation end product, and cytochalasin D, which inhibits actin polymerisation, results in the disorganisation of the desmin network (Diguet et al., 2011).

After exposure, immunocytochemistry was performed using an indirect immunoperoxidase technique, previously described by Botha et al. (2019). All immunocytochemical staining techniques were performed by the Pathology Section

of the Department of Paraclinical Sciences, Faculty of Veterinary Science, University of Pretoria. The slides were air-dried, fixed in 4% neutral buffered formalin for at least 30 min and rinsed with 70% alcohol for 10 min. Each slide was incubated in 3% hydrogen peroxide (in MeOH) for 15 min to supress endogenous peroxidase activity and rinsed three times with dH_2O. Microwave heat-induced epitope retrieval (HIER) followed, using either Tris-EDTA (pH 9) or citrate (pH 6) buffers, for 21 min at 96 °C for desmin and synemin staining, respectively. The slides were cooled for 15 min and rinsed five times with dH_2O. To facilitate non-specific immunoglobulin binding, slides were incubated with normal HS (1:10 in PBS, pH 7.6) supplemented with 0.1% BSA for 20 min in a humidified chamber at room temperature. The myoblasts were then incubated with either the desmin or synemin primary antibody (**Table 4.2**) for 1 h and subsequently rinsed three times with dH_2O followed by PBS buffer for 10 min.

Table 4.2 Antibodies used for immunocytochemistry staining of the C2C12 myoblasts.

Primary Antibody	Dilution	Manufacturer
Mouse Monoclonal Desmin (D33) Antibody	1:200	DakoCytomation, Denmark
Goat Polyclonal Synemin (S-16) Antibody	1:100	Santa Cruz Biotechnology, Inc.
Rabbit-Anti-Goat (link) Antibody	1:500	Dako, Glostrup, Denmark

Incubation with the synemin primary antibody, was followed by an additional incubation step with a rabbit-anti-goat antibody diluted in a PBS buffer (pH 7.6) supplemented with 0.1% BSA for 30 min in a humidified chamber at room temperature. All slides were incubated with the Dako REAL Envision Rabbit/Mouse polymer-based detection system for 30 min, rinsed three times with dH_2O as well as in PBS buffer for 10 min. The slides were incubated with a 3,3'-diaminobenzidine (DAB) chromogen for 2-3 min, rinsed with dH_2O, counter stained with haematoxylin for 15 sec and washed again with dH_2O. Finally, slides were dehydrated using increasing concentrations of alcohol, i.e., 70%, 96% and 100% and mounted using Entellan (Merck Millipore) for examination under a microscope.

Each slide was viewed and photographed using a BX63 Olympus Fluorescent microscope. Six (692 x 521 µm) images were taken and used for further analysis. The total number of myoblasts per image was counted using the positive cell detection tool from QuPath (Version 0.3.0) (Bankhead et al., 2017). The myoblasts were classified based on the haematoxylin optical density around the nucleus as negative (<0.2), light (0.2-0.5), medium (0.5-1.0) or dark (>1.0). The images were

manually scanned for any errors and corrected where necessary. The percentages of negative to dark stained myoblasts were calculated as a function of the total number of myoblasts counted, then averaged over the number of images.

4.3 Results

4.3.1 The Effect of Ionophores on the Microfilament and Microtubule Network

The morphology of the myoblasts differed between the three cell lines. The H9c2 myoblasts were relatively large spindle-to-stellate shaped, mono- or multinucleated cells. The L6 myoblasts in comparison were smaller, round-to-spindle shaped cells. Many of the myoblasts had elongated cell-to-cell protrusions reaching lengths in excess of the main body of the cell. C2C12 myoblasts were between H9c2 and L6 myoblasts in size, were spindle-to-stellate shaped and had long cell-to-cell protrusions. After staining, the negative controls (**Figure 4.1**) and solvent controls (**Figure 4.2**) were similar, having a normal mesh-like arrangement of polymerised actin filaments (**green**) and a dense filament network of β-tubulin (**red**). One nucleus per myoblast was commonly present in the middle of the cytoplasm. Some myoblasts undergoing mitosis were observed, with the microtubules forming the mitotic spindle visible (**Figure 4.1** and **Figure 4.2**, **white arrows**).

Cytochalasin D was used as a positive control and added 15 min before fixation which resulted in the disruption of the microfilaments (**Figure 4.3**). The myoblasts clumped together in a stellate shape, with long protrusions reaching outward. The microfilament network was broken into shorter filaments but remained intact around the nuclei of the myoblasts. Typical examples of affected myoblasts are demonstrated in the ROI (**Figure 4.3**, **ROI**).

Vinblastine sulphate was used as a positive control to inhibit microtubule formation and added an hour before the fixation step (**Figure 4.4**). The microfilament network of the myoblasts remained mostly normal with a mesh-like appearance. The microtubule network, however, became disorganised with short, rod-like stubs appearing. The aggregation of the microtubule network occurred more towards the periphery of the myoblasts, especially in H9c2 and C2C12 myoblasts. L6 myoblasts

appeared more rounded with less outward protrusions however, the microtubule-stubs were not as prevalent.

H9c2 myoblasts

H9c2 myoblasts exposed to monensin showed limited change in their microfilament network after 24 h exposure (**Figure 4.5** and **Figure 4.6**). However, after 48 and 72 h exposure a few myoblasts had disrupted microfilaments (**red arrows**), especially noticeable in shrinking and rounded myoblasts. Still, many of the myoblasts remained unaffected with microfilaments stretching uninterrupted across the cytoplasm. In contrast, the microtubule network was clearly disrupted (**blue arrows**), with 'gaps', most likely due to vesicles developing, visible in many of the myoblasts. These 'gaps' increased in number with longer exposure times but were not as noticeable in the microfilament network. Myoblasts exposed to 1 µM monensin were more affected compared to myoblasts exposed to 0.1 µM. In addition to the 'gaps', the tubulin network demonstrated less integrity and continuity compared to the negative and solvent controls. In some cases, it appeared as if tubulin concentrated around the position of the nuclei of the myoblasts (**green arrowheads**). The H9c2 myoblasts became shrunken and rounded with longer exposure times (**white circles**), in which case the finer architectural structure of both the microfilament and microtubule networks became lost whilst they were concentrated around the nucleus.

The H9c2 myoblasts were less affected by salinomycin (**Figure 4.7** and **Figure 4.8**) compared to those exposed to monensin, although similar changes were observed for both ionophores. The microfilament network remained largely unaffected, but limited disruption after 48 and 72 h exposure to 1 µM salinomycin was noticed (**red arrows**). The microtubule network contained 'gaps' (**blue arrows**), visible from exposure to 1 µM salinomycin from 24 h onwards. Additionally, the network appeared frayed compared to the negative control. A few myoblasts shrunk and lost their fine cytoskeletal architecture (**white circles**). Cytoskeletal debris could be seen between myoblasts after 72 h exposure to 1 µM salinomycin (**yellow arrows**).

H9c2 myoblasts exposed to 0.1 µM lasalocid (**Figure 4.9**, **ROI**) showed the least degree of change, with sparse 'gaps' visible in the microtubule network (**blue arrows**) after 72 h exposure and only the occasional myoblasts rounding up (**white**

circles). Both the number of 'gaps' and rounded myoblasts increased slightly with an increase in lasalocid concentration to 1 µM (**Figure 4.10**). The microfilament network remained largely unaffected, with single myoblasts showing disrupted filaments (**red arrows**). Additionally, cytoskeletal debris (**yellow arrows**) as well as myoblasts undergoing mitosis (**white arrows**) could be seen after 72 h exposure to lasalocid.

L6 myoblasts

The greater cytotoxic effect of monensin, especially on the L6 cell line (see **Chapter 3**, **Table 3.3**), was clearly evident on the microscopic fields available to view. Following exposure to 0.1 and 1 µM monensin the filamentous network was disrupted and appeared grainy (**Figure 4.11** and **Figure 4.12**, **red arrows**). The microtubule network was also severely disturbed and appeared less dense in comparison to the negative controls. 'Gaps' were also abundantly present within the microtubule network (**blue arrows**); however, due to the smaller size of the L6 myoblasts the 'gaps' were not as evident when compared to that of the larger H9c2 myoblasts. The myoblasts appeared smoother, with fewer cell-to-cell protrusions. Due to the cytotoxicity of monensin, the majority of the myoblasts rounded up (**white circles**) and clumped together, with the cytoskeletal elements concentrated around the nuclei. Cytoskeletal debris were also observed between myoblasts (**yellow arrows**).

Salinomycin exposure resulted in alterations of both cytoskeletal proteins investigated. Exposure to 0.1 µM salinomycin (**Figure 4.13**) had limited effects on the microfilament and microtubule network, with a few 'gaps' appearing in the microtubule network (**blue arrows**). Following exposure to 1 µM salinomycin, the microfilament network appeared slightly disrupted (**Figure 4.14**, **red arrows**) and became concentrated around the nuclei, especially after 48 and 72 h. Additionally, the microtubule network became disrupted with an increased number of 'gaps' appearing in the network (**blue arrows**). Tubulin was concentrated around the edges as well as the nuclei (**green arrowheads**) of some myoblasts exposed to 1 µM salinomycin for 48 and 72 h. With longer exposure times, the myoblasts shrunk and became round (**white circles**), and the cell-to-cell protrusions were lost. Some cytoskeletal debris (**yellow arrows**) could also be seen lying in between the myoblasts.

L6 myoblasts exposed to lasalocid were the least affected (**Figure 4.15** and **Figure 4.16**). The microfilament network remained relatively undisturbed, while the microtubule network of myoblasts exposed to 1 µM lasalocid was slightly disrupted. Some myoblasts had 'gaps' (**blue arrows**) present after 48 and 72 h exposure. A few myoblasts were shrunken and rounded (**white circles**). In addition to the affected myoblasts, myoblasts undergoing mitosis (**white arrows**) were also visible.

C2C12 myoblasts

After exposure to 0.1 µM monensin (**Figure 4.17**) no major alteration in the microfilament network could be discerned. However, a few myoblasts had disrupted microfilaments after 1 µM exposure (**Figure 4.18**, **red arrows**). In contrast, the microtubule network, similar to the other two cell lines, had 'gaps' (**blue arrows**) visible as soon as 24 h post-exposure. The tubulin network had reduced integrity, not being as dense as that of the negative and solvent controls and was concentrated around the nuclei (**green arrowheads**) of C2C12 myoblasts. In addition to the typical shrinking and round myoblasts (**white circles**) observed after ionophore exposure, some myoblasts also appeared to be slightly elongated.

Salinomycin exposure had a muted effect on C2C12 myoblasts, with no significant alteration in either the microfilament or microtubule network visible after 0.1 µM (**Figure 4.19**, **ROI**) exposure, except for a few round myoblasts (**white circles**). After exposure to 1 µM salinomycin (**Figure 4.20**), a few 'gaps' (**blue arrows**) were present in the microtubule network. As with monensin, salinomycin caused both round and elongated myoblasts to appear. Myoblasts undergoing mitosis were also visible (**Figure 4.20**, **white arrows**).

Exposure to either 0.1 or 1 µM lasalocid (**Figure 4.21** and **Figure 4.22**) resulted in no major differences in either the microfilament or microtubule network. A small number of myoblasts had 'gaps' in the microtubule network (**blue arrows**), but most were unaffected. A few myoblasts were shrunken and rounded (**white circles**) as a result of the ionophore exposure; however, there were also some myoblasts undergoing mitosis (**white arrows**).

It should be noted that debris (**yellow arrows**) of dead myoblasts were seen for most of the myoblasts exposed to the ionophores, especially at higher

concentrations and longer exposure times. The debris of both microfilaments and microtubules appeared broken and fractured, with the nuclei missing.
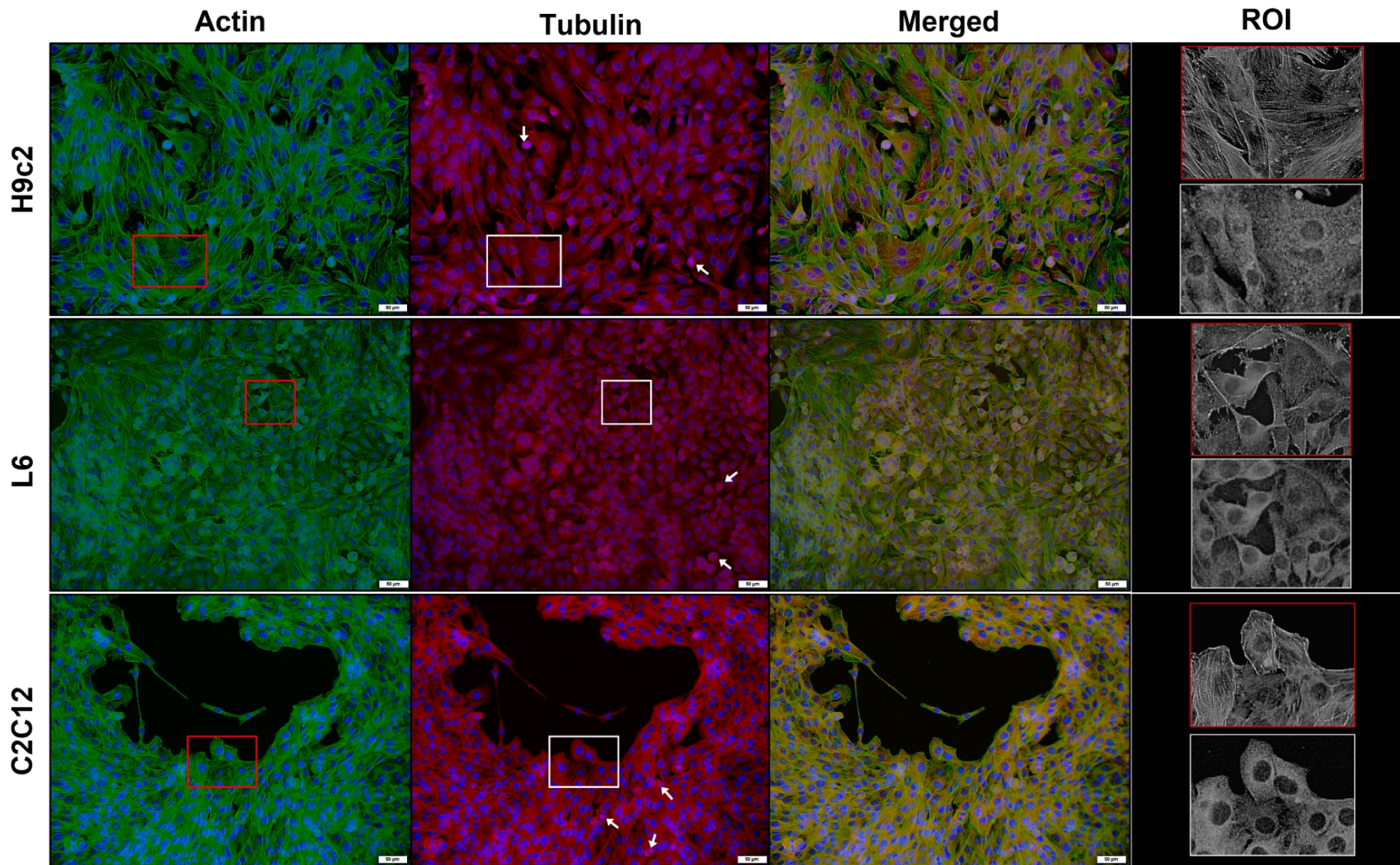
Figure 4.1 H9c2, L6 and C2C12 myoblasts cultured in complete DMEM medium (negative control) over a period of 72 h, stained with phalloidin-FITC (green), anti-β-tubulin-Cy3 (red) and DAPI (blue). The boxes bordering ROI are displayed on the right. White arrows indicate myoblasts undergoing mitosis. Scale bar = 50 μm.
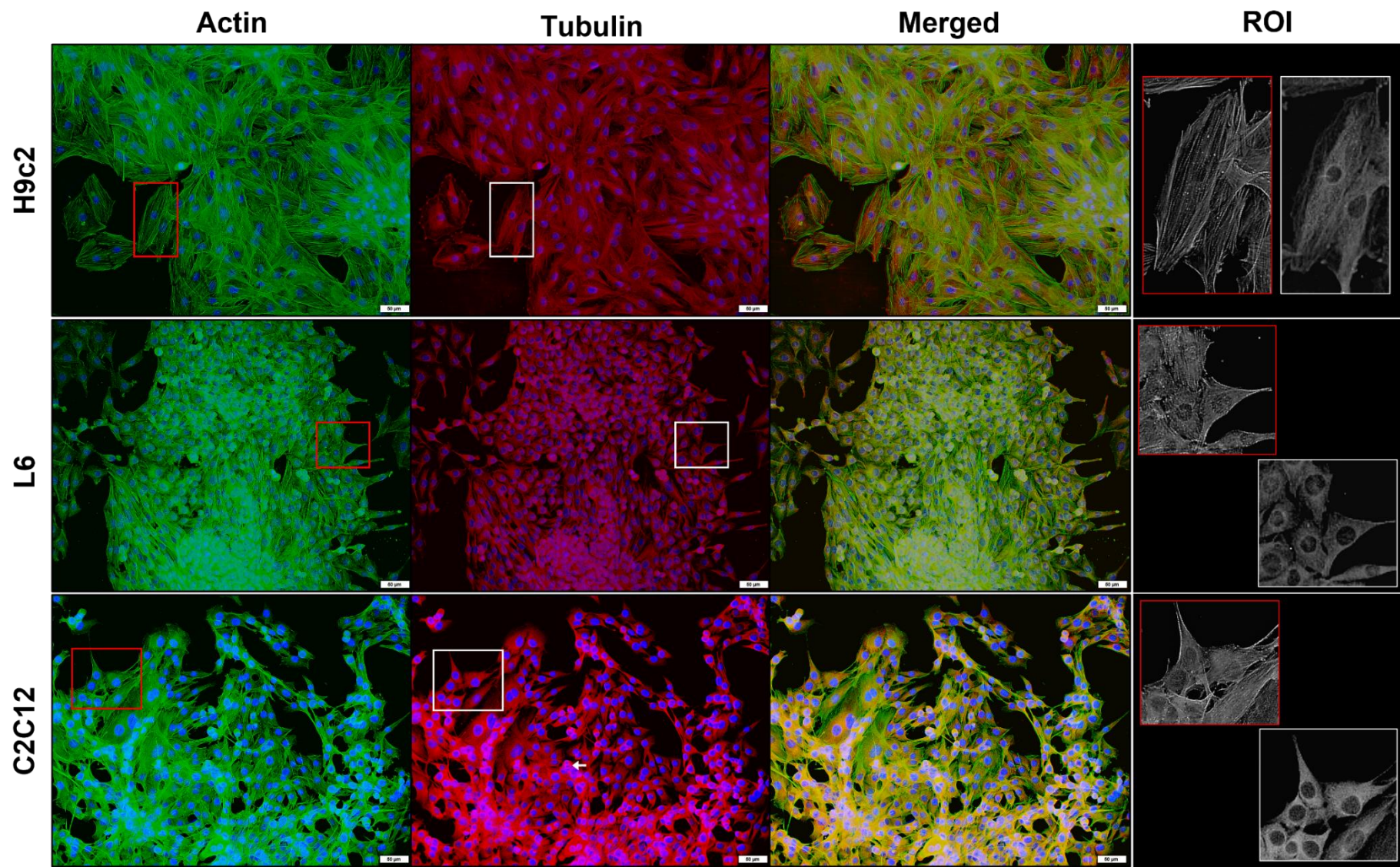
Figure 4.2 H9c2, L6 and C2C12 myoblasts cultured in the solvent control (0.1% MeOH) over a period of 72 h, stained with phalloidin-FITC (green), anti-β-tubulin-Cy3 (red) and DAPI (blue). The boxes bordering ROI are displayed on the right. The white arrow indicates myoblasts undergoing mitosis. Scale bar = 50 µm.
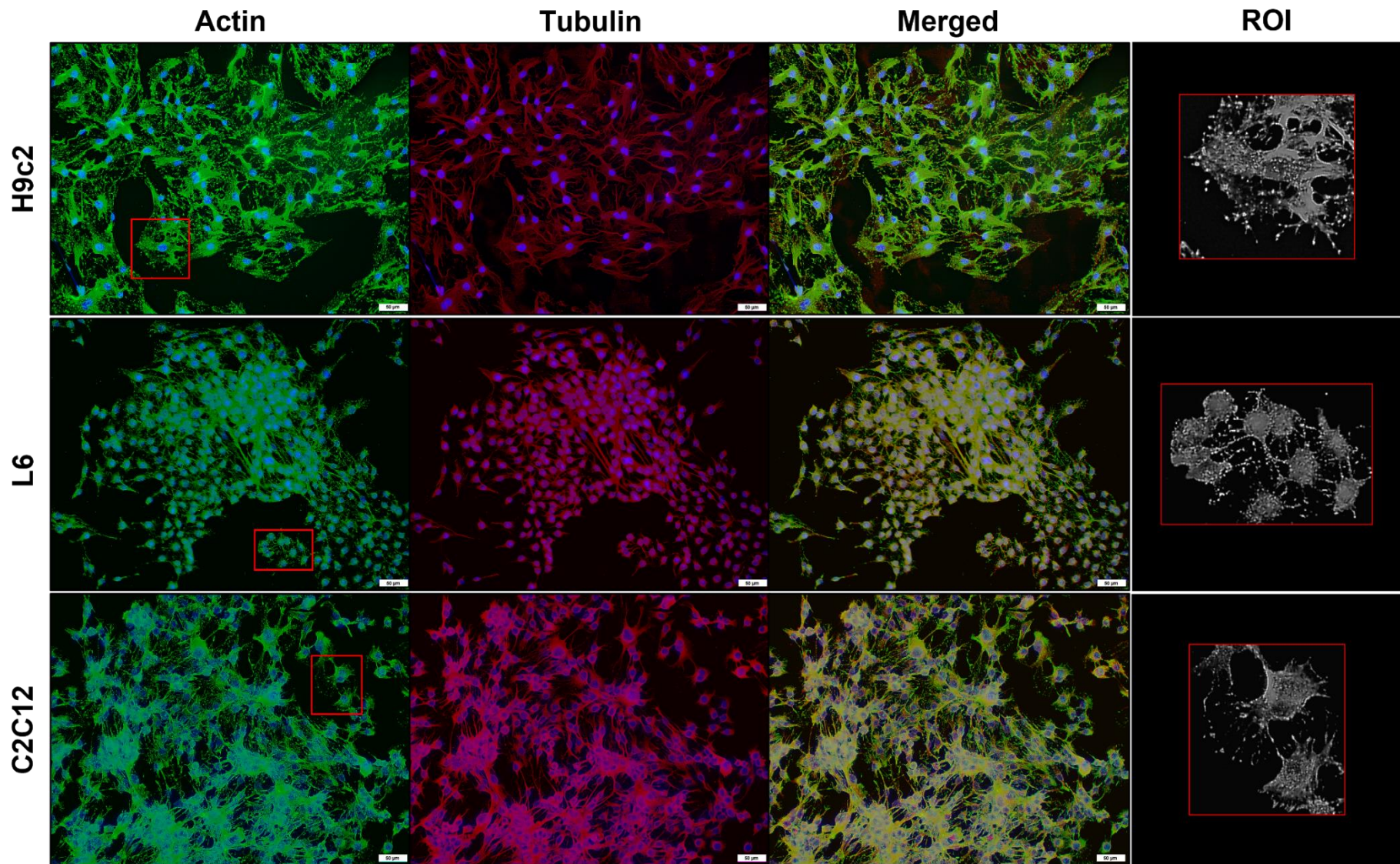
Figure 4.3 H9c2, L6 and C2C12 myoblasts exposed to 12 μM cytochalasin D for 15 min and stained with phalloidin-FITC (green), anti-β-tubulin-Cy3 (red) and DAPI (blue). The boxes bordering a ROI are displayed on the right indicating the fragmented microfilament network. Scale bar = 50 μm.
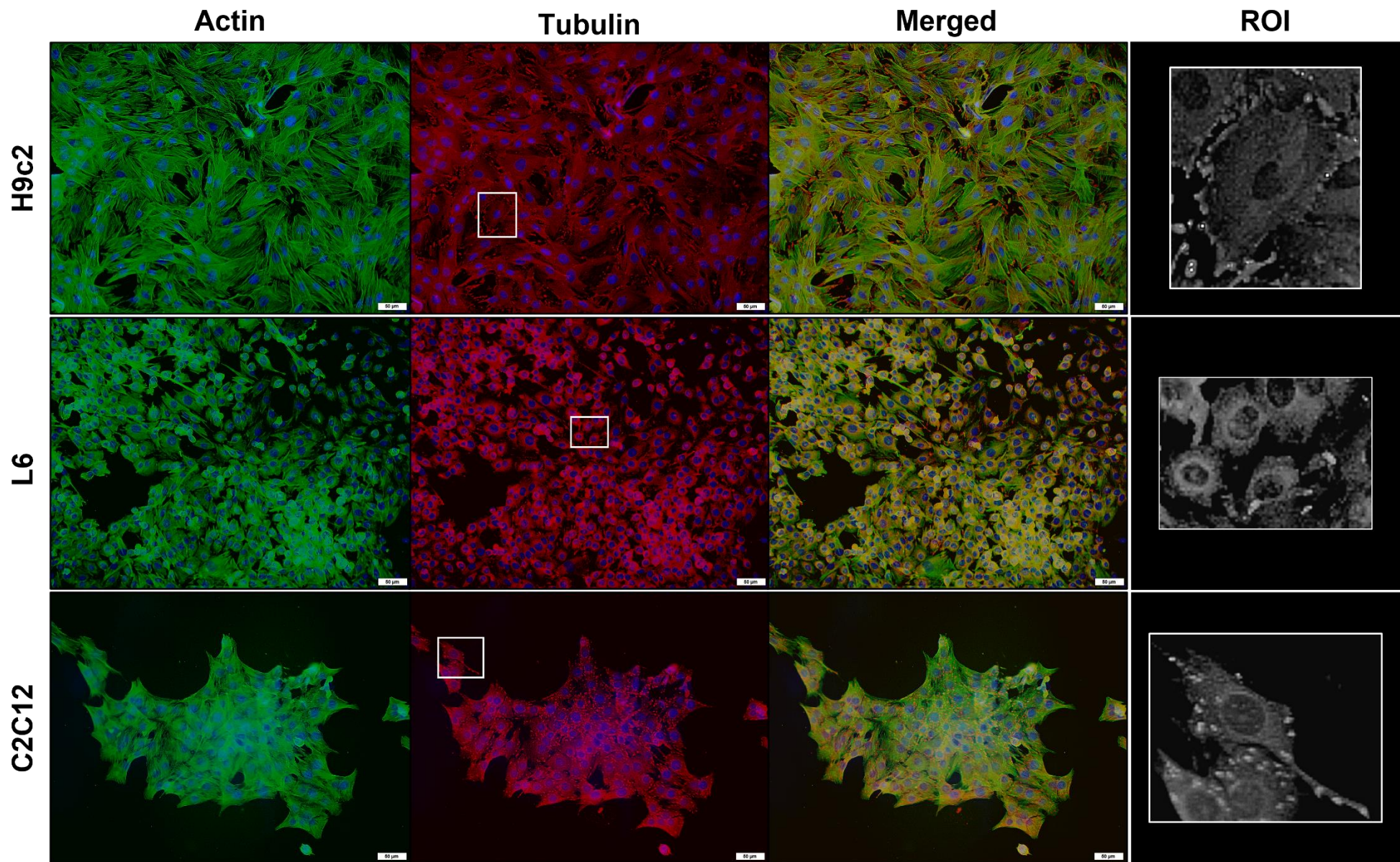
Figure 4.4 H9c2, L6 and C2C12 myoblasts exposed to 5 µM vinblastine for 1 h and stained with phalloidin-FITC (green), anti-β-tubulin-Cy3 (red) and DAPI (blue). The boxes bordering a ROI are displayed on the right indicating the short, stub-like microtubules. Scale bar = 50 µm.
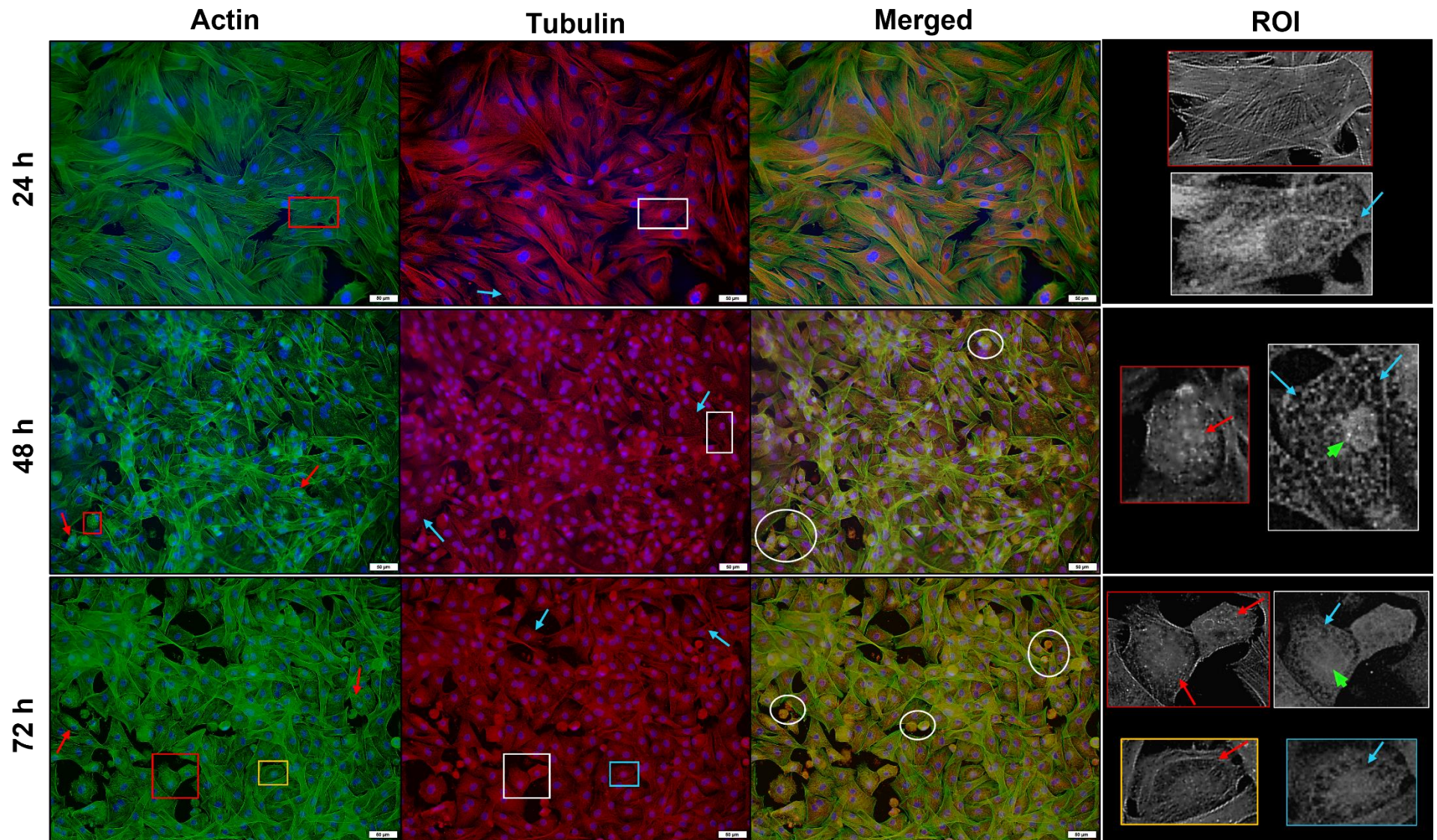
Figure 4.5 H9c2 myoblasts exposed to 0.1 µM monensin and stained with phalloidin-FITC (green), anti-β-tubulin-Cy3 (red) and DAPI (blue). The boxes bordering a ROI are displayed on the right. The blue and red arrows indicate 'gaps' in the microtubule network and myoblasts with disrupted microfilaments, respectively. White circles surround some of the shrinking myoblasts and the green arrowheads indicate concentrated tubulin around the nucleus. Scale bar = 50 µm.
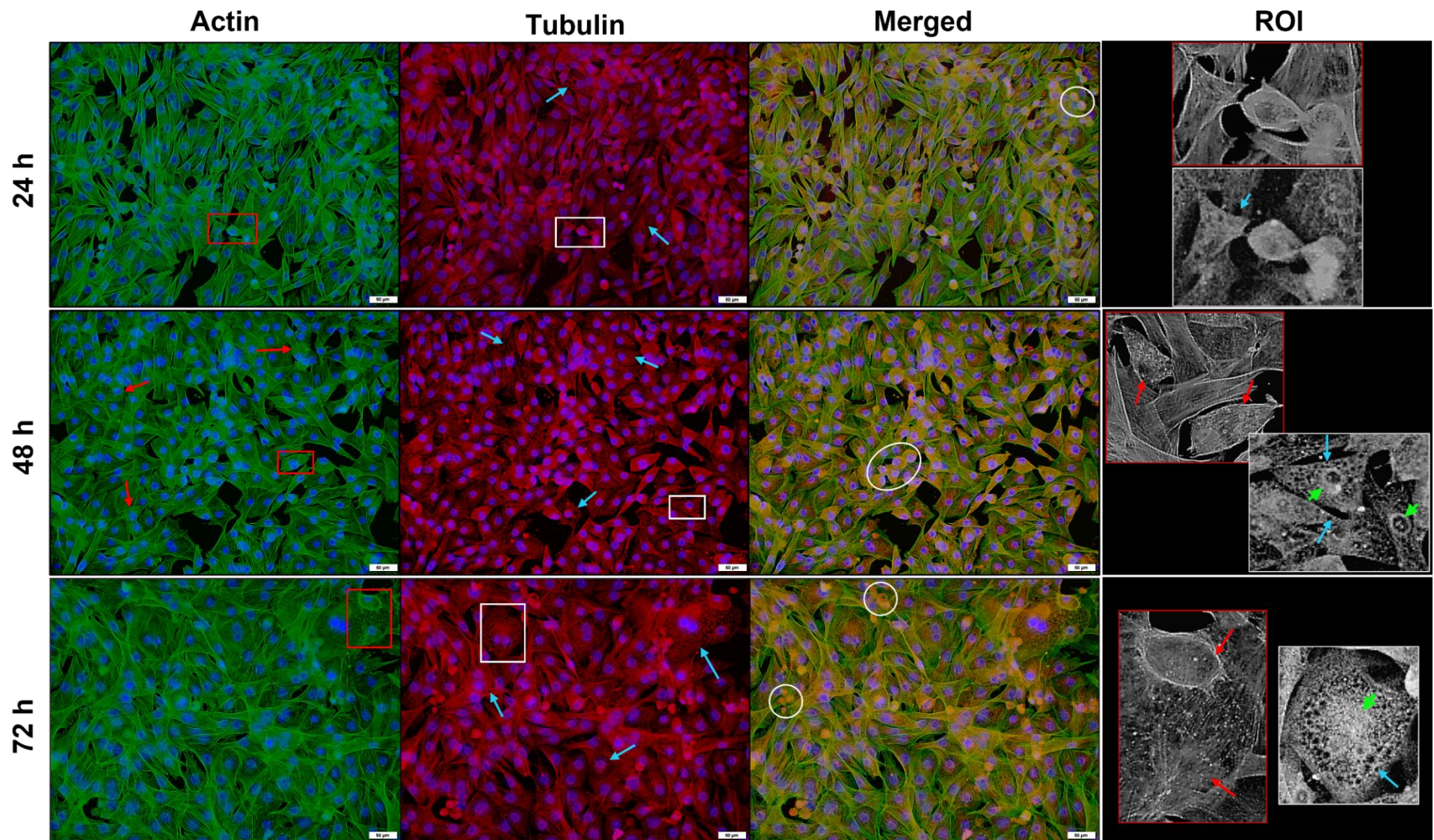
Figure 4.6 H9c2 myoblasts exposed to 1 μM monensin and stained with phalloidin-FITC (green), anti-β-tubulin-Cy3 (red) and DAPI (blue). The boxes bordering a ROI are displayed on the right. The blue and red arrows indicate 'gaps' in the microtubule network and myoblasts with disrupted microfilaments, respectively. White circles surround some of the shrinking myoblasts and the green arrowheads indicate concentrated tubulin around the nucleus. Scale bar = 50 μm.
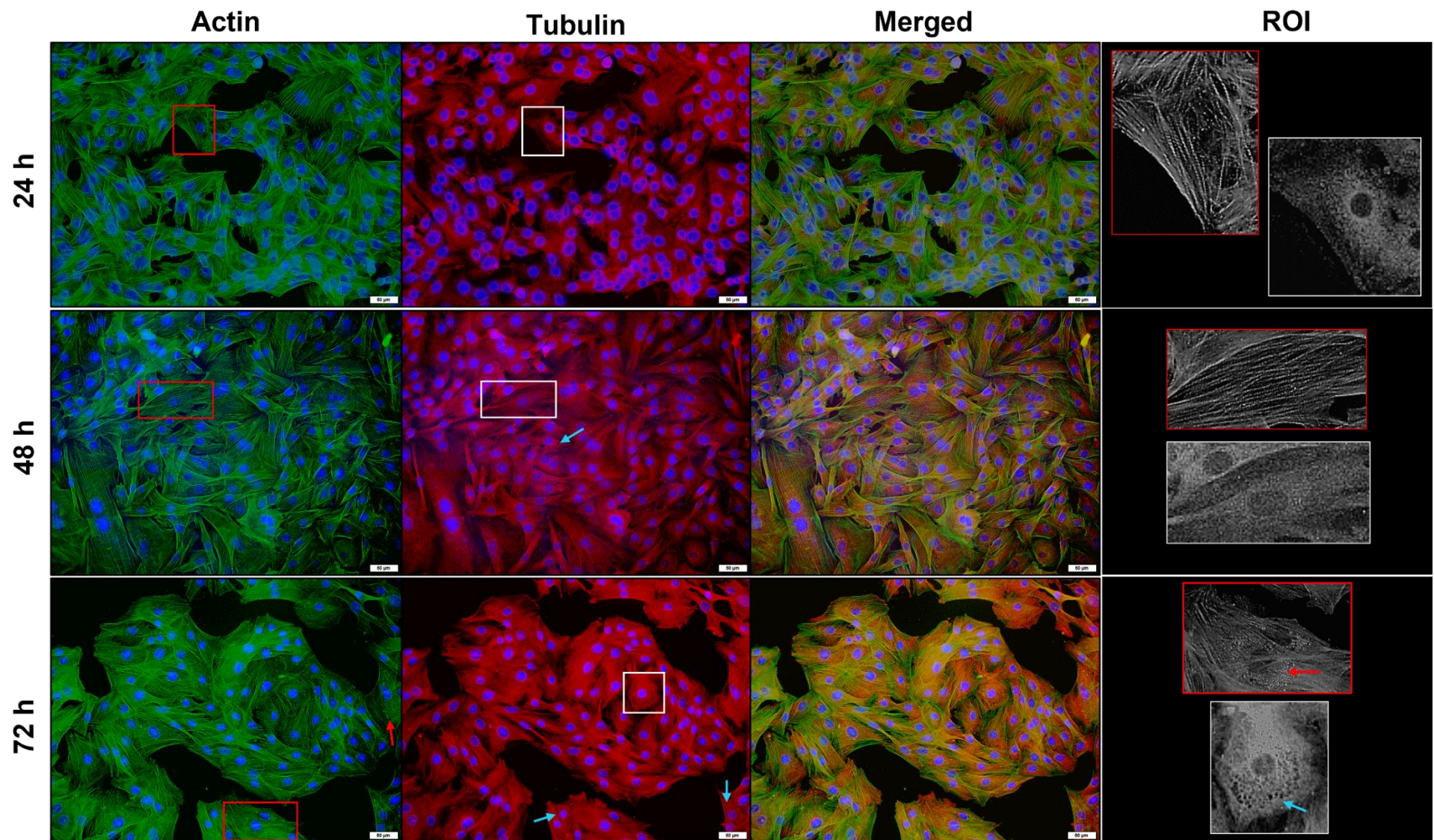
Figure 4.7 H9c2 myoblasts exposed to 0.1 µM salinomycin and stained with phalloidin-FITC (green), anti-β-tubulin-Cy3 (red) and DAPI (blue). The boxes bordering a ROI are displayed on the right. The blue and red arrows indicate 'gaps' in the microtubule network and myoblasts with disrupted microfilaments, respectively. Scale bar = 50 µm.

85
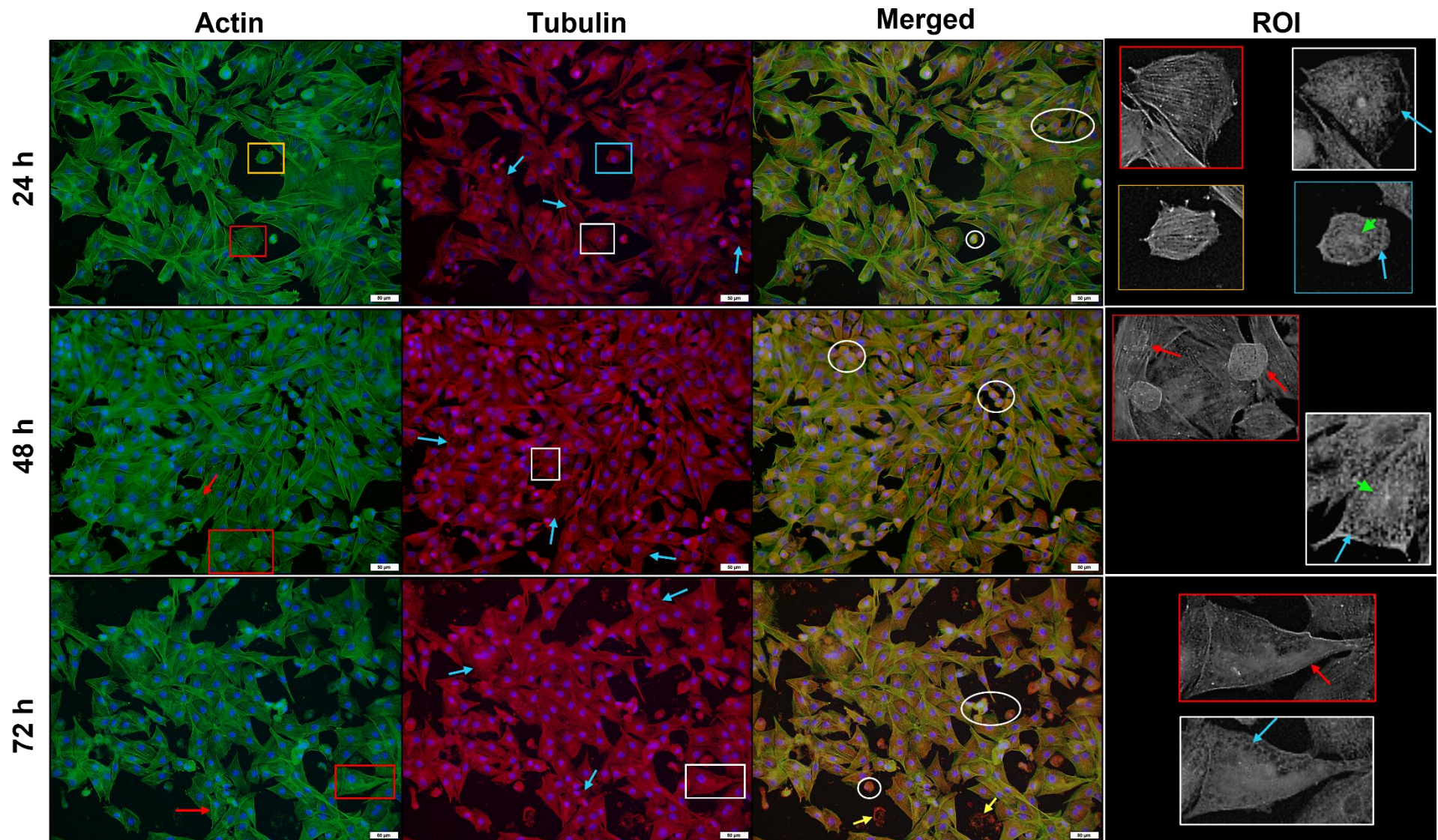
Figure 4.8 H9c2 myoblasts exposed to 1 µM salinomycin and stained with phalloidin-FITC (green), anti-β-tubulin-Cy3 (red) and DAPI (blue). The boxes bordering a ROI are displayed on the right. The blue and red arrows indicate 'gaps' in the microtubule network and myoblasts with disrupted microfilaments, respectively. White circles surround some of the shrinking myoblasts and the green arrowheads indicate concentrated tubulin around the nucleus. Cytoskeletal debris are indicated by the yellow arrows. Scale bar = 50 µm.
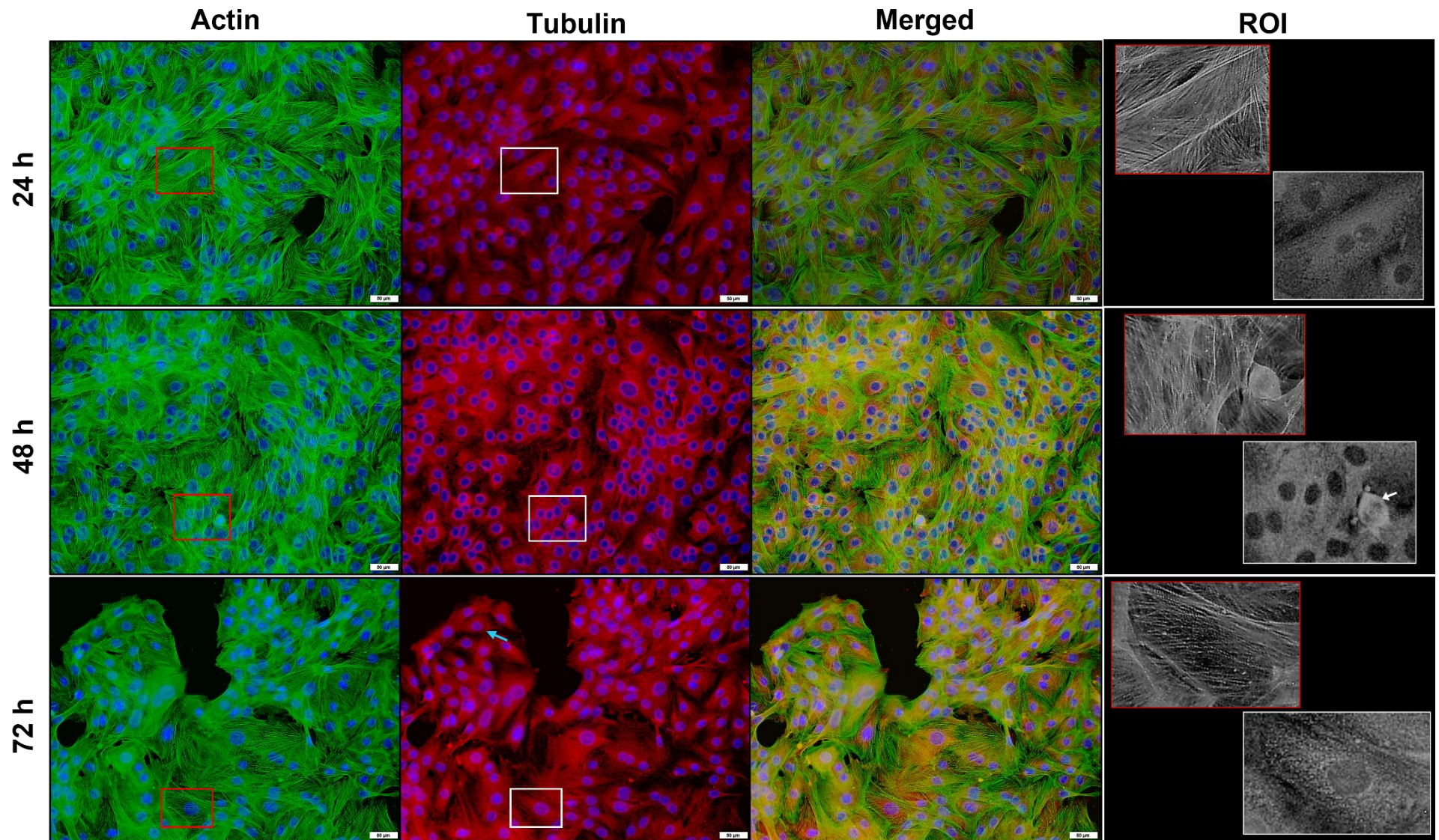
Figure 4.9 H9c2 myoblasts exposed to 0.1 µM lasalocid and stained with phalloidin-FITC (green), anti-β-tubulin-Cy3 (red) and DAPI (blue). The boxes bordering a ROI are displayed on the right with most myoblasts appearing unaffected. The blue arrow indicates 'gaps' in the microtubule network. Some myoblasts are undergoing mitosis (white arrow). Scale bar = 50 µm.
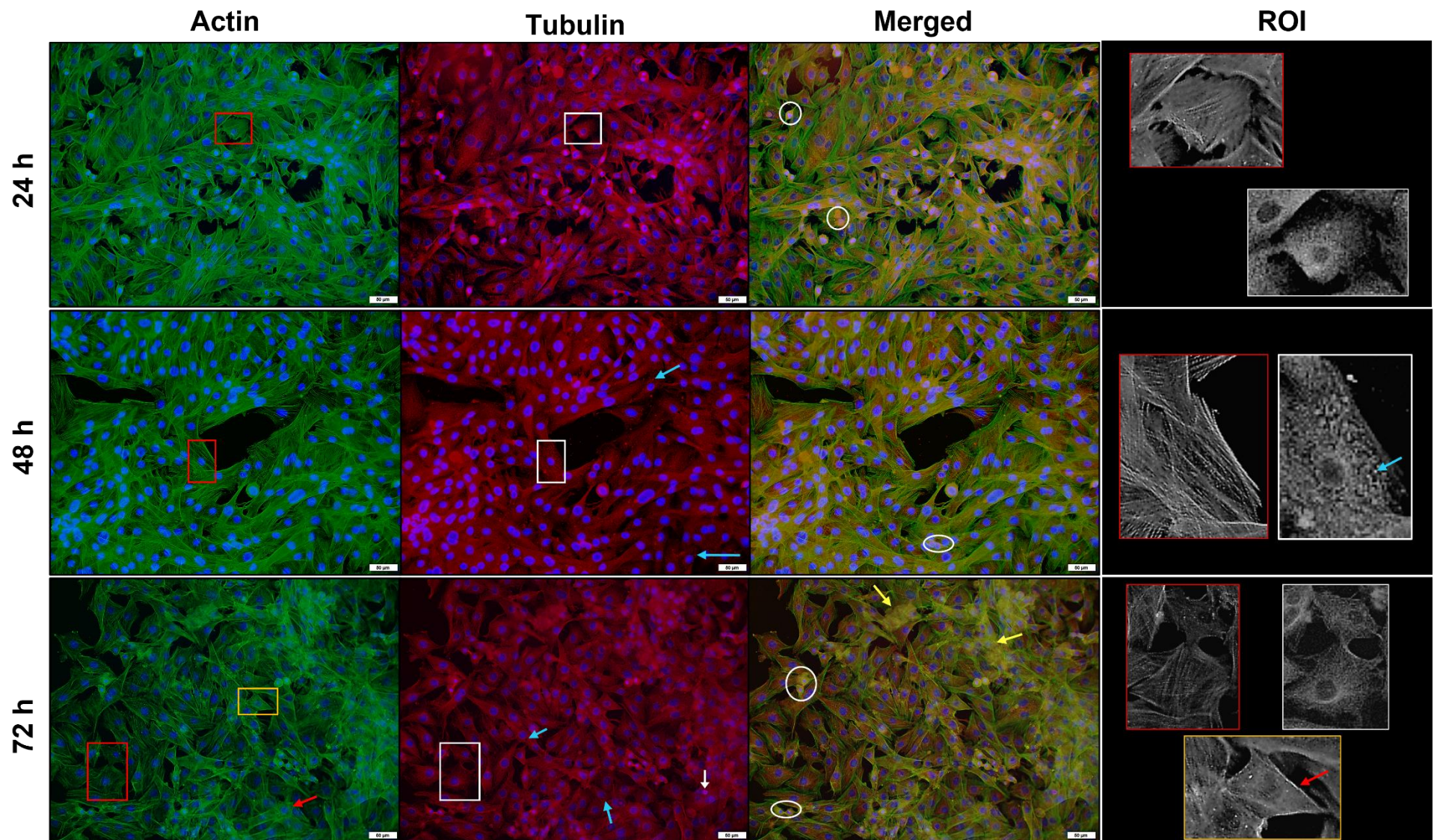
Figure 4.10 H9c2 myoblasts exposed to 1 μM lasalocid and stained with phalloidin-FITC (green), anti-β-tubulin-Cy3 (red) and DAPI (blue). The boxes bordering a ROI are displayed on the right. The blue and red arrows indicate 'gaps' in the microtubule network and myoblasts with disrupted microfilaments, respectively. White circles surround some of the shrinking myoblasts. Cytoskeletal debris are indicated by the yellow arrows. Some myoblasts are undergoing mitosis (white arrow). Scale bar = 50 μm.
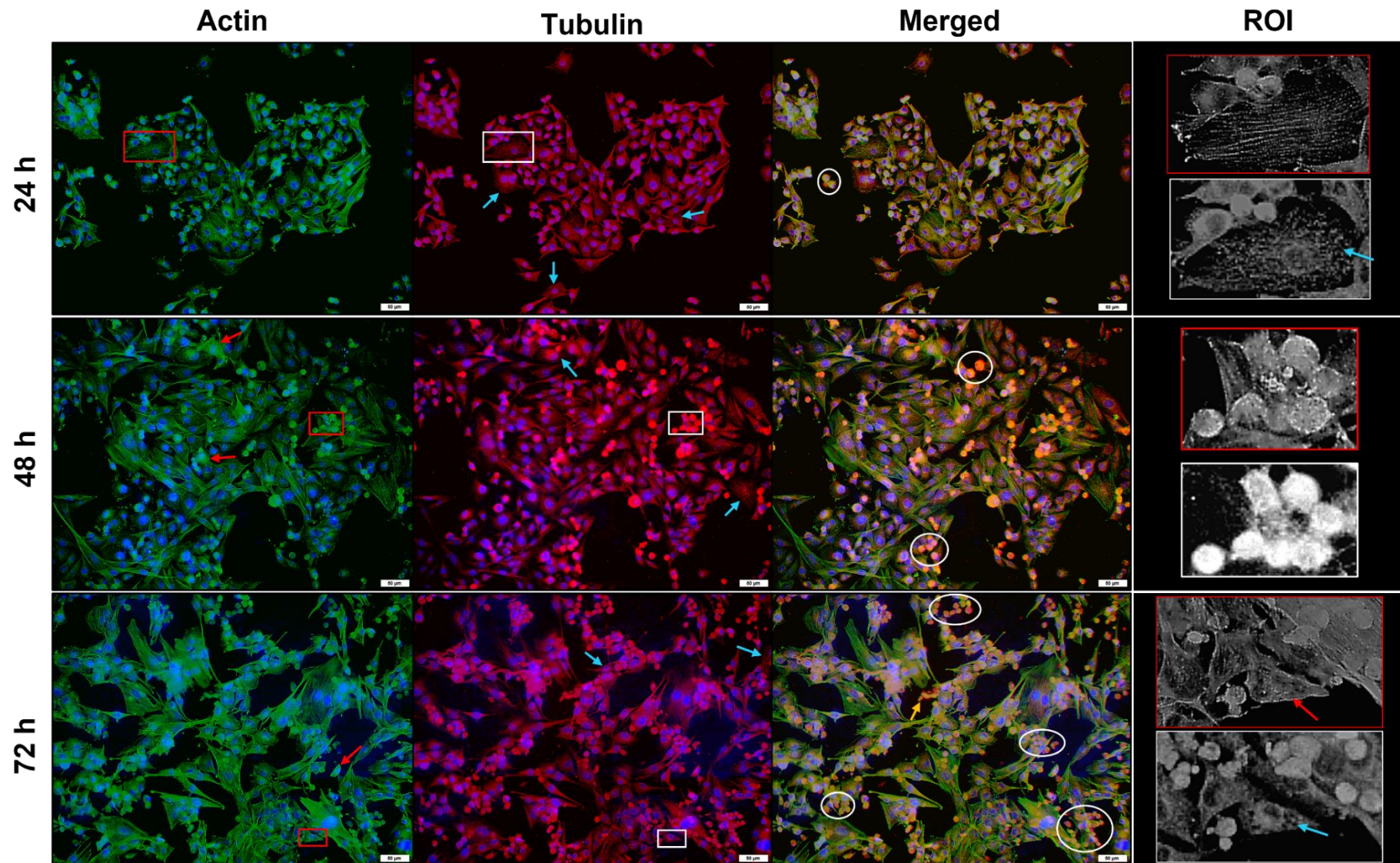
Figure 4.11 L6 myoblasts exposed to 0.1 µM monensin and stained with phalloidin-FITC (green), anti-β-tubulin-Cy3 (red) and DAPI (blue). The boxes bordering a ROI are displayed on the right. The blue and red arrows indicate 'gaps' in the microtubule network and myoblasts with disrupted microfilaments, respectively. White circles surround some of the shrinking myoblasts. The yellow arrows indicate debris. Scale bar = 50 µm.
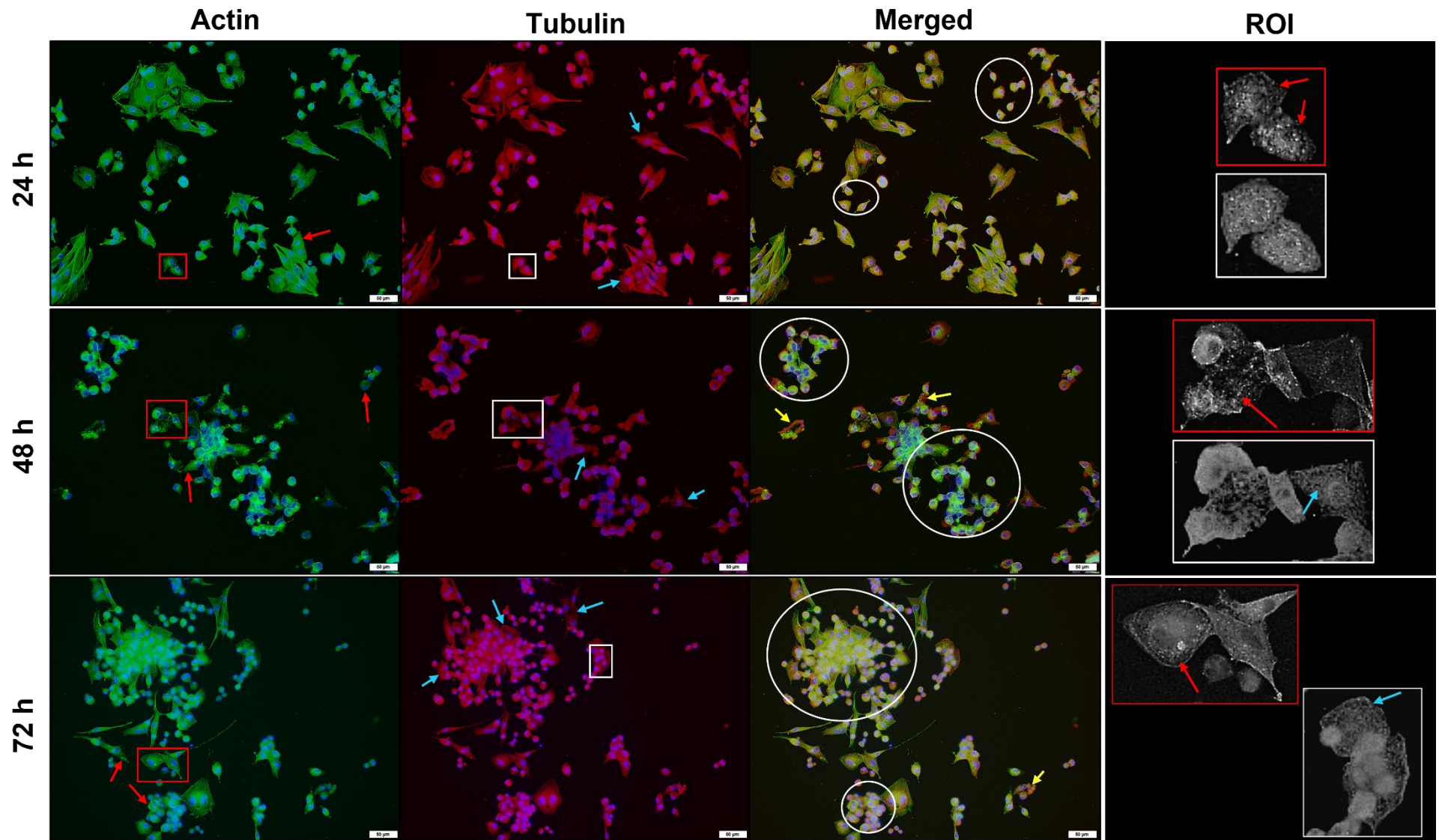
Figure 4.12 L6 myoblasts exposed to 1 μM monensin and stained with phalloidin-FITC (green), anti-β-tubulin-Cy3 (red) and DAPI (blue). The boxes bordering a ROI are displayed on the right. The blue and red arrows indicate 'gaps' in the microtubule network and myoblasts with disrupted microfilaments, respectively. White circles surround some of the shrinking myoblasts. The yellow arrows indicate cytoskeletal debris. Scale bar = 50 μm.
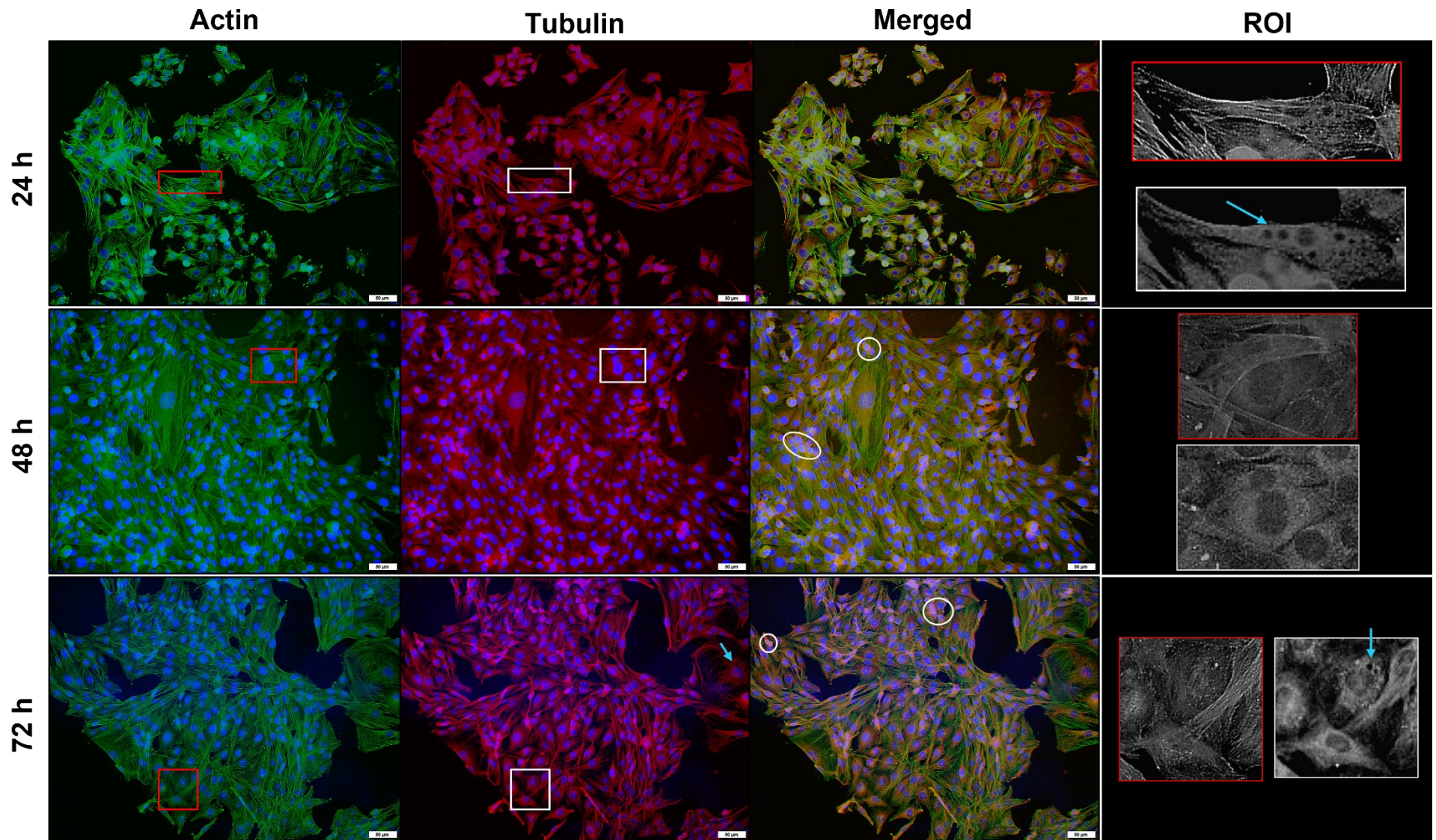
Figure 4.13 L6 myoblasts exposed to 0.1 μM salinomycin and stained with phalloidin-FITC (green), anti-β-tubulin-Cy3 (red) and DAPI (blue). The boxes bordering a ROI are displayed on the right. The blue arrows indicate 'gaps' in the microtubule network and the white circles surround some of the shrinking myoblasts. Scale bar = 50 μm.

91
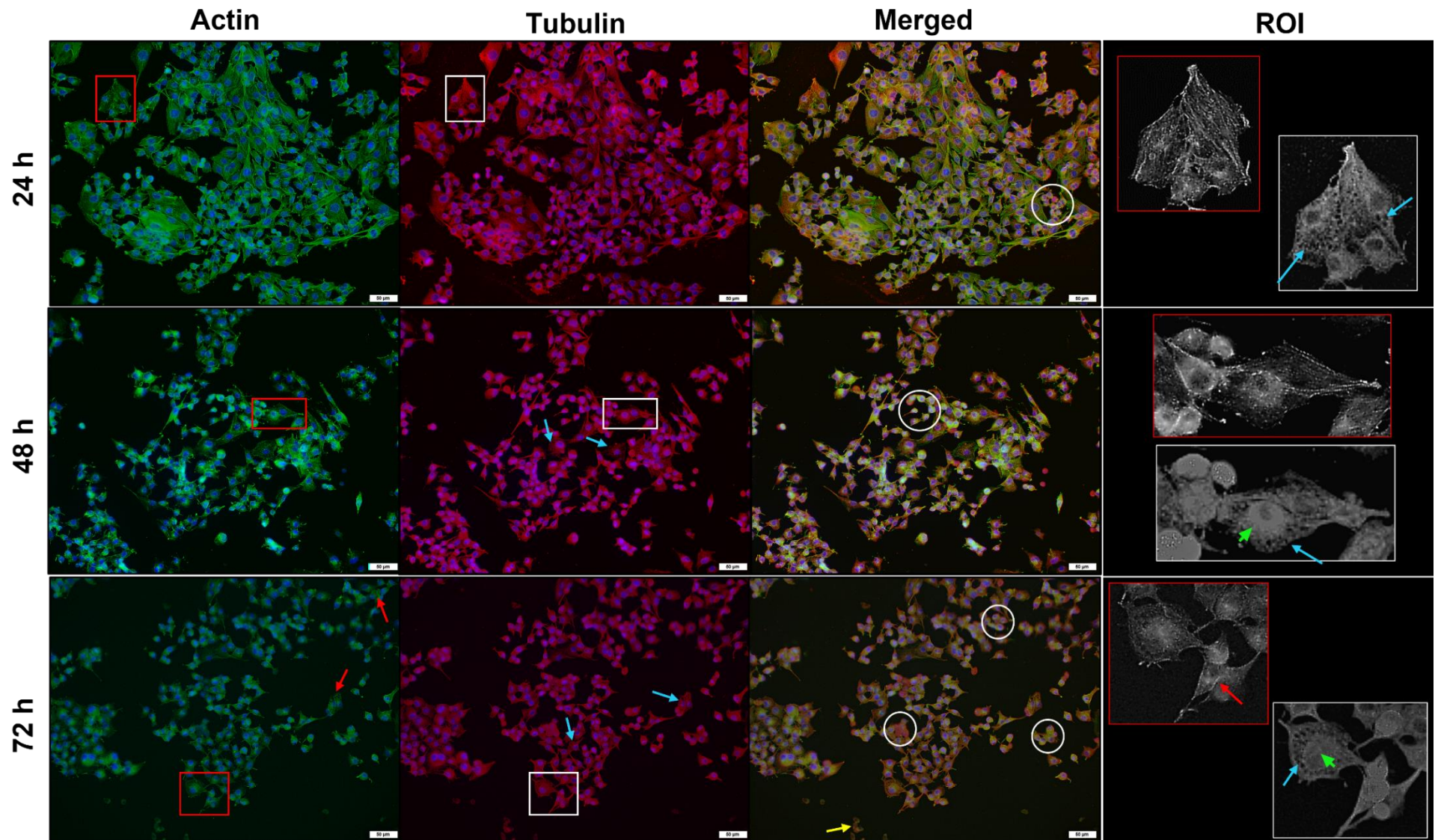
Figure 4.14 L6 myoblasts exposed to 1 µM salinomycin and stained with phalloidin-FITC (green), anti-β-tubulin-Cy3 (red) and DAPI (blue). The boxes bordering a ROI are displayed on the right. The blue and red arrows indicate 'gaps' in the microtubule network and myoblasts with disrupted microfilaments, respectively. White circles surround some of the shrinking myoblasts and the green arrowheads indicate concentrated tubulin around the nucleus. Cytoskeletal debris are indicated by the yellow arrows. Scale bar = 50 µm.

92
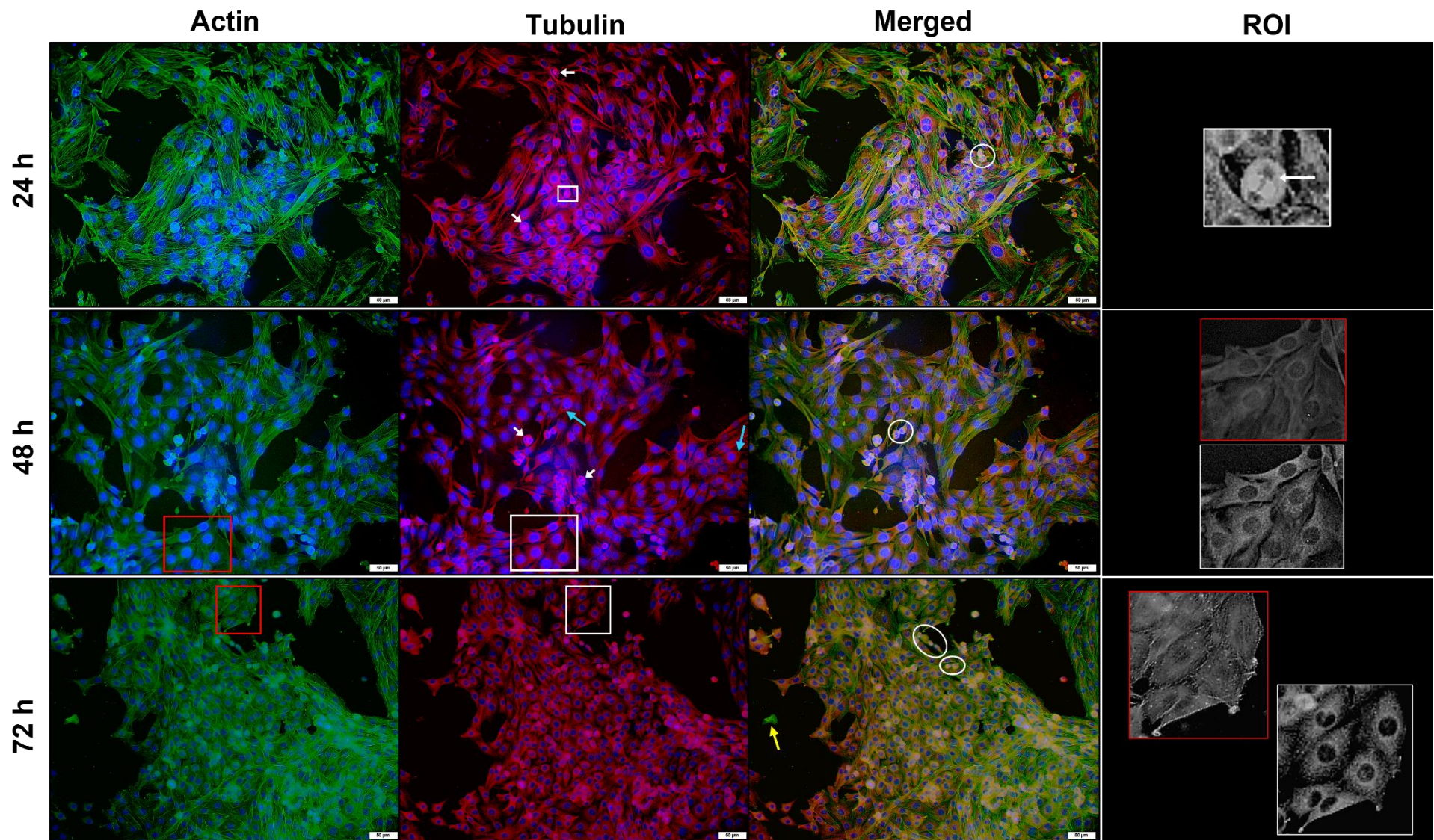
Figure 4.15 L6 myoblasts exposed to 0.1 µM lasalocid and stained with phalloidin-FITC (green), anti-β-tubulin-Cy3 (red) and DAPI (blue). The boxes bordering a ROI are displayed on the right. The blue arrows indicate gaps in the microtubule network. White circles and yellow arrows indicate rounded myoblasts and cytoskeletal debris, respectively. Some myoblasts are undergoing mitosis (white arrows). Scale bar = 50 µm.
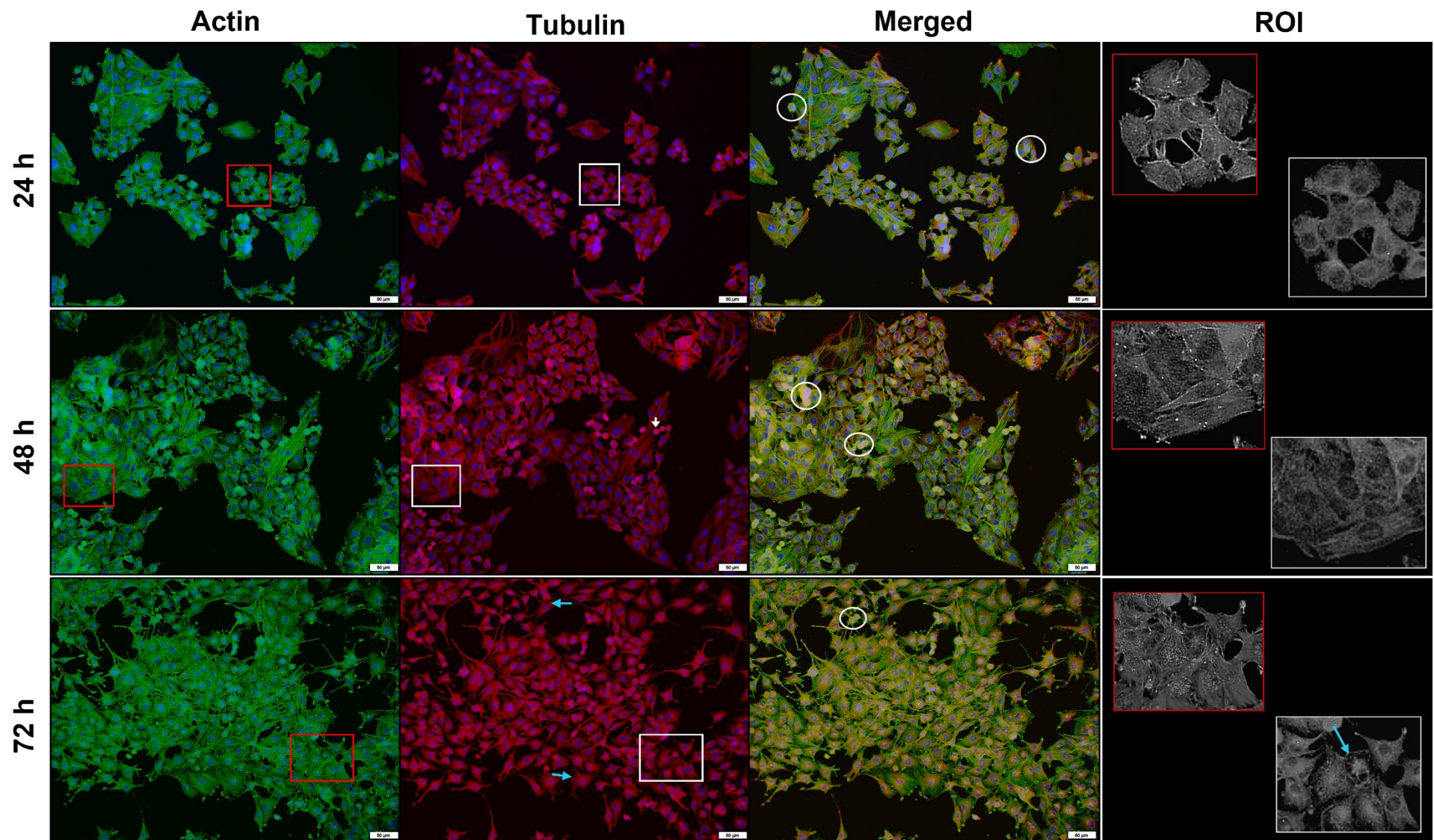
Figure 4.16 L6 myoblasts exposed to 1 µM lasalocid and stained with phalloidin-FITC (green), anti-β-tubulin-Cy3 (red) and DAPI (blue). The boxes bordering a ROI are displayed on the right. The blue arrows indicate gaps in the microtubule network and the white circles surround a few rounded myoblasts. Some myoblasts are undergoing mitosis (white arrow). Scale bar = 50 µm.

94
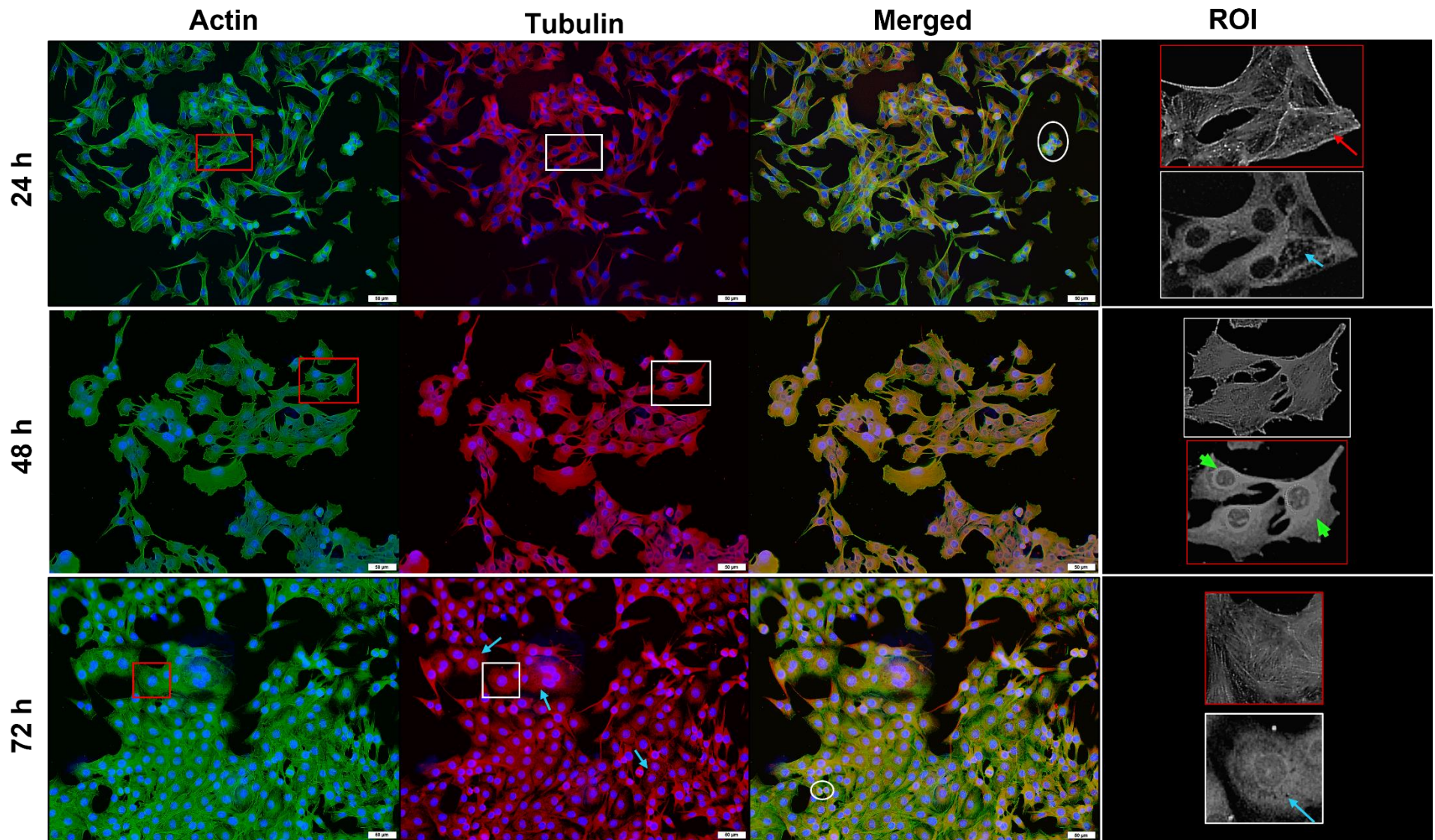
Figure 4.17 C2C12 myoblasts exposed to 0.1 µM monensin and stained with phalloidin-FITC (green), anti-β-tubulin-Cy3 (red) and DAPI (blue). The boxes bordering a ROI are displayed on the right. The blue and red arrows indicate 'gaps' in the microtubule network and myoblasts with disrupted microfilaments, respectively. White circles surround some of the shrinking myoblasts and the green arrowheads indicate concentrated tubulin around the nucleus. Scale bar = 50 µm.

95
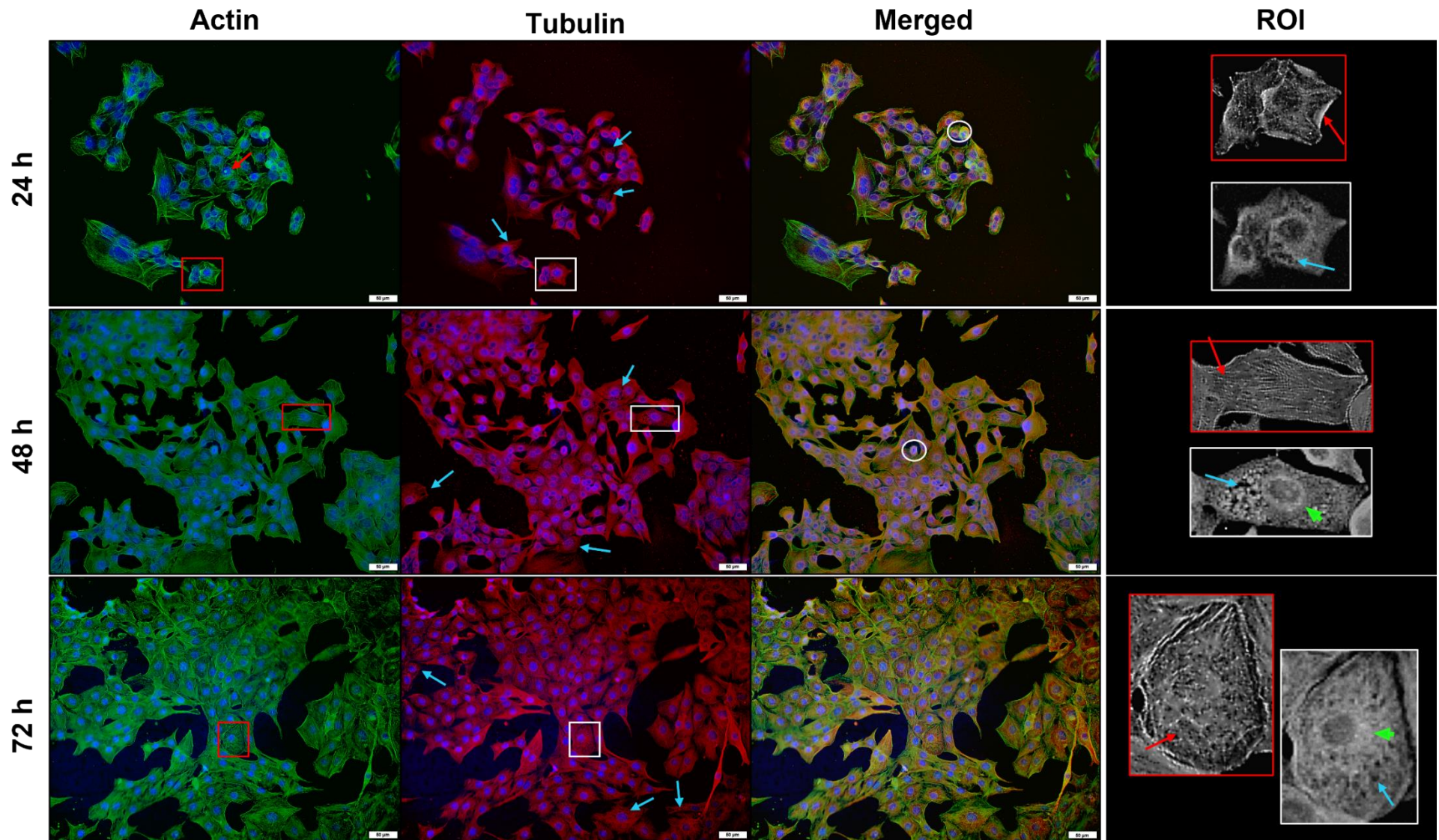
Figure 4.18 C2C12 myoblasts exposed to 1 μM monensin and stained with phalloidin-FITC (green), anti-β-tubulin-Cy3 (red) and DAPI (blue). The boxes bordering a ROI are displayed on the right. The blue and red arrows indicate 'gaps' in the microtubule network and myoblasts with disrupted microfilaments, respectively. White circles surround some of the shrinking myoblasts and the green arrowheads indicate concentrated tubulin around the nucleus. Scale bar = 50 μm.

96
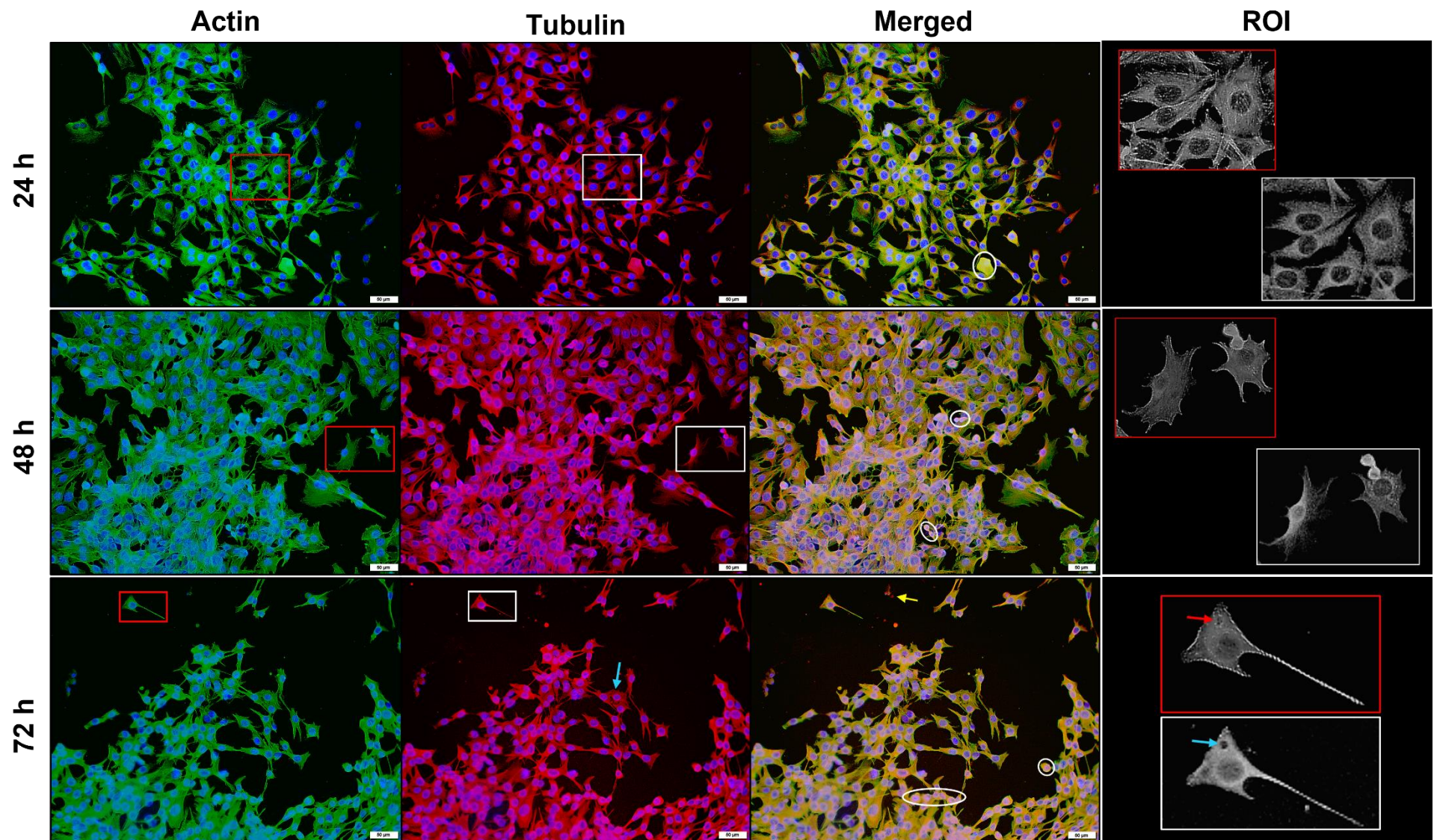
Figure 4.19 C2C12 myoblasts exposed to 0.1 µM salinomycin and stained with phalloidin-FITC (green), anti-β-tubulin-Cy3 (red) and DAPI (blue). The boxes bordering a ROI are displayed on the right. The blue and red arrows indicate 'gaps' in the microtubule network and myoblasts with disrupted microfilaments, respectively. White circles surround some of the shrinking myoblasts and cytoskeletal debris are indicated by the yellow arrow. Scale bar = 50 µm.
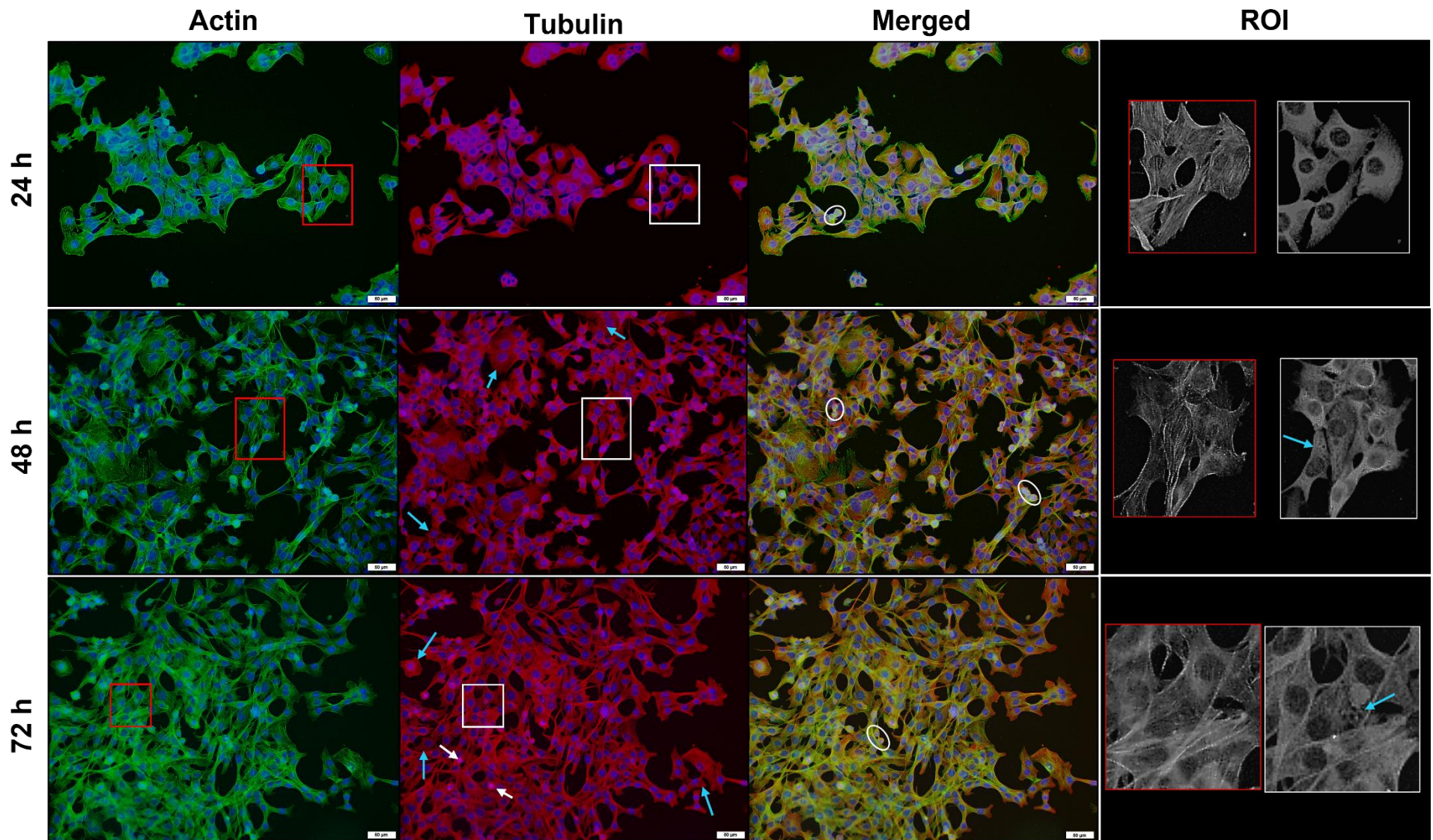
Figure 4.20 C2C12 myoblasts exposed to 1 µM salinomycin and stained with phalloidin-FITC (green), anti-β-tubulin-Cy3 (red) and DAPI (blue). The boxes bordering a ROI are displayed on the right. The blue arrows indicate 'gaps' in the microtubule network and white circles surround some of the shrinking myoblasts. Some of the myoblasts are undergoing mitosis (white arrows). Scale bar = 50 µm.
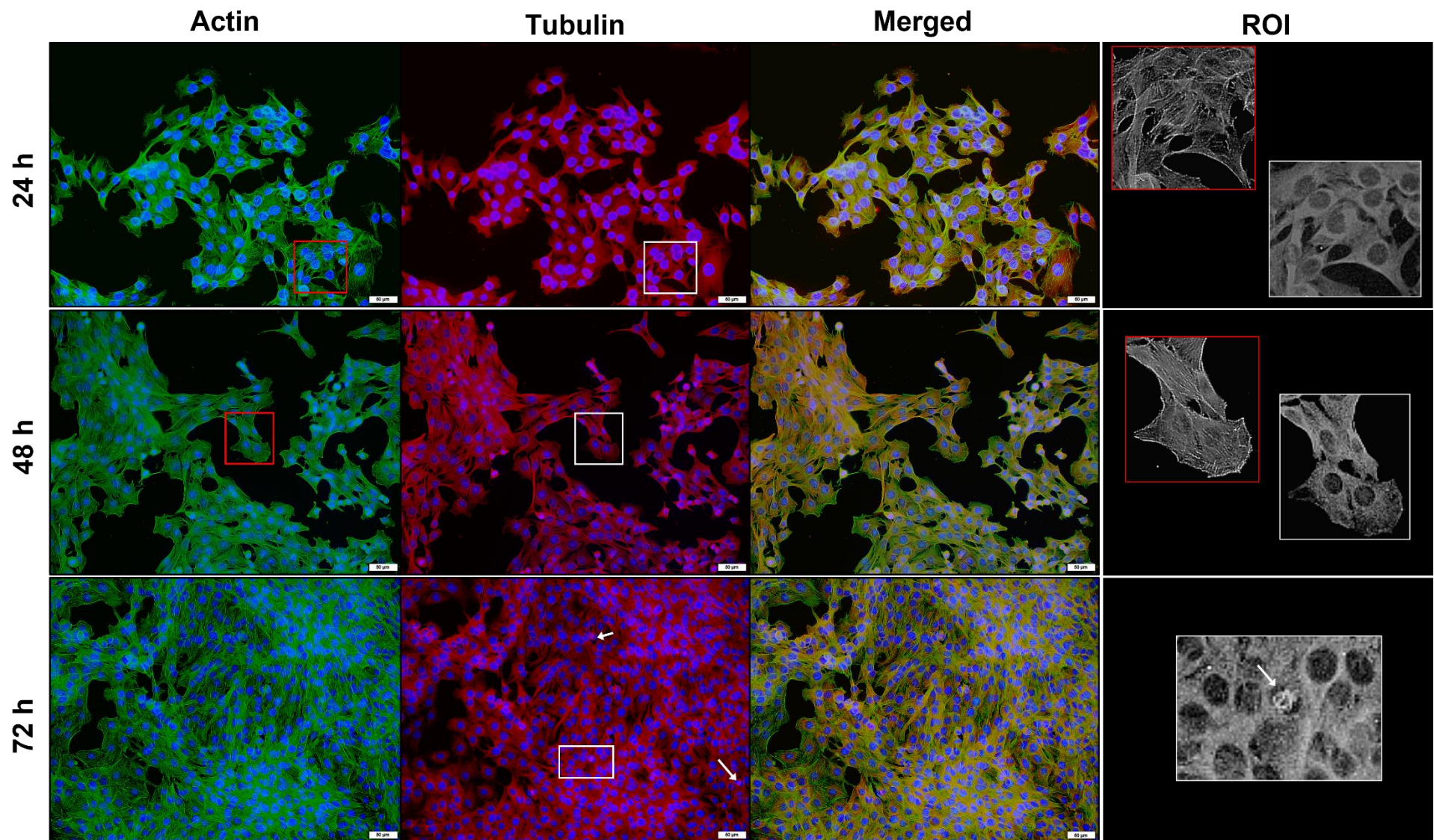
Figure 4.21 C2C12 myoblasts exposed to 0.1 µM lasalocid and stained with phalloidin-FITC (green), anti-β-tubulin-Cy3 (red) and DAPI (blue). The boxes bordering a ROI are displayed on the right. Some of the myoblasts are undergoing mitosis (white arrows). Scale bar = 50 µm.
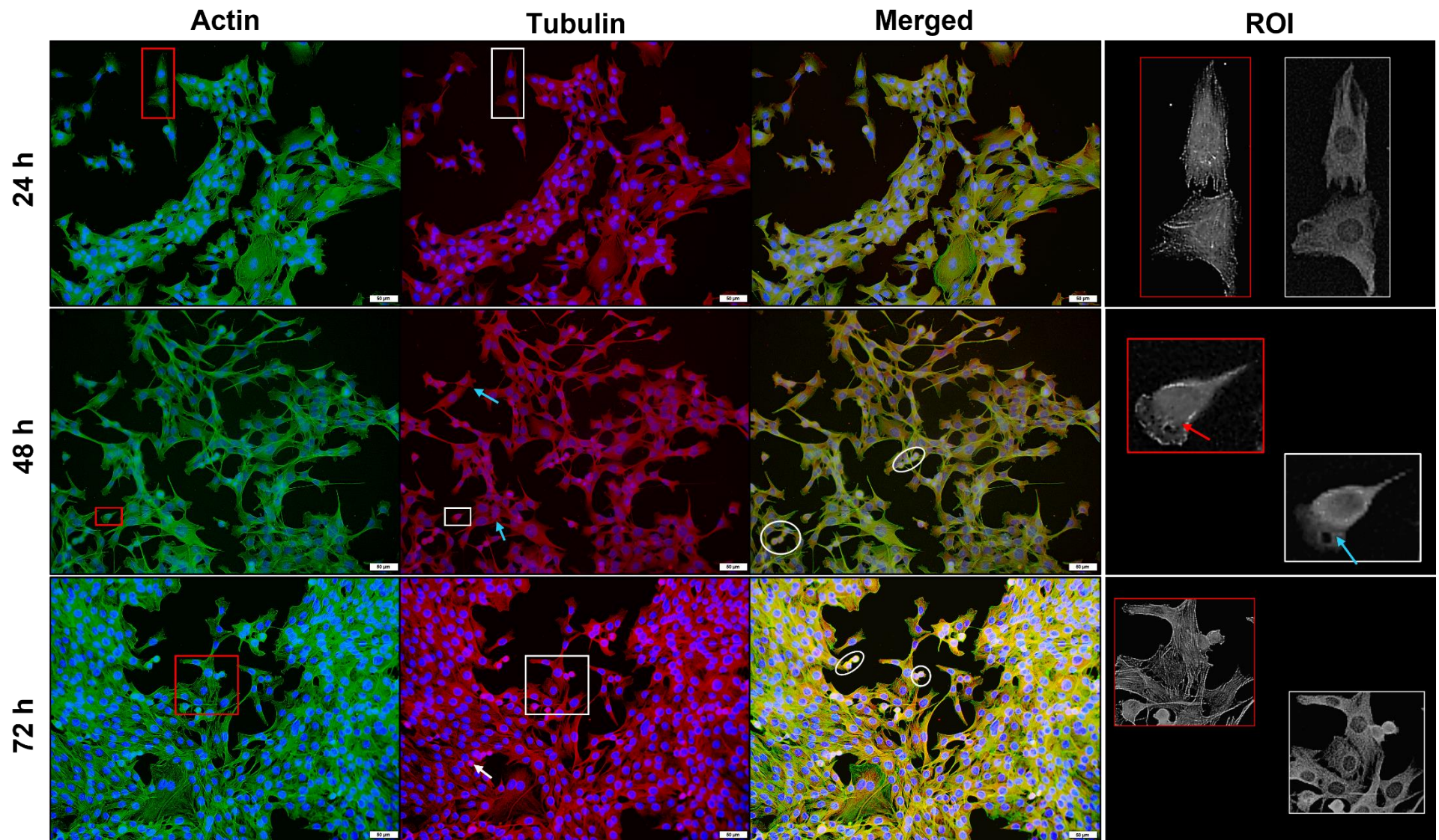
Figure 4.22 C2C12 myoblasts exposed to 1 µM lasalocid and stained with phalloidin-FITC (green), anti-β-tubulin-Cy3 (red) and DAPI (blue). The boxes bordering a ROI are displayed on the right. The blue and red arrows indicate 'gaps' in the microtubule network and myoblasts with disrupted microfilaments, respectively. White circles surround some of the shrinking myoblasts. Some of the myoblasts are undergoing mitosis (white arrow). Scale bar = 50 µm.

4.3.1 The Effect of the Ionophores on Desmin

C2C12 myoblasts were stained for desmin with H-DAB (the combination of haematoxylin and diaminobenzidine) after exposure to monensin, salinomycin and lasalocid for 24, 48 and 72 h. Desmin appeared brown in colour, indicating positive staining, while nuclei stained blue.

Glyoxal and cytochalasin D were used as positive controls. Glyoxal (1 mM) was added on the day of exposure, while cytochalasin D (20 µM) was added 30 min before fixation. Exposure to glyoxal caused disruption of desmin and a dot-like desmin aggregation pattern in the perinuclear region of the myoblasts at all three exposure times (**Figure 4.23 a**, **red arrowheads**). The perinuclear aggregates appeared as early as 24 h after exposure. Cytochalasin D exposure caused desmin to form filamentous protrusions radiating outwards from the nucleus (**Figure 4.23 b**).
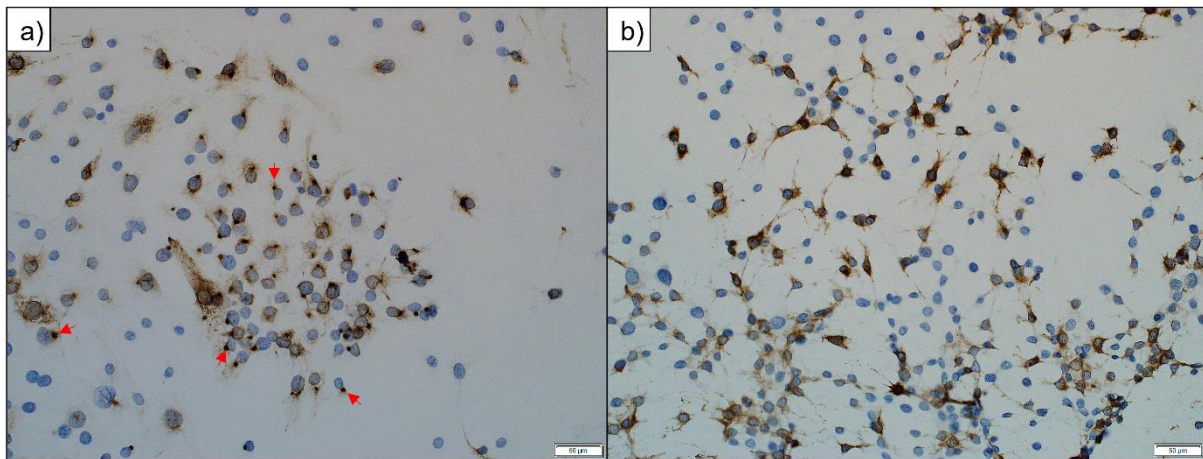
Figure 4.23 H-DAB immunocytochemical staining of C2C12 myoblasts for desmin after exposure to 1 mM glyoxal for 48 h (a) and 20 µM cytochalasin D for 30 min (b). Red arrows indicate dot-like desmin aggregation near the perinuclear region of the myoblasts. Scale bar = 50 µm.

The negative control of the myoblasts for all three exposure periods had desmin intermediate filaments distributed from the perinuclear region, appearing diffusely filamentous throughout the cytoplasm (**Figure 4.24 a-c**). The number of myoblasts per slide increased with longer exposure times. At 72 h, the intensity of desmin staining seemed to have decreased slightly (**Figure 4.24 c**). The solvent control (0.1% MeOH) (not shown) was similar to the negative control.

After 24 h, the desmin staining intensity and distribution in the C2C12 myoblasts exposed to monensin, salinomycin and lasalocid were comparable to that of the negative control (**Figure 4.24 d**, **g & j**). A few of the myoblasts exposed to either

monensin or salinomycin had 'gaps' visible between the desmin filaments (**yellow arrows**), with more appearing after 48 h exposure. The number of myoblasts on the slides exposed to monensin and salinomycin were visibly less compared to the negative control and some desmin debris could be seen. The myoblasts were stained darker around the nucleus compared to the control, indicating possible perinuclear desmin aggregation (**pink arrows**). The shape of the myoblasts was also narrower, with long protrusions extending from the myoblasts. At 72 h exposure to monensin and salinomycin (**Figure 4.24 f & i**), some of the myoblasts stained intense dark brown around the nucleus. Many myoblasts with 'gaps' were present and desmin debris was visible between myoblasts. Lasalocid had slightly fewer myoblasts compared to the negative control. No 'gaps' in the desmin network were present in the myoblasts exposed to lasalocid (**Figure 4.24 j**, **k & l**).

Semiquantitative analysis (**Figure 4.25**) revealed the percentage myoblasts stained different intensities categorised as negative, light, medium or dark depending on the optical density around the nuclei, as described in the Materials and Methods (**Section 4.2**). Myoblasts categorised as negative had no desmin and only the nuclei were present. At 24 h there were no significant difference between the percentage of negatively stained myoblasts ($p > 0.05$). Monensin had a larger percentage of desmin-negative myoblasts after 48 ($p < 0.001$) and 72 h ($p < 0.01$) exposures compared to the control. Salinomycin, in contrast, had more desmin-negative myoblasts compared to both the control ($p < 0.001$) and lasalocid ($p < 0.05$) after 48 h, but not after 72 h exposure. Lightly stained myoblasts had desmin filament located around the nucleus with low optical density. After 48 and 72 h, the negative control had significantly more lightly stained desmin myoblasts compared to both monensin and salinomycin ($p < 0.001$). Likewise, lasalocid exposure resulted in more lightly stained myoblasts after 48 and 72 h compared to both monensin and salinomycin ($p < 0.01$). The percentage of myoblasts stained and categorised as medium were comparable between the control and different ionophores over the 72-h exposure period. However, there were exceptions at 24 h between the control and myoblasts exposed to monensin ($p < 0.05$), as well as at 72 h between the control and myoblasts exposed to either monensin ($p < 0.05$) or salinomycin ($p < 0.001$). Finally, after 48 and 72 h both monensin and salinomycin exposure resulted in significantly more dark stained myoblasts compared to the control ($p < 0.05$).
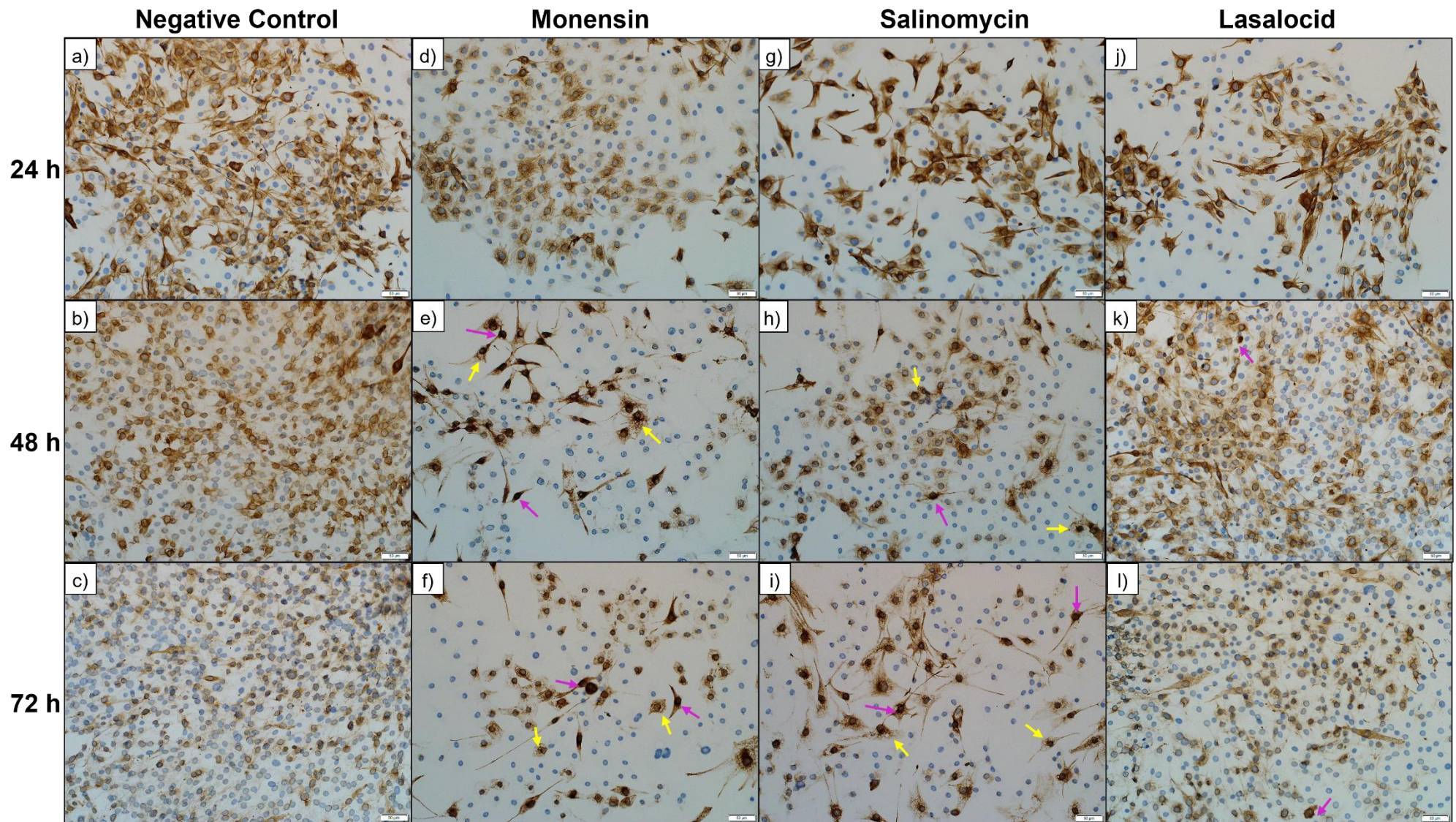
Figure 4.24 H-DAB immunocytochemical staining of C2C12 myoblasts for desmin. The myoblasts in the negative control were cultured in complete DMEM medium over a period of 72 h (a-c). Additionally, the myoblasts were exposed to 1 μM monensin (d-f), salinomycin (g-i) and lasalocid (j-l) for 24, 48 and 72 h. Myoblasts with desmin aggregation in the perinuclear region and 'gaps' within the desmin filament network are indicated with pink and yellow arrows, respectively. Scale bar = 50 μm.

In summary, exposure to lasalocid resulted in a staining pattern that resembled that of the control with darkly stained myoblasts remaining at a minimum. In contrasts, exposure to either monensin or salinomycin resulted in an increase in both the number of negative myoblasts as well as the number of darkly stained myoblasts.
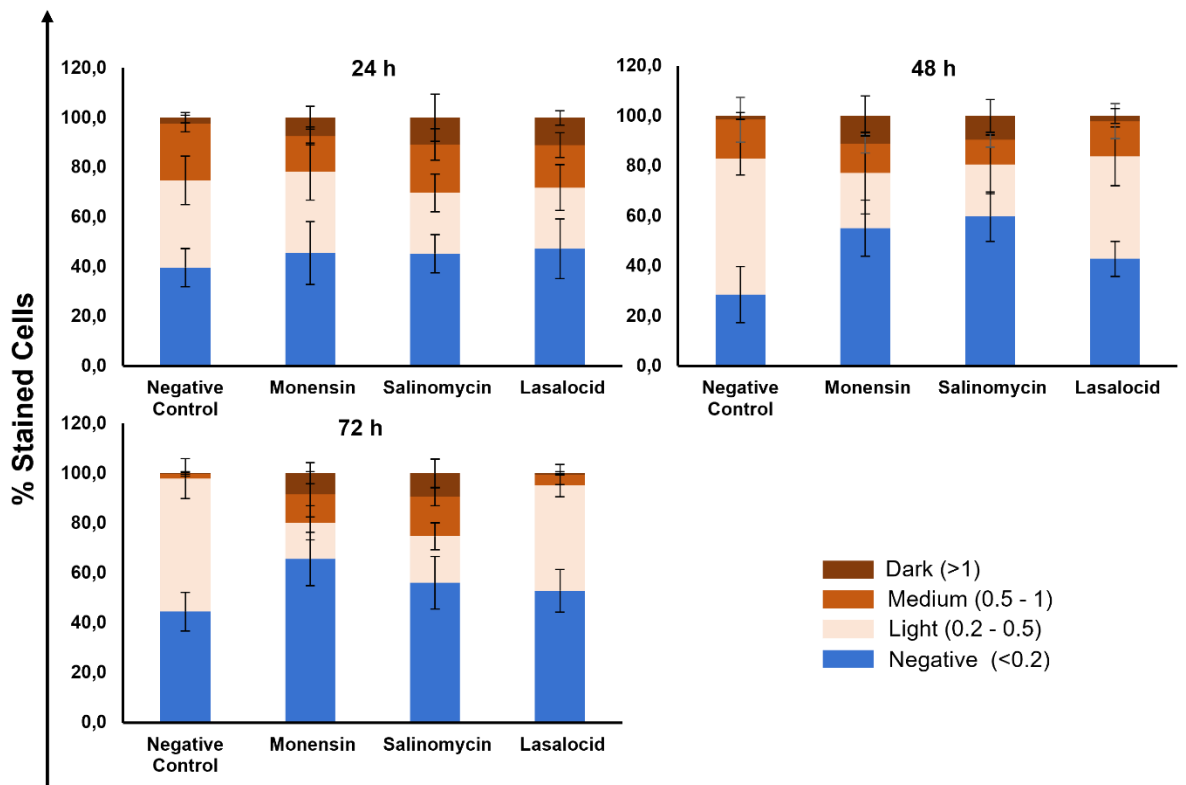
Figure 4.25 The percentage myoblasts categorised as staining negative, light, medium or dark for desmin after exposure to the ionophores for 24, 48 and 72 h. Six images were randomly taken from the slide and the perinuclear stain intensity was measured using QuPath positive cell detection and sorted into negative, light, medium and dark. The average myoblasts percentage over each category was calculated and displayed with standard deviation.

4.3.3 The Effect of the Ionophores on Synemin

The C2C12 myoblasts were stained for synemin after exposure to monensin, salinomycin and lasalocid for 24, 48 and 72 h. As with desmin, the synemin intermediate filaments stained light beige-brown and the nuclei stained blue. Synemin, however, did not stain as intensely as desmin.

Glyoxal and cytochalasin D were used as positive controls. Myoblasts exposed to 1 mM glyoxal for 24, 48 and 72 h had small, concentrated points of synemin adjacent to the nucleus (**Figure 4.26 a**, **red arrowheads**). Cytochalasin D exposure resulted in the reduction of the cytoplasm volume around the nucleus and thin filamentous protrusions extending between the myoblasts (**Figure 4.26 b**).
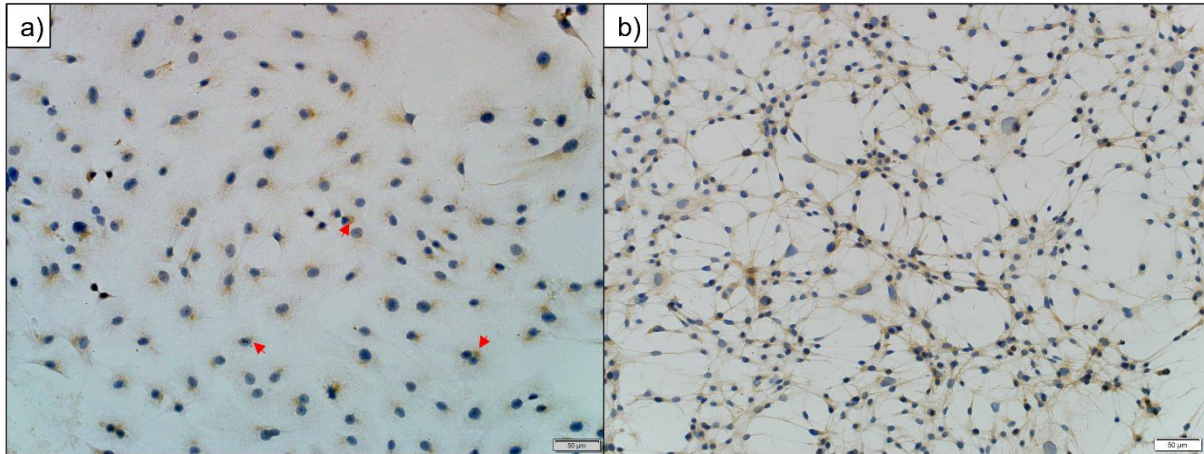
Figure 4.26 H-DAB immunocytochemical staining of C2C12 myoblasts for synemin after exposure to 1 mM glyoxal for 48 h (a) and 20 µM cytochalasin D for 30 min (b). Red arrows indicate dot-like synemin aggregation near the perinuclear region of the myoblasts. Scale bar = 50 µm.

The negative and solvent controls appeared similar, with synemin spread diffusely across the cytoplasm (**Figure 4.27 a-c**). A few myoblasts had a greater concentration of synemin filaments in the perinuclear region. The number of C2C12 myoblasts increased over the 72-h period.

After exposure to the ionophores, some 'gaps' appeared in the cytoplasm of synemin stained myoblasts (**Figure 4.27**, **yellow arrows**). Myoblasts exposed to monensin, had the greatest number of 'gaps', which increased with exposure time. Lasalocid, in contrast, had the fewest. Some myoblasts became thin, with the protrusions staining slightly darker. A few pyknotic nuclei could be seen in the samples as well. No other striking differences between the synemin staining pattern of the negative control and ionophore exposed myoblasts could be seen.
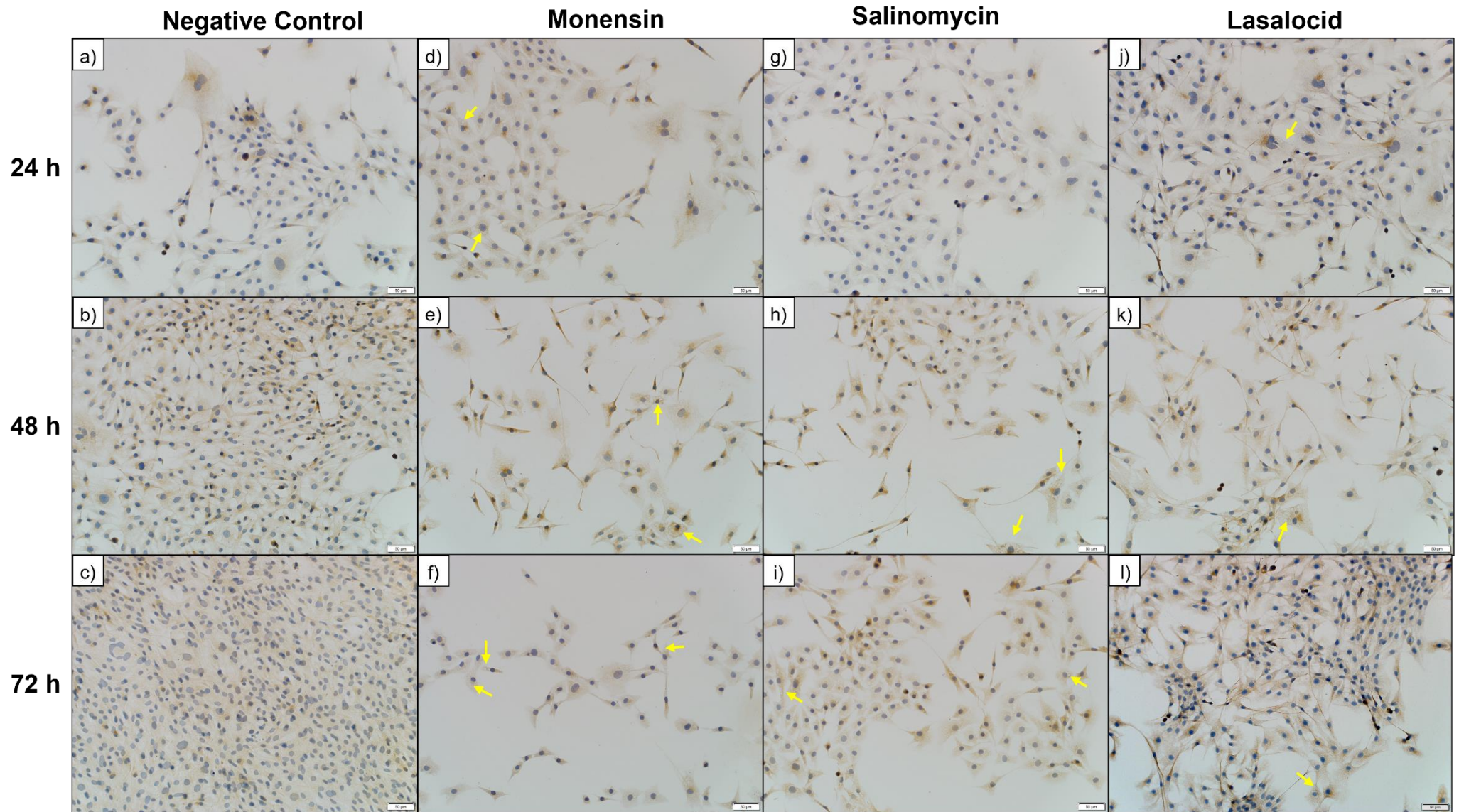
Figure 4.27 H-DAB immunocytochemical staining of C2C12 myoblasts for synemin. The myoblasts in the negative control were cultured in complete DMEM medium over a period of 72 h (a-c). Additionally, the myoblasts were exposed to 1 µM monensin (d-f), salinomycin (g-i) or lasalocid (j-l) for 24, 48 and 72 h. 'Gaps' within the synemin filament network are indicated with yellow arrows. Scale bar = 50 µm.

106

4.4 Discussion

Immunofluorescent techniques were used to determine whether the ionophores affected the microfilament and microtubule networks of the myoblasts. Ionophore exposure resulted in minimum to moderate change in the microfilament network. Most altered were the H9c2 and L6 myoblasts after prolonged exposure to either monensin or salinomycin. In contrast, the microfilament network of the C2C12 myoblasts was comparatively less affected. In the majority of the myoblasts, the normal mesh-like appearance of the microfilament network persisted, with long filaments stretching across the cytoplasm of larger myoblasts. The degree of organisation and length of the microfilaments determine the stiffness of a cell (Fletcher and Mullins, 2010). Highly branched and shorter microfilaments are usually associated with cellular movement (Fletcher and Mullins, 2010; Insall and Machesky, 2009; Paddock and Albrecht-Buehler, 1986). Ionophores have previously been reported to affect the actin cytoskeleton of cells (Schenk et al., 2015; Sun et al., 2017; Tilney et al., 1978). Salinomycin, increased the strength and stiffness of the microfilament network of liver cancer stem cells via the inhibition of the focal adhesion kinase (FAK) and extracellular signal-regulated kinase (ERK1/2) (Sun et al., 2017). Ionophores have also been used to trigger the polymerisation of actin in *Echinoderm* sperm by increasing intracellular pH (Tilney et al., 1978). In contrast, salinomycin halted pancreatic cancer cell proliferation and migration by disrupting the actin stress fibre integrity (Schenk et al., 2015).

The integrity of the microtubule filaments was obviously affected, and interruptions or 'gaps' in the network could be seen as early as 24 h post-exposure. These 'gaps', most likely corresponds to vesicles generated after ionophore exposure. 'Gaps' were more readily observed in the microtubule network compared to the microfilament network (e.g., **Figure 4.18**, **ROI**). These gaps were also much more distinct in the H9c2 cell line, perhaps due to the larger cytoplasm to nucleus ratio. In some cases, the microtubule network appeared less dense in exposed myoblasts. The microtubule network of a cell is involved in mitosis and transportation of cellular cargo (Fletcher and Mullins, 2010; Hohmann and Dehghani, 2019). When exposed to lasalocid, the axonal transport and amount of microtubules in frog sciatic nerves were decreased (Kanje et al., 1981). Increased Ca^{2+} concentrations inhibit microtubule polymerisation (Olmsted and Borisy, 1975; Weisenberg, 1972) and as

the intracellular Ca^{2+} concentration is elevated, either directly via lasalocid or indirectly via monensin or salinomycin, exposure to the ionophores could result in decreased microtubule formation.

Monensin and salinomycin are more toxic compared to lasalocid (**Chapter 3**, **Table 3.2**) and thus, at the concentrations tested, their affects appear to be greater. After exposure to lethal ionophore concentrations the myoblasts rounded-up, as seen previously with light microscopy (**Chapter 3**, **Figure 3.10**). These round myoblasts had both the microfilaments and microtubules concentrated around the nucleus, with discernment of the finer structural detail of these networks lost. This was most apparent in L6 myoblasts exposed to monensin (**Figure 4.11** and **Figure 4.12**). The rounding of the myoblasts and loss of architecture possibly indicate degradation of the cytoskeleton. Additionally, with higher ionophore concentrations and longer exposure times many myoblasts detached and died, leaving behind cytoskeletal debris, lacking nuclei. Not all myoblasts, however, were lethally damaged. In some cases, specifically after exposure to lasalocid, myoblasts undergoing mitosis were visible, with the mitotic spindle evident. This indicates that myoblast proliferation was not completely halted under these circumstances. The $EC_{50}s$ obtained for lasalocid were equal to or above 1 µM (**Chapter 3**, **Table 3.2**), and thus myoblast proliferation is not unexpected when exposed to 0.1 µM concentrations.

In addition to the microfilament and microtubule networks, the effect of ionophores on the intermediate filaments, desmin and synemin, was investigated using immunocytochemistry. C2C12 myoblasts exposed to either monensin or salinomycin for 48 and 72 h had a slightly altered distribution of desmin filaments (**Figure 4.24** and **Figure 4.25**). In low density cultures, an increase in the number of thin and elongated myoblasts were seen. Desmin was aggregated in the perinuclear region of the affected myoblasts. In control myoblasts desmin staining was more diffusely filamentous throughout the cytoplasm. Synemin is known to co-polymerise with desmin at the Z-disk (Mizuno et al., 2001). However, in this study synemin appeared minimally affected (**Figure 4.27**), although akin to both the microtubules and desmin, 'gaps' could be seen dispersed throughout the network. Similar results were obtained in a study exposing C2C12 myoblasts to geigerin, a myotoxic compound, with desmin aggregating in the perinuclear region while synemin remained unaltered (Botha et al., 2019).

Desmin confers both shape and resilience to myoblasts and myofibers, giving structural integrity to the cells (Mermelstein et al., 2005). The disorganisation of desmin filaments is associated with various myopathies and are characterised by the accumulation of desmin in certain inclusions, sarcoplasmic bodies, cytoplasmic bodies and granulo-filamentous material. Furthermore, desmin also determines the intracellular location of mitochondria in the myocyte and regulates their respiratory function (Capetanaki, 2002; Milner et al., 2000). Thus, disorganisation and loss of desmin filaments after ionophore exposure could alter mitochondrial distribution and feasibly result in energy deficiency. Additionally, the sequestration of excess intracellular Ca^{2+} into the mitochondria could further decrease mitochondrial respiration (Wrogemann and Pena, 1976).

Ultrastructural studies of animals exposed to toxic doses of ionophores indicate myofibrillar degeneration and necrosis with the disruption of the contractile apparatus (Confer et al., 1983; Van Vleet and Ferrans, 1984a). The intercalated disks in the myofibers of sheep exposed to monensin were irregular, with mild Z-disk streaming and indistinct A and I bands (Confer et al., 1983). In more chronic stages, dense granular material, representing disrupted Z-disks, was present (Confer et al., 1983). Desmin is primarily associated with the Z-disk of striated muscle (Agnetti et al., 2021; Costa et al., 2004; Paulin and Li, 2004), thus disruption of desmin could contribute to myofibrillar degeneration. Desmin is a substrate for Ca^{2+}-activated proteases such as calpains (Aweida et al., 2018; Elamrani et al., 1995). It is thus possible that the increase in cytoplasmic Ca^{2+} causes the activation of these proteases, which in turn is responsible for the degradation of the desmin filaments. In fact, salinomycin activates calpain and triggers calpain-mediated cell death in murine dorsal root ganglion neurons (Boehmerle and Endres, 2011). However, various concentrations of leupeptin, a protease inhibitor, failed to protect frog skeletal muscles from damage after exposure to the ionophore calcimycin *in vitro* (Duncan et al., 1979), therefore implying that myofibrillar damage was not due to Ca^{2+}-activated proteases.

In conclusion, the primary cytoskeletal filaments affected in this *in vitro* study following ionophore exposure, were the microtubule and desmin intermediate filament networks. The microfilament and synemin networks were only slightly affected. As the myoblasts shrunk and became more rounded, both the microfilament and microtubule networks concentrated around the nucleus.

Chapter 5: The Effect of Monensin, Salinomycin and Lasalocid on the Ultrastructure of H9c2 and L6 myoblasts

5.1 Introduction

Ionophores, through their disruption of ion homeostasis and various concurrent downstream effects, alter tissue and cellular ultrastructure. In cardiac and skeletal muscles of sheep and pigs that died as a result of monensin toxicosis, the myofibers were often disrupted with swollen mitochondria and an increased number of electron-lucent vesicles within the cytoplasm (Confer et al., 1983; Van Vleet and Ferrans, 1984a, b). In pigs that died of acute monensin toxicosis, mitochondria were either swollen or condensed, depending on the severity of the insult (Van Vleet and Ferrans, 1984a, b). The myocytes undergo degeneration and necrosis, followed by macrophage infiltration and attempts at repair. Likewise, in horses dosed with monensin, hepatocytes suffer similar alterations after ionophore exposure, in addition to an increase in the number of smooth ER, peroxisomes and lipid droplets within the cytoplasm (Mollenhauer et al., 1981).

In vitro exposure of cells and tissues to ionophores induces mitochondrial condensation and excessive vesiculation within the cytoplasm (Mollenhauer et al., 1990; Paddock and Albrecht-Buehler, 1986). Various cancer cell lines, following ionophore exposure, die via apoptosis with an autophagic component (Ketola et al., 2010; Kiełbasiński et al., 2020; Kim et al., 2017b; Kim et al., 2016; Park et al., 2003; Park et al., 2002). Cells undergoing apoptosis exhibit ultrastructural changes including cell shrinkage, karyorrhexis, chromatin condensation and the formation of apoptotic bodies (Burattini and Falcieri, 2013; Kerr et al., 1972; Kroemer et al., 2009). Necrosis, on the other hand, generally exhibit cell swelling with both swollen organelles and nuclei present within the cytoplasm (Kroemer et al., 2009). The plasma membrane of necrotic cells is compromised, leaking cellular content into the surrounding environment. Autophagic vesicles, found in both apoptotic and necrotic cells, as well as being the major component in autophagic cell death, are double membraned organelles that often contain sequestered and degraded cytoplasmic material (Kroemer et al., 2009).

This chapter focuses on the ultrastructural changes that occur in H9c2 and L6 myoblasts after *in vitro* exposure to 0.1 µM monensin, salinomycin and lasalocid for 48 h using transmission and scanning electron microscopy (TEM and SEM). Additionally, the distribution of β-tubulin in L6 myoblasts after ionophore exposure was investigated using immunogold-labelling.

5.2 Materials & Methods

5.2.1 Sample Preparation and Fixation for Transmission Electron Microscopy

H9c2 and L6 myoblasts were seeded into a 6-well plate (100 000 myoblasts/ml) and allowed 24 h to adhere and stabilise. The myoblasts were exposed to 0.1 µM monensin, salinomycin and lasalocid for 48 h. A negative (complete DMEM) and solvent control (0.1% MeOH) were also included.

Post-exposure the medium was removed, and the myoblasts fixed with 2.5% glutaraldehyde in 0.075 M phosphate buffer (pH 7.4) for at least 1 h. The myoblasts were carefully removed from the well surface with a cell scraper, transferred to a microtube and centrifuged at 950 x g. The pellets were rinsed three times with 0.075 M phosphate buffer for 10 min each. A second fixation step, with a 1% osmium tetroxide (OsO_4) solution for 1 h was performed, followed by washing the pellets three times for 10 min with dH_2O.

The samples were dehydrated with increasing ethanol (EtOH) concentrations i.e., 50, 70, 90, 96 and 100% EtOH for 10 min at a time, and finally left in 100% EtOH for at least 1 h. The EtOH was replaced with propylene oxide for 10 min and slowly infiltrated with an epoxy resin mixture. The samples were first incubated with 2:1 propylene oxide/epoxy resin, followed by 1:2 propylene oxide/epoxy resin for 1 h at a time. The resin mixture was replaced with pure epoxy for 2 to 3 h, then imbedded in TAAB 812 epoxy resin (Luft, 1961) and left in an oven overnight at 65 °C to polymerise.

The resin blocks were cut into thin sections, ~100 nm thick, using a Leica EM UC7 microtome (Leica Microsystems, Wetzlar, Germany) and placed on a 300 x 75 copper grid (Agar Scientific). Each grid was stained for 6 min with uranyl acetate and

3 min with lead citrate (Reynolds, 1963). The grids were viewed using a JEOL JEM 1400-FLASH transmission electron microscope (Jeol Ltd., Tokyo, Japan).

5.2.2 Sample Preparation and Fixation for Scanning Electron Microscopy

H9c2 and L6 myoblasts were seeded onto 10 mm sterile coverslips in a 24-well plate (100 000 myoblasts/ml) and allowed 24 h to adhere and stabilise. The myoblasts were exposed to 0.1 µM monensin, salinomycin and lasalocid for 48 h. Both a negative (complete DMEM) and solvent control (0.1% MeOH) were also included.

The fixation and dehydration procedures were carried out on the coverslips as described above up to the second dehydration step with 100% EtOH. Afterwards, the coverslips were first incubated in a 1:1 EtOH and 1,1,1,3,3,3-hexamethyldisilazane (HMDS) (Merck) mixture, then in 100% HMDS both for 30 min at room temperature. Finally, the coverslips were left in 100% HMDS overnight to allow all the HMDS to evaporate.

The coverslips were attached to an aluminium stub using 12 mm carbon adhesive tabs (Electron Microscopy Sciences) and coated with carbon using the EmiTech K950X sputter coater (Emitech, Montigny-le-Bretonneux, France). However, due to the samples charging they were later coated with chromium using the Quorum Q150T ES sputter coater (Quorum, East Sussex, United Kingdom). Samples were viewed using a Zeiss SUPRA 55VP scanning electron microscope at the EM unit of the Sefako Makgatho Health Sciences University.

5.2.3 Immunogold Labelling of β-Tubulin in L6 Myoblasts

Transmission electron microscopy in combination with immunogold labelling was used to investigate the distribution of β-tubulin in L6 myoblasts. For future work, the primary antibody's ability to bind to β-tubulin in H9c2 and C2C12 myoblasts were also confirmed using a western blot.

Table 5.1 Antibodies used for the western blot and immunogold labelling of β-tubulin.

Antibody	Manufacturer	Technique and Dilution
Anti-β Tubulin Antibody - Loading Control	Abcam	Western Blot (1:500) Immunogold labelling (1:100)
Goat Anti-Rabbit IgG H&L (HRP)	Abcam	Western Blot (1:2000)
Goat F(ab')2 Anti-rabbit IgG H&L (10 nm Gold)	Abcam	Immunogold labelling (1:50)

Western Blot - Protein Extraction

A western blot was performed as a positive control, to confirm that the primary antibody binds to β-tubulin in L6, C2C12 and H9c2 myoblasts. The myoblasts were cultured in a 6-well plate and extracted using a radioimmunoprecipitation assay (RIPA) buffer (Sigma-Aldrich) supplemented with a protease inhibitor cocktail (Thermo Scientific) and ethylenediaminetetraacetic acid (EDTA). The myoblasts were removed from the well surface using a cell scraper, transferred to a microtube and sonicated for 1 min. Thereafter, the myoblasts were centrifuged at 8 000 x g for 5 min and the supernatant transferred to a new tube. All the steps described above were carried out on ice. The supernatant was stored at -20 °C until further use.

Western Blot - Bradford Assay

The protein concentration in each lysate was determined using the Bradford Assay (Bradford, 1976). Standards were prepared by diluting 2 mg/ml BSA protein standard (Sigma-Aldrich), in diluent (1/10 extraction buffer in PBS). Additionally, each lysate was diluted 1/10 in PBS. The protein concentration of both the standards and diluted cell lysates were determined by adding 5 µl of standard/lysate and 250 µl Bradford Reagent (Sigma-Aldrich) into a 96-well plate. The assay plate was then shaken on a QB-9001 Microporous Quick Shaker (Hinotek Group Ltd., Ningbo, China) for 30 sec and incubated in the dark for 5 min at room temperature, before reading the absorbance at 595 nm. The absorbance of the blank containing only diluent was subtracted from all other measurements. A standard curve was plotted using the absorbance values versus the known protein concentrations. The linear equation generated was used to calculate the concentration of proteins per lysate. The concentration was multiplied by the dilution factor of ten as the lysate was initially diluted 1/10 in PBS.

Western Blot – SDS-Page Electrophoresis and Blotting

On the day of the experiment the supernatant was combined with Laemmli buffer, containing stacking gel buffer, 10% sodium dodecyl sulphate (SDS), glycerol, mercaptoethanol and 0.01% bromophenol blue, in a 1:1 ratio. The samples were boiled for 10 min at 100 °C, followed by immediate loading into a 10% mini-PROTEAN TGX precast gel (Bio-Rad Laboratories) alongside a Blue Prestained Protein Standard, Broad Range (11-190 kDa) (New England Biolabs). Two gels were run simultaneously at 70 V for about 2 h using a BioRad Electrophoresis Unit (Bio Rad Laboratories, Hercules, CA, USA). After removing the gels, one gel was stained with GelCode Blue Stain Reagent (Thermo Scientific) overnight until protein bands were visible.

The second gel was assembled into a sandwich containing four layers of filter paper on both sides of the gel and a Hybond ECL Nitrocellulose membrane (Amersham Pharmacia Biotech). All components of the sandwich were soaked in transfer buffer (25 mM Tris, 150 mM glycine pH 8.3, 20% MeOH) for 15 min. The proteins were transferred onto the membrane using a semi-dry transfer technique. The Biometra Fastblot system was used at 30 V for 45 min. The membrane containing the transferred proteins was incubated overnight at 4 °C in blocking buffer containing 3% milk powder (Skim milk powder, OXOID) and 0.05% Tween in PBS. Afterwards, the membrane was washed three times for 10 min each using washing buffer (0.05% Tween in PBS) and incubated with the primary antibody (1:500) for 1 h at room temperature (**Table 5.1**). The membrane was again washed three times before and after incubation with the secondary antibody (1:2000) for 30 min (**Table 5.1**). The colour on the gel was developed by mixing solution A (60 mg 4-chloro-naphthol and 20 ml ice cold MeOH) and solution B (60 µl H_2O_2 and 100 ml PBS) and leaving the gel in these solutions for around 20 min.

Sample Fixation for Immunogold Labelling

L6 myoblasts were seeded into a 6-well plate and exposed to 0.1 µM monensin, salinomycin and lasalocid for 48 h, as previously described. Post-exposure the medium was removed from the wells and the myoblasts were fixed with a solution containing 0.8% glutaraldehyde and 4% paraformaldehyde in 0.1 M PBS with 50 mM lysine (pH 7.2) (Oko and Maravei, 1995). The samples were transferred into a microtube and rinsed three times with 0.1 M PBS (pH 7.2-7.4) for 5 min, before being

incubated in 50 mM NH$_4$Cl (in 0.1 M PBS) overnight at 4 °C. The samples were rinsed with PBS, dehydrated in graded EtOH up to 90% and infiltrated progressively with increasing gradients of LR White in 90% EtOH until 100% concentration of LR White was achieved. After a final change of LR White containing 0.1% w/v benzoin ethyl ether, the embedded tissues in gelatine capsules were polymerised overnight at 60 °C. The polymerised samples were sectioned with a Leica EM UC7 microtome and placed onto 300 x 75 nickel grids (Agar Scientific). The above fixation method was performed at the Electron Microscopy Unit, Department of Anatomy and Physiology, Faculty of Veterinary Science, University of Pretoria.

Immunogold Labelling of L6 Myoblasts

The grids were first rinsed with ddH$_2$O three times for 1 min each, before being incubated in normal goat serum (Merck Millipore) diluted 1/30 with antiserum (0.01 M PBS, pH 7.4, 0.15 M NaCl, 0.1% BSA, 0.01% sodium azide) for 30 min at room temperature (Sarraf, 2000). Subsequently, the grids were incubated with the primary antibody (1:100 in PBS) overnight at 4 °C (**Table 5.1**). The following day, the grids were washed sequentially with 0.05 M Tris-HCl (pH 7.4) and 0.05 M Tris-HCl containing 0.1% BSA (pH 7.4) three times for 1 min each, then left in 0.05 M Tris-HCl containing 1% BSA (pH 8.2) for 15 min. The grids were incubated with the secondary antibody (**Table 5.1**) in Tris-HCl containing 1% BSA (pH 8.2) for 3 h at room temperature and again sequentially washed with 0.05 M Tris-HCl containing 0.1% BSA, 0.05 M Tris-HCl and finally ddH$_2$O three times for 1 min each. The grids were counterstained with uranyl acetate and lead citrate as described above and viewed using a JEM JEOL 1400-FLASH TEM.

5.3 Results

5.3.1 The Ultrastructural Changes of H9c2 and L6 Myoblasts after Exposure to Monensin, Salinomycin and Lasalocid

The Ultrastructure of H9c2 Myoblasts

H9c2 myoblasts are relatively large, elongated cells, generally tapered at both ends with a layer of microfilaments arranged underneath the plasma membrane (**Figure 5.1** and **Figure 5.2**, **green arrows**). Large, oval-shaped nuclei are usually near the centre of the myoblasts containing one or two nucleoli. Rough endoplasmic reticulum (RER) with homogeneous content were distributed throughout the cytoplasm either

as tubular or vesicular structures (**Figure 5.1 c-e**, **g & h** and **Figure 5.2 d-g & h**). Ribosomes were associated with the RER as well as scattered throughout the cytoplasm. The Golgi apparatus were generally located in proximity of the nucleus, with flat cisternae stacking on top of each other (**Figure 5.1 a & e-g** and **Figure 5.2 a**, **e & f**). The mitochondria were round to oval and sometimes slightly stretched with the mitochondrial membranes and cristae visible (**Figure 5.1 f-h** and **Figure 5.2 d**, **g & h**). The cytoplasm contained various vesicles and some autophagic vesicles (**Figure 5.1 d & e** and **Figure 5.2 g**). A few myelin figures, possibly as an artefact of fixation, were also present in some myoblasts (**Figure 5.2 f**).

Exposure to 0.1 µM monensin for 48 h, resulted in the formation of a large number of electron-lucent vesicles clustered together in the cytoplasm (**Figure 5.3**). The mitochondria were condensed, with a very dark mitochondrial matrix and distinct cristae (**white asterisks**). The mitochondria still maintained their round to slightly stretched shape in most cases, however some had a U-shape (**Figure 5.3 c & g**). The cisternae of the Golgi apparatus were swollen, no longer appearing as a flat stack. A few necrotic myoblasts with a disrupted plasma membrane and damaged cytoplasmic material were observed (**Figure 5.3 d**). The nuclei remained unaffected, except in a few cases where chromatin condensation occurred (**red asterisks**). In **Figure 5.3 c**, a number of nuclear pores can be seen as a result of the level at which the section was cut. Some myelin figures and autophagic vesicles were also visible (**Figure 5.3 e**, **g & h**). The RER was dispersed in between the vesicles but was mostly unaffected with homogeneous content and the ribosomes still associated with the ER membrane (**Figure 5.3 e-h**).

Salinomycin exposure induced similar changes in the myoblasts compared to monensin, but to a lesser extent; for instance, the mitochondria were not as electron-dense (**Figure 5.4 f-h**). The Golgi apparatus were swollen, and electron-lucent vesicles were present within the cytoplasm (**Figure 5.4 b-e**, **g & h**). Myelin figures and autophagic vesicles could be seen dispersed throughout the cytoplasm (**Figure 5.4 b-d & f**). The RER and nuclei remained mostly unaffected, though some nuclei were lobulated (**Figure 5.4 c**). Lipid droplets could be seen within the cytoplasm of a few myoblasts (**Figure 5.4 b-d & h**). The plasma membrane remained intact.

After exposure to lasalocid, H9c2 myoblasts contained electron-lucent vesicles (**Figure 5.5**). The Golgi apparatus were swollen, however some of the cisternae on the cis-face of the Golgi remained flat, while large vesicles were present on the trans-face (**Figure 5.5 b & c**). Myelin figures and autophagic vesicles could be seen throughout the myoblasts (**Figure 5.5 b**, **e & f**). The RER and nuclei of the myoblasts were unaffected. The mitochondria remained mostly unaltered, however, a few lacked cristae and were slightly damaged. The microfilament network below the plasma membrane (**green arrows**) as well as the plasma membrane remained intact. A few myoblasts had lipid droplets within their cytoplasm (**Figure 5.5 e**).

The Ultrastructure of L6 Myoblasts

The L6 myoblasts are round-to-spindle-shaped cells, with a large nucleus near the centre of the myoblast (**Figure 5.6** and **Figure 5.7**). The Golgi apparatus were generally in close proximity to the nucleus. Rough endoplasmic reticulum were dispersed throughout the cytoplasm in continuous stretches with homogeneous content. Ribosomes were closely associated with the RER membranes, while also present freely throughout the cytoplasm. A few vesicles and autophagic vesicles were scattered around the myoblast (**Figure 5.6 d**, **e**, **& g** and **Figure 5.7 a**, **c & f**), including endo- and exocytotic vesicles (**blue arrowheads**). The myoblasts contained many mitochondria, ranging from small and round, to long and slightly stretched. A few relatively large mitochondria were present within some myoblasts (**Figure 5.6 d**). The plasma membrane was intact with small protrusions seen budding from the membranes (**orange arrows**).

When exposed to 0.1 µM monensin for 48 h the myoblasts' cytoplasm became filled with electron-lucent vesicles of various sizes (**Figure 5.8**). In some cases, the vesicles fused together resulting in larger, less distinct vesicles within the cytoplasm (**Figure 5.8 d & h**). A few vesicles connected to the outside of the myoblast. Autophagic vesicles and myelin figures were dispersed between the electron-lucent vesicles (**Figure 5.8 a**, **b**, **d-f & h**). Severely affected myoblasts appeared round, with a slightly condensed cytoplasm and in these myoblasts, the small membrane protrusions were absent (**Figure 5.8 a & d**). Instead, larger apoptotic bodies were seen containing cytoplasmic organelles (**red arrows**). The nuclei of affected myoblasts diverged slightly from the common oval-to-round shape in the negative and solvent controls, being more lobulated (**Figure 5.8 e**). Chromatin condensation

was observed in many myoblasts (**red asterisks**), with dark clumps of chromatin located on the periphery of the nucleus. Aggregates of free chromatin were visible in myoblasts further along the process of apoptosis, the nuclear envelope having disintegrated (**Figure 5.8 d**). Cellular debris and remnants of apoptotic bodies were also observed between myoblasts, indicating necrosis and secondary necrosis (not shown). The mitochondria of the myoblasts were condensed with a very dark matrix (**white asterisks**). Additionally, a few, dark and elongated mitochondria were present within the cytoplasm (**Figure 5.8 e**). The Golgi apparatus were swollen, but some of the cisternae were still clearly defined stacking neatly on top of each other (**Figure 5.8 h**). The RER and ribosomes were dispersed throughout the cytoplasm, while the content of the RER remained homogeneous. In a few myoblasts, the RER was encircling the nucleus in long continuous stretches (**Figure 5.8 c**).

Salinomycin exposure resulted in electron-lucent vesicles throughout the cytoplasm of some myoblasts (**Figure 5.9**). The affected myoblasts appeared less compared to myoblasts exposed to monensin and there were fewer vesicles per cell. Chromatin condensation could be seen in the more affected myoblasts (**red asterisks**). In some cases, a large, electron-dense chromatin aggregation was observed free within the cytoplasm after the nuclear envelope was disrupted (not shown). The Golgi apparatus were relatively swollen, with distended cisternae (**Figure 5.9 c & g**), while the RER and associated ribosomes remained unaffected. The majority of the mitochondria were normal with distinct cristae; however, a few were condensed (**white asterisks**). Additionally, a number of large, round-to-square shaped mitochondria were found within the cytoplasm of some myoblasts (**Figure 5.9 d & h**). A few myoblasts had a condensed cytoplasm (**Figure 5.9 a & e**). The small membrane protrusions were absent in many of the myoblasts and a few apoptotic bodies were noted. A couple of autophagic vesicles, filled with deteriorating cellular content, were found within the cytoplasm (**Figure 5.9 e & g**).

After lasalocid exposure, fewer myoblasts had electron-lucent vesicles within their cytoplasm (**Figure 5.10**). Some small to medium sized vesicles could be seen in proximity to the Golgi apparatus, which was only slightly distended (**Figure 5.10 d & h**). A few autophagic vesicles and myelin figures were observed in between the other organelles (**Figure 5.10 b**, **d**, **f & h**). The majority of the mitochondria remained unaffected, with a few rare cases where the mitochondria were condensed with

swollen cristae (**white asterisks**). Groups of relatively large mitochondria were observed in the cytoplasm in a number of myoblasts. The nuclei remained generally unaffected, with the exception of a few having slight irregular forms. A few apoptotic myoblasts, with apoptotic bodies were observed amongst the other myoblasts (**red arrows**) and some myoblasts had a condensed cytoplasm (**Figure 5.10 c & g**). Normal RER were dispersed throughout the cytoplasm in continuous stretches or in shorter more vesiculated form. Where the RER was dilated, the content was homogeneous, and the ribosomes were still associated to the membrane.
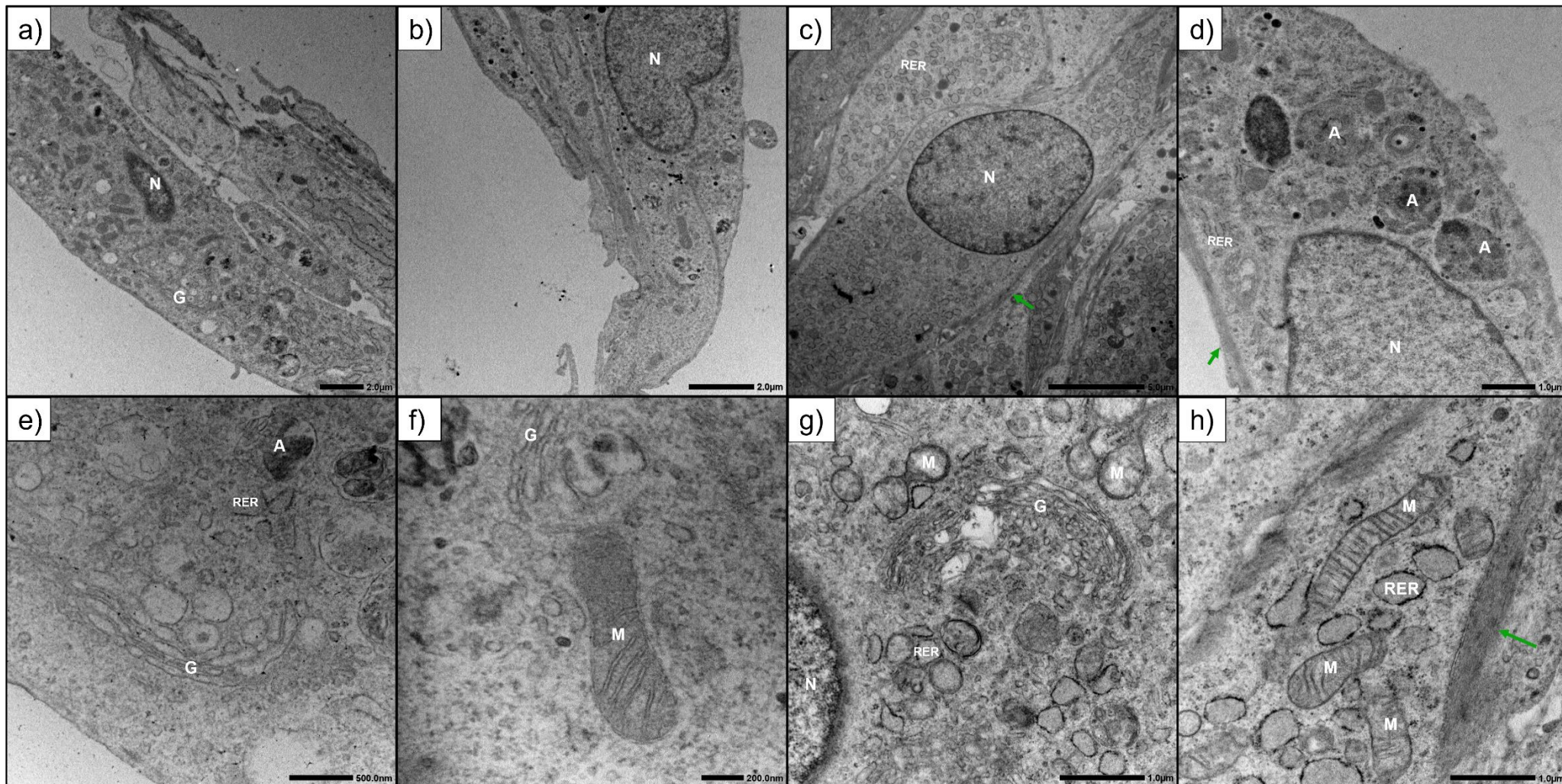
Figure 5.1 Electron micrographs of H9c2 myoblasts incubated in complete DMEM medium for 48 h (negative control). The green arrows mark the layer of microfilaments underneath the plasma membrane. A-autophagic vesicles, G-Golgi apparatus, N-nucleus, M-mitochondria and RER-rough endoplasmic reticulum. Scale bars are indicated at the bottom right.
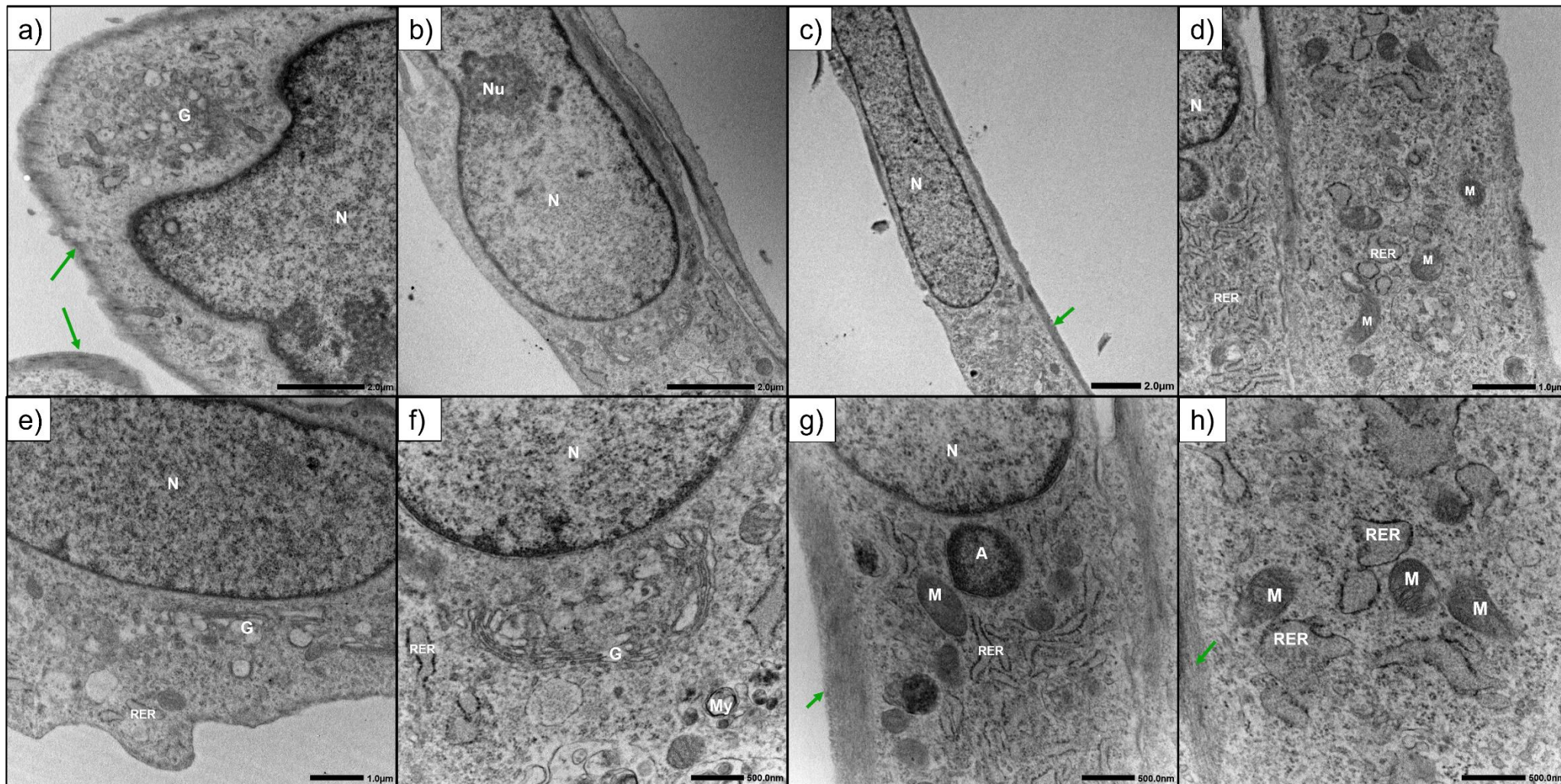
Figure 5.2 Electron micrographs of H9c2 myoblasts incubated in complete DMEM medium with 0.1% MeOH for 48 h (solvent control). The green arrows mark the layer of microfilaments underneath the plasma membrane. A-autophagic vesicles, G-Golgi apparatus, N-nucleus, M-mitochondria, My-myelin figures and RER-rough endoplasmic reticulum. Scale bars are indicated at the bottom right.
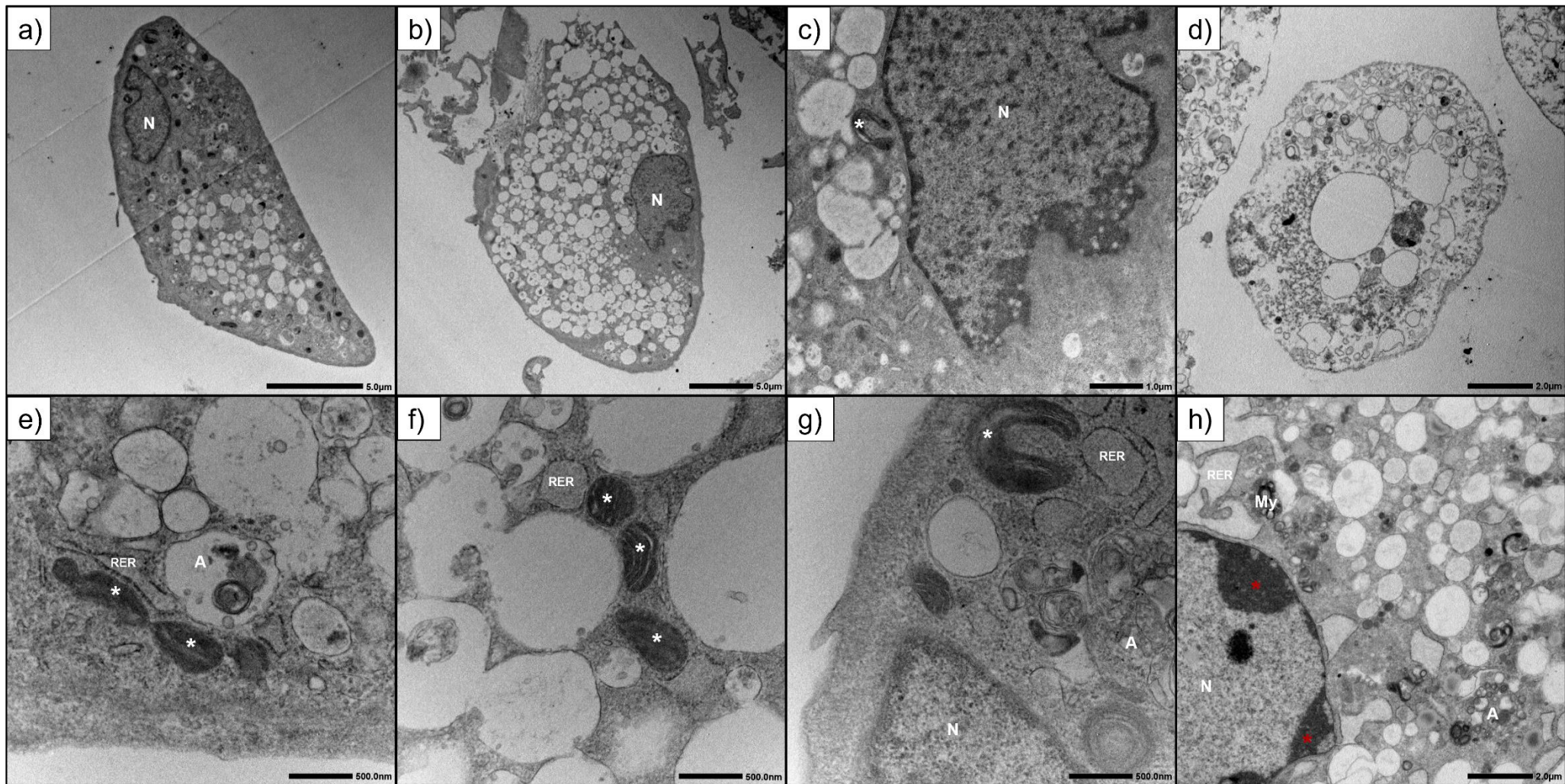
Figure 5.3 Electron micrographs of H9c2 myoblasts exposed to 0.1 µM monensin for 48 h. Condensed mitochondria and condensed chromatin are indicated with white asterisks and red asterisks, respectively. A-autophagic vesicles G-Golgi apparatus, N-nucleus, M-mitochondria, My-myelin figures and RER-rough endoplasmic reticulum. Scale bars are indicated at the bottom right.
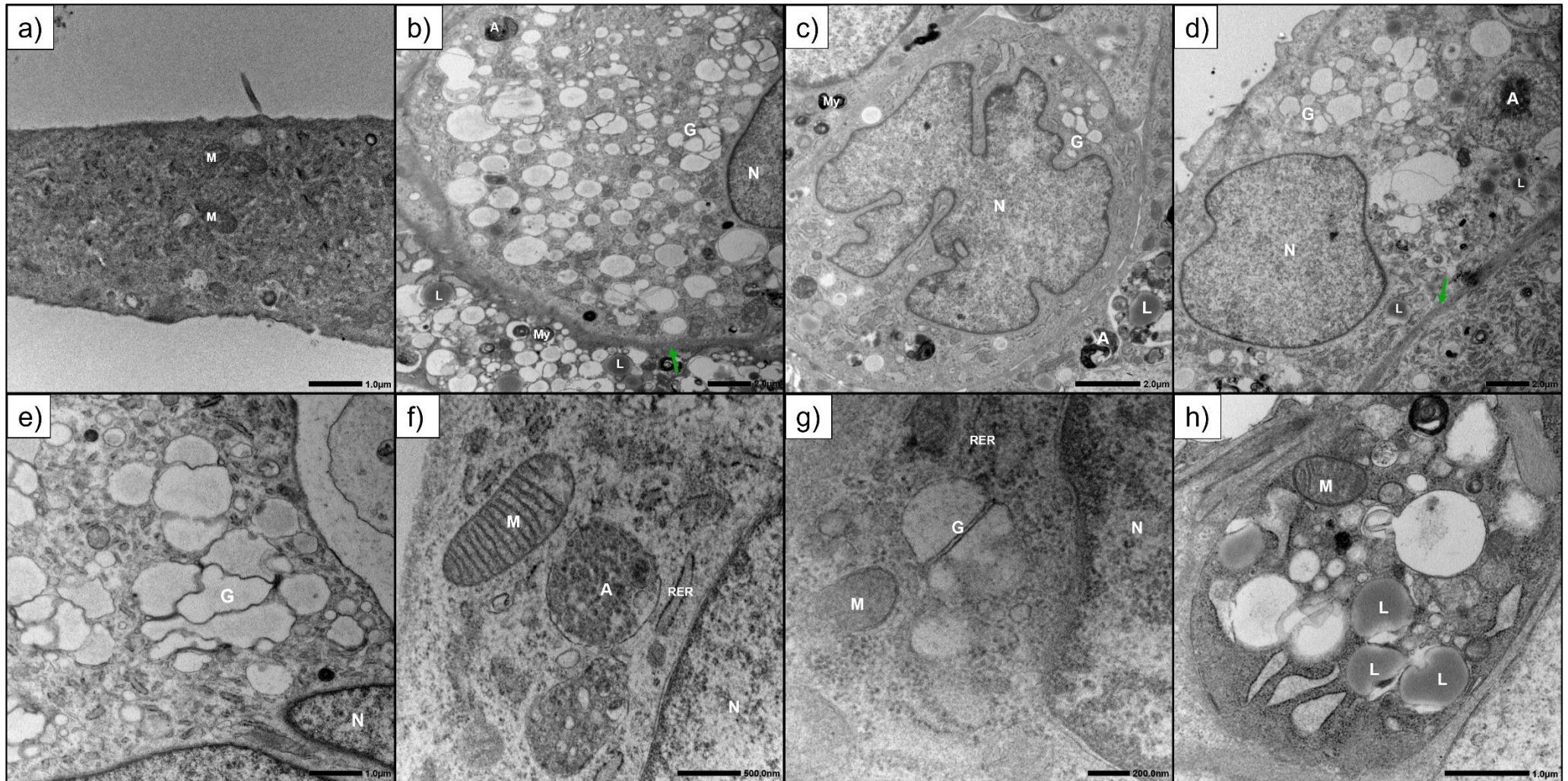
Figure 5.4 Electron micrographs of H9c2 myoblasts exposed to 0.1 µM salinomycin for 48 h. The green arrows mark the layer of microfilaments underneath the plasma membrane. A-autophagic vesicles, G-Golgi apparatus, L-lipid droplet, N-nucleus, M-mitochondria, My-myelin figures and RER-rough endoplasmic reticulum. Scale bars are indicated at the bottom right.
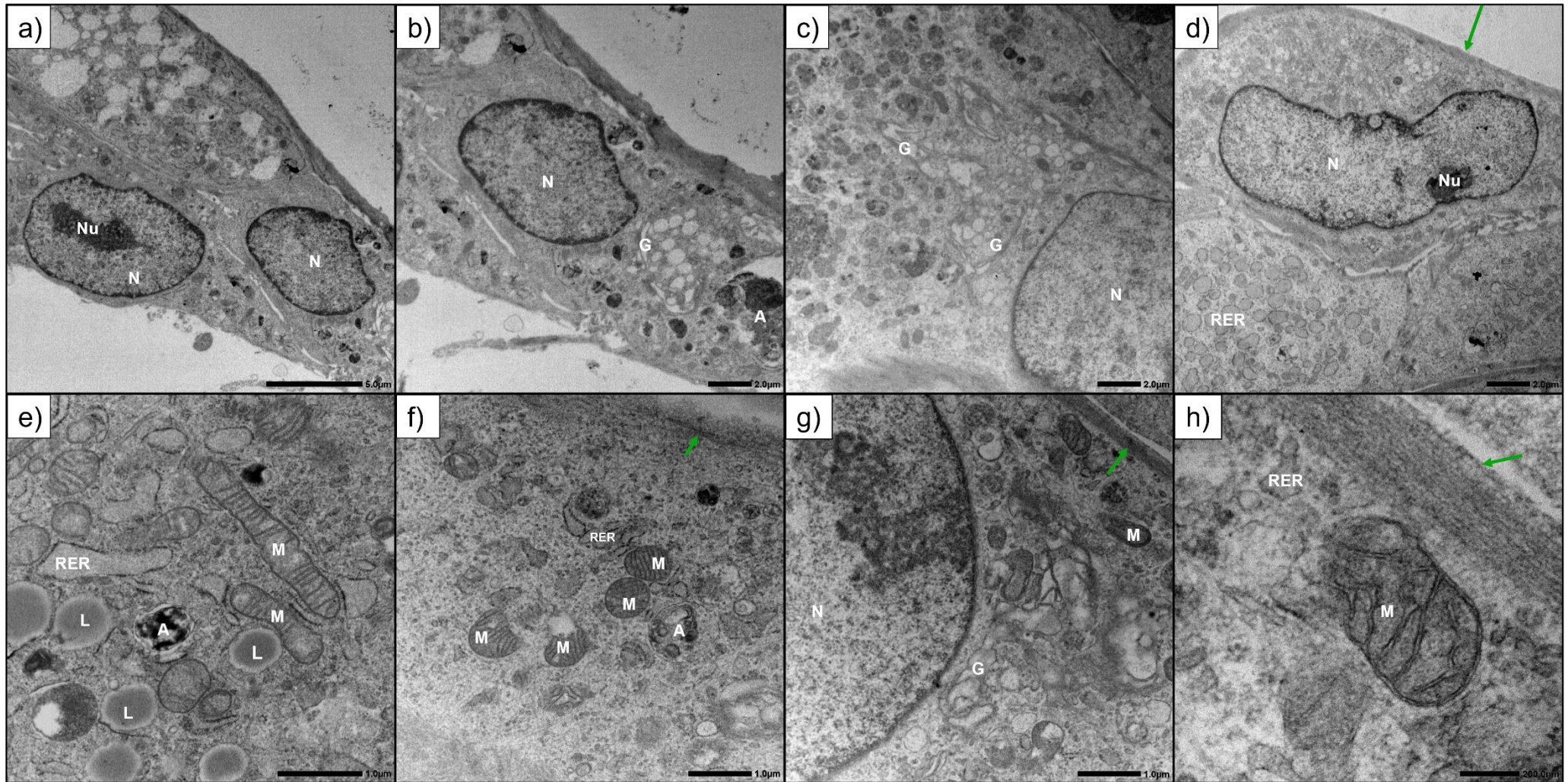
Figure 5.5 Electron micrographs of H9c2 myoblasts exposed to 0.1 µM lasalocid for 48 h. The green arrows mark the layer of microfilaments underneath the plasma membrane. A-autophagic vesicles, G-Golgi apparatus, L-lipid droplet, N-nucleus, Nu-nucleolus, M-mitochondria and RER-rough endoplasmic reticulum. Scale bars are indicated at the bottom right.
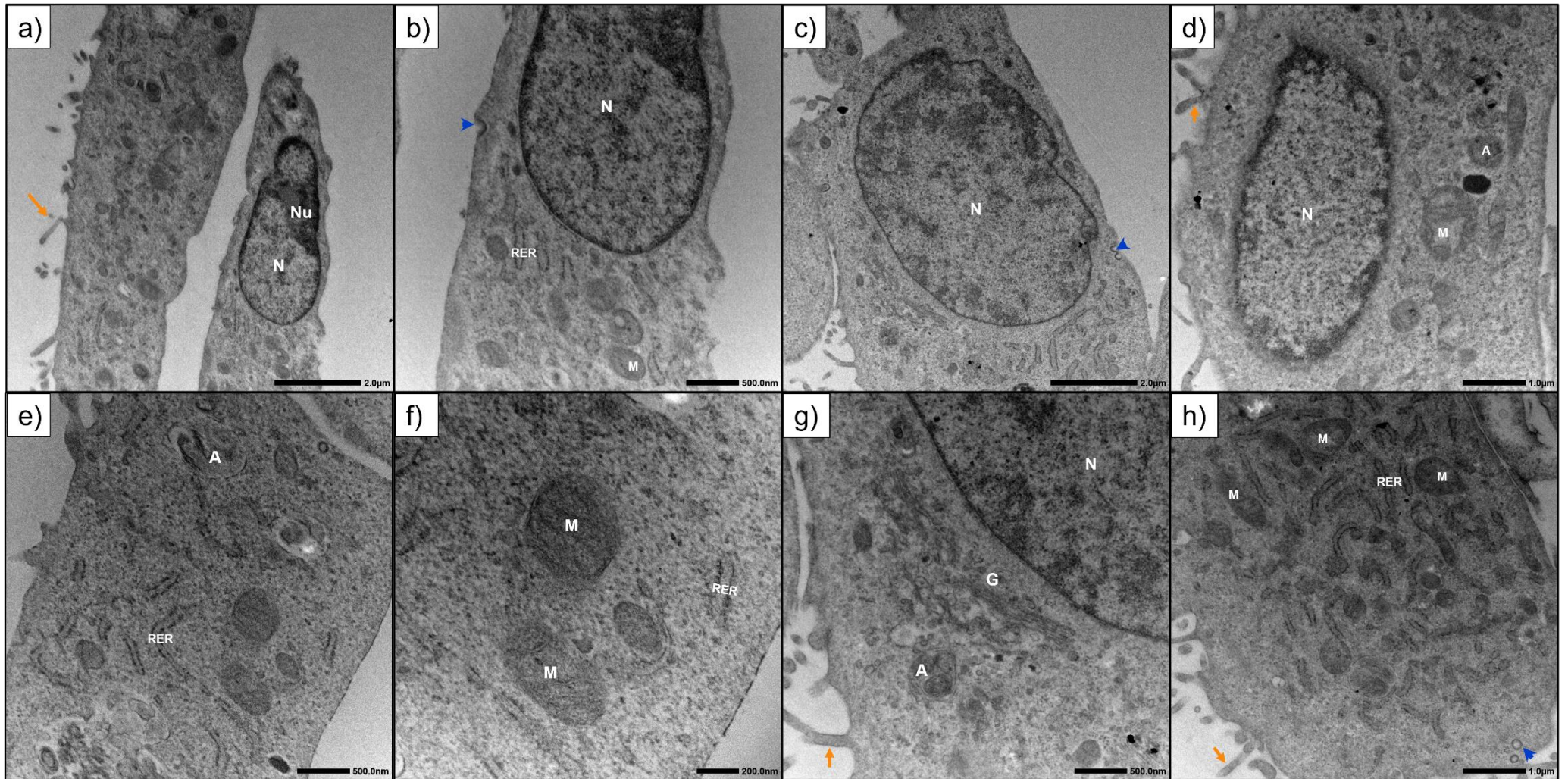
Figure 5.6 Electron micrographs of L6 myoblasts incubated in complete DMEM medium for 48 h (negative control). The orange arrows show small membrane protrusions, and the blue arrowheads indicate endo- and exocytotic vesicles. A-autophagic vesicles, G-Golgi apparatus, N-nucleus, M-mitochondria and RER-rough endoplasmic reticulum. Scale bars are indicated at the bottom right.
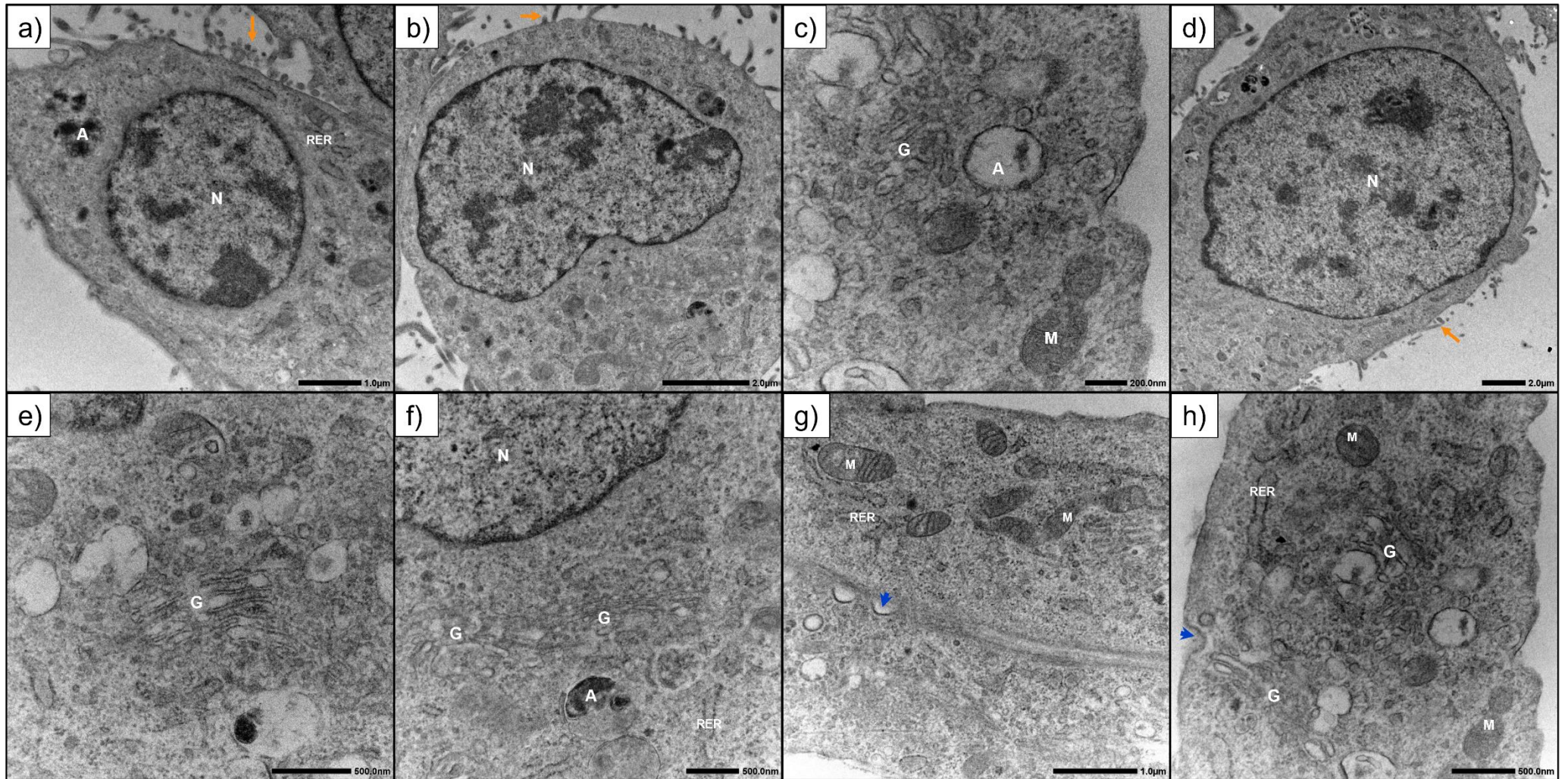
Figure 5.7 Electron micrographs of L6 myoblasts incubated in complete DMEM medium with 0.1% MeOH for 48 h (solvent control). The orange arrows show small membrane protrusions, and the blue arrowheads indicate endo- and exocytotic vesicles. A-autophagic vesicles, G-Golgi apparatus, N-nucleus, M-mitochondria and RER-rough endoplasmic reticulum. Scale bars are indicated at the bottom right.
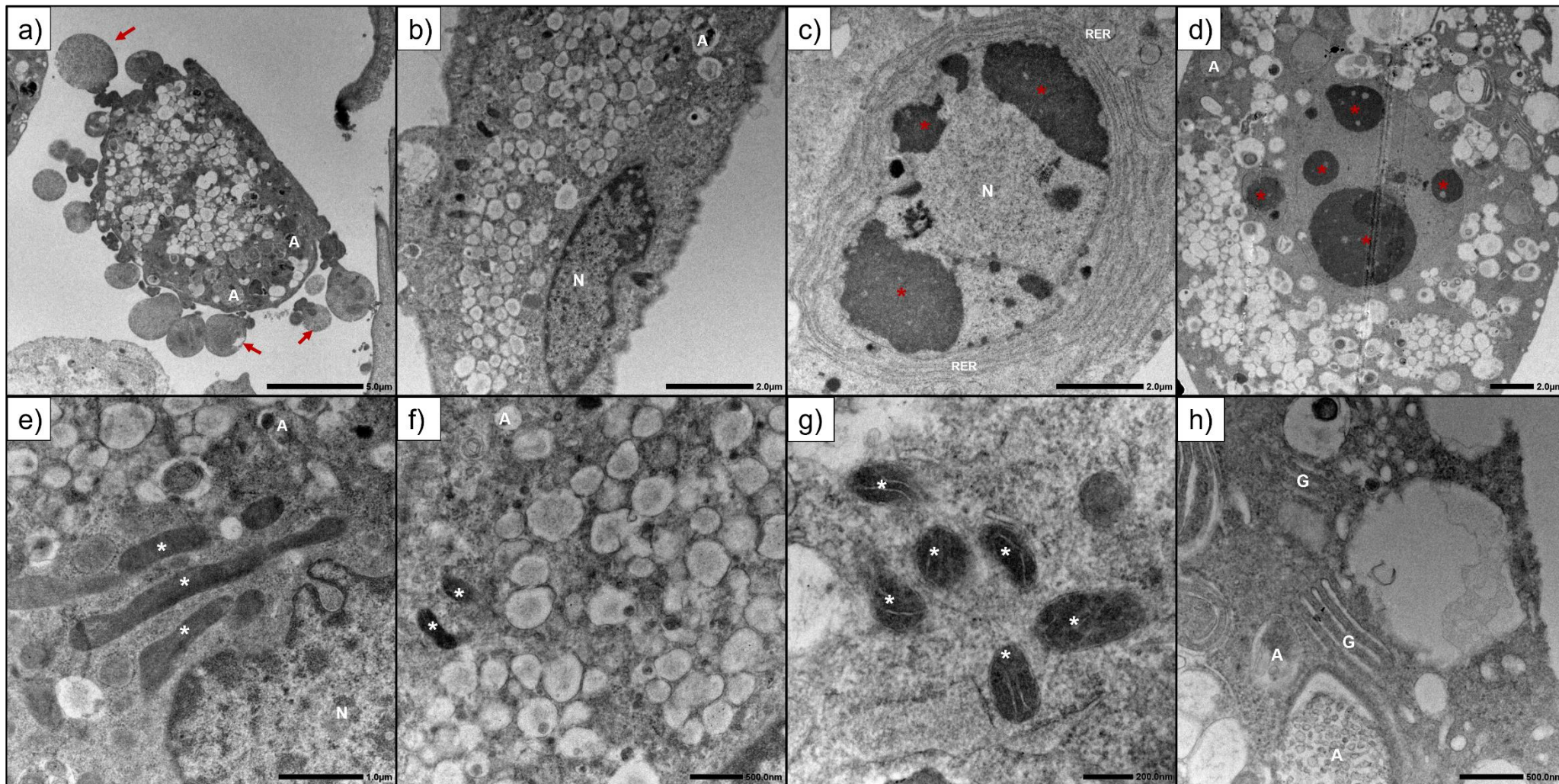
Figure 5.8 Electron micrographs of L6 myoblasts exposed to 0.1 µM monensin for 48 h. The red arrows indicate apoptotic bodies. Condensed mitochondria and chromatin are indicated with white and red asterisks, respectively. A-autophagic vesicles, G-Golgi apparatus, N-nucleus and RER-rough endoplasmic reticulum. Scale bars are indicated at the bottom right.
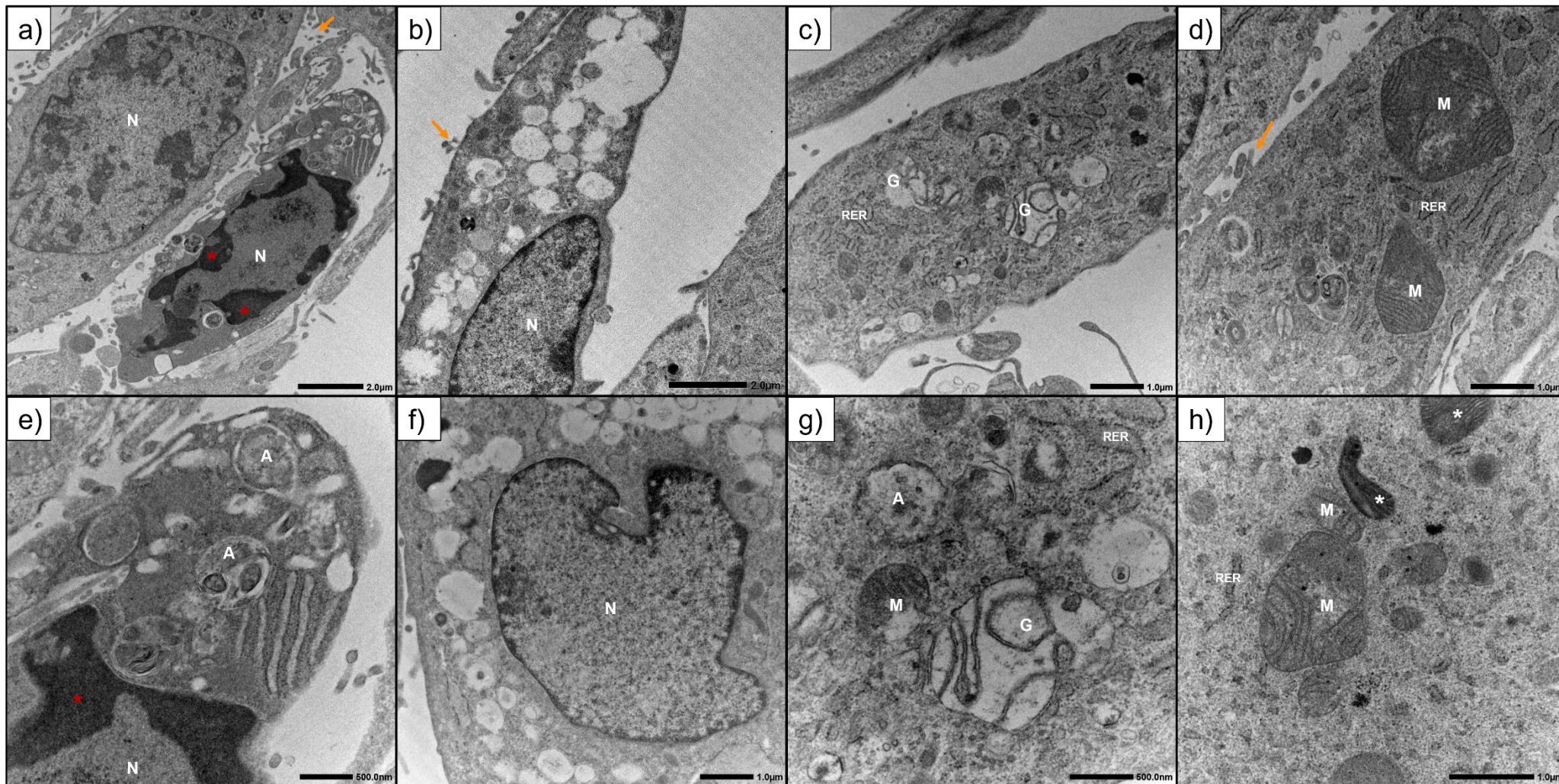
Figure 5.9 Electron micrographs of L6 myoblasts exposed to 0.1 µM salinomycin for 48 h. The orange arrows indicate membrane protrusions. Condensed chromatin is indicated with red asterisks. A-autophagic vesicles, G-Golgi apparatus, N-nucleus, M-mitochondria and RER-rough endoplasmic reticulum. Scale bars are indicated at the bottom right.
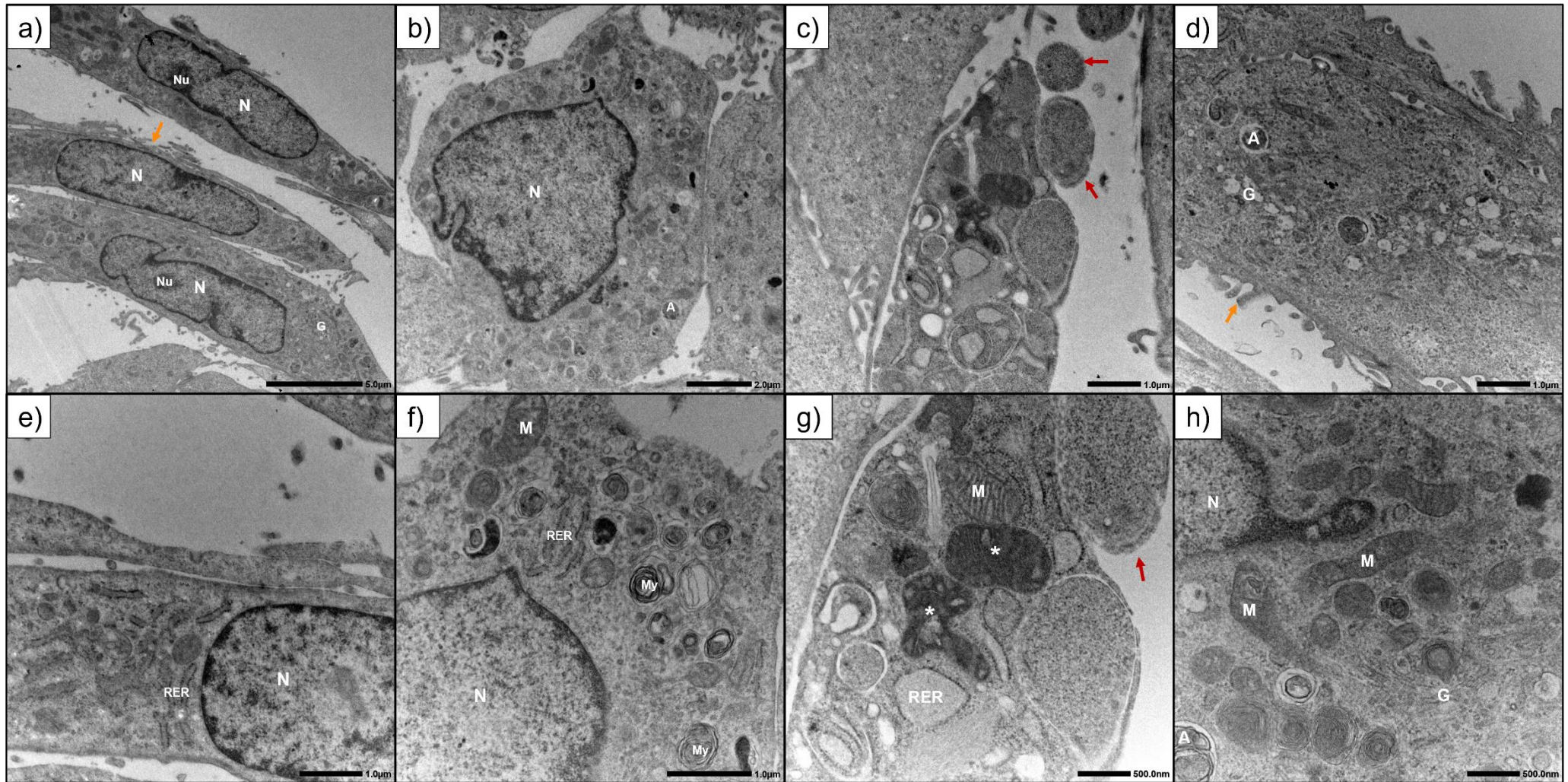
Figure 5.10 Electron micrographs of L6 myoblasts exposed to 0.1 µM lasalocid for 48 h. The orange and red arrows indicate membrane protrusions and apoptotic bodies, respectively. Condensed mitochondria are indicated with white asterisks. A-autophagic vesicles, G-Golgi apparatus, N-nucleus, M-mitochondria, My-myelin figures and RER-rough endoplasmic reticulum. Scale bars are indicated at the bottom right.

5.3.2 The Surface Ultrastructural Changes of H9c2 and L6 Myoblasts after Exposure to Monensin, Salinomycin and Lasalocid

The Surface Ultrastructure of H9c2 Myoblasts

Analysis of the surface morphology of H9c2 myoblasts in both the negative and solvent controls revealed large, flat cells covering the slides (**Figure 5.11** and **Figure 5.12**). The nuclei of the myoblasts could be seen lying beneath the plasma membranes, represented by round-to-oval shaped areas (**blue arrowheads**). Various bumps, likely owing to the presence of cellular organelles, were scattered around the nuclei and throughout the myoblasts. A few small finger-like protrusions were projecting from the surface of the cell surface (**orange arrows**). Some myoblasts were rounder or had a more defined three-dimensional shape, rather than growing flat against the surface of the slide (**Figure 5.11 e & f** and **Figure 5.12 d-f**). The plasma membranes of these myoblasts contained various ridges and protrusions, being less smooth compared to flatter myoblasts. Notably, drying artefacts, in the form of cracks, were visible on the myoblasts' surface. These artefacts were present in both cell lines as well as in both the control and treated samples.

After exposure to 0.1 µM monensin for 48 h the majority of the myoblasts had indentations distributed throughout, giving them a lunar surface or pockmarked appearance (**Figure 5.13 a-c**). The indentations were up to a few micrometres wide and clearly defined. Additionally, the number of round myoblasts increased compared to that of the control. A couple of these myoblasts appeared smooth lacking surface protrusions, but with some openings visible (**green arrow**). Others were apoptotic with a collection of apoptotic bodies projecting outwards (**red arrow**). Finally, there were several necrotic myoblasts with cell debris attached to the slide (**Figure 5.13 f**).

Salinomycin exposure had less of an effect on the H9c2 myoblasts compared to monensin, with fewer myoblasts displaying a pockmarked appearance (**Figure 5.14**). However, indentations in affected myoblasts were distributed throughout the entire cell, except where the nucleus was located (**Figure 5.14 a-d**). A number of round myoblasts lacking surface detail were observed, with some showing openings

(**green arrow**). A few apoptotic myoblasts were present (**red arrow**), but not as many as after monensin exposure.

After exposure to lasalocid, the majority of the myoblasts resembled that of the controls (**Figure 5.15**). The position of the nucleus was clearly defined (**blue arrowheads**), while bumps, due to cellular organelles, were visible throughout the rest of the myoblast. Various protrusions could be seen originating from the myoblast surface (**orange arrows**), especially in rounded myoblasts. A limited number of myoblasts contained indentations close to the area around the nucleus (**pink arrow**).

The Surface Ultrastructure of L6 Myoblasts

The L6 myoblasts were commonly elongated and covered in surface protrusions (**Figure 5.16** and **Figure 5.17**). These protrusions were either small, finger-like or bulkier bleb-like structures (**orange arrows**). Additionally, the controls had many rounded myoblasts with a three-dimensional conformation featuring various membrane structures such as small protrusions and frills. As with the H9c2 myoblasts, drying artefacts were seen in the controls as well as in myoblasts exposed to the different ionophores.

Monensin exposure resulted in a large number of both pockmarked and rounded myoblasts (**Figure 5.18**). The pockmarked myoblasts had large, well-defined indentations clearly visible throughout the entire cell, except for at the location of the nucleus (**Figure 5.18 a-d**). The overall number of protrusions were less compared to the control myoblasts. Rounded myoblasts were either smooth, appearing to have lost their surface structures, but containing openings in their membranes (**green arrows**), or were apoptotic (**red arrows**). Some necrotic myoblasts were observed, with cellular debris clinging to the surface of the slide (**Figure 5.18 f**). In these, the remanent structures of vesicles responsible for the surface indentations were visible.

After salinomycin exposure, less myoblasts had visible indentations, however these indentations were still clearly defined (**Figure 5.19**). There were a number of smooth, rounded myoblasts lacking surface structures, distributed in between the other myoblasts. Furthermore, a few apoptotic myoblasts were present (**red arrow**). However, many of the myoblasts remained unaffected, being elongated or rounded with small surface protrusions (**orange arrows**).

Finally, lasalocid exposure resulted in the least change to the surface of the myoblasts, with the majority of the myoblasts resembling that of the control (**Figure 5.20**). The myoblasts were either elongated or rounded and contained many surface projections (**orange arrows**). Very few myoblasts had any indentations, and they were not as well defined as after monensin and salinomycin exposure (**pink arrow**). Individual apoptotic myoblasts were observed (**red arrow**).
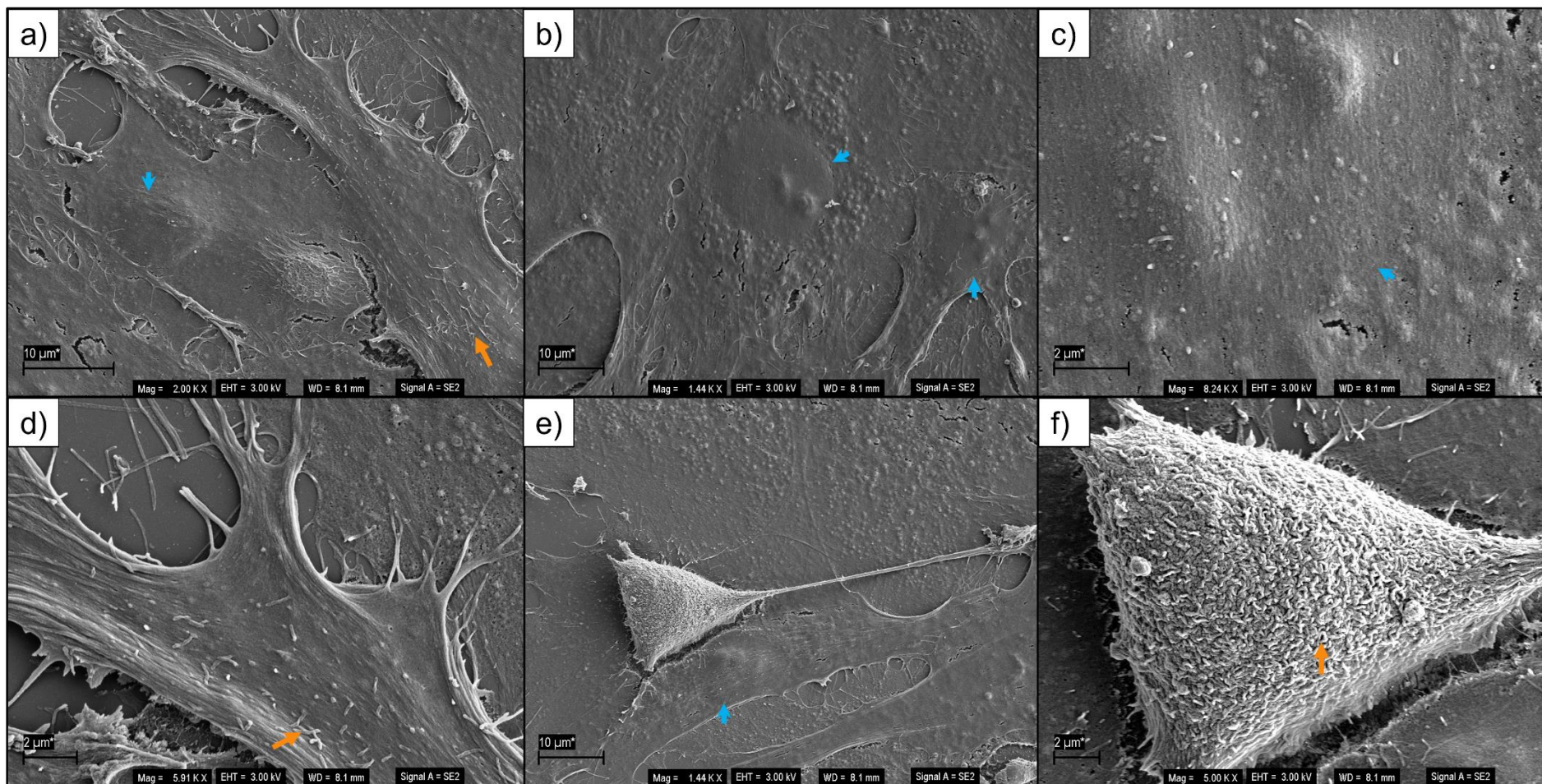
Figure 5.11 Scanning electron micrographs of H9c2 myoblasts incubated in complete DMEM for 48 h. The blue arrowheads and orange arrows indicate the position of the nuclei and membrane protrusions, respectively. Scale bars are indicated at the bottom left.
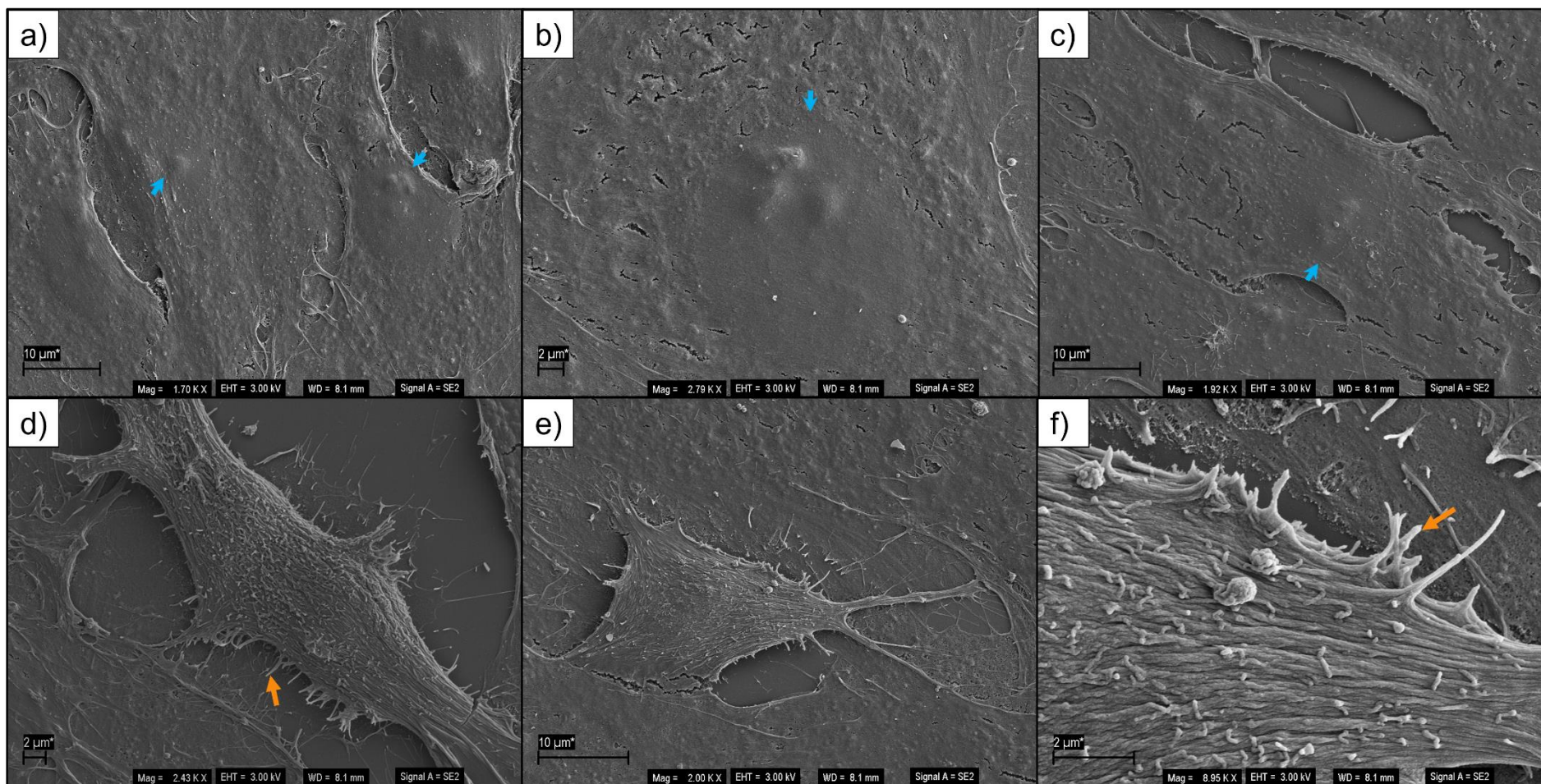
Figure 5.12 Scanning electron micrographs of H9c2 myoblasts incubated in the solvent control (0.1% MeOH) for 48 h. The blue arrowheads and orange arrows indicate the position of the nuclei and membrane protrusions, respectively. Scale bars are indicated at the bottom left.
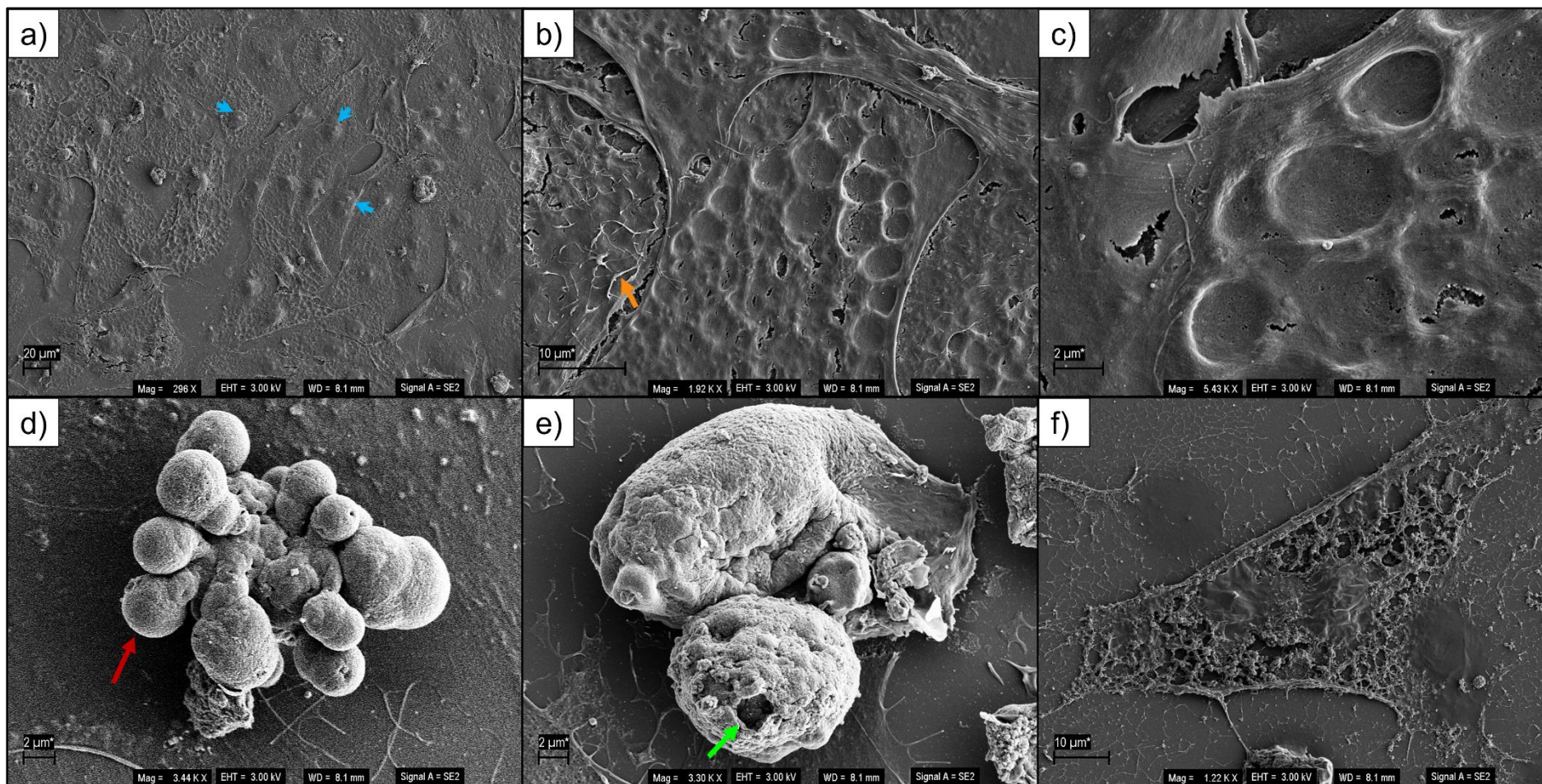
Figure 5.13 Scanning electron micrographs of H9c2 myoblasts exposed to 0.1 µM monensin for 48 h. The blue arrowheads and orange arrow indicate the position of the nuclei and membrane protrusions, respectively. A myoblast undergoing apoptosis is indicated by the red arrow and an opening within a rounded myoblast is indicated by the green arrow. Scale bars are indicated at the bottom left.
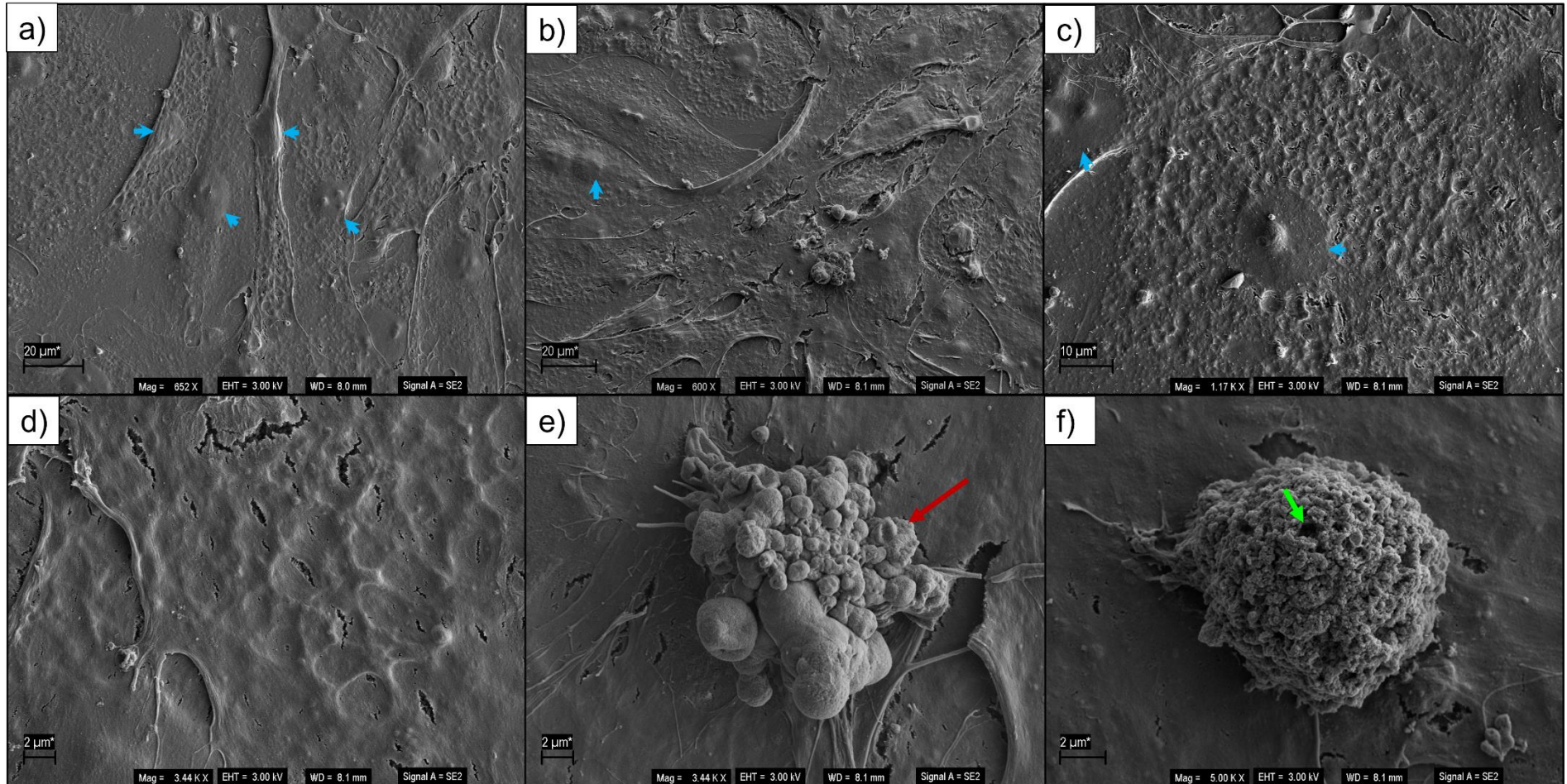
Figure 5.14 Scanning electron micrographs of H9c2 myoblasts exposed to 0.1 μM salinomycin for 48 h. The blue arrowheads indicate the position of the nuclei. A myoblast undergoing apoptosis is indicated by the red arrow and an opening within a rounded myoblast is indicated by the green arrow. Scale bars are indicated at the bottom left.
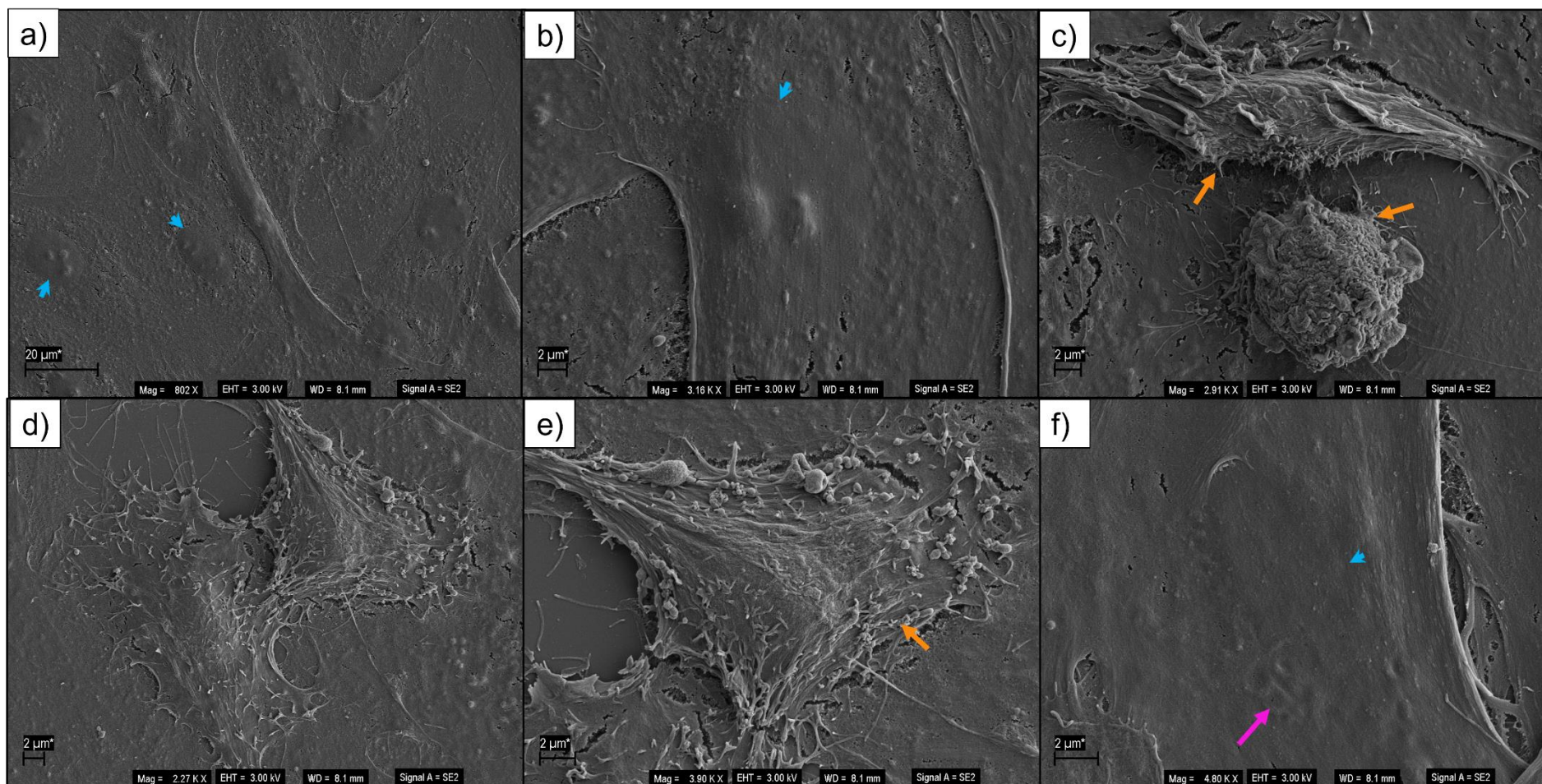
Figure 5.15 Scanning electron micrographs of H9c2 myoblasts exposed to 0.1 µM lasalocid for 48 h. The blue arrowheads and orange arrows indicate the position of the nuclei and membrane protrusions, respectively. The pink arrow indicates shallow indentations. Scale bars are indicated at the bottom left.
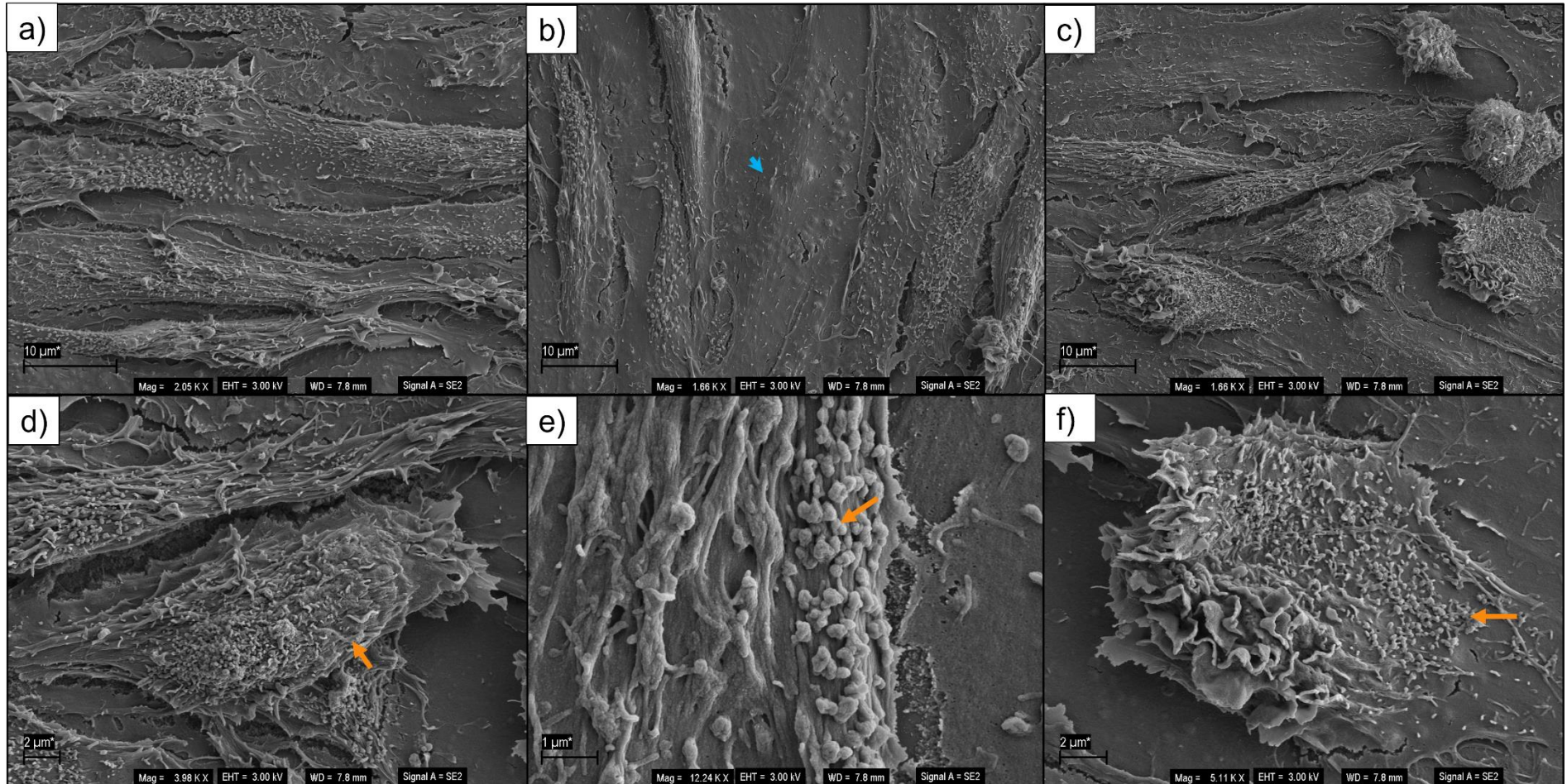
Figure 5.16 Scanning electron micrographs of L6 myoblasts incubated in complete DMEM medium for 48 h. The blue arrowhead and orange arrows indicate the position of a nucleus and membrane protrusions, respectively. Scale bars are indicated at the bottom left.
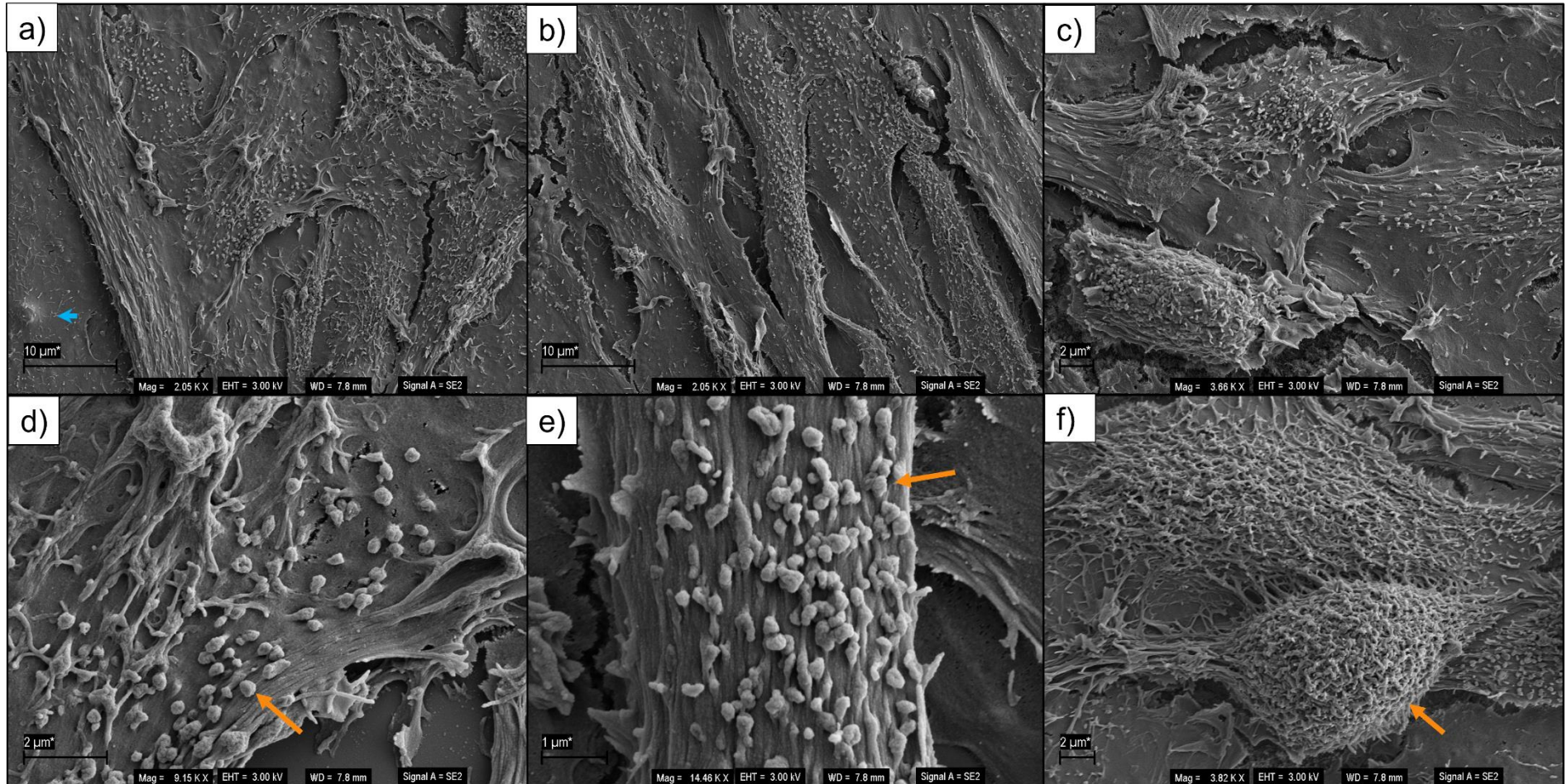
Figure 5.17 Scanning electron micrographs of L6 myoblasts incubated in the solvent control (0.1% MeOH) for 48 h. The blue arrowhead and orange arrows indicate the position of a nucleus and membrane protrusions, respectively. Scale bars are indicated at the bottom left.
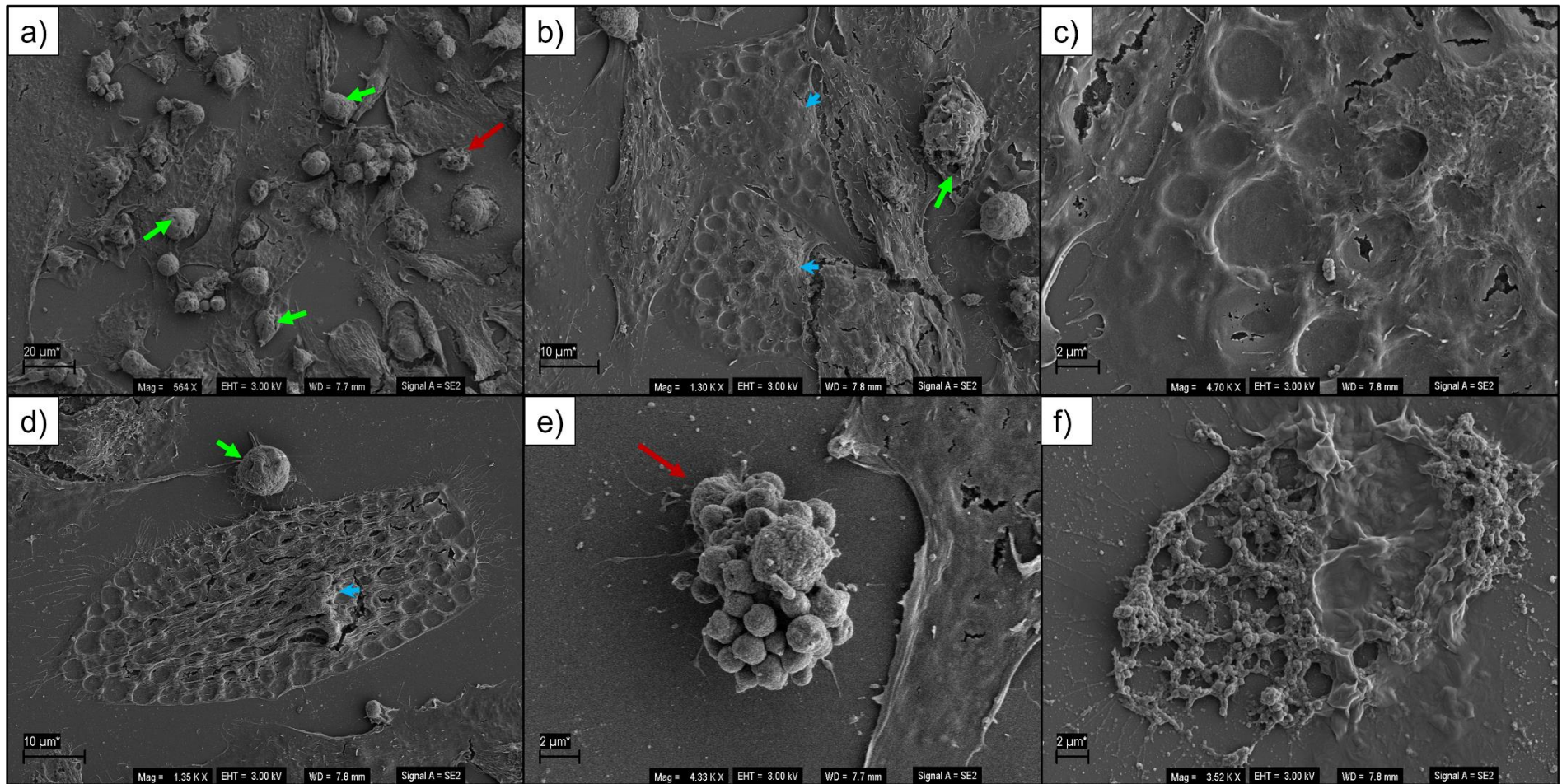
Figure 5.18 Scanning electron micrographs of L6 myoblasts exposed to 0.1 µM monensin for 48 h. The blue arrowheads indicate the position of the nuclei. Myoblasts undergoing apoptosis are indicated with red arrows and openings within rounded myoblasts are indicated by the green arrows. Scale bars are indicated at the bottom left.
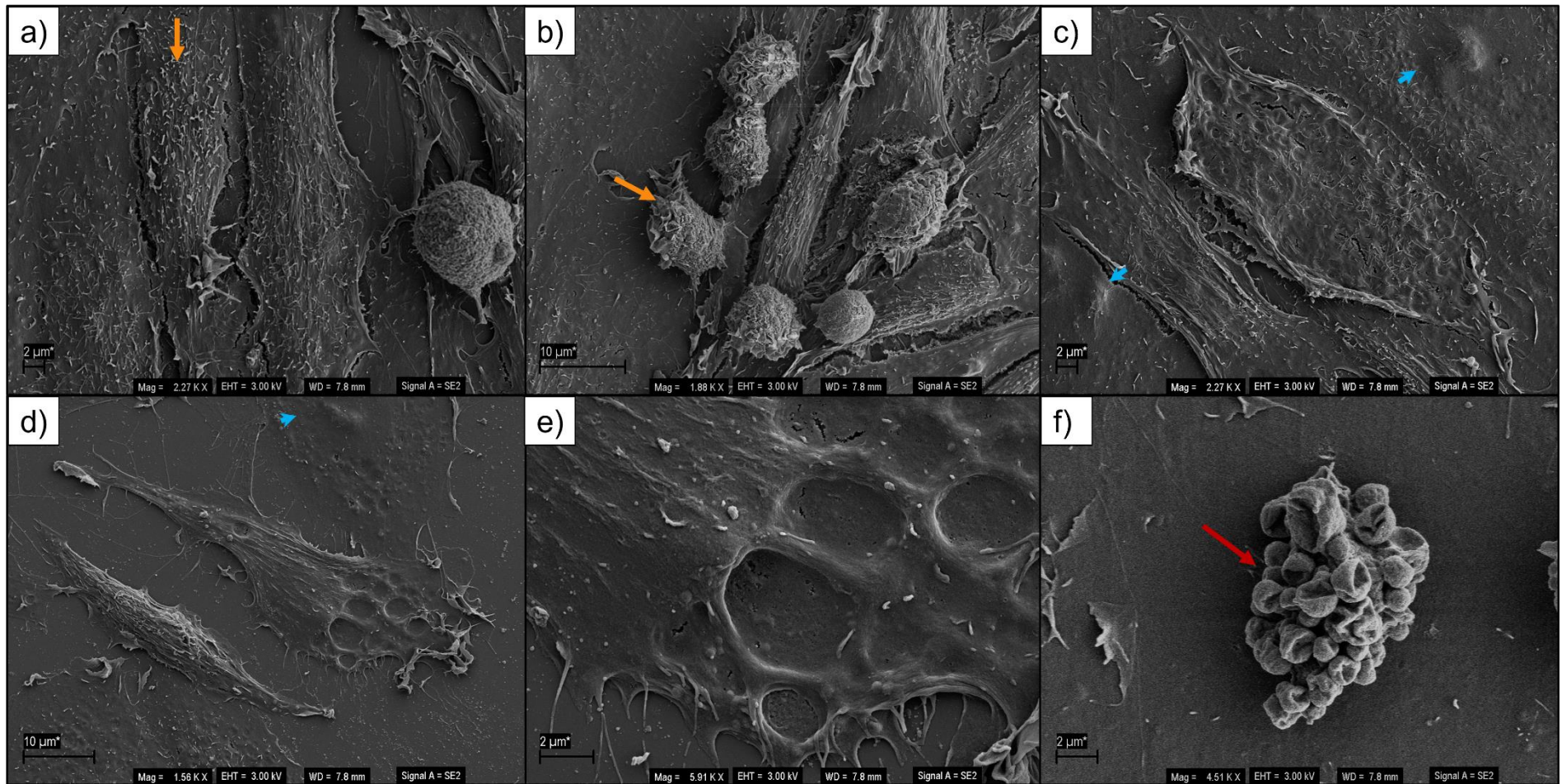
Figure 5.19 Scanning electron micrographs of L6 myoblasts exposed to 0.1 µM salinomycin for 48 h. The blue arrowheads and orange arrows indicate the position of the nuclei and membrane protrusions, respectively. A myoblast undergoing apoptosis is indicated with the red arrow. Scale bars are indicated at the bottom left.
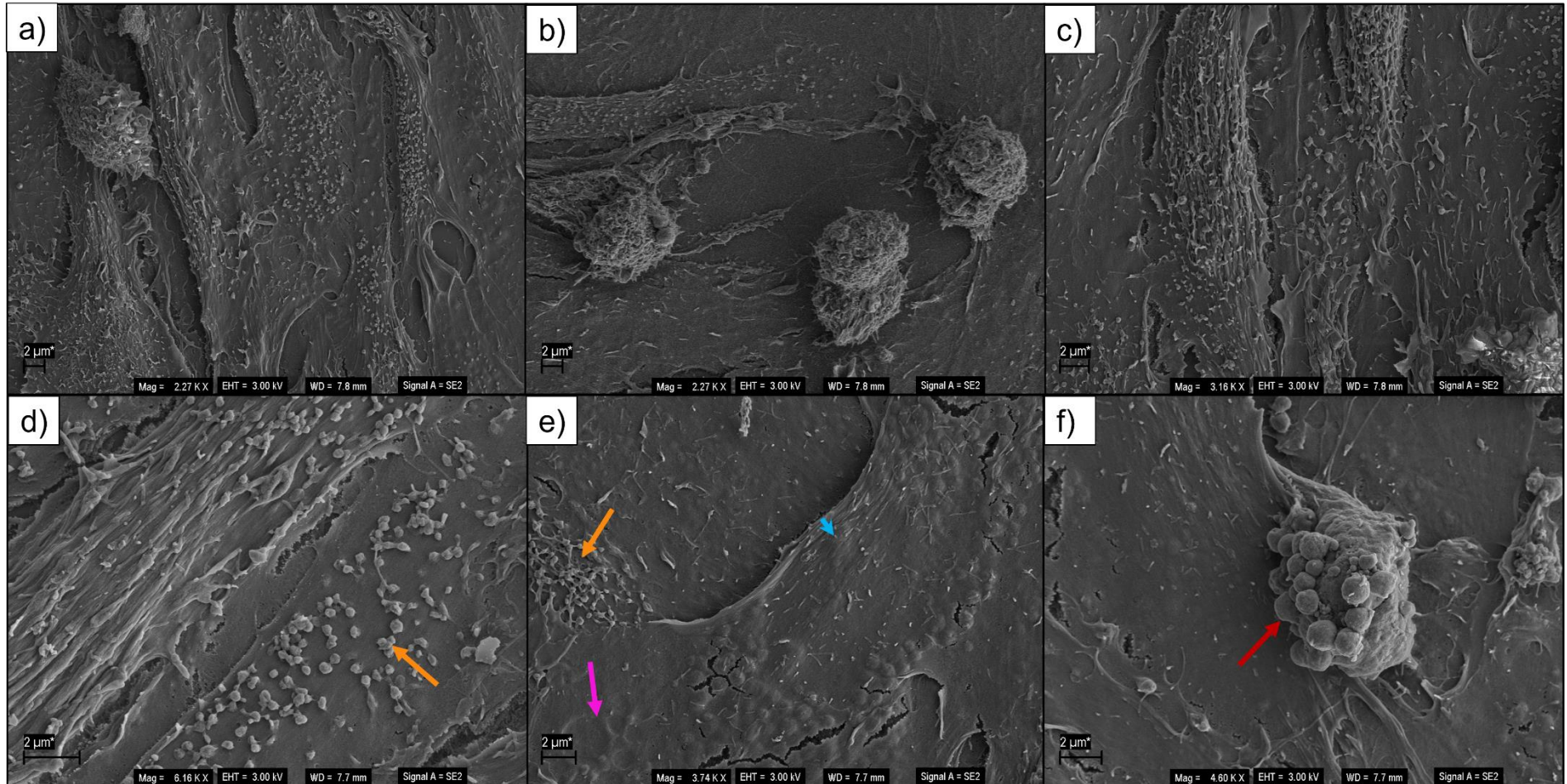
Figure 5.20 Scanning electron micrographs of L6 myoblasts exposed to 0.1 μM lasalocid for 48 h. The blue arrowhead and orange arrows indicate the position of a nucleus and membrane protrusions, respectively. The pink arrow indicates shallow indentations. A myoblasts undergoing apoptosis is indicated with the red arrow. Scale bars are indicated at the bottom left.

5.3.3 Immunogold Labelling of β-Tubulin in L6 Myoblasts

Protein Extraction and Western Blot

To support the immunogold-labelling results, a western blot was performed to confirm that the primary anti-β-tubulin antibody binds to β-tubulin in L6, C2C12 and H9c2 myoblasts. The Bradford protein assay was used to determine the total protein concentration in the cell lysates. A linear standard curve was generated using known BSA concentrations (**Figure 5.21**).
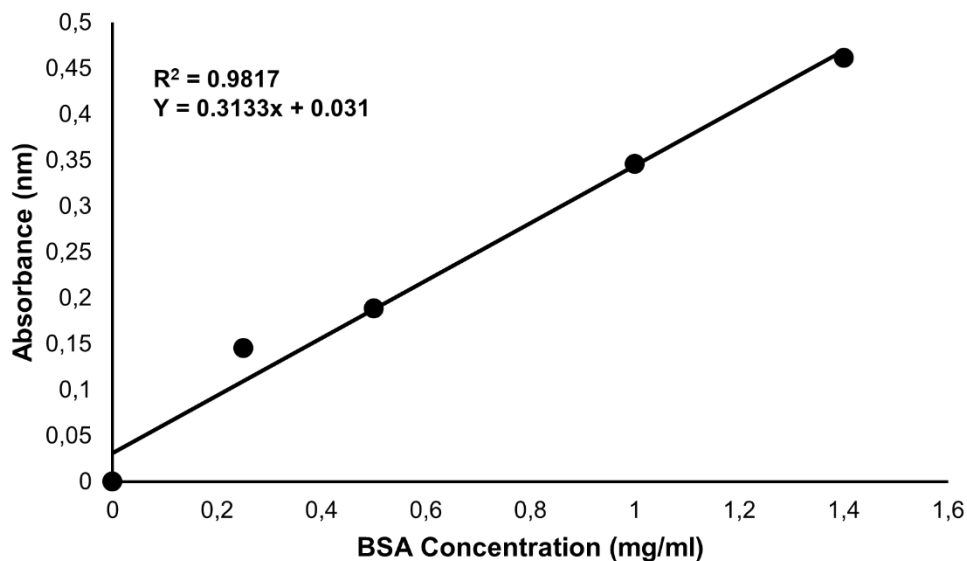
Figure 5.21 The Bradford standard curve with the absorbance at 595 nm for known BSA concentrations (mg/ml). The standard curve was used to calculate the protein concentrations of the lysates using the linear equation generated.

The absorbance values generated for the cell lysates were inserted in the equation in **Figure 5.21**, reflecting the linear relationship for the BSA concentration range tested, to determine the protein concentrations (**Table 5.2**). As the lysates were diluted 1:10 in PBS to prevent the extraction buffer from interfering with the Bradford reagent, the calculated concentrations were multiplied with 10.

143

Table 5.2 The protein concentrations (mg/ml) of the myoblast lysates calculated using the equation generated from the Bradford assay standard curve.

Description	Average Absorbance	Dilution Factor	Total Protein Concentration (mg/ml)
L6 Myoblast Lysate	0.121	10	2.86
C2C12 Myoblast Lysate	0.062	10	0.98
H9c2 Myoblast Lysate	0.152	10	3.87

After determining that the protein concentrations of the lysates were sufficient, an SDS-PAGE gel and subsequent Western Blot were performed (**Figure 5.22**). Two gels were run in parallel. The first gel was stained with GelCode Blue Stain Reagent to visualise the protein bands on the gel (**Figure 5.22**, **Left**). The protein bands separated according to size, with a similar band pattern appearing for all three cell lines. The proteins were transferred over to the nitrocellulose membrane during the western blot and stained with the primary anti-β-tubulin antibody and a secondary goat anti-rabbit IgG H&L (HRP) antibody. All three lanes developed a dark band close to the 50 kDa molecular weight marker almost immediately after exposing the double-labelled membrane to the developing solution (**Figure 5.22**, **Right**). Thus, the primary antibody can be used to bind to β-tubulin in all three cell lines with very little non-specific binding to other proteins within the myoblasts.
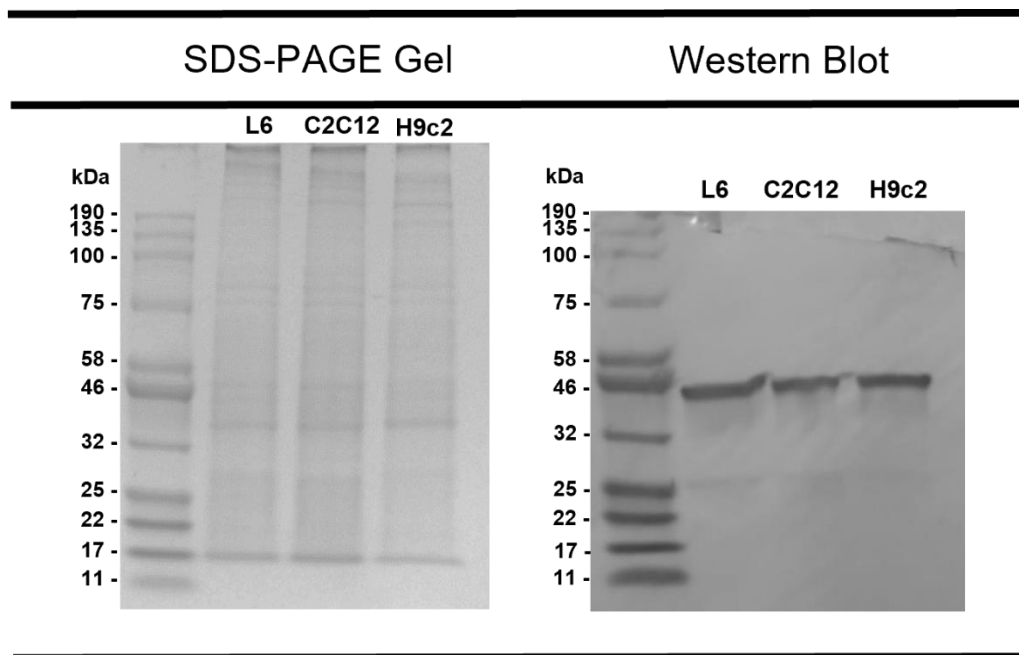
Figure 5.22 An SDS-PAGE gel and western blot of the proteins in the myoblast lysate. The lysate extracted from L6, C2C12 and H9c2 myoblasts was first run on an SDS-PAGE gel (left) then transferred over to a nitrocellulose membrane and labelled for β-tubulin (right). The protein ladder sizes are indicated on the left.

Immunogold Labelling of L6 Myoblasts for β-Tubulin

To determine the distribution of β-tubulin in L6 myoblasts, immunogold-labelling in combination with electron microscopy was used. As the samples were fixed and embedded using a method to preserve the epitopes for antibody binding, the ultrastructural detail and contrast were compromised. The cellular membranes lacked definition and contrast; however, the RER and nuclei could be identified.

When incubated with only the secondary antibody the myoblasts had very few to no markers visible within the myoblasts themselves or in the surrounding areas (**Figure 5.23**). Interference by non-specific immunogold labelling by the secondary antibody could thus be ruled out or considered minimal. The negative and solvent controls had a consistent distribution of β-tubulin throughout the myoblast's cytoplasm. However, there was no clear difference observed in terms of the distribution of β-tubulin between the controls (**Figure 5.23**) and myoblasts exposed to the ionophores (**Figure 5.24**). The immunogold markers did not concentrate around the nuclei of the myoblasts exposed to the ionophores and were found in between the RER, but seldom within. Both the controls (as a result of the fixation method) and the

myoblasts exposed to the ionophores had electron-lucent vesicles present within the cytoplasm, with the latter having more. Almost no immunogold particles were found in these electron-lucent vesicles. Notably, β-tubulin was located within the nuclei of all myoblasts, though less abundant when compared to the cytoplasm.
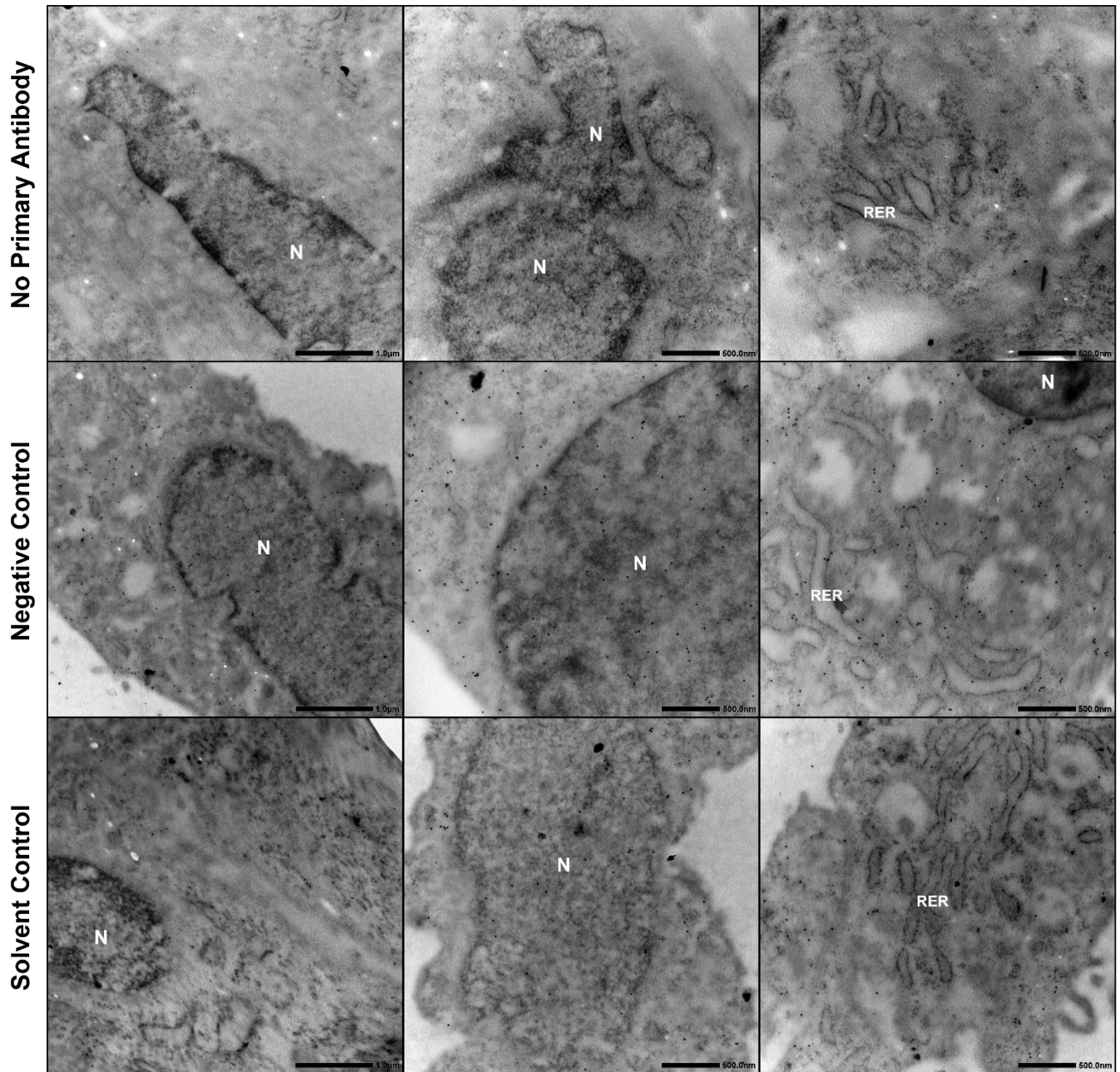
Figure 5.23 Immunogold labelling of β-tubulin in L6 myoblasts incubated with no primary antibody, cultured in complete DMEM medium (negative control) and in DMEM medium containing 0.1% MeOH (solvent control). N-nucleus and RER-rough endoplasmic reticulum. Scale bars are indicated at the bottom right.
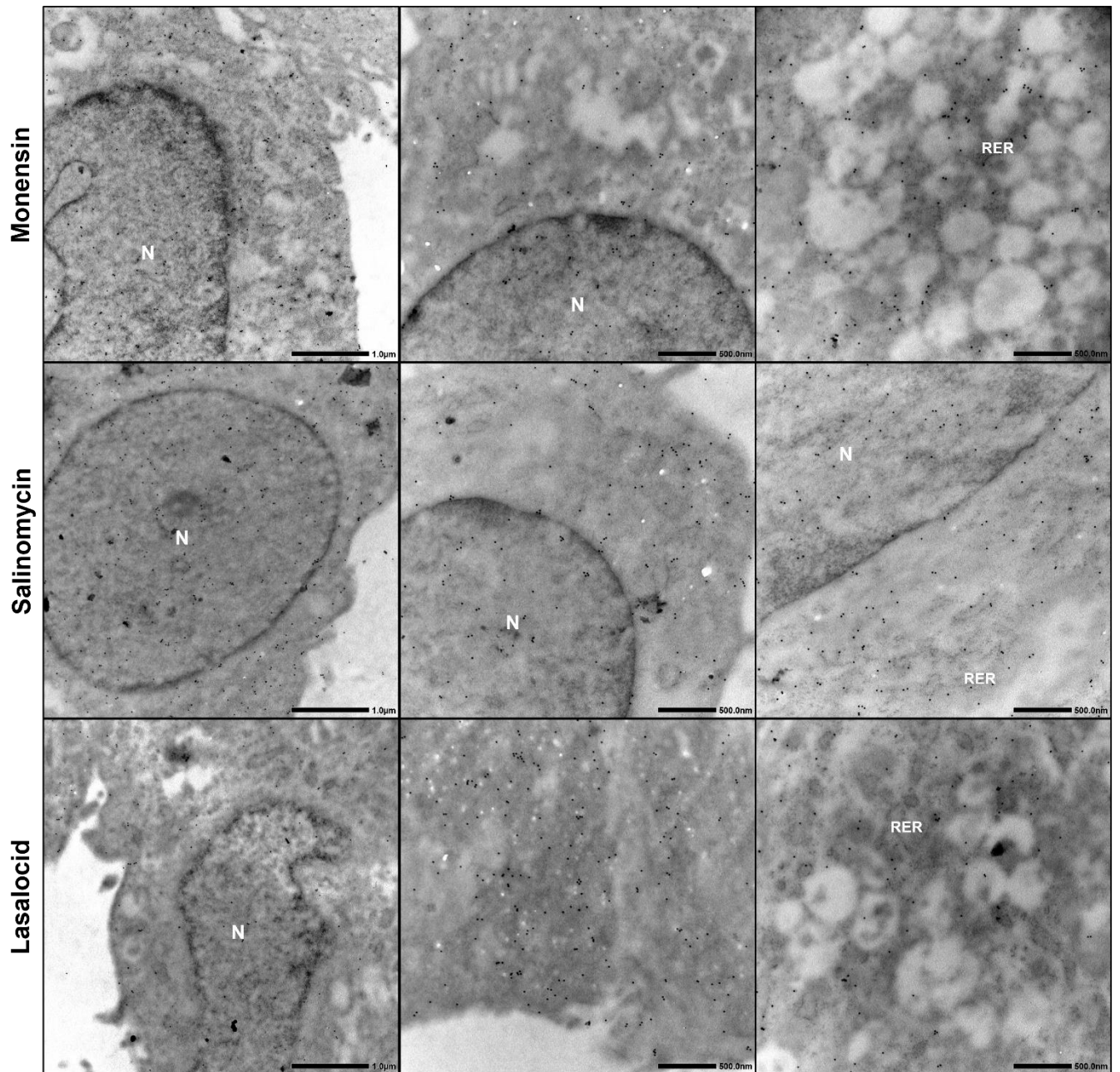
Figure 5.24 Immunogold labelling of β-tubulin in L6 myoblasts exposed to 0.1 μM monensin, salinomycin and lasalocid for 48 h. N-nucleus and RER-rough endoplasmic reticulum. Scale bars are indicated at the bottom right.

5.4 Discussion

Ionophore exposure induced ultrastructural changes in both the H9c2 and L6 myoblasts. With TEM, the most prominent findings were the swollen Golgi apparatus and an increased number of electron-lucent vesicles present within the myoblasts. After exposure to monensin, these vesicles entirely filled the cytoplasm of some myoblasts, with other organelles distributed in between. The vesiculated appearance of the myoblasts were similar to that seen with the light microscope in **Figure 3.10**. Comparable changes within the Golgi apparatus, specifically at the trans-face of the Golgi, were observed following exposure of cells and tissue sections to ionophores (Mollenhauer et al., 1990; Paddock and Albrecht-Buehler, 1986). This was verified in **Figure 5.5** (**a & b**) where the cis-face of the Golgi apparatus remained flat while larger vesicles could be seen accumulating at the trans-face. Ionophore exposure results in the concentration of osmotically active ions within the cisternae of the Golgi apparatus in exchange for H^+, leading to an influx of water and subsequent swelling (Boss et al., 1984; Mollenhauer et al., 1990). The disrupted osmotic balance as well as the inhibition of cellular transport at the trans-face of the Golgi apparatus contributed to the accumulation of vesicles within the cytoplasm (Mollenhauer et al., 1990). Furthermore, scanning electron micrographs of myoblasts exposed to the ionophores, especially to monensin, revealed the surface of the myoblasts covered with indentations. These indentations presumably also correspond to the vesicles generated within the cytoplasm and were distributed throughout the affected myoblasts.

In addition to the effect on the Golgi apparatus, monensin exposure resulted in mitochondrial condensation in both the H9c2 and L6 myoblasts. Furthermore, a number of mitochondria were likewise condensed after exposure to salinomycin and lasalocid, though to a lesser degree compared to monensin. As with the swelling of Golgi apparatus, mitochondrial condensation is frequently demonstrated after *in vitro* exposure to ionophores (Mollenhauer et al., 1990; Paddock and Albrecht-Buehler, 1986). The skeletal and cardiac muscles of livestock suffering from ionophore toxicosis have swollen mitochondria distributed throughout the myofibers (Confer et al., 1983; Mollenhauer et al., 1981; Van Vleet and Ferrans, 1984a, b). Of note however, is the elongated, condensed mitochondria seen in L6 myoblasts exposed to monensin (**Figure 5.8 e**). Although not universally present in all monensin treated

myoblasts, some myoblasts had mitochondria elongated up to 4 µm. Abnormal mitochondria elongation can occur as a result of ionic stress. In the freshwater alga, *Micrasterias denticulate*, ionic stress induced mitochondrial elongation and fusion (Steiner et al., 2018). The authors hypothesised that the elongation of the mitochondria could assist with the maintenance of mitochondrial processes such as respiration, as elongation increases the matrix volume and may prevent stress-induced rupture of the mitochondrial outer membrane. Since ionophores disturb mitochondrial ion homeostasis and membrane potential, the mitochondria could conceivably elongate to maintain their oxidative phosphorylation capacity.

The nuclei of the myoblasts were affected with chromatin marginalisation and condensation was observed (**Figure 5.3, Figure 5.8** and **Figure 5.9**, **red asterisks**). This is usually indicative of apoptosis, as discussed below. Furthermore, some of the nuclei appeared lobulated. Nuclear lobulation is dependent on various factors including the cytoskeletal network, specifically microtubules and microtubule motor proteins that create tension in the nuclear envelope promoting distortions (Biedzinski et al., 2020; Olins and Olins, 2004). During the early stages of apoptosis, cytoplasmic condensation is followed by nuclear lobulation before the cell eventually fragments into various apoptotic bodies (Burattini and Falcieri, 2013; Krajčí et al., 2000). However, slight nuclear lobulation, when viewed under TEM, does not necessarily indicate an aberration in nuclear morphology as the TEM sections viewed is only a very thin section of the entire sample.

Autophagy is a process by which cells recycle nutrients and assists with energy homeostasis. Although autophagic vesicles were present in the controls, there were slightly more autophagic vesicles after the myoblasts were exposed to the ionophores. Autophagy have been reported to play a cytoprotective role after ionophore exposure, with its inhibition resulting in enhanced apoptosis (Kim et al., 2017a; Kim et al., 2017b; Kim et al., 2016). Additionally, ionophores could affect autophagy either by increasing the number of autophagic vesicles or lowering their degradation ability as a result of shifting lysosomal pH (Grinde, 1983; Mahtal et al., 2020; Mollenhauer et al., 1990).

After ionophore exposure, several of the myoblasts, especially the L6 myoblasts, were undergoing apoptosis with clear chromatin condensation and apoptotic body

formation as viewed using TEM (**Figure 5.8** to **Figure 5.10**). Scanning electron micrographs also revealed apoptotic myoblasts in both the H9c2 and L6 cell lines (**Figure 5.13**, **Figure 5.14** and **Figure 5.18** to **Figure 5.20**), with monensin exposure resulting in more apoptotic myoblasts compared to both salinomycin and lasalocid exposure. Additionally, many rounded myoblasts lacking surface structures were observed, which could be an indication of early apoptosis (Burattini and Falcieri, 2013). Toxic ionophore concentrations can cause Ca^{2+} overload, increased production of ROS and disrupt the mitochondrial membrane potential (Boehmerle and Endres, 2011; Novilla, 2018; Przygodzki et al., 2005), which can lead to apoptosis. In fact, ionophores induce apoptosis in various cancer cell lines, which was attributed to oxidative stress and disrupted mitochondrial membrane potential (Ketola et al., 2010; Kim et al., 2017a; Kim et al., 2016). In cell cultures, apoptotic bodies cannot be disposed of by phagocytic cells and are left to undergo secondary necrosis; leaving behind cellular debris as noted after exposure of L6 myoblasts to monensin (not shown). In contrast to apoptosis, necrotic cells feature swollen organelles and a disrupted plasma membrane (Kroemer et al., 2009). Although a majority of the myoblasts exhibited swollen Golgi apparatus and a collection of electron-lucent vesicles, the other organelles such as the nuclei, RER and mitochondria were not swollen, and the plasma membranes remained intact. However, some necrotic H9c2 and L6 myoblasts were observed after monensin exposure (**Figure 5.3 d**). Additionally, more necrotic myoblasts and cellular debris were identified using the SEM in both the cell lines (**Figure 5.13** and **Figure 5.18**). It is possible that necrotic myoblasts were lost during the washing steps of TEM preparation, thus resulting in them being underrepresented in the TEM sections and more readily viewed using SEM. Various factors such as excess Ca^{2+}, lipid peroxidation and a lack of cellular energy can drive a cell towards favouring necrosis. Additionally, cells can exhibit a combination of apoptotic and necrotic features (Nicotera and Melino, 2004).

The slight disparity between ultrastructural changes *in vitro* and *in vivo* caused by ionophore exposure can be attributed to the systemic effect of ionophores on the whole organism. Ionophores are directly added to the cells or tissues *in vitro*, exposing them to much higher ionophore concentrations than what would be present within the extracellular fluid around tissues (Mollenhauer et al., 1990). After

ingestion, ionophores are transformed by the liver into metabolites that could potentially have additional properties and toxic effects. Moreover, damage to one organ can subsequently impact the function of another, as is the case with congestive heart failure (Decloedt et al., 2012). Finally, ionophores affect the release of humoral agents such as catecholamines which contribute to Ca^{2+} overload, which can affect the muscles (Shen and Patel, 1977).

The distribution of β-tubulin, as demonstrated by immunogold labelling, did not differ between the control myoblasts and myoblasts exposed to the ionophores. The increased number of vesicles within the cytoplasm, resulting from ionophore exposure, lacked any gold particles, indicating that no β-tubulin was present in the vesicles. This corroborates the presence of 'gaps' observed within the microtubule network using immunofluorescence (**Chapter 4**). Without the additional osmium fixation step, both the contrast and ultrastructural preservation of the samples were affected since osmium binds to and stabilise lipids. The nuclei, however, could be easily distinguished and contained immunogold labelled β-tubulin, though less compared to the cytoplasm. It has been reported that the β_{II}-tubulin isotype occurs in the nuclei of transformed cells (Walss-Bass et al., 2002). The primary antibody used in this study to detect β-tubulin is a β-tubulin loading control and have previously been used with L6 myoblasts (Abcam). The western blot has also confirmed that the antibody binds to β-tubulin in both H9c2 and C2C12 myoblasts (**Figure 5.22**) and can be used in future studies.

In conclusion, the ultrastructure of H9c2 and L6 myoblasts was affected following exposure to monensin, salinomycin and lasalocid. Using TEM, ionophore exposure primarily affects the Golgi apparatus and mitochondria of the myoblasts, and results in the accumulation of electron-lucent vesicles within the cytoplasm. Using SEM, these vesicles appear as indentations on the surface of affected myoblasts, resulting in the myoblasts having a pockmarked appearance. After ionophore exposure H9c2 and L6 myoblasts exhibit both necrotic and apoptotic features.

Chapter 6: General Discussion and Conclusion

6.1 Discussion

The overall aim of this project was to investigate the cytotoxic-, subcellular- and ultrastructural effects of selected carboxylic ionophore antibiotics, namely monensin, salinomycin and lasalocid, on cardiac and skeletal myoblasts *in vitro*.

Monensin was the most cytotoxic of the ionophores, having the greatest effect on cell viability, cell morphology and cell ultrastructure at the concentrations tested. Salinomycin resulted in similar alterations, but to a slightly lesser extent, while lasalocid exposure induced the least effects on the different myoblasts. The marked difference in toxicity of the ionophores could potentially be attributed to their transport kinetics as well as their binding affinities to selected cations and H^+ (Pressman, 1976). Additionally, myoblasts might be more tolerant to changes in certain cation concentrations compared to other cations. For instance, there are various organelles such as the mitochondria and RER that serve as buffers that protect the cell from increased intracellular Ca^{2+} concentrations (S Smaili et al., 2013).

Due to the different growth rates of the myoblasts, the initial seeding concentration of the cell lines for the experiments varied. Nevertheless, the rat L6 cell line appeared to be most affected following ionophore exposure, while the mouse C2C12 cell line was the least affected. Correspondingly, *in vivo* results suggest that rats are more susceptible to ionophore exposure compared to mice (see **Table 2.2**). Differences in susceptibility of animal species towards ionophores are influenced by a variety of toxicokinetic factors such as absorption, metabolism and excretion. Horses, for instance, are much more susceptible to ionophore toxicosis as they are unable to rapidly clear ionophores from the blood due to the limited oxidative efficiency of P450 demethylating enzyme compared to other species (Donoho, 1984; Nebbia et al., 2001).

The MTT viability assay used to determine the cytotoxic effect of the various ionophores on the myoblasts (**Chapter 3**), is based on mitochondrial function (Mosmann, 1983). Ionophores affect mitochondrial membrane potential and oxidative phosphorylation, through increased intracellular Ca^{2+} and the production of

ROS (Ketola et al., 2010; Kim et al., 2017a; Kim et al., 2017b; Przygodzki et al., 2005). In this project, both fluorescent imaging (**Figure 3.12**) and TEM (**Figures 5.8** - **5.10**) demonstrated that the ionophores affect the mitochondrial network, morphology and matrix density. Cellular energy deficiency, as a result of the disruption of mitochondrial oxidative phosphorylation, reduces the efficiency of ATPases and exacerbates the disruption of ion homeostasis. Moreover, the intermediate filament desmin binds directly to mitochondria and affect both their location and respiratory ability (Capetanaki, 2002; Dayal et al., 2020; Milner et al., 2000). Thus, ionophores could also perturb mitochondrial function considering their effect on desmin distribution (**Figure 4.24** and **Figure 4.25**).

Furthermore, exposing cardiac and skeletal myoblasts to ionophores *in vitro* resulted in the formation of vesicles within the cytoplasm as seen in **Figure 3.10** as well as in **Figures 5.3** to **5.5** and **Figures 5.8** to **5.10**. Additionally, the vesicles in the myoblasts caused a pockmarked appearance on their surfaces, as observed with SEM (**Figures 5.13** to **5.15** and **Figures 5.18** to **5.20**). These vesicles probably arises from the disruption of the osmotic balance as well as from the inhibition of intracellular trafficking at the Golgi apparatus (Mollenhauer et al., 1990). As the Golgi apparatus is usually located near the nuclei of the myoblasts (**Figure 5.1** to **5.10**), it could explain why the vesicles often first appeared around the perinuclear region of the myoblasts (**Figure 3.10**). Furthermore, these vesicles were visible within the cytoskeletal networks of the myoblasts (**Chapter 4**). Both the microtubule and desmin filaments demonstrated clear 'gaps' where these vesicles formed. The synemin network, and to a lesser extent the microfilament network, also displayed these 'gaps'. Besides, no immunogold labelling of β-tubulin was present in the vesicles (**Figure 5.24**), thus corroborating the gaps observed in the microtubular network.

The ionophores affected the cytoskeletal networks of both the cardiac and skeletal myoblasts (**Chapter 4**). The microtubule and microfilament networks of the H9c2 and L6 myoblasts were noticeably affected, while the microfilament network of the C2C12 myoblasts was less affected. In contrast, immunocytochemical studies and semiquantitative analysis showed that the desmin intermediate filament network of C2C12 myoblasts exposed to toxic concentrations of monensin and salinomycin aggregated around the perinuclear region (**Figure 4.24** and **Figure 4.25**). Increased

intracellular Ca^{2+} concentrations induced by ionophore exposure could trigger Ca^{2+} activated proteases which, in turn, targets and disrupts cytoskeletal proteins, for example desmin (Aweida et al., 2018; Elamrani et al., 1995). Similarly, to desmin aggregation, an increase in the concentration of β-tubulin around the nuclei of exposed myoblasts were observed in fluorescent imaging (see **ROI** of **Figures 4.5**; **4.6**; **4.8**; **4.14**; **4.17** and **4.18**, **green arrowheads**), however this could not be confirmed using immunogold labelling (**Figure 5.24**). This discrepancy could be due to TEM sections representing a very thin fraction of the entire sample, as well as the impaired preservation of cellular ultrastructure in the embedded myoblasts labelled with immunogold. Still the marked effect of toxic ionophore concentrations on the different cytoskeletal components could contribute to the disrupted contractile apparatus and muscle lesions reported in animals exposed to toxic ionophore doses (Confer et al., 1983; Van Vleet and Ferrans, 1984a, b). Additionally, the concentration of microtubules around the nuclei could potentially result in the lobulation of the nuclear envelope as depicted in **Figure 5.4**.

Ionophore exposure resulted in cell death either via apoptosis or necrosis as seen during ultrastructural analysis (**Chapter 5**). Apoptosis is usually characterised as an energy dependent process driven by the activation of caspases, that result in several distinct morphological features including shrinking cells, chromatin condensation and the formation of apoptotic bodies (Kerr et al., 1972). Both H9c2 and L6 myoblasts exposed to 0.1 μM of the ionophores for 48 h, exhibited these features as identified with TEM, as well as myoblasts with a damaged plasma membrane and a disrupted cytoplasm indicating the myoblasts were undergoing necrosis (**Figure 5.3**, **Figure 5.8** and **Figure 5.10**). Interestingly, necrosis is often associated with the swelling of intracellular organelles, however, other than the Golgi apparatus, most of the organelles remained unaffected. Investigating the surface of the myoblasts with SEM revealed both apoptotic (**Figure 5.13**, **Figure 5.14** and **Figure 5.18** to **Figure 5.20**, **red arrows**) and necrotic myoblasts (**Figure 5.13**, **f** and **Figure 5.18**, **f**) in H9c2 and L6 cell lines following ionophore exposure. More apoptotic myoblasts were present after monensin exposure when compared to either salinomycin or lasalocid exposure. Accordingly, the percentage myoblasts with DNA fragmentation, an early indicator of apoptosis, were the highest after monensin exposure as determined

using a TUNEL assay (**Figure 3.14**). The percentage myoblasts with DNA fragmentation also increased following exposure to higher ionophore concentrations.

6.2 Future Research and Recommendations

Future research possibilities into the effects of ionophores *in vitro* are discussed below. The project can be expanded into different directions depending on the area of focus (**Figure 6.1**).

One of the first focus areas might be to differentiate the various myoblast cell lines and then investigate the effects of the ionophores on the myotubes. Due to the ongoing problems experienced, as well as time and budget constraints, it was decided not to continue with further experiments involving the differentiated cell lines during this project. However, this could be an area of future research as differentiated myotubes resemble muscle more closely. A lower H9c2 passage number could assist with differentiating the cardiac myoblasts into myotubes. Additionally, investigations to increase attachment between the myotubes and the coverslip/well surface need to be performed. In this project, various methods to facilitate attachment were attempted including covering the coverslips in poly-L-lysine as well as using Permanox^{TM} plastic slides (Thermo Scientific), with minimal success (not shown). In the case where the successful, robust differentiation and attachment of the myotubes are achieved, an additional study could be to investigate whether ionophore exposure inhibits differentiation. A previous study has concluded that depolymerisation of cells reduced their differentiation ability (Blackiston et al., 2009).

This project focused on the effects of ionophores on selected cytoskeletal proteins, specifically microtubules, microfilaments, desmin and synemin. However, there are many cytoskeletal proteins and investigation focusing on αβ-crystallin, troponin and myosin etc, can further increase our understanding of the effects of ionophores on cytoskeletal elements. Western blots can be used to determine the effect of ionophore exposure on the quantity and degradation of cytoskeletal proteins. In this project it was confirmed that the primary anti-β-tubulin antibody will bind to β-tubulin of all three cell lines i.e., H9c2, L6 and C2C12 (**Figure 5.22**), and could thus be used for further experimentation. Additionally, the increased intracellular Ca^{2+} concentrations caused by ionophore exposure could activate various Ca^{2+}

proteases, such as calpain which can target the cytoskeleton for degradation. However, conflicting results have been reported (Boehmerle and Endres, 2011; Duncan et al., 1979). Therefore, whether and under what circumstances ionophore exposure will result in the activation of calpain should be investigated. It should also be evaluated if calpain is one of the major causes of the disruption and perinuclear aggregation of desmin in C2C12 myoblasts after monensin and salinomycin exposure.

One of the primary cellular targets of ionophore toxicosis is the mitochondria and the *in vitro* effects of the ionophores on mitochondria can be further explored. Confocal microscopy and tomography are tools that can be used to investigate mitochondria in more detail. Quantitative analysis can be carried out using a combination of confocal fluorescent images (either 2D or 3D) and the Mitochondrial Analyzer plugin for Fiji ImageJ. Additionally, tomography is a TEM technique that allows for the 3D modelling of cellular constructs from conventional TEM samples. As mitochondria form branched networks, tomography can be used to gain a better understanding of the effects of ionophores on these mitochondrial networks.

The method of cell death induced by ionophore exposure can be further analysed using techniques such as gene knockouts and flow cytometry. The results of the current studies suggest that myoblasts exhibit the morphological features of both apoptosis and necrosis. However, morphological examination alone is not sufficient to classify the method of cell death and need to be supported by biochemical and molecular techniques (Kroemer et al., 2009). It should be interesting to see whether the cell death pathway depends on the concentration and duration of the insult.

The last recommendation for future research is to determine the cytotoxic, subcellular and ultrastructural effects of ionophores on neuronal cell lines *in vitro*. Both salinomycin and lasalocid have previously been reported to have neurotoxic effects and cases of accidental ionophore intoxication have resulted in neurotoxic effects in both cats and dogs (Bosch et al., 2018; Pakozdy et al., 2010; Segev et al., 2004; Van der Linde-Sipman et al., 1999). The effect of ionophores on the cytoskeleton of neuronal cell lines can be investigated. In fact, lasalocid exposure resulted in decreased quantities of microtubules in frog sciatic nerves (Kanje et al., 1981).
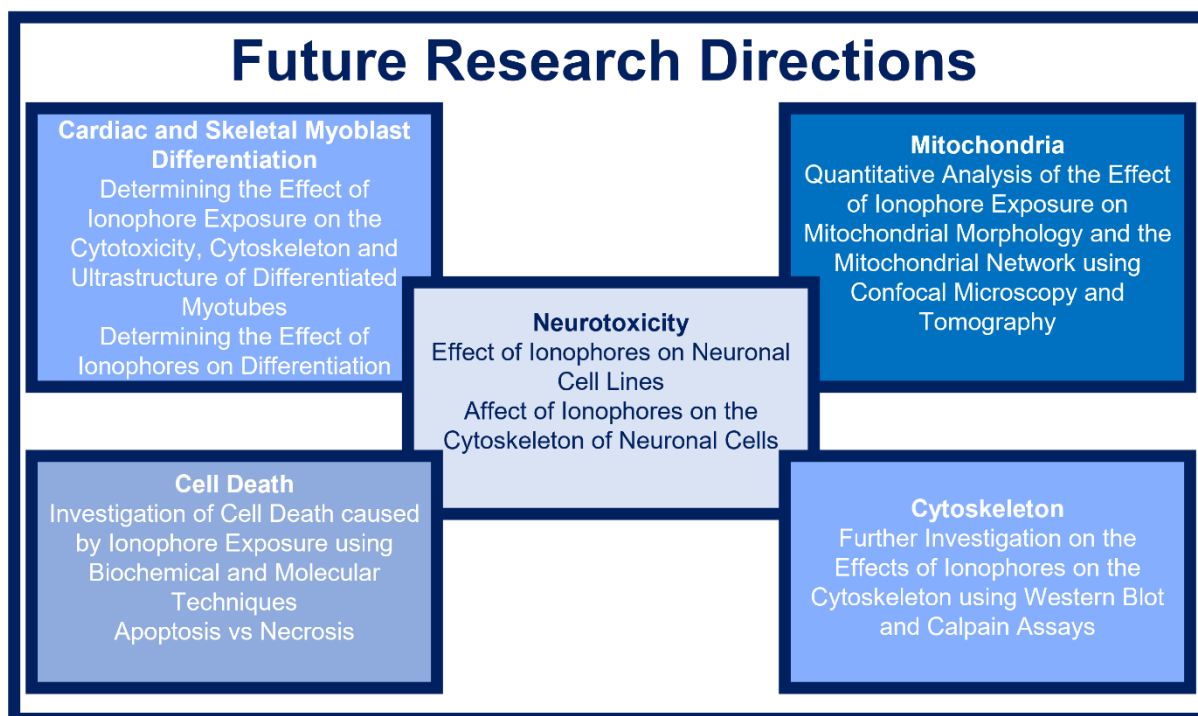
Figure 6.1 Possible future research areas regarding ionophores.

6.3 Conclusion

Of the three ionophores evaluated, monensin was the most cytotoxic *in* vitro. However, the effects of all three ionophores on the myoblasts were similar, although varying in degree and intensity. This indicates that the disruption of ion homeostasis is the primary cause of ionophore toxicity, rather than the direct effect of any one specific ionophore. The main cytoskeletal elements affected by ionophore exposure was the microtubules and desmin intermediate filaments. The microfilament network was also affected, but only in H9c2 and L6 myoblasts. Transmission electron microscopy indicated the mitochondria and Golgi apparatus as being the cellular organelles most affected by ionophore exposure. Most prominently featured following ionophore exposure is vesicles distributed throughout the cytoplasm of affected myoblasts. These vesicles were even detected in the various cytoskeletal networks, as well as on the surface of the myoblasts demonstrated with SEM. Finally, this project has the potential to be further expanded into various areas of research.

This *in vitro* study addressed the pathophysiological changes of lesions observed in cardiac and skeletal muscles of animals affected with ionophore toxicosis, by using

cardiac and skeletal myoblasts. The effect of monensin, salinomycin and lasalocid seen on certain filaments of the cytoskeletal network and ultrastructure of the myoblasts could potentially contribute to the explanation of the lesions observed during histopathological examination of cardiac and skeletal muscles of affected animals.

Chapter 7: References

Abafe, O.A., Gatyeni, P., Matika, L., 2020. A multi-class multi-residue method for the analysis of polyether ionophores, tetracyclines and sulfonamides in multi-matrices of animal and aquaculture fish tissues by ultra-high performance liquid chromatography tandem mass spectrometry. Food Additives and Contaminants: Part A 37, 438-450.

Abcam, Anti-beta Tubulin antibody - Loading Control (ab6046). https://www.abcam.com/beta-tubulin-antibody-loading-control-ab6046.html (accessed 27 July 2022).

Abdul Kadir, L., Stacey, M., Barrett-Jolley, R., 2018. Emerging roles of the membrane potential: action beyond the action potential. Frontiers in Physiology 9, 1661.

Adovelande, J., Schrével, J., 1996. Carboxylic ionophores in malaria chemotherapy: The effects of monensin and nigericin on *Plasmodium falciparum in vitro* and *Plasmodium vinckei petteri in vivo*. Life Sciences 59, 309-315.

Adrian, R., Chandler, W., Hodgkin, A.L., 1970. Slow changes in potassium permeability in skeletal muscle. The Journal of Physiology 208, 645-668.

Agnetti, G., Herrmann, H., Cohen, S., 2021. New roles for desmin in the maintenance of muscle homeostasis. The Federation of European Biochemical Societies Journal.

Aleman, M., Magdesian, K.G., Peterson, T.S., Galey, F.D., 2007. Salinomycin toxicosis in horses. Journal of the American Veterinary Medical Association 230, 1822-1826.

Alexander, B., Browse, D., Reading, S., Benjamin, I., 1999. A simple and accurate mathematical method for calculation of the EC50. Journal of Pharmacological and Toxicological Methods 41, 55-58.

Anderson, D.E., 2008. Ionophores: Salinomycin toxicity in camelids, In: Zoo and Wild Animal Medicine. Elsevier, pp. 50-54.

Ankarcrona, M., Dypbukt, J.M., Bonfoco, E., Zhivotovsky, B., Orrenius, S., Lipton, S.A., Nicotera, P., 1995. Glutamate-induced neuronal death: a succession of necrosis or apoptosis depending on mitochondrial function. Neuron 15, 961-973.

Antoszczak, M., Huczyński, A., 2019. Salinomycin and its derivatives–A new class of multiple-targeted "magic bullets". European Journal of Medicinal Chemistry 176, 208-227.

Aoi, W., Marunaka, Y., 2014. Importance of pH homeostasis in metabolic health and diseases: crucial role of membrane proton transport. BioMed Research International 2014, 598986.

Ashkenazi, A., Dixit, V.M., 1998. Death receptors: signaling and modulation. Science, 1305-1308.

Ashrafihelan, J., Eisapour, H., Erfani, A.M., Kalantary, A.A., Amoli, J.S., Mozafari, M., 2014. High mortality due to accidental salinomycin intoxication in sheep. Interdisciplinary Toxicology 7, 173-176.

Aslantürk, Ö.S., 2018. In vitro cytotoxicity and cell viability assays: principles, advantages, and disadvantages. Genotoxicity-A predictable risk to our actual world 2, 64-80.

Aweida, D., Rudesky, I., Volodin, A., Shimko, E., Cohen, S., 2018. GSK3-β promotes calpain-1–mediated desmin filament depolymerization and myofibril loss in atrophy. Journal of Cell Biology 217, 3698-3714.

Baehrecke, E.H., 2002. How death shapes life during development. Nature Reviews Molecular Cell Biology 3, 779-787.

Bagaméry, F., Varga, K., Kecsmár, K., Vincze, I., Szökő, É., Tábi, T., 2021. The Impact of Differentiation on Cytotoxicity and Insulin Sensitivity in Streptozotocin Treated SH-SY5Y Cells. Neurochemical Research 46, 1350-1358.

Bankhead, P., Loughrey, M.B., Fernández, J.A., Dombrowski, Y., McArt, D.G., Dunne, P.D., McQuaid, S., Gray, R.T., Murray, L.J., Coleman, H.G., James, J.A., Salto-Tellez, M., Hamilton, P.W., 2017. QuPath: Open source software for digital pathology image analysis. Scientific Reports 7, 16878.

Bastianello, S.S., McGregor, Heather L., Penrith, Mary-Louise, Fourie, N., 1996. A chronic cardiomyopathy in feedlot cattle attributed to toxic levels of salinomycin in the feed. Journal of the South African Veterinary Association 67, 38-41.

Berger, J., Rachlin, A., Scott, W., Sternbach, L., Goldberg, M., 1951. The isolation of three new crystalline antibiotics from streptomyces. Journal of the American Chemical Society 73, 5295-5298.

Berghe, T.V., Vanlangenakker, N., Parthoens, E., Deckers, W., Devos, M., Festjens, N., Guerin, C., Brunk, U., Declercq, W., Vandenabeele, P., 2010. Necroptosis, necrosis and secondary necrosis converge on similar cellular disintegration features. Cell Death and Differentiation 17, 922-930.

Bertini, S., Feirrero, S., Berny, P., 2003. A new improved high performance thin layer chromatography (HPTLC) method for the detection of ionophore antibiotics in feeds and animal tissues. Journal of Liquid Chromatography and Related Technologies 26, 147-156.

Biedzinski, S., Agsu, G., Vianay, B., Delord, M., Blanchoin, L., Larghero, J., Faivre, L., Théry, M., Brunet, S., 2020. Microtubules control nuclear shape and gene expression during early stages of hematopoietic differentiation. The European Molecular Biology Organization Journal 39, e103957.

Binarová, P., Tuszynski, J., 2019. Tubulin: structure, functions and roles in disease. Cell 8, 1294.

Blackiston, D.J., McLaughlin, K.A., Levin, M., 2009. Bioelectric controls of cell proliferation: ion channels, membrane voltage and the cell cycle. Cell Cycle 8, 3527-3536.

Boehmerle, W., Endres, M., 2011. Salinomycin induces calpain and cytochrome c-mediated neuronal cell death. Cell Death and Disease 2, 168.

Bonfoco, E., Krainc, D., Ankarcrona, M., Nicotera, P., Lipton, S.A., 1995. Apoptosis and necrosis: two distinct events induced, respectively, by mild and intense insults with N-methyl-D-aspartate or nitric oxide/superoxide in cortical cell cultures. Proceedings of the National Academy of Sciences 92, 7162-7166.

Bortner, C.D., Cidlowski, J.A., 2003. Uncoupling cell shrinkage from apoptosis reveals that Na+ influx is required for volume loss during programmed cell death. Journal of Biological Chemistry 278, 39176-39184.

Bosch, L., Bersenas, A.M., Bateman, S., 2018. Acute polyneuromyopathy with respiratory failure secondary to monensin intoxication in a dog. Journal of Veterinary Emergency and Critical Care 28, 62-68.

Boss, W., Morré, D., Mollenhauer, H., 1984. Monensin-induced swelling of Golgi apparatus cisternae mediated by a proton gradient. European Journal of Cell Biology 34, 1-8.

Botha, C.J., Venter, E.A., Ferreira, G.C., Phaswane, R.M., Clift, S.J., 2019. Geigerin-induced disorganization of desmin, an intermediate filament of the cytoskeleton, in a murine myoblast cell line (C2C12). Toxicon 167, 162-167.

Bradford, M.M., 1976. A rapid and sensitive method for the quantitation of microgram quantities of protein utilizing the principle of protein-dye binding. Analytical biochemistry 72, 248-254.

Branco, A.F., Pereira, S.P., Gonzalez, S., Gusev, O., Rizvanov, A.A., Oliveira, P.J., 2015. Gene expression profiling of H9c2 myoblast differentiation towards a cardiac-like phenotype. Public Library of Science One 10, 0129303.

Braun, A.P., 2012. Two-pore domain potassium channels: variation on a structural theme. Channels 6, 139-140.

Brennan, M.A., Cookson, B.T., 2000. *Salmonella* induces macrophage death by caspase-1-dependent necrosis. Molecular Microbiology 38, 31-40.

Britzi, M., Shimshoni, J., Edery, N., Cuneah, O., Younis, A., Blech, E., Oren, P., Perl, S., Pozzi, P., 2017. Acute salinomycin and maduramicin toxicosis in lactating sows. Israel Journal of Veterinary Medicine 72, 42-48.

Burattini, S., Falcieri, E., 2013. Analysis of cell death by electron microscopy, In: Necrosis. Springer, pp. 77-89.

Capetanaki, Y., 2002. Desmin cytoskeleton: a potential regulator of muscle mitochondrial behavior and function. Trends in Cardiovascular Medicine 12, 339-348.

Capetanaki, Y., Bloch, R.J., Kouloumenta, A., Mavroidis, M., Psarras, S., 2007. Muscle intermediate filaments and their links to membranes and membranous organelles. Experimental Cell Research 313, 2063-2076.

Carlsson, L., Thornell, L.E., 2001. Desmin-related myopathies in mice and man. Acta Physiologica Scandinavica 171, 341-348.

Carpenter, J.A., Charbonneau, G., Josephson, G., 2005. Tiamulin and narasin toxicosis in nursery pigs. Journal of Swine Health and Production 13, 333-336.

Clarke, P.G., 1990. Developmental cell death: morphological diversity and multiple mechanisms. Anatomy and Embryology 181, 195-213.

Clausen, M.J.V., Poulsen, H., 2013. Sodium/potassium homeostasis in the cell, In: Metallomics and the Cell. Springer, pp. 41-67.

Cone Jr, C.D., Cone, C.M., 1976. Induction of mitosis in mature neurons in central nervous system by sustained depolarization. Science 192, 155-158.

Confer, A., Reavis, D., Panciera, R., 1983. Light and electron microscopic changes in cardiac and skeletal muscle of sheep with experimental monensin toxicosis. Veterinary Pathology 20, 590-602.

Costa, M., Escaleira, R., Cataldo, A., Oliveira, F., Mermelstein, C., 2004. Desmin: molecular interactions and putative functions of the muscle intermediate filament protein. Brazilian Journal of Medical and Biological Research 37, 1819-1830.

Curzer, H.J., Perry, G., Wallace, M.C., Perry, D., 2016. The three Rs of animal research: what they mean for the institutional animal care and use committee and why. Science and Engineering Ethics 22, 549-565.

Cybulski, W., Radko, L., Rzeski, W., 2015. Cytotoxicity of monensin, narasin and salinomycin and their interaction with silybin in HepG2, LMH and L6 cell cultures. Toxicology *in Vitro* 29, 337-344.

D'Alessandro, S., Corbett, Y., Ilboudo, D.P., Misiano, P., Dahiya, N., Abay, S.M., Habluetzel, A., Grande, R., Gismondo, M.R., Dechering, K.J., 2015. Salinomycin and other ionophores as a new class of antimalarial drugs with transmission-blocking activity. Antimicrobial Agents and Chemotherapy 59, 5135-5144.

Danese, A., Patergnani, S., Bonora, M., Wieckowski, M.R., Previati, M., Giorgi, C., Pinton, P., 2017. Calcium regulates cell death in cancer: Roles of the mitochondria and mitochondria-associated membranes (MAMs). Biochimica et Biophysica Acta (BBA)-Bioenergetics 1858, 615-627.

Dayal, A.A., Medvedeva, N.V., Nekrasova, T.M., Duhalin, S.D., Surin, A.K., Minin, A.A., 2020. Desmin interacts directly with mitochondria. International Journal of Molecular Sciences 21, 8122.

de Torres, C., Munell, F., Ferrer, I., Reventós, J., Macaya, A., 1997. Identification of necrotic cell death by the TUNEL assay in the hypoxic-ischemic neonatal rat brain. Neuroscience Letters 230, 1-4.

Decloedt, A., Verheyen, T., De Clercq, D., Sys, S., Vercauteren, G., Ducatelle, R., Delahaut, P., van Loon, G., 2012. Acute and long-term cardiomyopathy and delayed neurotoxicity after accidental lasalocid poisoning in horses. Journal of Veterinary Internal Medicine 26, 1005-1011.

Diaz, G.J., Aguillón, Y., Cortés, A., 2018. Effects on health, performance, and tissue residues of the ionophore antibiotic salinomycin in finishing broilers (21 to 38 d). Poultry Science 97, 1922-1928.

Diguet, N., Mallat, Y., Ladouce, R., Clodic, G., Prola, A., Tritsch, E., Blanc, J., Larcher, J.-C., Delcayre, C., Samuel, J.-L., 2011. Muscle creatine kinase deficiency triggers both actin depolymerization and desmin disorganization by advanced glycation end products in dilated cardiomyopathy. Journal of Biological Chemistry 286, 35007-35019.

Donoho, A., 1984. Biochemical studies on the fate of monensin in animals and in the environment. Journal of animal science 58, 1528-1539.

Dougherty, R., 2005. Extensions of DAMAS and benefits and limitations of deconvolution in beamforming, In: 11th AIAA/CEAS Aeroacoustics Conference, p. 2961.

Dowling, L., 1992. Ionophore toxicity in chickens: A review of pathology and diagnosis. Avian Pathology: Journal of the World Veterinary Poultry Association 21, 355-368.

Duffield, T., Bagg, R., DesCoteaux, L., Bouchard, E., Brodeur, M., DuTremblay, D., Keefe, G., LeBlanc, S., Dick, P., 2002. Prepartum monensin for the reduction of energy associated disease in postpartum dairy cows. Journal of Dairy Science 85, 397-405.

Duncan, C., Smith, J., Greenaway, H.C., 1979. Failure to protect frog skeletal muscle from ionophore-induced damage by the use of the protease inhibitor leupeptin. Comparative Biochemistry and Physiology Part C: Comparative Pharmacology 63, 205-207.

Dypbukt, J.M., Ankarcrona, M., Burkitt, M., Sjöholm, Å., Ström, K., Orrenius, S., Nicotera, P., 1994. Different prooxidant levels stimulate growth, trigger apoptosis, or produce necrosis of insulin-secreting RINm5F cells. The role of intracellular polyamines. Journal of Biological Chemistry 269, 30553-30560.

Ebel, J.G., Wachs, T., Henion, J.D., 2004. Rapid forensic selected reaction monitoring liquid chromatography/mass spectrometry determination of ionophore antibiotics found at toxic levels in animal feeds. Journal of AOAC International 87, 25-30.

Edinger, A.L., Thompson, C.B., 2004. Death by design: apoptosis, necrosis and autophagy. Current Opinion in Cell Biology 16, 663-669.

Elamrani, N., Brustis, J.J., Dourdin, N., Balcerzak, D., Poussard, S., Cottin, P., Ducastaing, A., 1995. Desmin degradation and Ca2+− dependent proteolysis during myoblast fusion. Biology of the Cell 85, 177-183.

Elmore, S., 2007. Apoptosis: a review of programmed cell death. Toxicologic Pathology 35, 495-516.

Estrada-O, S., Célis, H., Calderón, E., Gallo, G., Montal, M., 1974. Model translocators for divalent and monovalent ion transport in phospholipid membranes. The Journal of Membrane Biology 18, 201-218.

Festjens, N., Berghe, T.V., Vandenabeele, P., 2006. Necrosis, a well-orchestrated form of cell demise: signalling cascades, important mediators and concomitant immune response. Biochimica et Biophysica Acta (BBA)-Bioenergetics 1757, 1371-1387.

Fink, S.L., Cookson, B.T., 2005. Apoptosis, pyroptosis, and necrosis: mechanistic description of dead and dying eukaryotic cells. Infection and Immunity 73, 1907-1916.

Fischer, S., Maclean, A.A., Liu, M., Cardella, J.A., Slutsky, A.S., Suga, M., Moreira, J.F., Keshavjee, S., 2000. Dynamic changes in apoptotic and necrotic cell death correlate with severity of ischemia–reperfusion injury in lung transplantation. American Journal of Respiratory and Critical Care Medicine 162, 1932-1939.

Fletcher, D.A., Mullins, R.D., 2010. Cell mechanics and the cytoskeleton. Nature 463, 485-492.

Fourie, N., Bastianello, S.S., Nel, P., Kellerman, T.S., Prozesky, L., 1991. Cardiomyopathy of ruminants induced by the litter of poultry fed on rations containing the ionophore antibiotic, maduramicin. 1. Epidemiology, clinical signs and clinical pathology. Onderstepoort Journal of Veterinary Research 58, 291-296.

Freedman, B.D., Price, M., Deutsch, C., 1992. Evidence for voltage modulation of IL-2 production in mitogen-stimulated human peripheral blood lymphocytes. The Journal of Immunology 149, 3784-3794.

Freshney, I., 2001. Application of cell cultures to toxicology, In: Cell Culture Methods for *In Vitro* Toxicology. Springer, pp. 9-26.

Gad, S., Reilly, C., Siino, K., Gavigan, F., Witz, G., 1985. Thirteen Cationic Ionophores: Their Acute Toxicity, Neurobehavioral and Membrane Effects. Drug and Chemical Toxicology 8, 451-468.

Galitzer, S., Oehme, F., Bartley, E., Dayton, A., 1986. Lasalocid toxicity in cattle: Acute clinicopathological changes. Journal of Animal Science 62, 1308-1316.

Galluzzi, L., Kepp, O., Kroemer, G., 2012a. Mitochondria: master regulators of danger signalling. Nature Reviews Molecular cell biology 13, 780-788.

Galluzzi, L., Vitale, I., Aaronson, S.A., Abrams, J.M., Adam, D., Agostinis, P., Alnemri, E.S., Altucci, L., Amelio, I., Andrews, D.W., 2018. Molecular mechanisms of

cell death: recommendations of the Nomenclature Committee on Cell Death 2018. Cell Death and Differentiation 25, 486-541.

Galluzzi, L., Vitale, I., Abrams, J., Alnemri, E., Baehrecke, E., Blagosklonny, M., Dawson, T.M., Dawson, V., El-Deiry, W., Fulda, S., 2012b. Molecular definitions of cell death subroutines: recommendations of the Nomenclature Committee on Cell Death 2012. Cell Death and Differentiation 19, 107-120.

Gavrieli, Y., Sherman, Y., Ben-Sasson, S.A., 1992. Identification of programmed cell death in situ via specific labeling of nuclear DNA fragmentation. Journal of Cell Biology 119, 493-501.

Geor, R., Robinson, W., 1985. Suspected monensin toxicosis in feedlot cattle. Australian Veterinary Journal 62, 130-131.

Golab, T., Barton, S.J., Scroggs, R.E., 1973. Colorimetric method for monensin. Journal of the Association of Official Analytical Chemists 56, 171-173.

Goldman, D.E., 1943. Potential, impedance, and rectification in membranes. The Journal of General Physiology 27, 37-60.

Golstein, P., Kroemer, G., 2007. Cell death by necrosis: towards a molecular definition. Trends in Biochemical Sciences 32, 37-43.

Gonzalez, M., Barkema, H.W., Keefe, G.P., 2005. Monensin toxicosis in a dairy herd. The Canadian Veterinary Journal 46, 910-912.

Goodrich, R., Garrett, J., Gast, D., Kirick, M., Larson, D., Meiske, J., 1984. Influence of monensin on the performance of cattle. Journal of Animal Science 58, 1484-1498.

Grinde, B., 1983. Effect of carboxylic ionophores on lysosomal protein degradation in rat hepatocytes. Experimental Cell Research 149, 27-35.

Grossmann, J., 2002. Molecular mechanisms of "detachment-induced apoptosis—Anoikis". Apoptosis 7, 247-260.

Gruys, E., Perreira, C., Bila, C., 2001. Accidental monensin toxicosis in horses in Mozambique. Journal of the South African Veterinary Association 72, 163-164.

Gupta, P.B., Onder, T.T., Jiang, G., Tao, K., Kuperwasser, C., Weinberg, R.A., Lander, E.S., 2009. Identification of selective inhibitors of cancer stem cells by high-throughput screening. Cell 138, 645-659.

Gy, C., Leclere, M., Bélanger, M.C., Allano, M., Beauchamp, G., Lavoie, J.P., 2020. Acute, subacute and chronic sequelae of horses accidentally exposed to monensin-contaminated feed. Equine Veterinary Journal 52, 848-856.

Haag, G.O., Errecalde, J., Mestorino, N., 2011. Determination of ionophore antibiotics in food animals by thin-layer chromatography method. American Association of Pharmaceutical Scientists PharmSciTech 12, 96.

Hahn, G.M., Shiu, E.C., 1983. Effect of pH and elevated temperatures on the cytotoxicity of some chemotherapeutic agents on Chinese hamster cells in vitro. Cancer Research 43, 5789-5791.

Hall, J.O., 2000. Ionophore use and toxicosis in cattle. Veterinary Clinics: Food Animal Practice 16, 497-509.

Hall, J.O., 2003. Ionophores, In: Clinical Veterinary Toxicology. Elsevier Health Sciences, pp. 120-127.

Hanson, L., Eisenbeis, H., Givens, S., 1981. Toxic effects of lasalocid in horses. American Journal of Veterinary Research 42, 456-461.

Hazards, E.P.o.B., Koutsoumanis, K., Allende, A., Alvarez-Ordóñez, A., Bolton, D., Bover-Cid, S., Chemaly, M., Davies, R., De Cesare, A., Herman, L., 2021. Maximum levels of cross-contamination for 24 antimicrobial active substances in non-target feed. Part 1: Methodology, general data gaps and uncertainties. European Food Safety Authority Journal 19, e06852.

Hermawan, A., Wagner, E., Roidl, A., 2016. Consecutive salinomycin treatment reduces doxorubicin resistance of breast tumor cells by diminishing drug efflux pump expression and activity. Oncology Reports 35, 1732-1740.

Hohmann, T., Dehghani, F., 2019. The cytoskeleton—a complex interacting meshwork. Cells 8, 362.

Horvath, S., 1980. Cytotoxicity of drugs and diverse chemical agents to cell cultures. Toxicology 16, 59-66.

Horvitz, H.R., 1994. Genetic control of programmed cell death in the nematode *Caenorhabditis elegans*, In: Apoptosis. Springer, pp. 1-13.

Iljin, K., Ketola, K., Vainio, P., Halonen, P., Kohonen, P., Fey, V., Grafström, R.C., Perälä, M., Kallioniemi, O., 2009. High-throughput cell-based screening of 4910 known drugs and drug-like small molecules identifies disulfiram as an inhibitor of prostate cancer cell growth. Clinical Cancer Research 15, 6070-6078.

Insall, R.H., Machesky, L.M., 2009. Actin dynamics at the leading edge: from simple machinery to complex networks. Developmental cell 17, 310-322.

Jablonská, E., Kubásek, J., Vojtěch, D., Ruml, T., Lipov, J., 2021. Test conditions can significantly affect the results of *in vitro* cytotoxicity testing of degradable metallic biomaterials. Scientific Reports 11, 1-9.

Jaka, O., Casas-Fraile, L., de Munain, A.L., Saenz, A., 2015. Costamere proteins and their involvement in myopathic processes. Expert Reviews in Molecular Medicine 17.

Jang, Y., Shin, J.S., Yoon, Y.-S., Go, Y.Y., Lee, H.W., Kwon, O.S., Park, S., Park, M.-S., Kim, M., 2018. Salinomycin inhibits influenza virus infection by disrupting endosomal acidification and viral matrix protein 2 function. Journal of Virology 92, e01441-01418.

Janmey, P.A., McCulloch, C.A., 2007. Cell mechanics: integrating cell responses to mechanical stimuli. Annual Review of Biomedical Engineering 9, 1-34.

Jiang, J.P., Downing, S.E., 1990. Catecholamine cardiomyopathy: review and analysis of pathogenetic mechanisms. The Yale Journal of Biology and Medicine 63, 581.

Kanje, M., Edstro, A., Hanson, M., 1981. Inhibition of rapid axonal transport *in vitro* by the ionophores X-537 A and A 23187. Brain Research 204, 43-50.

Kaushik, V., Yakisich, J.S., Kumar, A., Azad, N., Iyer, A.K., 2018. Ionophores: Potential use as anticancer drugs and chemosensitizers. Cancers 10, 360.

Kay, A.R., 2017. How cells can control their size by pumping ions. Frontiers in Cell and Developmental Biology 5, 41.

Kerr, J.F., Wyllie, A.H., Currie, A.R., 1972. Apoptosis: a basic biological phenomenon with wideranging implications in tissue kinetics. British Journal of Cancer 26, 239-257.

Ketola, K., Vainio, P., Fey, V., Kallioniemi, O., Iljin, K., 2010. Monensin is a potent inducer of oxidative stress and inhibitor of androgen signaling leading to apoptosis in prostate cancer cells. Molecular Cancer Therapeutics 9, 3175-3185.

Kiełbasiński, K., Peszek, W., Grabarek, B.O., Boroń, D., Wierzbik-Strońska, M., Oplawski, M., 2020. Effect of Salinomycin on Expression Pattern of Genes Associated with Apoptosis in Endometrial Cancer Cell Line. Current Pharmaceutical Biotechnology 21, 1269-1277.

Kim, K.-Y., Kim, S.-H., Yu, S.-N., Park, S.-G., Kim, Y.-W., Nam, H.-W., An, H.-H., Yu, H.-S., Kim, Y.W., Ji, J.-H., 2017a. Lasalocid induces cytotoxic apoptosis and cytoprotective autophagy through reactive oxygen species in human prostate cancer PC-3 cells. Biomedicine and Pharmacotherapy 88, 1016-1024.

Kim, K.-Y., Park, K.-I., Kim, S.-H., Yu, S.-N., Park, S.-G., Kim, Y.W., Seo, Y.-K., Ma, J.-Y., Ahn, S.-C., 2017b. Inhibition of autophagy promotes salinomycin-induced apoptosis via reactive oxygen species-mediated PI3K/AKT/mTOR and ERK/p38 MAPK-dependent signaling in human prostate cancer cells. International Journal of Molecular Sciences 18, 1088.

Kim, K.Y., Kim, S.H., Yu, S.N., Park, S.K., Choi, H.D., Yu, H.S., Ji, J.H., Seo, Y.K., Ahn, S.C., 2015. Salinomycin enhances doxorubicin-induced cytotoxicity in multidrug resistant MCF-7/MDR human breast cancer cells via decreased efflux of doxorubicin. Molecular Medicine Reports 12, 1898-1904.

Kim, S.-H., Choi, Y.-J., Kim, K.-Y., Yu, S.-N., Seo, Y.-K., Chun, S.-S., Noh, K.-T., Suh, J.-T., Ahn, S.-C., 2016. Salinomycin simultaneously induces apoptosis and autophagy through generation of reactive oxygen species in osteosarcoma U2OS cells. Biochemical and Biophysical Research Communications 473, 607-613.

Kimes, B., Brandt, B., 1976. Properties of a clonal muscle cell line from rat heart. Experimental Cell Research 98, 367-381.

Kischkel, F.C., Hellbardt, S., Behrmann, I., Germer, M., Pawlita, M., Krammer, P.H., Peter, M.E., 1995. Cytotoxicity-dependent APO-1 (Fas/CD95)-associated proteins form a death-inducing signaling complex (DISC) with the receptor. The European Molecular Biology Organization Journal 14, 5579-5588.

Kostin, S., Pool, L., Elsässer, A., Hein, S., Drexler, H.C., Arnon, E., Hayakawa, Y., Zimmermann, R., Bauer, E., Klövekorn, W.-P., 2003. Myocytes die by multiple mechanisms in failing human hearts. Circulation Research 92, 715-724.

Krajčí, D., Mareš, V., Lisá, V., Španová, A., Vorlíček, J., 2000. Ultrastructure of nuclei of cisplatin-treated C6 glioma cells undergoing apoptosis. European Journal of Cell Biology 79, 365-376.

Kroemer, G., Galluzzi, L., Vandenabeele, P., Abrams, J., Alnemri, E.S., Baehrecke, E., Blagosklonny, M., El-Deiry, W., Golstein, P., Green, D., 2009. Classification of cell death: recommendations of the Nomenclature Committee on Cell Death 2009. Cell Death and Differentiation 16, 3-11.

Kroemer, G., Levine, B., 2008. Autophagic cell death: the story of a misnomer. Nature Reviews Molecular Cell Biology 9, 1004-1010.

Kuznetsov, A.V., Javadov, S., Grimm, M., Margreiter, R., Ausserlechner, M.J., Hagenbuchner, J., 2020. Crosstalk between mitochondria and cytoskeleton in cardiac cells. Cells 9, 222.

Lagarde, F., Beausoleil, C., Belcher, S.M., Belzunces, L.P., Emond, C., Guerbet, M., Rousselle, C., 2015. Non-monotonic dose-response relationships and endocrine disruptors: a qualitative method of assessment. Environmental Health 14, 1-15.

Laisne, M.-C., Michallet, S., Lafanechère, L., 2021. Characterization of Microtubule Destabilizing Drugs: A Quantitative Cell-Based Assay That Bridges the Gap between Tubulin Based-and Cytotoxicity Assays. Cancers 13, 5226.

Lane, J.D., Yonekawa, T., Thorburn, A., 2013. Autophagy and cell death. Essays in Biochemistry 55, 105-117.

Lavine, M.D., Arrizabalaga, G., 2012. Analysis of monensin sensitivity in *Toxoplasma gondii* reveals autophagy as a mechanism for drug induced death. Public Library of Science One 7.

Lehn, J., Sauvage, J., 1971. Cation and cavity selectivities of alkali and alkaline-earth "cryptates". Journal of the Chemical Society D: Chemical Communications, 440-441.

Leist, M., Single, B., Castoldi, A.F., Kühnle, S., Nicotera, P., 1997. Intracellular adenosine triphosphate (ATP) concentration: a switch in the decision between apoptosis and necrosis. The Journal of Experimental Medicine 185, 1481-1486.

Levin, S., Bucci, T.J., Cohen, S.M., Fix, A.S., Hardisty, J.F., Legrand, E.K., Maronpot, R.R., Trump, B.F., 1999. The nomenclature of cell death: recommendations of an ad hoc Committee of the Society of Toxicologic Pathologists. Toxicologic Pathology 27, 484-490.

Liu, Y., Shoji-Kawata, S., Sumpter, R.M., Wei, Y., Ginet, V., Zhang, L., Posner, B., Tran, K.A., Green, D.R., Xavier, R.J., 2013. Autosis is a Na+, K+-ATPase–regulated form of cell death triggered by autophagy-inducing peptides, starvation, and hypoxia–ischemia. Proceedings of the National Academy of Sciences 110, 20364-20371.

Lu, D., Choi, M.Y., Yu, J., Castro, J.E., Kipps, T.J., Carson, D.A., 2011. Salinomycin inhibits Wnt signaling and selectively induces apoptosis in chronic lymphocytic leukemia cells. Proceedings of the National Academy of Sciences 108, 13253-13257.

Luft, J.H., 1961. Improvements in epoxy resin embedding methods. The Journal of Biophysical and Biochemical Cytology 9, 409-414.

Lund, L.M., Kerr, J.P., Lupinetti, J., Zhang, Y., Russell, M.A., Bloch, R.J., Bond, M., 2012. Synemin isoforms differentially organize cell junctions and desmin filaments in neonatal cardiomyocytes. The Federation of American Societies for Experimental Biology Journal 26, 137-148.

Mahtal, N., Wu, Y., Cintrat, J.-C., Barbier, J., Lemichez, E., Gillet, D., 2020. Revisiting old Ionophore Lasalocid as a novel inhibitor of multiple toxins. Toxins 12, 26.

Majno, G., Joris, I., 1995. Apoptosis, oncosis, and necrosis. An overview of cell death. The American Journal of Pathology 146, 3-15.

Manmuan, S., Sakunrangsit, N., Ketchart, W., 2017. Salinomycin overcomes acquired tamoxifen resistance through AIB 1 and inhibits cancer cell invasion in endocrine resistant breast cancer. Clinical and Experimental Pharmacology and Physiology 44, 1042-1052.

Marques, R.d.S., Cooke, R.F., 2021. Effects of ionophores on ruminal function of beef cattle. Animals 11, 2871.

Matsuoka, T., Novilla, M., Thomson, T., Donoho, A., 1996. Review of monensin toxicosis in horses. Journal of Equine Veterinary Science 16, 8-15.

Mattson, M.P., 1998. Modification of ion homeostasis by lipid peroxidation: Roles in neuronal degeneration and adaptive plasticity. Trends in Neurosciences 21, 53-57.

Mehlhorn, H., Pooch, H., Raether, W., 1983. The action of polyether ionophorous antibiotics (monensin, salinomycin, lasalocid) on developmental stages of *Eimeria tenella* (Coccidia, Sporozoa) *in vivo* and *in vitro*: Study by light and electron microscopy. Zeitschrift für Parasitenkunde 69, 457-471.

Meima, M.E., Mackley, J.R., Barber, D.L., 2007. Beyond ion translocation: structural functions of the sodium–hydrogen exchanger isoform-1. Current Opinion in Nephrology and Hypertension 16, 365-372.

Meingassner, J., Schmook, F., Czok, R., Mieth, H., 1979. Enhancement of the anticoccidial activity of polyether antibiotics in chickens by tiamulin. Poultry Science 58, 308-313.

Ménard, C., Pupier, S., Mornet, D., Kitzmann, M., Nargeot, J., Lory, P., 1999. Modulation of L-type calcium channel expression during retinoic acid-induced differentiation of H9C2 cardiac cells. Journal of Biological Chemistry 274, 29063-29070.

Mermelstein, C., Amaral, L., Rebello, M., Reis, J., Borojevic, R., Costa, M., 2005. Changes in cell shape and desmin intermediate filament distribution are associated with down-regulation of desmin expression in C2C12 myoblasts grown in the absence of extracellular Ca2+. Brazilian Journal of Medical and Biological Research 38, 1025-1032.

Milner, D.J., Mavroidis, M., Weisleder, N., Capetanaki, Y., 2000. Desmin cytoskeleton linked to muscle mitochondrial distribution and respiratory function. The Journal of Cell Biology 150, 1283-1298.

Milo, R., Phillips, R., 2015. Concentrations and Absolute Numbers, In: Cell Biology by the Numbers. Garland Science, pp. 127-135.

Miskimins, D., Neiger, R., 1996. Monensin toxicosis in swine. Journal of Veterinary Diagnostic Investigation 8, 396-397.

Mitani, M., Yamanishi, T., Miyazaki, Y., Ōtake, N., 1976. Salinomycin effects on mitochondrial ion translocation and respiration. Antimicrobial Agents and Chemotherapy 9, 655-660.

Mitchison, T., Kirschner, M., 1984. Dynamic instability of microtubule growth. Nature 312, 237-242.

Mizuno, Y., Guyon, J.R., Watkins, S.C., Mizushima, K., Sasaoka, T., Imamura, M., Kunkel, L.M., Okamoto, K., 2004. β-synemin localizes to regions of high stress in human skeletal myofibers. Muscle and Nerve: Official Journal of the American Association of Electrodiagnostic Medicine 30, 337-346.

Mizuno, Y., Thompson, T.G., Guyon, J.R., Lidov, H.G., Brosius, M., Imamura, M., Ozawa, E., Watkins, S.C., Kunkel, L.M., 2001. Desmuslin, an intermediate filament protein that interacts with α-dystrobrevin and desmin. Proceedings of the National Academy of Sciences 98, 6156-6161.

Mollenhauer, H.H., Morré, D.J., Rowe, L.D., 1990. Alteration of intracellular traffic by monensin; mechanism, specificity and relationship to toxicity. Biochimica et Biophysica Acta (BBA)-Reviews on Biomembranes 1031, 225-246.

Mollenhauer, H.H., Rowe, L., Cysewski, S., Witzel, D., 1981. Ultrastructural observations in ponies after treatment with monensin. American Journal of Veterinary Research 42, 35-40.

Mormone, E., Matarrese, P., Tinari, A., Cannella, M., Maglione, V., Farrace, M.G., Piacentini, M., Frati, L., Malorni, W., Squitieri, F., 2006. Genotype-dependent priming to self-and xeno-cannibalism in heterozygous and homozygous lymphoblasts from patients with Huntington's disease. Journal of Neurochemistry 98, 1090-1099.

Mosmann, T., 1983. Rapid colorimetric assay for cellular growth and survival: application to proliferation and cytotoxicity assays. Journal of Immunological Methods 65, 55-63.

Muylle, E., Vandenhende, C., Oyaert, W., Thoonen, H., Vlaeminck, K., 1981. Delayed monensin sodium toxicity in horses. Equine Veterinary Journal 13, 107-108.

Nakagawa, T., Yuan, J., 2000. Cross-talk between two cysteine protease families: activation of caspase-12 by calpain in apoptosis. The Journal of Cell Biology 150, 887-894.

Nakamura, M., Kunimoto, S., Takahashi, Y., Naganawa, H., Sakaue, M., Inoue, S., Ohno, T., Takeuchi, T., 1992. Inhibitory effects of polyethers on human immunodeficiency virus replication. Antimicrobial Agents and Chemotherapy 36, 492-494.

Nebbia, C., Ceppa, L., Dacasto, M., Nachtmann, C., Carletti, M., 2001. Oxidative monensin metabolism and cytochrome P450 3A content and functions in liver microsomes from horses, pigs, broiler chicks, cattle and rats. Journal of Veterinary Pharmacology and Therapeutics 24, 399-403.

Nel, P., Kellerman, TS, Schultz, R. Anitra, Van Aarde, N., Coetzer, JAW, Basson, AT, Fourie, N., Van der Walt, J., 1988. Salinomycin poisoning in horses. Journal of the South African Veterinary Association 59, 103.

Nicotera, P., Melino, G., 2004. Regulation of the apoptosis–necrosis switch. Oncogene 23, 2757-2765.

Nocerini, M., Honeyfield, D., Carlson, J., Breeze, R., 1985. Reduction of 3-methylindole production and prevention of acute bovine pulmonary edema and emphysema with lasalocid. Journal of Animal Science 60, 232-238.

Norberg, E., Gogvadze, V., Ott, M., Horn, M., Uhlen, P., Orrenius, S., Zhivotovsky, B., 2008. An increase in intracellular Ca 2+ is required for the activation of mitochondrial calpain to release AIF during cell death. Cell Death and Differentiation 15, 1857-1864.

Norbury, C.J., Hickson, I.D., 2001. Cellular responses to DNA damage. Annual Review of Pharmacology and Toxicology 41, 367-401.

Novilla, M., 1992. The veterinary importance of the toxic syndrome induced by ionophores. Veterinary and Human Toxicology 34, 66-70.

Novilla, M.N., 2018. Ionophores, In: Veterinary Toxicology. Elsevier, pp. 1073-1092.

O'Neill, A., Williams, M.W., Resneck, W.G., Milner, D.J., Capetanaki, Y., Bloch, R.J., 2002. Sarcolemmal organization in skeletal muscle lacking desmin: evidence for cytokeratins associated with the membrane skeleton at costameres. Molecular Biology of the Cell 13, 2347-2359.

O'Mahony, J., Moloney, M., Whelan, M., Danaher, M., 2012. Feed additives and veterinary drugs as contaminants in animal feed–the problem of cross-contamination during feed production, In: Animal Feed Contamination. Elsevier, pp. 385-410.

Oko, R., Maravei, D., 1995. Distribution and possible role of perinuclear theca proteins during bovine spermiogenesis. Microscopy Research and Technique 32, 520-532.

Olins, A.L., Olins, D.E., 2004. Cytoskeletal influences on nuclear shape in granulocytic HL-60 cells. BMC Cell Biology 5, 1-18.

Olmsted, J., Borisy, G., 1975. Ionic and nucleotide requirements for microtubule polymerization *in vitro*. Biochemistry 14, 2996-3005.

Oruc, H., Cangul, I., Cengiz, M., Yilmaz, R., 2011. Acute lasalocid poisoning in calves associated with off-label use. Journal of Veterinary Pharmacology and Therapeutics 34, 187-189.

Osweiler, G.D., 1996. Toxicology, In: The National Veterinary Medical Series for Independent Study. Williams and Wilkins, Philadelphia, pp. 338-339.

Ovchinnikov, Y.A., Ivanov, V., Shkrob, A., 1974. Membrane-active Complexones. Elsevier, Amsterdam.

Overholtzer, M., Mailleux, A.A., Mouneimne, G., Normand, G., Schnitt, S.J., King, R.W., Cibas, E.S., Brugge, J.S., 2007. A nonapoptotic cell death process, entosis, that occurs by cell-in-cell invasion. Cell 131, 966-979.

Owles, P.J., 1984. Identification of monensin, narasin, salinomycin and lasalocid in pre-mixes and feeds by thin-layer chromatography. Analyst 109, 1331-1333.

Paddock, S.W., Albrecht-Buehler, G., 1986. Distribution of microfilament bundles during rotation of the nucleus in 3T3 cells treated with monensin. Experimental Cell Research 163, 525-538.

Page, M.J., Di Cera, E., 2006. Role of Na+ and K+ in enzyme function. Physiological Reviews 86, 1049-1092.

Pakozdy, A., Challande-Kathman, I., Doherr, M., Cizinauskas, S., Wheeler, S.J., Oevermann, A., Jaggy, A., 2010. Retrospective study of salinomycin toxicosis in 66 cats. Veterinary Medicine International 2010, 147142.

Park, W.H., Kim, E.S., Jung, C.W., Kim, B.K., Lee, Y.Y., 2003. Monensin-mediated growth inhibition of SNU-C1 colon cancer cells via cell cycle arrest and apoptosis. International Journal of Oncology 22, 377-382.

Park, W.H., Seol, J.G., Kim, E.S., Kang, W.K., Im, Y.H., Jung, C.W., Kim, B.K., Lee, Y.Y., 2002. Monensin-mediated growth inhibition in human lymphoma cells through cell cycle arrest and apoptosis. British Journal of Haematology 119, 400-407.

Patten, V., Chabaesele, I., Sishi, B., Van Vuuren, D., 2017. Cardiomyocyte differentiation: experience and observations from 2 laboratories: cardiomyocyte differentiation. SA Heart 14, 96-107.

Paulin, D., Li, Z., 2004. Desmin: a major intermediate filament protein essential for the structural integrity and function of muscle. Experimental Cell Research 301, 1-7.

Pedersen, C.J., 1967. Cyclic polyethers and their complexes with metal salts. Journal of the American Chemical Society 89, 7017-7036.

Perry, T., Beeson, W., Mohler, M., 1976. Effect of monensin on beef cattle performance. Journal of Animal Science 42, 761-765.

Pitre, A., Davis, N., Paul, M., Orr, A.W., Skalli, O., 2012. Synemin promotes AKT-dependent glioblastoma cell proliferation by antagonizing PP2A. Molecular Biology of the Cell 23, 1243-1253.

Plumlee, K.H., Johnson, B., Galey, F.D., 1995. Acute salinomycin toxicosis of pigs. Journal of Veterinary Diagnostic Investigation 7, 419-420.

Potter, E., VanDuyn, R., Cooley, C., 1984. Monensin toxicity in cattle. Journal of Animal Science 58, 1499-1511.

Pressman, B.-C., Harris, E., Jagger, W., Johnson, J., 1967. Antibiotic-mediated transport of alkali ions across lipid barriers. Proceedings of the National Academy of Sciences of the United States of America 58, 1949-1956.

Pressman, B.C., 1976. Biological applications of ionophores. Annual Review of Biochemistry 45, 501-530.

Pressman, B.C., Fahim, M., 1982. Pharmacology and toxicology of the monovalent carboxylic ionophores. Annual Review of Pharmacology and Toxicology 22, 465-490.

Przygodzki, T., Sokal, A., Bryszewska, M., 2005. Calcium ionophore A23187 action on cardiac myocytes is accompanied by enhanced production of reactive oxygen species. Biochimica et Biophysica Acta (BBA)-Molecular Basis of Disease 1740, 481-488.

Qin, L.-s., Jia, P.-f., Zhang, Z.-q., Zhang, S.-m., 2015. ROS-p53-cyclophilin-D signaling mediates salinomycin-induced glioma cell necrosis. Journal of Experimental and Clinical Cancer Research 34, 1-12.

Qu, X., Zou, Z., Sun, Q., Luby-Phelps, K., Cheng, P., Hogan, R.N., Gilpin, C., Levine, B., 2007. Autophagy gene-dependent clearance of apoptotic cells during embryonic development. Cell 128, 931-946.

Radko, L., Cybulski, W., Rzeski, W., 2011. Cytotoxicity studies of lasalocid and silibinin in rat hepatoma cell culture. Bulletin of the Veterinary Institute in Pulawy 55, 547-554.

Radko, L., Cybulski, W., Rzeski, W., 2013a. Cytoprotective effect of silybin against lasalocid-induced toxicity in HepG2 cells. Polish Journal of Veterinary Sciences 16, 275–282.

Radko, L., Cybulski, W., Rzeski, W., 2013b. The protective effect of silybin against lasalocid cytotoxic exposure on chicken and rat cell lines. BioMed Research International 2013, 783519.

Raff, M., 1998. Cell suicide for beginners. Nature 396, 119-122.

Redfern, C.P., Todd, C., 1988. The effects of retinoic acid on rat epidermal cells *in vitro*: changes in patterns of protein phosphorylation in relation to growth and differentiation. Experimental Cell Research 174, 367-377.

Reeves, J.P., 1998. Na+/Ca2+ exchange and cellular Ca2+ homeostasis. Journal of Bioenergetics and Biomembranes 30, 151-160.

Reichenbach, D.D., Benditt, E.P., 1970. Catecholamines and cardiomyopathy: the pathogenesis and potential importance of myofibrillar degeneration. Human Pathology 1, 125-150.

Renehan, A.G., Booth, C., Potten, C.S., 2001. What is apoptosis, and why is it important? Education and debate. British Medical Journal 322, 1536-1538.

Reynolds, E.S., 1963. The use of lead citrate at high pH as an electron-opaque stain in electron microscopy. The Journal of Cell Biology 17, 208-212.

Richardson, L., Raun, A., Potter, E., Cooley, C., Rathmacher, R., 1976. Effect of monensin on rumen fermentation *in vitro* and *in vivo*. Journal of Animal Science 43, 657-664.

Robison, P., Caporizzo, M.A., Ahmadzadeh, H., Bogush, A.I., Chen, C.Y., Margulies, K.B., Shenoy, V.B., Prosser, B.L., 2016. Detyrosinated microtubules buckle and bear load in contracting cardiomyocytes. Science 352, aaf0659.

Robison, P., Prosser, B.L., 2017. Microtubule mechanics in the working myocyte. The Journal of Physiology 595, 3931-3937.

Russell, M.A., Lund, L.M., Haber, R., McKeegan, K., Cianciola, N., Bond, M., 2006. The intermediate filament protein, synemin, is an AKAP in the heart. Archives of Biochemistry and Biophysics 456, 204-215.

S Smaili, S., JS Pereira, G., M Costa, M., K Rocha, K., Rodrigues, L., G do Carmo, L., Hirata, H., Hsu, Y.-T., 2013. The role of calcium stores in apoptosis and autophagy. Current Molecular Medicine 13, 252-265.

Saelens, X., Festjens, N., Walle, L.V., Van Gurp, M., Van Loo, G., Vandenabeele, P., 2004. Toxic proteins released from mitochondria in cell death. Oncogene 23, 2861-2874.

Salles, M.S., de Barros Lombardo, C., Barros, S., 1994. Ionophore antibiotic (narasin) poisoning in rabbits. Veterinary and Human Toxicology 36, 437-444.

Sandercock, D., Mitchell, M., 2004. The role of sodium ions in the pathogenesis of skeletal muscle damage in broiler chickens. Poultry Science 83, 701-706.

Sarraf, C.E., 2000. Immunolabeling for electron microscopy, In: Diagnostic and Therapeutic Antibodies. Springer, pp. 439-452.

Schenk, M., Aykut, B., Teske, C., Giese, N.A., Weitz, J., Welsch, T., 2015. Salinomycin inhibits growth of pancreatic cancer and cancer cell migration by disruption of actin stress fiber integrity. Cancer Letters 358, 161-169.

Schindelin, J., Arganda-Carreras, I., Frise, E., Kaynig, V., Longair, M., Pietzsch, T., Preibisch, S., Rueden, C., Saalfeld, S., Schmid, B., 2012. Fiji: an open-source platform for biological-image analysis. Nature Methods 9, 676-682.

Segev, G., Baneth, G., Levitin, B., Aroch, I., Shlosberg, I., 2004. Accidental poisoning of 17 dogs with lasalocid. Veterinary Record 155, 174-176.

Shen, C., Patel, D.J., 1977. Biogenic amine-ionophore interactions: Structure and dynamics of lasalocid (X537A) complexes with phenethylamines and catecholamines in nonpolar solution. Proceedings of the National Academy of Sciences 74, 4734-4738.

Shimshoni, J.A., Britzi, M., Pozzi, P.S., Edery, N., Berkowitz, A., Bouznach, A., Cuneah, O., Soback, S., Bellaiche, M., Younis, A., 2014. Acute maduramicin toxicosis in pregnant gilts. Food and Chemical Toxicology 68, 283-289.

Shlosberg, A., Perl, S., Harmelin, A., Hanji, V., Bellaiche, M., Bogin, E., Cohen, R., Markusfeld-Nir, O., Shpigel, N., Eisenberg, Z., 1997. Acute maduramicin toxicity in calves. Veterinary Record 140, 643-646.

Shoji, K., Ohashi, K., Sampei, K., Oikawa, M., Mizuno, K., 2012. Cytochalasin D acts as an inhibitor of the actin–cofilin interaction. Biochemical and Biophysical Research Communications 424, 52-57.

Smith, C.A., Farrah, T., Goodwin, R.G., 1994. The TNF receptor superfamily of cellular and viral proteins: activation, costimulation, and death. Cell 76, 959-962.

Smith, C.K., Galloway, R.B., White, S.L., 1981. Effect of ionophores on survival, penetration, and development of *Eimeria tenella* sporozoites *in vitro*. The Journal of Parasitology 67, 511-516.

Souza, A., Machado, F., Celes, M., Faria, G., Rocha, L., Silva, J., Rossi, M., 2005. Mitochondrial damage as an early event of monensin-induced cell Injury in cultured fibroblasts L929. Journal of Veterinary Medicine Series A 52, 230-237.

Spires, H., Algeo, J., 1983. Laidlomycin butyrate—an ionophore with enhanced intraruminal activity. Journal of Animal Science 57, 1553-1560.

Steiner, P., Luckner, M., Kerschbaum, H., Wanner, G., Lütz-Meindl, U., 2018. Ionic stress induces fusion of mitochondria to 3-D networks: an electron tomography study. Journal of Structural Biology 204, 52-63.

Stillwell, E., Cone, C., Cone, C., 1973. Stimulation of DNA synthesis in CNS neurones by sustained depolarisation. Nature New Biology 246, 110-111.

Story, P., Doube, A., 2004. A case of human poisoning by salinomycin, an agricultural antibiotic. The New Zealand Medical Journal 117.

Sulik, M., Stępień, K., Stefańska, J., Huczyński, A., Antoszczak, M., 2020. Antibacterial activity of singly and doubly modified salinomycin derivatives. Bioorganic and Medicinal Chemistry Letters 30, 127062.

Sun, J., Luo, Q., Liu, L., Yang, X., Zhu, S., Song, G., 2017. Salinomycin attenuates liver cancer stem cell motility by enhancing cell stiffness and increasing F-actin formation via the FAK-ERK1/2 signalling pathway. Toxicology 384, 1-10.

Tappel, A.L., 1980. Vitamin E and selenium protection from *in vivo* lipid peroxidation. Annals of the New York Academy of Sciences 355, 18-31.

The Ministry of Health SA, 1977. Regulations - preservatives and antioxidants.

Tilney, L.G., Kiehart, D.P., Sardet, C., Tilney, M., 1978. Polymerization of actin. IV. Role of Ca++ and H+ in the assembly of actin and in membrane fusion in the acrosomal reaction of *echinoderm* sperm. The Journal of Cell Biology 77, 536-550.

Todd, G., Novilla, M., Howard, L., 1984. Comparative toxicology of monensin sodium in laboratory animals. Journal of Animal Science 58, 1512-1517.

Tournu, H., Carroll, J., Latimer, B., Dragoi, A.-M., Dykes, S., Cardelli, J., Peters, T.L., Eberle, K.E., Palmer, G.E., 2017. Identification of small molecules that disrupt vacuolar function in the pathogen *Candida albicans*. Public Library of Science One 12, e0171145.

Tyagi, M., Patro, B.S., 2019. Salinomycin reduces growth, proliferation and metastasis of cisplatin resistant breast cancer cells via NF-kB deregulation. Toxicology *in Vitro* 60, 125-133.

Urrego, D., Tomczak, A.P., Zahed, F., Stühmer, W., Pardo, L.A., 2014. Potassium channels in cell cycle and cell proliferation. Philosophical Transactions of the Royal Society B: Biological Sciences 369, 20130094.

Van der Linde-Sipman, J., Van Den Ingh, T., Van Nes, J., Verhagen, H., Kersten, J., Beynen, A., Plekkringa, R., 1999. Salinomycin-induced polyneuropathy in cats: morphologic and epidemiologic data. Veterinary Pathology 36, 152-156.

Van Vleet, J., Amstutz, H.E., Weirich, W., Rebar, A., Ferrans, V., 1983. Acute monensin toxicosis in swine: effect of graded doses of monensin and protection of swine by pretreatment with selenium-vitamin E. American Journal of Veterinary Research 44, 1460-1468.

Van Vleet, J., Ferrans, V., 1984a. Ultrastructural alterations in skeletal muscle of pigs with acute monensin myotoxicosis. The American Journal of Pathology 114, 461-471.

Van Vleet, J., Ferrans, V., 1984b. Ultrastructural alterations in the atrial myocardium of pigs with acute monensin toxicosis. The American Journal of Pathology 114, 367-379.

Varadarajan, S., Tanaka, K., Smalley, J.L., Bampton, E.T., Pellecchia, M., Dinsdale, D., Willars, G.B., Cohen, G.M., 2013. Endoplasmic reticulum membrane reorganization is regulated by ionic homeostasis. Public Library of Science One 8, e56603.

Vladutiu, G.D., 1984. Immunocytochemical localization on β-hexosaminidase and electron-microscopic characterization of human fibroblasts following treatment with monensin and nigericin. Bioscience Reports 4, 1079-1088.

Vudathala, D., Murphy, L., 2012. Rapid method for the simultaneous determination of six ionophores in feed by liquid chromatography/mass spectrometry. Journal of AOAC International 95, 1016-1022.

Walss-Bass, C., Xu, K., David, S., Fellous, A., Ludueña, R.F., 2002. Occurrence of nuclear βII-tubulin in cultured cells. Cell and Tissue Research 308, 215-223.

Weete, J., El Moughith, A., Touze-Soulet, J.-M., 1989. Inhibition of growth, lipid, and sterol biosynthesis by monensin in fungi. Experimental Mycology 13, 85-94.

Weisenberg, R.C., 1972. Microtubule formation *in vitro* in solutions containing low calcium concentrations. Science 177, 1104-1105.

Weppelman, R., Olson, G., Smith, D., Tamas, T., Van Iderstine, A., 1977. Comparison of anticoccidial efficacy, resistance and tolerance of narasin, monensin and lasalocid in chicken battery trials. Poultry Science 56, 1550-1559.

Williams, J.B., Napoli, J.L., 1985. Metabolism of retinoic acid and retinol during differentiation of F9 embryonal carcinoma cells. Proceedings of the National Academy of Sciences 82, 4658-4662.

Wilson, G., Chiu, S., 1993. Mitogenic factors regulate ion channels in Schwann cells cultured from newborn rat sciatic nerve. The Journal of Physiology 470, 501-520.

Wilson, J., 1980. Toxic myopathy in a dog associated with the presence of monensin in dry food. The Canadian Veterinary Journal 21, 30-31.

Witkamp, R.F., Nijmeijer, S.M., Monshouwer, M., Miert, A.S.V., 1995. The antibiotic tiamulin is a potent inducer and inhibitor of cytochrome P4503A via the formation of a stable metabolic intermediate complex: Studies in primary hepatocyte cultures and liver microsomes of the pig. Drug Metabolism and Disposition 23, 542-547.

Wong, D.T., Berg, D.H., Hamill, R.H., Wilkinson, J.R., 1977. Ionophorous properties of narasin, a new polyether monocarboxylic acid antibiotic, in rat liver mitochondria. Biochemical Pharmacology 26, 1373-1376.

Wrogemann, K., Pena, S., 1976. Mitochondrial calcium overload: A general mechanism for cell-necrosis in muscle diseases. The Lancet 307, 672-674.

Yaffe, D., 1968. Retention of differentiation potentialities during prolonged cultivation of myogenic cells. Proceedings of the National Academy of Sciences of the United States of America 61, 477-483.

Zavala, G., Anderson, D.A., Davis, J.F., Dufour-Zavala, L., 2011. Acute monensin toxicosis in broiler breeder chickens. Avian diseases 55, 516-521.

Zheng, D., Saikumar, P., Weinberg, J.M., Venkatachalam, M.A., 1997. Internucleosomal DNA cleavage triggered by plasma membrane damage during necrotic cell death. The American Journal of Pathology 151, 1205-1213.

Zhou, Y., Liang, C., Xue, F., Chen, W., Zhi, X., Feng, X., Bai, X., Liang, T., 2015. Salinomycin decreases doxorubicin resistance in hepatocellular carcinoma cells by inhibiting the β-catenin/TCF complex association via FOXO3a activation. Oncotarget 6, 10350-10365.

Zysk, G., Bejo, L., Schneider-Wald, B., Nau, R., Heinz, H.P., 2000. Induction of necrosis and apoptosis of neutrophil granulocytes by *Streptococcus pneumoniae*. Clinical and Experimental Immunology 122, 61-66.

Appendix

The appendix contains the following information.

- Research Ethics Committee Approval (REC070-19).
- Published Article: The *In Vitro* Cytotoxic Effects of Ionophore Exposure on Selected Cytoskeletal Proteins of C2C12 Myoblasts.

Faculty of Veterinary Science

Research Ethics Committee

Project Title	**The cytotoxic and ultrastructural effects of monensin, salinomycin and lasalocid on cardiac and skeletal muscle myoblasts in vitro**
Project Number	**REC070-19**
Researcher / Principal Investigator	**Miss D Henn**

DIissertation / Thesis submitted for	**Doctoral**

Supervisor	**Prof CJ Botha**

APPROVED	Date: **2019-05-06**
CHAIRMAN: UP Research Ethics Committee	Signature:

Office of the Chairman: Research Ethics Committee
Room 2-24, Pathology Building, Onderstepoort
University of Pretoria, Private Bag X04
Onderstepoort 0110, South Africa
Tel +27 (0)12 529 8052
Email
www.up.ac.za

Fakulteit Veeartsenykunde
Lefapha la Diseanse tša Bongakadiruiwa

The *In Vitro* Cytotoxic Effects of Ionophore Exposure on Selected Cytoskeletal Proteins of C2C12 Myoblasts

Danielle Henn *, Annette Venter, Gezina C. H. Ferreira and Christo J. Botha

Department of Paraclinical Sciences, Faculty of Veterinary Science, University of Pretoria, Onderstepoort 0110, South Africa; annette.venter@up.ac.za (A.V.); arina.ferreira@up.ac.za (G.C.H.F.); christo.botha@up.ac.za (C.J.B.)
* Correspondence: daniellehenn@tuks.co.za

Abstract: Carboxylic ionophores, such as monensin, salinomycin and lasalocid, are polyether antibiotics used widely in production animals for the control of coccidiosis, as well as for the promotion of growth and feed efficiency. Although the benefits of using ionophores are undisputed, cases of ionophore toxicosis do occur, primarily targeting the cardiac and skeletal muscles of affected animals. The 3-[4,5-dimethylthiazol-2yl]-2,5-diphenyl tetrazolium bromide (MTT) viability assay was used to determine the cytotoxicity of monensin, salinomycin and lasalocid on mouse skeletal myoblasts (C2C12). Immunocytochemistry and immunofluorescent techniques were, in turn, performed to investigate the effects of the ionophores on the microfilament, microtubule and intermediate filament, i.e., desmin and synemin networks of the myoblasts. Monensin was the most cytotoxic of the three ionophores, followed by salinomycin and finally lasalocid. Monensin and salinomycin exposure resulted in the aggregation of desmin around the nuclei of affected myoblasts. The synemin, microtubule and microfilament networks were less affected; however, vesicles throughout the myoblast's cytoplasm produced gaps within the microtubule and, to a limited extent, the synemin and microfilament networks. In conclusion, ionophore exposure disrupted desmin filaments, which could contribute to the myofibrillar degeneration and necrosis seen in the skeletal muscles of animals suffering from ionophore toxicosis.

Keywords: C2C12 myoblasts; cytoskeleton; cytotoxicity; desmin; ionophores

Key Contribution: Monensin, followed by salinomycin and lasalocid, was the most cytotoxic *in vitro*. Ionophore exposure affects the intermediate filament desmin in C2C12 myoblasts.

1. Introduction

Carboxylic ionophores are polyether antibiotics widely used in the production animal industry due to their selective toxicity against bacteria and protozoan parasites, as well as their ability to improve feed efficiency in ruminants [1–5]. However, it is not uncommon for animals to ingest a dosage that exceeds safety margins, either resulting from feed-mixing errors or extra-label use, and subsequently suffer from ionophore toxicosis [6–15]. Treatment of ionophore toxicosis is largely symptomatic and supportive [12–14], and a poor prognosis is associated with suspected myocardial damage [11,16]. Ionophores act by forming dynamically reversible, lipid-soluble cation complexes and facilitating the movement of ions across biological membranes. The resulting changes in the net movement of ions within the cell disrupt ion homeostasis, causing, among others, calcium overload, production of reactive oxygen species (ROS) and disruption of cellular membranes [3]. Striated muscles are the primary targets of ionophore toxicosis, and clinical signs are thus mainly associated with skeletal muscle and myocardial dysfunction. Signs and symptoms of ionophore toxicosis include anorexia, ataxia, depression, diarrhea, dyspnea, hypoactivity, recumbency and weakness [6,8,12,16–21]. On auscultation of the heart, tachycardia and

cardiac arrhythmias are present [6,8,11,15,17,18]. Lesions are time- and dosage-dependent and are often absent in animals that die immediately after ionophore exposure. Morphological effects of ionophore toxicosis on cardiac and skeletal muscle comprise degeneration, necrosis, and repair with a variable inflammatory component [7,8,21–24].

Ultrastructural examination of the skeletal muscles from sheep that suffered from experimental monensin toxicosis revealed disorganization of the sarcomere, exhibiting mild Z-disk streaming and indistinct A- and I-bands [22]. Further progression of ionophore toxicosis later developed into total disruption of the Z-disk with granular material visible. The sarcomere is the most basic contractile unit of a muscle, with actin (thin) and myosin (thick) filaments, working in tandem alongside various other proteins, adenosine triphosphate (ATP), and calcium to facilitate contraction. Desmin, a muscle-specific intermediate filament is found primarily at the Z-disk of the sarcomere and assists with maintaining muscle cytoarchitecture [25–28]. Additionally, desmin regulates the positioning of mitochondria within the cytoplasm, thus affecting their respiratory ability [29,30]. Synemin, another intermediate filament, co-polymerizes with desmin at the Z-disk and assists with structural support, connects desmin to the extracellular environment [31–33] and functions in various signaling pathways [34,35]. Although not part of the sarcomere, the microtubule network is associated with desmin at the Z-disk and mechanically couples the sarcomere to the non-sarcomeric cytoskeleton [36,37]. The aim of this study was to investigate the *in vitro* cytotoxicity of monensin, salinomycin and lasalocid on C2C12 myoblasts and to determine the effects of the ionophores on the cytoskeletal proteins, desmin, synemin, β-tubulin and actin.

2. Results

2.1. The In Vitro Cytotoxic Effect of Monensin, Salinomycin and Lasalocid on C2C12 Myoblasts

2.1.1. The Effect of Ionophore Exposure on Cell Viability

The effect of monensin, salinomycin and lasalocid on C2C12 myoblast viability was investigated over a 72 h exposure period using the MTT viability assay. The ionophore toxicity was dose- and time-dependent, with the percentage cell survival inversely proportional to the ionophore concentrations and exposure duration (Figure 1). The log dose–response curves after 48 and 72 h exposure closely resembled each other, with the percentage cell survival being slightly lower after 72 h. Increased concentrations of both monensin and salinomycin resulted in a sharp decline in the percentage of viable cells after 48 and 72 h of exposure, whereas after 24 h exposure, ionophores exhibited a smaller effect on cell survival.
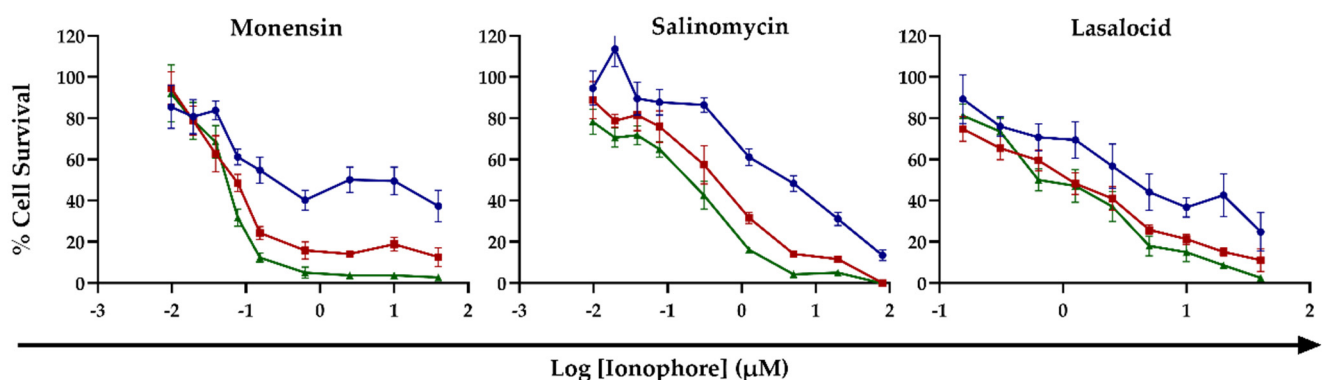
Figure 1. The log dose-response curves of C2C12 myoblasts exposed to monensin, salinomycin and lasalocid for 24, 48 and 72 h. Mean ± SEM. (Legend -●- 24 h, -■- 48 h, -▲- 72 h.).

The half-maximal effective concentrations (EC$_{50}$s) ranged from the low micromolar to low nanomolar range, decreasing sharply from 24 to 48 h exposure (Table 1). There were significant differences ($p < 0.05$) between the EC$_{50}$s at 24 h [a] compared to the EC$_{50}$s at both 48 [b] and 72 h [b] exposures of salinomycin and lasalocid, respectively. Of the three

ionophores, monensin [c] was the most toxic, having significantly lower EC$_{50}$s compared to both salinomycin [d] and lasalocid [d] after 48 and 72 h exposure ($p < 0.05$). Salinomycin was the second most cytotoxic ionophore tested, while lasalocid was the least cytotoxic, with EC$_{50}$s remaining within the low micromolar range even after 72 h exposure.

Table 1. The EC$_{50}$s (μM) of monensin, salinomycin and lasalocid on C2C12 myoblasts reported as the mean $\pm$ the standard error of the mean.

		Monensin	**Salinomycin**	**Lasalocid**
	24 h	† ($n = 5$)	4.04 ± 1.01 ($n = 5$) [a]	8.68 ± 5.38 ($n = 4$) [a]
C2C12 cells	48 h	0.04 ± 0.01 ($n = 5$) [c]	0.45 ± 0.13 ($n = 5$) [b,d]	1.38 ± 0.54 ($n = 4$) [b,d]
	72 h	0.02 ± 0.01 ($n = 5$) [c]	0.26 ± 0.06 ($n = 5$) [b,d]	1.46 ± 0.59 ($n = 4$) [b,d]

† The EC$_{50}$ falls between 0.15 and 10 μM. n = biological repeats. Significant differences between the EC$_{50}$s of the ionophores as well as between the EC$_{50}$s at different exposure periods are indicated using [a & b] (vertical columns) and [c & d] (horizontal columns), respectively.

2.1.2. Morphological Alterations of C2C12 Myoblasts

Investigation of the myoblast morphology after ionophore exposure using phase-contrast microscopy (Figure 2) revealed that affected myoblasts were filled with translucent vesicles (yellow arrows). The vesicles initially appeared around the perinuclear region, eventually filling up the cytoplasm. Some myoblasts became spherical and detached from the surface. Monensin exhibited the greatest effect on the myoblasts (Figure 2), in terms of reduction in adherent myoblasts and with the majority of the myoblasts containing cytoplasmic vesicles.
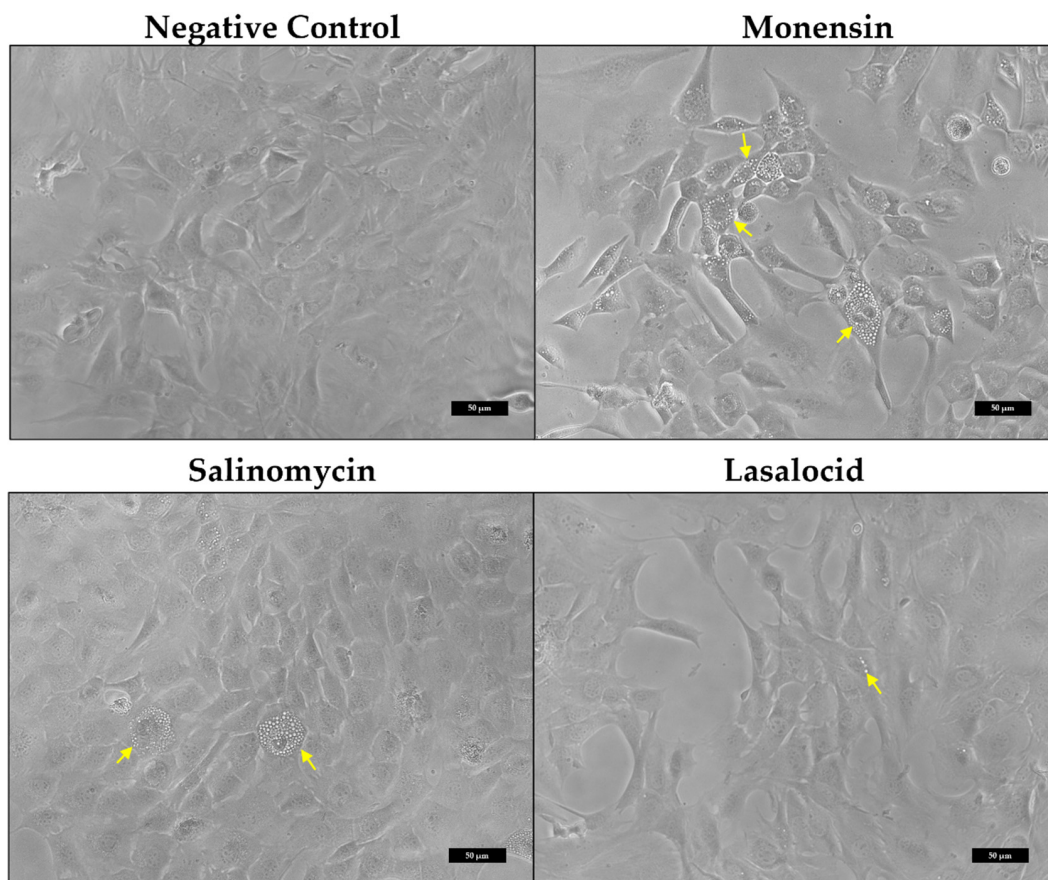
Figure 2. C2C12 myoblasts after exposure to 1 μM monensin, salinomycin and lasalocid for 48 h. The cytoplasm of exposed myoblasts becomes filled with translucent vesicles (yellow arrows). The scale bar = 50 μm.

2.2. The In Vitro Effect of Ionophores on Desmin and Synemin in C2C12 Myoblasts

2.2.1. Desmin

Desmin is seen in the C2C12 myoblasts, stained a light brown color following antibody binding and visualization with the chromogen, 3,3′-diaminobenzidine (DAB). In the negative control, desmin appeared as a diffusely filamentous network throughout the cytoplasm, exhibiting slight condensation in the perinuclear region (Figure 3). The increase in the number of myoblasts was also concomitant with an increase in incubation time. At 72 h, the labelling intensity of desmin seemed to have decreased slightly. The solvent control (0.1% methanol (MeOH)) (not shown) was similar to that of the negative control. Glyoxal (1 mM) and cytochalasin D (20 µM) were used as positive controls. Exposure to glyoxal caused a dot-like desmin aggregation pattern near the perinuclear region of the myoblasts (Figure 3, red arrows). In contrast, cytochalasin D exposure caused desmin to form filamentous protrusions radiating outwards from the nucleus.
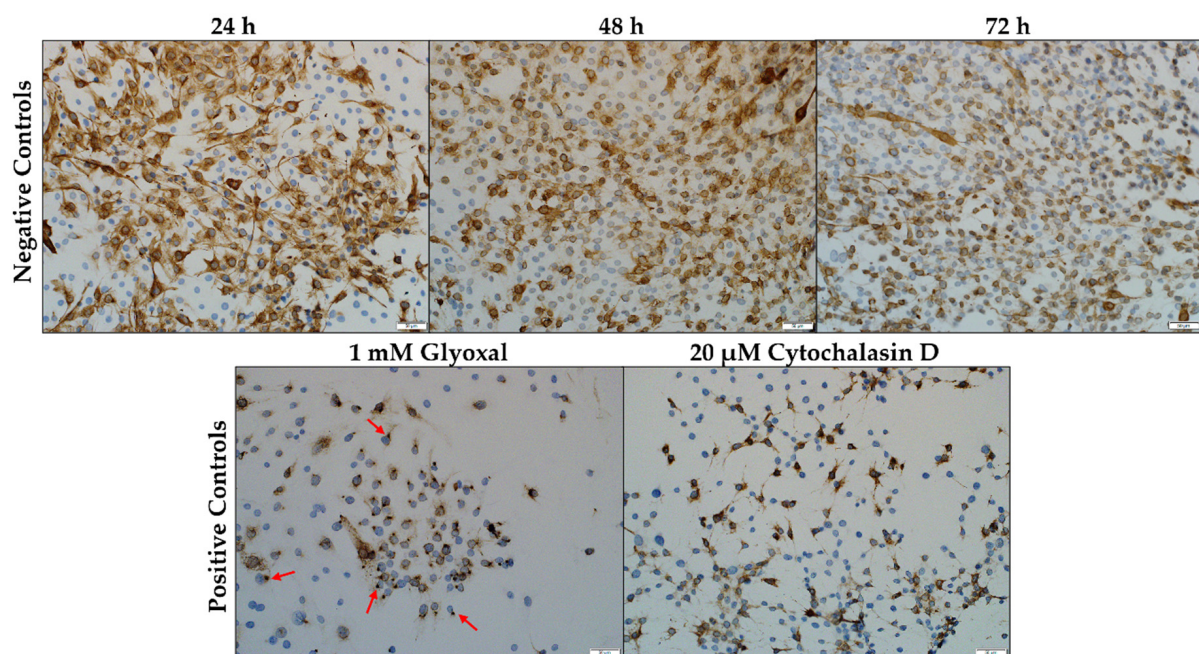
Figure 3. C2C12 myoblasts stained for desmin. The negative control consisted of C2C12 myoblasts incubated in DMEM medium over a 72 h period. Glyoxal and Cytochalasin D were used as positive controls. Desmin aggregates are indicated by the red arrows. Scale bar = 50 µm.

Ionophore exposure affected the distribution of desmin within the C2C12 myoblasts (Figure 4a). After 24 h exposure, the myoblasts appeared similar to that of the negative control. Gaps (yellow arrows) were visible within the desmin network after 48 h exposure, particularly in myoblasts exposed to monensin and salinomycin. Desmin debris were also present, and the number of myoblasts on the slides was visibly less compared to that of the negative control. Myoblasts were stained darker around the nuclei (purple arrows), indicating possible perinuclear desmin aggregation, and appeared elongated compared to that of the negative control. Lasalocid exposure resulted in slightly fewer myoblasts, while few to no gaps were present within the desmin network.

Semiquantitative analysis (Figure 4b) revealed the percentage of myoblasts stained with different intensities. At 24 h, no significant difference in the percentage of negatively stained myoblasts were observed ($p > 0.05$). After 48 h, myoblasts exposed to 1 µM of either monensin or salinomycin had a larger percentage of negatively stained myoblasts compared to the control ($p < 0.001$). Salinomycin also had more negatively stained myoblasts compared to lasalocid ($p < 0.5$). However, at 72 h exposure, only myoblasts exposed to monensin had a significantly larger percentage of desmin-negative myoblasts compared to the control ($p < 0.01$).
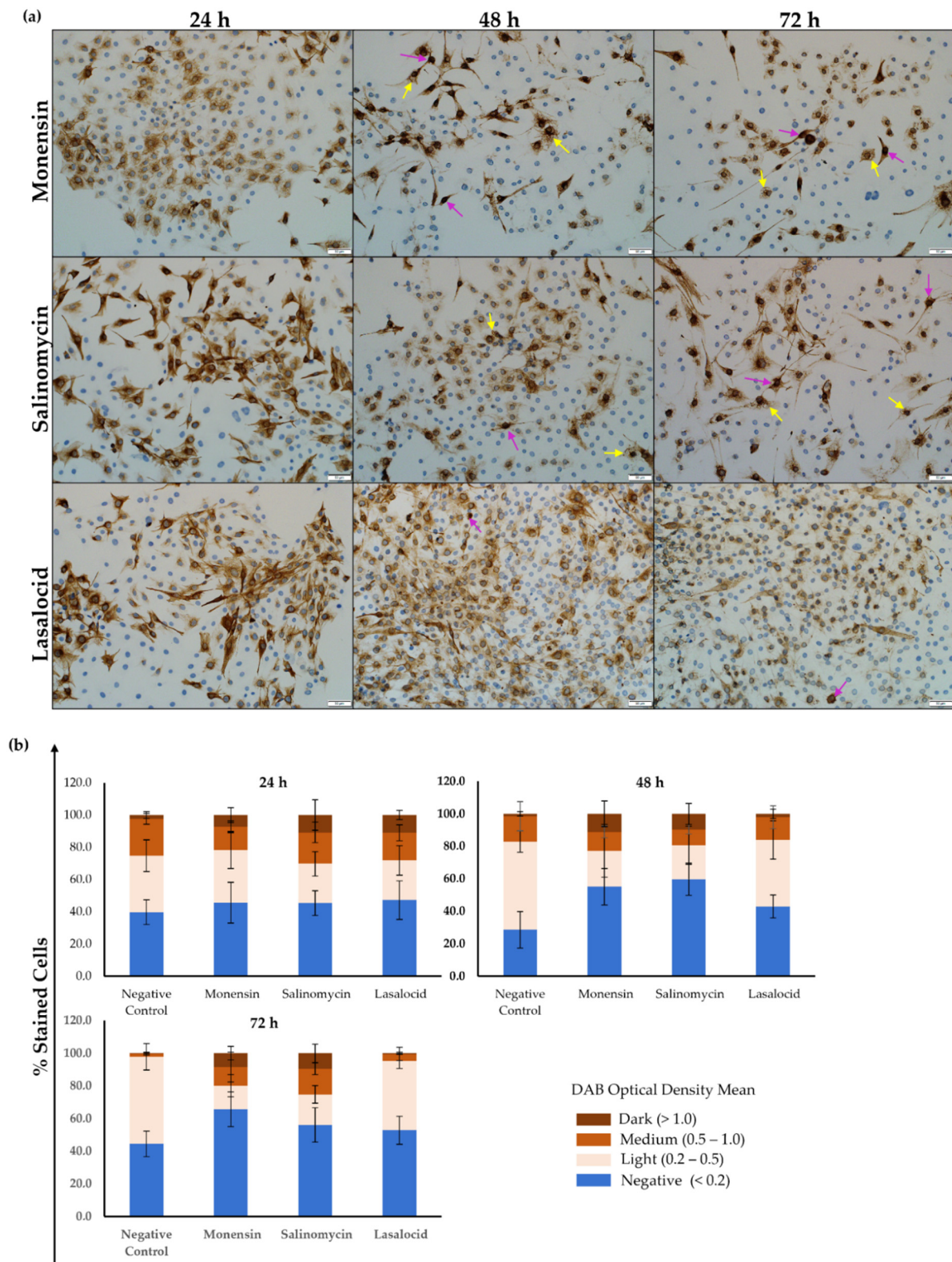
Figure 4. (**a**) C2C12 myoblasts stained for desmin after exposure to 1 μM monensin, salinomycin and lasalocid over a period of 72 h. Myoblasts that stained darker around the nucleus are indicated by purple arrows. Yellow arrows indicate vesicles/gaps within the desmin network. (**b**) Semiquantitative analysis of the desmin staining intensity.

Lightly stained myoblasts had desmin filaments visible within the cytoplasm, usually located around the nucleus, but with low optical density. After 48 and 72 h exposure, both the negative control ($p < 0.001$) and lasalocid ($p < 0.01$) had significantly more lightly stained myoblasts compared to either salinomycin or monensin.

In general, myoblasts stained and categorized as medium were similar between the control and the different ionophores over the 72 h exposure period, with exceptions between the control and monensin at 24 h ($p < 0.05$), as well as between the control and both monensin ($p < 0.05$) and salinomycin ($p < 0.001$) at 72 h.

Finally, in case of exposure to monensin and salinomycin, a significantly ($p < 0.05$) higher percentage of myoblasts stained dark after 48 and 72 h compared to both the control and lasalocid.

In summary, the percentage of darkly stained myoblasts remained minimal in the negative control over the 72 h exposure period, while the number of myoblasts stained with medium intensity decreased with longer exposure times. However, the number of lightly stained myoblasts increased with the exposure time. Desmin labelling of C2C12 myoblasts, exposed to either monensin or salinomycin, had a significantly larger number of myoblasts ($p < 0.05$) classified as either medium or dark. Additionally, there were more desmin-negative myoblasts after 48 and 72 h exposure to monensin and salinomycin compared to the negative control. Myoblasts exposed to 1 µM lasalocid resembled those of the negative control.

2.2.2. Synemin

As with desmin, synemin distribution within the C2C12 myoblasts were investigated using a primary antibody followed by DAB staining; however, synemin exhibited a considerably less intense brown color. The negative and solvent (not shown) controls were similar, with synemin spread diffusely across the cytoplasm (Figure 5). A few myoblasts exhibited a higher concentration of synemin in the perinuclear region. The number of C2C12 myoblasts increased over the 72 h period. Glyoxal and cytochalasin D were used as positive controls. Myoblasts exposed to 1 mM glyoxal had small, concentrated dots of synemin adjacent to the nucleus (Figure 5, red arrows). Cytochalasin D exposure resulted in the reduction in the cytoplasm volume around the nucleus with thin filamentous protrusions reaching between the myoblasts.
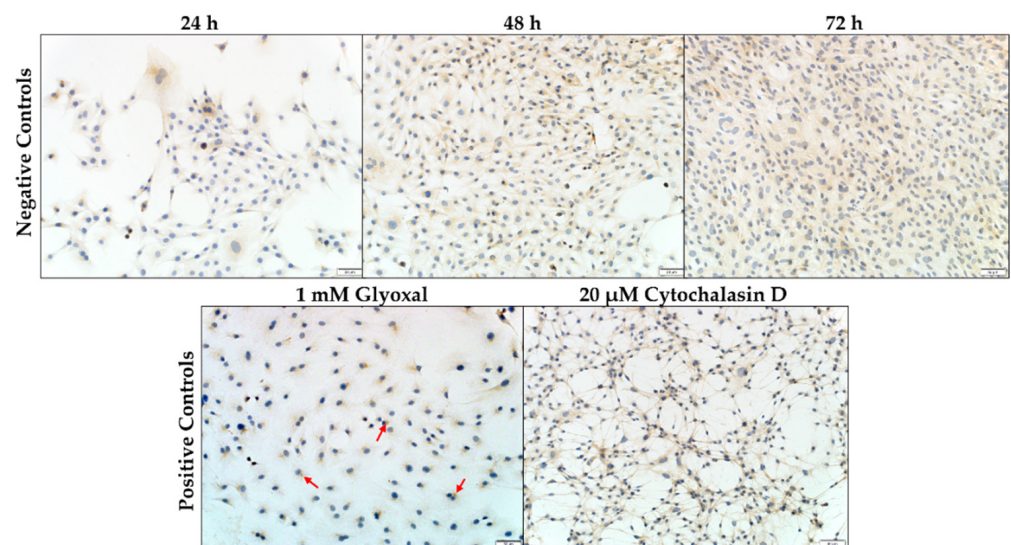
Figure 5. C2C12 myoblasts stained for synemin. The negative control consisted of C2C12 myoblasts incubated in DMEM medium over a 72 h period. Glyoxal and Cytochalasin D were used as positive controls. Synemin aggregation is indicated with red arrows. Scale bar = 50 µm.

After ionophore exposure, faint gaps appeared within the synemin network of the myoblasts (Figure 6, yellow arrows). Myoblasts exposed to monensin had the greatest number of gaps, which correlated with an increase in exposure time. Lasalocid, in contrast, exhibited the lowest number of gaps. Some myoblasts were elongated, with the protrusions staining slightly darker. A few pyknotic nuclei could be seen in the samples as well. No other obvious differences could be observed between synemin staining of the negative control and ionophore-exposed myoblasts.
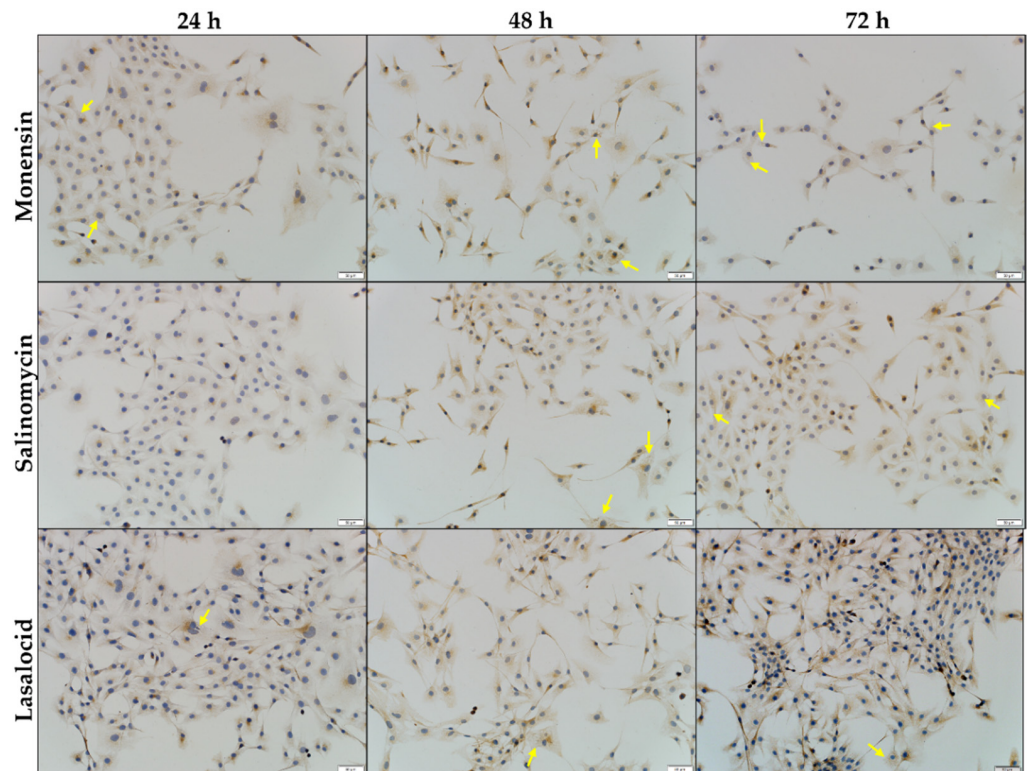
Figure 6. C2C12 myoblasts stained for synemin after exposure to 1 µM monensin, salinomycin and lasalocid over a period of 72 h. Yellow arrows indicate vesicles/gaps within the synemin network. Scale bar = 50 µm.

2.3. The In Vitro Effect of the Ionophores on the Microfilament and Microtubule Networks of C2C12 Myoblasts

Immunofluorescence techniques were used to investigate the effect of ionophore exposure on the microfilaments and microtubules of C2C12 myoblasts. After staining, the negative and solvent controls had a normal mesh-like arrangement of polymerized actin filaments (green) and a dense network of β-tubulin filaments (red) (Figure 7). The myoblasts generally contained one centrally located nucleus (blue) per myoblast. A few myoblasts were in the process of mitosis, as indicated by the visible mitotic spindle (white arrows). Cytochalasin D and vinblastine sulphate were used as positive controls, since they are known inhibitors of actin polymerization and microtubule formation, respectively. Cytochalasin D was added 15 min before fixation, which resulted in the disruption of the microfilament network. Typical examples of affected myoblasts are demonstrated in Figure 7, under the region of interest (ROI). Vinblastine sulphate, added an hour before fixation, resulted in a disorganized microtubular network with short, stub-like threads appearing.
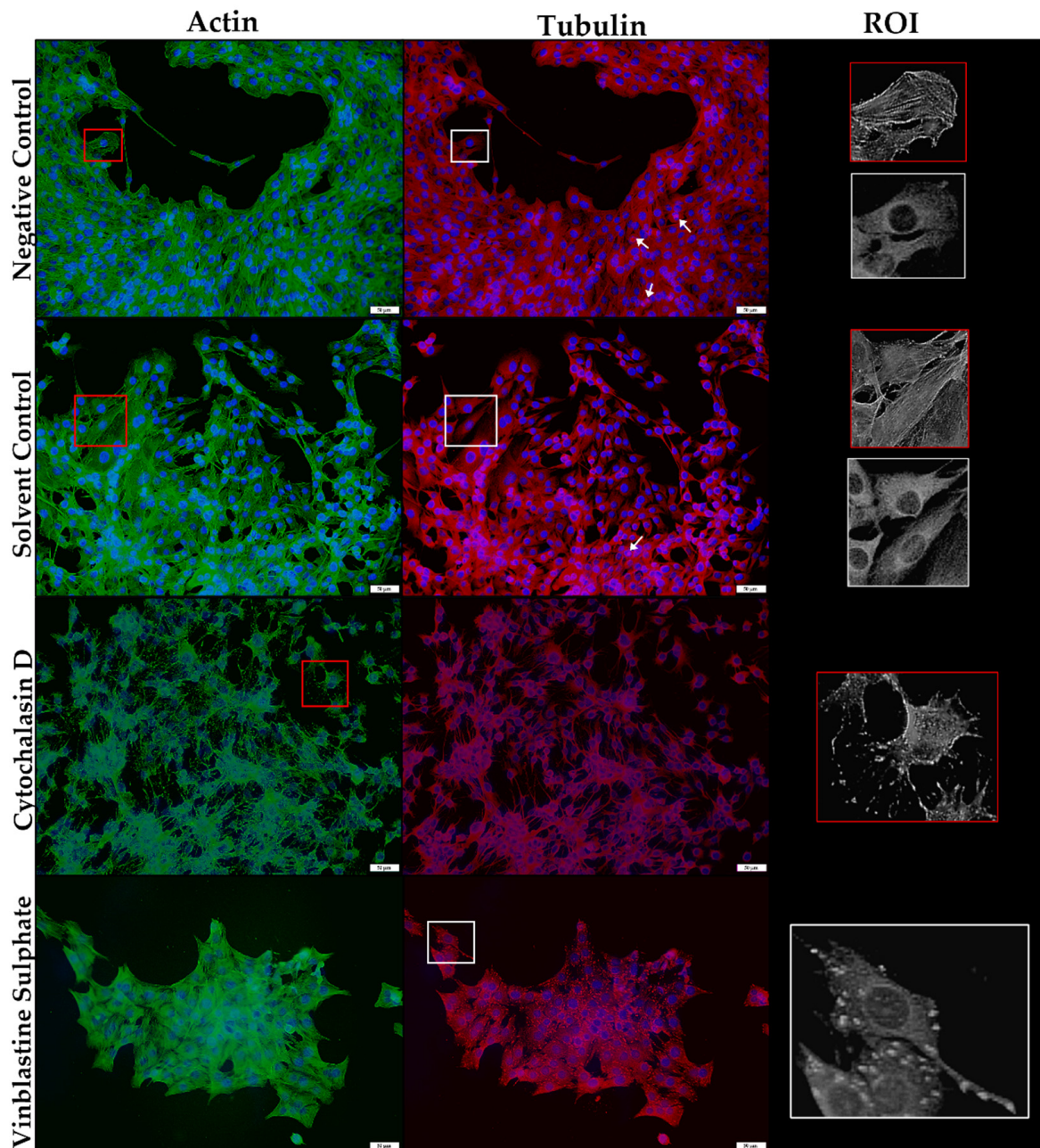
Figure 7. The microfilament (green) and microtubule (red) network of C2C12 myoblast controls stained using phalloidin-FITC and anti-β-tubulin-Cy3, respectively. The nuclei were counterstained with DAPI (blue). The ROI shows a close-up of selected myoblasts. White arrows indicate myoblasts undergoing mitosis. Scale bar = 50 μm.

After exposure to 0.1 μM monensin for 48 h, the microfilament network was minimally affected (Figure 8). However, a few myoblasts showed disruption of the filamentous network after 1 μM exposure. In contrast, the microtubule network exhibited clear gaps (blue arrows) and stained darker around the nuclei of the cells compared to that of the controls. In addition to 'rounded' myoblasts, others appeared to be elongated.
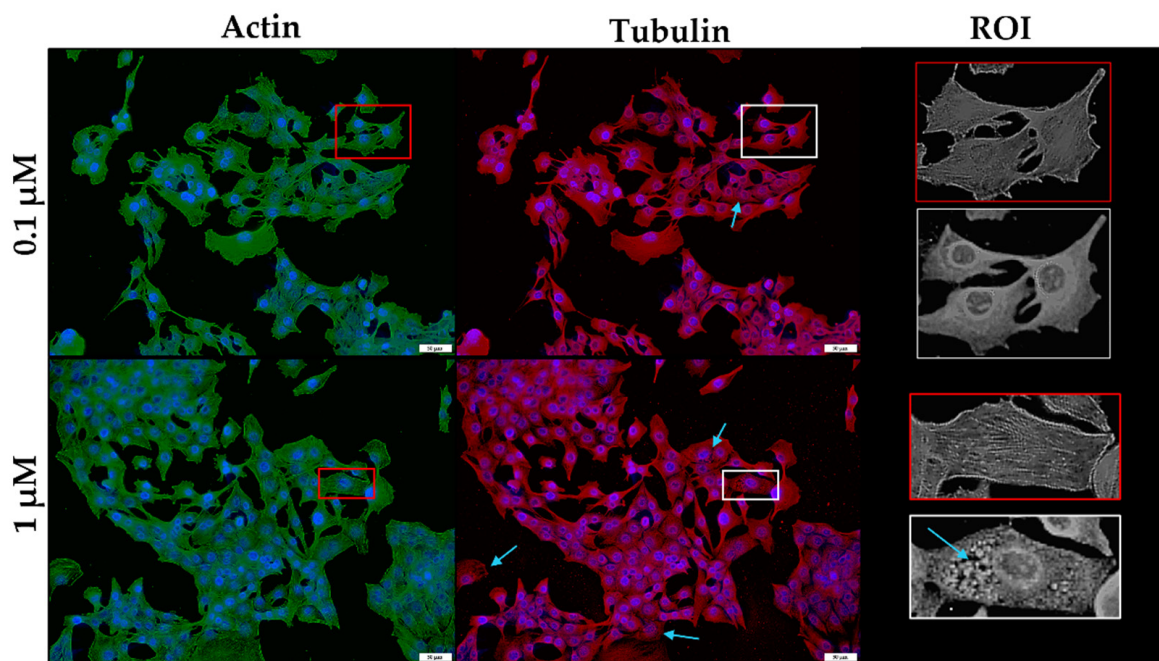
Figure 8. The microfilament (green) and microtubule (red) network of C2C12 myoblasts exposed to monensin for 48 h, stained using phalloidin-FITC and anti-β-tubulin-Cy3, respectively. The nuclei were counterstained with DAPI (blue). Blue arrows indicate myoblasts with gaps within the microtubule network. The ROI shows a close-up of selected myoblasts. Scale bar = 50 μm.

Salinomycin exposure resulted in similar, but less obvious effects on these networks within C2C12 myoblasts (Figure 9). The microtubule network contained a few gaps (blue arrows); however, the microfilament network remained mostly unaffected. As with monensin, salinomycin exposure prompted the appearance of both round and elongated myoblasts.
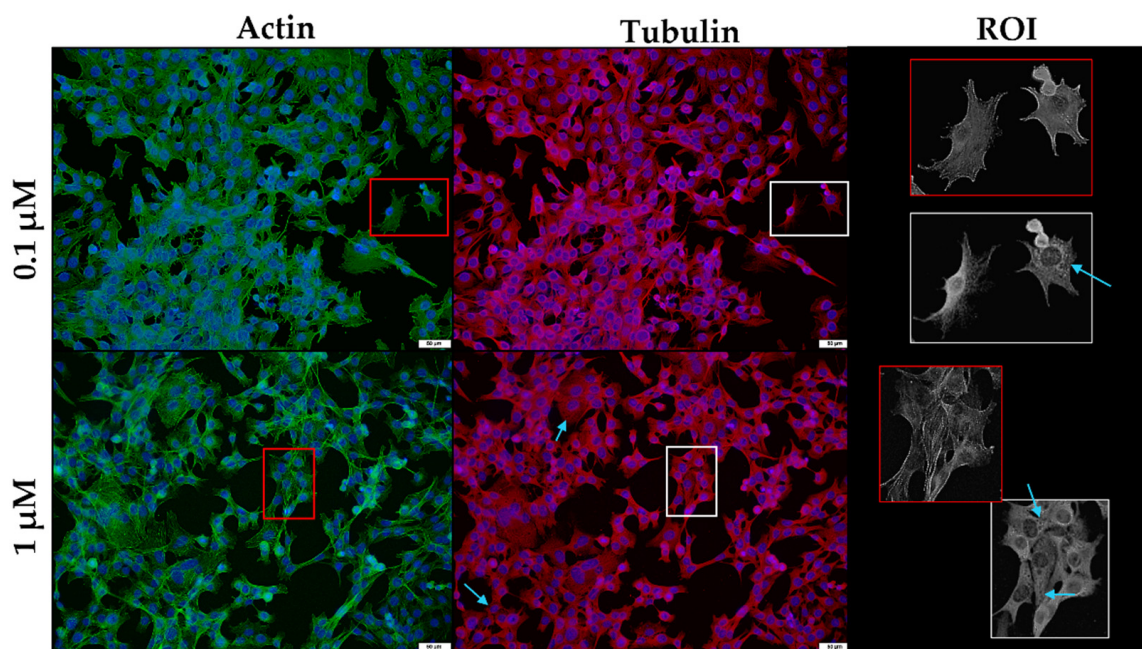
Figure 9. The microfilament (green) and microtubule (red) network of C2C12 myoblasts exposed to salinomycin for 48 h, stained using phalloidin-FITC and anti-β-tubulin-Cy3, respectively. The nuclei were counterstained with DAPI (blue). Blue arrows indicate myoblasts with gaps within the microtubule network. The ROI shows a close-up of selected myoblasts. Scale bar = 50 μm.

Exposure to 0.1 or 1 µM lasalocid resulted in no obvious effects in either the microfilament or microtubule network (Figure 10). A small number of myoblasts contained gaps (blue arrows) within the microtubule network; however, most remained unaffected. Noticeably, a few myoblasts were undergoing mitosis (white arrows).
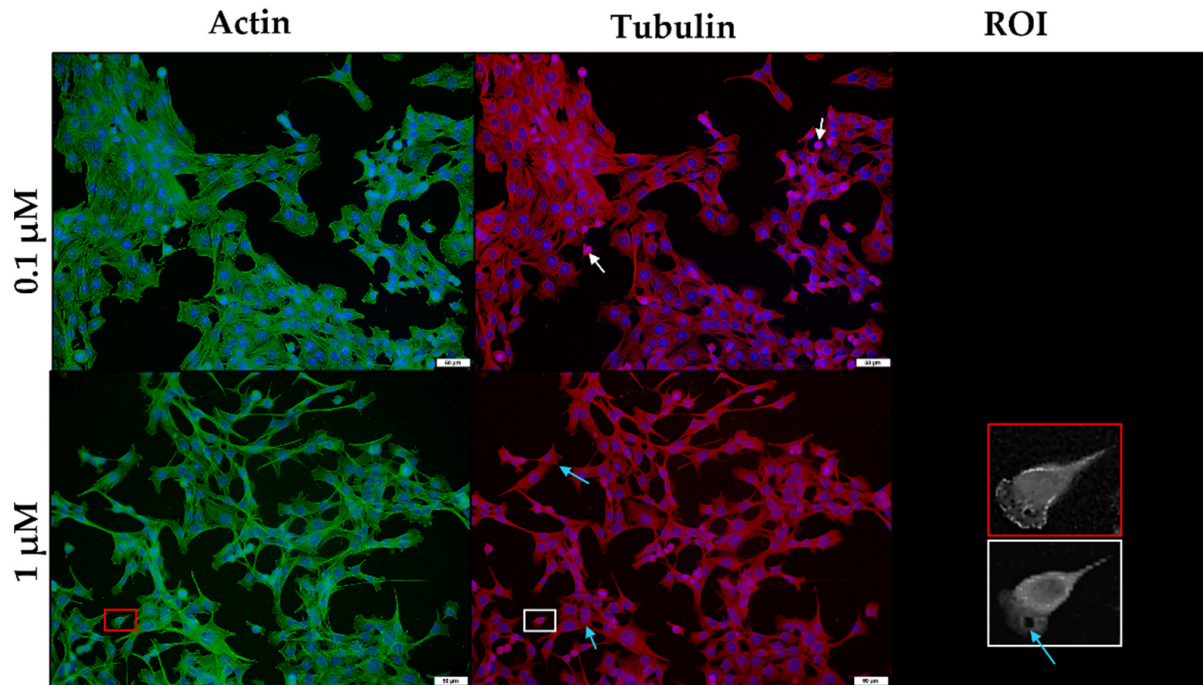

Figure 10. The microfilament (green) and microtubule (red) network of C2C12 myoblasts exposed to lasalocid for 48 h, stained using phalloidin-FITC and anti-β-tubulin-Cy3, respectively. The nuclei were counterstained with DAPI (blue). White arrows indicate myoblasts undergoing mitosis; blue arrows indicate myoblasts with gaps within the microtubule network. The ROI shows a close-up of selected myoblasts. Scale bar = 50 µm.

3. Discussion

The cytotoxicity of the carboxylic ionophores, monensin, salinomycin and lasalocid, were evaluated in C2C12 myoblasts using the MTT assay. Of the three ionophores tested, monensin had the greatest cytotoxicity, followed by salinomycin and, finally, lasalocid (Table 1). These results follow a similar trend as LD_{50} data reported in the literature [3,16,18,20,21,38]. Mice are more susceptible to salinomycin (57.4 mg/kg) compared to monensin (70–96 mg/kg); however, lasalocid (100–146 mg/kg) exhibited the lowest toxic effect, which corroborates findings of the current *in vitro* study. Pharmacokinetic aspects such as absorption, distribution, metabolism, and excretion, have a large impact on *in vivo* toxicity. After ingestion, ionophores are extensively metabolized within the liver and subsequently excreted in bile [3]. However, in the presence of drugs that interfere with the metabolic degradation of the ionophores, e.g., tiamulin [2,10], tissues are exposed to higher concentrations of ionophores and for longer periods, thus increasing their toxic effect. Comparatively, the toxicity of the ionophores, at the exposure times measured, increased considerably during the 72 h maximum exposure period, with initial EC_{50}s in the micromolar range, decreasing to the low nanomolar range at longer exposure times. The *in vitro* cytotoxicity of ionophores on various cancer cell lines have previously been investigated with the EC_{50}s ranging from the high micromolar range to the low nanomolar range depending on the cell line and the duration of exposure [39–42].

Investigation of the myoblast's morphology using phase-contrast microscopy revealed the formation of abundant translucent vesicles following exposure to the ionophores,

especially for monensin (Figure 2). In severely affected myoblasts, the entire cytoplasm was filled with these vesicles. It is surmised that the vesicles originate from the Golgi apparatus as a result of blocked cellular transport [43] or due to the disrupted osmotic balance. The Golgi apparatus is commonly located near the nuclei of the cells, possibly explaining why the vesicles usually first appear within the perinuclear region. Initially, C2C12 myoblasts are spindle-to-stellate shaped cells that can exhibit long cell-to-cell protrusions, especially noticeable in low density cultures. However, following exposure, the myoblasts 'rounded-up' and detached from their surroundings. Ionophores induce cytotoxicity by disruption of the ion homeostasis and resultant downstream effects [3]. Toxic ionophore concentrations can disrupt the mitochondrial membrane potential, affecting oxidative phosphorylation and increasing the production of ROS [44]. Subsequently, the lack of energy exacerbates the ion imbalance, and the ROS further damages the organelles and plasma membrane. Additionally, calcium overload, lipid peroxidation and altered cellular pH also contributes to cellular toxicity [3].

In this study, monensin and salinomycin had a greater cytotoxic effect on the myoblasts compared to lasalocid, which agrees with the cytotoxic effects observed within the cytoskeletal network after exposure to these ionophores. For example, some of the C2C12 myoblasts exposed to lasalocid still continued to undergo mitosis, indicating that proliferation was still ongoing (Figure 10). As the EC_{50}s obtained for lasalocid was above 1 μM, it is not unexpected that a few myoblasts were actively proliferating.

After monensin and salinomycin exposure, the desmin intermediate filament aggregated perinuclearly (Figure 4). Desmin is a critical component in the myofiber network, and various myopathies are associated with its disruption and aggregation [27]. Additionally, desmin plays a role in determining the intracellular location of mitochondria and regulating their respiratory function [29,30]. Therefore, the disruption and loss of desmin filaments could potentially exacerbate the energy deficiency caused by ionophore exposure.

The integrity of the microtubule network was slightly affected as well. Gaps were visible within the microtubule network and the microtubules were concentrated around the nuclei of the myoblasts (Figures 8–10). The gaps correspond to vesicles generated after ionophore exposure (Figure 2). As previously mentioned, ionophore exposure *in vitro* disrupts cellular transport and increases the number of vesicles found within the cytoplasm [43]. Various functions such as the transportation of cellular "cargo" and mitosis require a functioning microtubular network. Increased cytoplasmic calcium could also potentially disrupt these functions as it results in decreased microtubule formation [45,46]. For example, both axonal transport and the quantity of microtubules were decreased in frog sciatic nerves after exposure to lasalocid, which increased intracellular calcium concentrations [47].

The synemin and microfilament networks were not greatly affected by ionophore exposure, except for the slight gaps within both networks.

The cytoskeleton performs an important role in the structural integrity and functioning of muscle. Ultrastructural studies of skeletal muscles of animals affected following ionophore exposure reported myofibrillar degeneration and necrosis, with disrupted contractile apparatus [22,23]. The disruption in the desmin intermediate filament network observed in the current study could thus contribute to the myofibrillar degeneration previously reported, as desmin is primarily associated with the Z-disk of striated muscle [25–28].

Desmin is also a substrate for various calcium-activated proteases, such as calpains, which could potentially be responsible for the degradation of desmin filaments. Salinomycin reportedly activates calpain in murine dorsal root ganglion neurons [48]. In contrast, a study using leupeptin, a protease inhibitor, failed in protecting frog skeletal muscles from damage after exposure to the ionophore, calcimycin, *in vitro,* implying that myofibrillar damage might be due to another mechanism other than calcium activated proteases [49]. Future studies could focus on whether ionophores activate calpain within myoblasts and muscle tissues.

4. Conclusions

Of the three carboxylic ionophores investigates, monensin was the most cytotoxic *in vitro*, followed by salinomycin and lasalocid. The main cytoskeletal element of C2C12 myoblasts affected by ionophore exposure was the desmin intermediate filament network. The microtubule network was also affected, but to a lesser extent.

5. Materials and Methods

5.1. Cell Culture

The mouse skeletal muscle cell line, C2C12, obtained from the American Type Culture Collection (ATCC® CRL-1772™) was used for this study. The myoblasts were cultured in Dulbecco's Modified Eagle's Medium (DMEM) (PAN Biotech, Aidenbach, Germany) supplemented with 100 U penicillin/mL and 100 U streptomycin/mL (Lonza, Verviers, Belgium) and 10% fetal calf serum (Gibco, Origin Brazil, Grand Island, NY, USA). The myoblasts were incubated in a humidified atmosphere with 5% CO_2, at 37 °C and periodically sub-cultured to prevent the culture from reaching confluency.

5.2. Exposure to the Ionophores

C2C12 myoblasts were seeded into 96-well plates at a concentration of 10,000 myoblasts/mL and incubated for 24 h to allow the myoblasts time to attach and reach the log-phase of growth prior to commencing with exposure.

Monensin sodium (MW: 692.85 g/mol), salinomycin sodium (MW: 772.98 g/mol) and lasalocid A sodium (MW: 612.77 g/mol) were obtained from Dr Ehrenstorfer® (Augsburg, Germany). The purity of the ionophores, as indicated on the certificate of analysis, were 98.4, 78.8 and 96.8%, respectively.

As the ionophores were easily solubilized in MeOH, stock solutions were prepared by dissolving the ionophores in MeOH up to a concentration of 40 mM. The solutions were then further diluted with DMEM media, with a final solvent concentration of 0.1% MeOH. The cytotoxic effect of the ionophores were determined after 24, 48 and 72 h.

5.3. Cell viability Assay

Cell viability was measured using a modified MTT assay first described by Mosmann et al. (1983) [50]. Briefly, post exposure, the 96-well plates were washed with phosphate-buffered saline (PBS) (Sigma-Aldrich, St. Louis, MO, USA), followed by the addition of 200 µL complete DMEM medium and 20 µL 5 mg/mL MTT (in PBS) (Sigma-Aldrich, St. Louis, MO, USA). Incubation was continued for 2 h in the dark, in a humidified atmosphere with 5% CO_2, at 37 °C, before the medium was decanted and 100 µL DMSO added to each well. The absorbance and background absorbance were read at 570 nm and 630 nm, respectively, using a Synergy HT BioTek microplate reader (BIO-TEK Instruments, Winooski, VT, USA). Viability was expressed as a percentage of the solvent control after subtracting the media control. Additionally, doxorubicin was used as a positive control for the MTT assay (not shown).

5.4. Immunocytochemical Detection and Analysis of Desmin and Synemin Intermediate Filaments

C2C12 myoblasts were cultured in DMEM supplemented with 10% FBS, 100 U penicillin/mL and 100 U streptomycin/mL. Myoblasts were seeded into an 8-well chamber slide (10,000 cells/mL) and allowed 24 h to attach to the surface, before being exposed to 1 µM monensin, salinomycin and lasalocid for 24, 48 and 72 h, respectively. Due to the varying cytotoxicity between the different ionophore and exposure times, it was decided to use 1 µM as it falls slightly below the EC_{50}s of lasalocid, but above those of monensin and salinomycin after 48 and 72 h exposure. The controls used during this study included a negative control (complete DMEM medium), a solvent control (0.1% MeOH) and two positive controls (1 mM glyoxal added on the day of exposure, as well as 20 µM cytochalasin D added 30 min before fixation).

After exposure, immunocytochemistry was performed using an indirect immunoperoxidase technique as previously described by Botha et al. (2019) [51]. The slides were air-dried and fixed in 4% neutral buffered formalin for at least 30 min, followed by rinsing the slides using 70% alcohol for an additional 10 min. To suppress any endogenous peroxidase activity, each slide was incubated in 3% hydrogen peroxide (in MeOH) for 15 min. Microwave heat-induced epitope retrieval (HIER) followed, using Tris-EDTA (pH 9) and citrate (pH 6) buffer solutions, for desmin and synemin staining, respectively. To facilitate non-specific immunoglobulin binding, slides were incubated with normal horse serum (1:10 in PBS, pH 7.6) containing 0.1% bovine serum albumin (BSA) for 20 min in a humidified chamber at room temperature. The myoblasts were incubated with either the mouse monoclonal desmin (D33) antibody (1:200) (DakoCytomation, Glostrup, Denmark) or the goat polyclonal synemin (S-16) antibody (1:100) (Santa Cruz Biotechnology, Inc. Santa Cruz, CA, USA) for 1 h. Following this, slides incubated with the synemin polyclonal antibody were incubated with a rabbit anti-goat antibody (Dako, Glostrup, Denmark), diluted 1:500 in PBS containing 0.1% BSA, for 30 min in a humidified chamber at room temperature. All slides were incubated with the Dako REAL Envision Rabbit/Mouse polymer-based detection system (Dako, Glostrup, Denmark) performed according to the manufacturer's instructions. The slides were incubated with DAB chromogen for 1–2 min, rinsed with distilled water, counter stained with hematoxylin for 15 sec and washed again with distilled water. Finally, slides were dehydrated with 70%, 96% and 100% alcohol and mounted using Entellan (Merck Millipore, Darmstadt, Germany) and coverslips for examination under a microscope. Each slide was viewed and photographed using the BX63 Olympus microscope (Tokyo, Japan). Six (692 × 521 µm) images were taken and used for further analysis. Semiquantitative analysis on the staining intensity of desmin was performed using QuPath (Version 0.3.0, open-source software) [52] positive cell detection function (Figure 4b). The staining intensity was categorized based on different threshold values of the DAB optical density mean. The total number of nuclei per image was counted and classified as negative (<0.2), light (0.2–0.5), medium (0.5–1.0) or dark (>1.0) depending on the optical density around the nucleus. Myoblasts categorized as negative had no desmin surrounding the nucleus. Each image was then manually scanned for errors and corrected where necessary. The percentages were calculated as a function of the total number of myoblasts counted, then averaged over the six images.

5.5. Immunofluorescent Detection of Actin and β-Tubulin

Immunofluorescent staining was performed as previously described by Botha et al. (2019) [51]. The C2C12 myoblasts were seeded onto sterile 10 mm-diameter coverslips placed in a 24-well plate and given 24 h to adhere to the coverslips. The myoblasts were exposed to 0.1 and 1 µM monensin, salinomycin and lasalocid, respectively, for 48 h. Cytochalasin D (Sigma-Aldrich, St. Louis, MO, USA) and vinblastine sulphate (Sigma-Aldrich, St. Louis, MO, USA) were used as positive controls for microfilament and microtubule network disruption, respectively. The myoblasts were exposed to 12 µM cytochalasin D for 15 min and 5 µM vinblastine sulphate for an hour at 37 °C, just prior to fixation. Exposure was followed by a washing step, gently shaking the myoblasts in PBS for 5 min, before fixing the myoblasts with 100% ice-cold acetone (Merck) at −20 °C for 10 min. The acetone was removed, and the 5 min wash step was repeated twice. Actin was stained by the addition of 1 µg/mL phalloidin-fluorescein isothiocyanate (FITC) (Sigma-Aldrich, St. Louis, MO, USA) prepared in PBS and incubated for 30 min at 37 °C. Before staining for β-tubulin, the myoblasts were first incubated with 1% BSA (Biowest, Nuaillé, France) in PBS to block all nonspecific binding cites, followed by incubation with 1 µg/mL (1:100 in PBS) monoclonal anti-β-tubulin-Cy3 (Sigma-Aldrich, St. Louis, MO, USA) for 1 h at 37 °C. After washing three times with PBS to remove the excess stain, the nuclei were counterstained with 1.3 µg/mL DAPI (in ddH$_2$O) for 15 min at 37 °C. The washing step was then again repeated 3 times. Finally, the coverslips were mounted on a microscope slide with Prolong^{TM} Gold antifade reagent (Molecular Probes, Eugene, OR, USA) and

sealed to prevent drying of the sample. The samples were viewed with an Olympus BX63 Fluorescent microscope (Tokyo, Japan). The fluorescent images were merged using Fiji–ImageJ (open-source software) [53]. The images were deconvoluted using the Diffraction PSF 3D and Iterative Deconvolve 3D plugins [54].

5.6. Statistical Analysis

All EC$_{50}$s were calculated using the non-computational method first described by Alexander et al. (1999) [55]. Further statistical analysis was performed using GraphPad Prism version 9.0 (GraphPad Software, San Diego, CA, USA). Normality was determined using the Shapiro–Wilk normality test. Significant differences were determined using analysis of variance (ANOVA), followed by an ad hoc Tukey's test, to determine differences between individual samples from the cytotoxicity assays as well as the semi-quantitative desmin analysis.

References

1. Marques, R.D.S.; Cooke, R.F. Effects of Ionophores on Ruminal Function of Beef Cattle. *Animals* **2021**, *11*, 2871. [CrossRef]
2. Meingassner, J.G.; Schmook, F.P.; Czok, R.; Mieth, H. Enhancement of the Anticoccidial Activity of Polyether Antibiotics in Chickens by Tiamulin. *Poult. Sci.* **1979**, *58*, 308–313. [CrossRef] [PubMed]
3. Novilla, M.N. Ionophores. In *Veterinary Toxicology*; Elsevier: Amsterdam, The Netherlands, 2018; pp. 1073–1092.
4. Perry, T.W.; Beeson, W.M.; Mohler, M.T. Effect of Monensin on Beef Cattle Performance. *J. Anim. Sci.* **1976**, *42*, 761–765. [CrossRef]
5. Weppelman, R.M.; Olson, G.; Smith, D.A.; Tamas, T.; Van Iderstine, A. Comparison of Anticoccidial Efficacy, Resistance and Tolerance of Narasin, Monensin and Lasalocid in Chicken Battery Trials. *Poult. Sci.* **1977**, *56*, 1550–1559. [CrossRef] [PubMed]
6. Aleman, M.; Magdesian, K.G.; Peterson, T.S.; Galey, F.D. Salinomycin toxicosis in horses. *J. Am. Vet. Med. Assoc.* **2007**, *230*, 1822–1826. [CrossRef]
7. Ashrafihelan, J.; Eisapour, H.; Erfani, A.M.; Kalantary, A.A.; Amoli, J.S.; Mozafari, M. High mortality due to accidental salinomycin intoxication in sheep. *Interdiscip. Toxicol.* **2014**, *7*, 173–176. [CrossRef]
8. Bastianello, S.S.; McGregor Heather, L.; Mary-Louise, P.; Fourie, N. A chronic cardiomyopathy in feedlot cattle at-tributed to toxic levels of salinomycin in the feed. *J. S. Afr. Vet. Assoc.* **1996**, *67*, 38–41.
9. Britzi, M.; Shimshoni, J.; Edery, N.; Cuneah, O.; Younis, A.; Blech, E.; Oren, P.; Perl, S.; Pozzi, P. Acute salinomycin and maduramicin toxicosis in lactating sows. *Isr. J. Vet. Med.* **2017**, *72*, 42–48.
10. Carpenter, J.A.; Charbonneau, G.; Josephson, G. Tiamulin and narasin toxicosis in nursery pigs. *J. Swine Health Prod.* **2005**, *13*, 333–336.
11. Gy, C.; LeClere, M.; Bélanger, M.; Allano, M.; Beauchamp, G.; Lavoie, J. Acute, subacute and chronic sequelae of horses accidentally exposed to monensin-contaminated feed. *Equine Vet. J.* **2020**, *52*, 848–856. [CrossRef]
12. Oruc, H.H.; Cangul, I.T.; Cengiz, M.; Yilmaz, R. Acute lasalocid poisoning in calves associated with off-label use. *J. Vet. Pharmacol. Ther.* **2010**, *34*, 187–189. [CrossRef] [PubMed]
13. Pakozdy, A.; Challande-Kathman, I.; Doherr, M.; Cizinauskas, S.; Wheeler, S.J.; Oevermann, A.; Jaggy, A. Retrospective study of salinomycin toxicosis in 66 cats. *Vet. Med. Int.* **2010**, *2010*, 147142. [CrossRef] [PubMed]

14. Segev, G.; Baneth, G.; Levitin, B.; Aroch, I.; Shlosberg, I. Accidental poisoning of 17 dogs with lasalocid. *Vet. Rec.* **2004**, *155*, 174–176. [CrossRef] [PubMed]

15. Zavala, G.; Anderson, D.A.; Davis, J.F.; Dufour-Zavala, L. Acute Monensin Toxicosis in Broiler Breeder Chickens. *Avian Dis.* **2011**, *55*, 516–521. [CrossRef] [PubMed]

16. Hall, J.O. Ionophore use and toxicosis in cattle. *Vet. Clin. Food Anim. Pract.* **2000**, *16*, 497–509. [CrossRef]

17. Fourie, N.; Bastianello, S.S.; Prozesky, L.; Nel, P.W.; Kellerman, T.S. Cardiomyopathy of ruminants induced by the litter of poultry fed on rations containing the ionophore antibiotic, maduramicin. I. Epidemiology, clinical signs and clinical pathology. *Onderstepoort J. Vet. Res.* **1991**, *58*, 291–296.

18. Galitzer, S.J.; Oehme, F.W.; Bartley, E.E.; Dayton, A.D. Lasalocid Toxicity in Cattle: Acute Clinicopathological Changes. *J. Anim. Sci.* **1986**, *62*, 1308–1316. [CrossRef]

19. Gruys, E.; Perreira, C.; Bila, C. Accidental monensin toxicosis in horses in Mozambique. *J. S. Afr. Vet. Assoc.* **2001**, *72*, 163–164.

20. Potter, E.; VanDuyn, R.; Cooley, C. Monensin toxicity in cattle. *J. Anim. Sci.* **1984**, *58*, 1499–1511. [CrossRef]

21. Todd, G.C.; Novilla, M.N.; Howard, L.C. Comparative Toxicology of Monensin Sodium in Laboratory Animals. *J. Anim. Sci.* **1984**, *58*, 1512–1517. [CrossRef]

22. Confer, A.W.; Reavis, D.U.; Panciera, R.J. Light and Electron Microscopic Changes in Cardiac and Skeletal Muscle of Sheep with Experimental Monensin Toxicosis. *Vet. Pathol.* **1983**, *20*, 590–602. [CrossRef] [PubMed]

23. Van Vleet, J.F.; Ferrans, V.J. Ultrastructural alterations in skeletal muscle of pigs with acute monensin myotoxicosis. *Am. J. Pathol.* **1984**, *114*, 461–471. [PubMed]

24. Van Vleet, J.F.; Ferrans, V.J. Ultrastructural alterations in the atrial myocardium of pigs with acute monensin toxicosis. *Am. J. Pathol.* **1984**, *114*, 367–379.

25. Agnetti, G.; Herrmann, H.; Cohen, S. New roles for desmin in the maintenance of muscle homeostasis. *FEBS J.* **2021**, *289*, 2755–2770. [CrossRef] [PubMed]

26. Costa, M.L.; Escaleira, R.; Cataldo, A.; Oliveira, F.; Mermelstein, C.S. Desmin: Molecular interactions and putative functions of the muscle intermediate filament protein. *Braz. J. Med. Biol. Res.* **2004**, *37*, 1819–1830. [CrossRef]

27. Mermelstein, C.; Amaral, L.; Rebello, M.; Reis, J.; Borojevic, R.; Costa, M. Changes in cell shape and desmin intermediate filament distribution are associated with down-regulation of desmin expression in C2C12 myoblasts grown in the absence of extracellular Ca^{2+}. *Braz. J. Med. Biol. Res.* **2005**, *38*, 1025–1032. [CrossRef]

28. Paulin, D.; Li, Z. Desmin: A major intermediate filament protein essential for the structural integrity and function of muscle. *Exp. Cell Res.* **2004**, *301*, 1–7. [CrossRef]

29. Capetanaki, Y. Desmin Cytoskeleton A Potential Regulator of Muscle Mitochondrial Behavior and Function. *Trends Cardiovasc. Med.* **2002**, *12*, 339–348. [CrossRef]

30. Milner, D.J.; Mavroidis, M.; Weisleder, N.; Capetanaki, Y. Desmin cytoskeleton linked to muscle mitochondrial distribution and respiratory function. *J. Cell Biol.* **2000**, *150*, 1283–1298. [CrossRef]

31. Lund, L.M.; Kerr, J.P.; Lupinetti, J.; Zhang, Y.; Russell, M.A.; Bloch, R.J.; Bond, M. Synemin isoforms differentially organize cell junctions and desmin filaments in neonatal cardiomyocytes. *FASEB J.* **2012**, *26*, 137–148. [CrossRef]

32. Mizuno, Y.; Thompson, T.G.; Guyon, J.R.; Lidov, H.G.; Brosius, M.; Imamura, M.; Ozawa, E.; Watkins, S.C.; Kunkel, L.M. Desmuslin, an intermediate filament protein that interacts with α-dystrobrevin and desmin. *Proc. Natl. Acad. Sci. USA* **2001**, *98*, 6156–6161. [CrossRef] [PubMed]

33. Mizuno, Y.; Guyon, J.R.; Watkins, S.C.; Mizushima, K.; Sasaoka, T.; Imamura, M.; Kunkel, L.M.; Okamoto, K. β-synemin localizes to regions of high stress in human skeletal myofibers. *Muscle Nerve Off. J. Am. Assoc. Electrodiagn. Med.* **2004**, *30*, 337–346. [CrossRef] [PubMed]

34. Pitre, A.; Davis, N.; Paul, M.; Orr, A.W.; Skalli, O. Synemin promotes AKT-dependent glioblastoma cell proliferation by antagonizing PP2A. *Mol. Biol. Cell* **2012**, *23*, 1243–1253. [CrossRef]

35. Russell, M.A.; Lund, L.M.; Haber, R.; McKeegan, K.; Cianciola, N.; Bond, M. The intermediate filament protein, synemin, is an AKAP in the heart. *Arch. Biochem. Biophys.* **2006**, *456*, 204–215. [CrossRef]

36. Robison, P.; Caporizzo, M.A.; Ahmadzadeh, H.; Bogush, A.I.; Chen, C.Y.; Margulies, K.B.; Shenoy, V.B.; Prosser, B.L. Detyrosinated microtubules buckle and bear load in contracting cardiomyocytes. *Science* **2016**, *352*, aaf0659. [CrossRef]

37. Robison, P.; Prosser, B.L. Microtubule mechanics in the working myocyte. *J. Physiol.* **2017**, *595*, 3931–3937. [CrossRef] [PubMed]

38. Gad, S.; Reilly, C.; Siino, K.; Gavigan, F.; Witz, G. Thirteen Cationic Ionophores: Their Acute Toxicity, Neurobehavioral and Membrane Effects. *Drug Chem. Toxicol.* **1985**, *8*, 451–468. [CrossRef] [PubMed]

39. Cybulski, W.; Radko, L.; Rzeski, W. Cytotoxicity of monensin, narasin and salinomycin and their interaction with silybin in HepG2, LMH and L6 cell cultures. *Toxicol. Vitr.* **2015**, *29*, 337–344. [CrossRef]

40. Kiełbasiński, K.; Peszek, W.; Grabarek, B.O.; Boroń, D.; Wierzbik-Strońska, M.; Oplawski, M. Effect of Salinomycin on Expression Pattern of Genes Associated with Apoptosis in Endometrial Cancer Cell Line. *Curr. Pharm. Biotechnol.* **2020**, *21*, 1269–1277. [CrossRef]

41. Iljin, K.; Ketola, K.; Vainio, P.; Halonen, P.; Kohonen, P.; Fey, V.; Grafström, R.C.; Perälä, M.; Kallioniemi, O. High-throughput cell-based screening of 4910 known drugs and drug-like small molecules identifies disulfiram as an inhibitor of prostate cancer cell growth. *Clin. Cancer Res.* **2009**, *15*, 6070–6078. [CrossRef]

42. Tyagi, M.; Patro, B.S. Salinomycin reduces growth, proliferation and metastasis of cisplatin resistant breast cancer cells via NF-kB deregulation. *Toxicol. Vitr.* **2019**, *60*, 125–133. [CrossRef]

43. Mollenhauer, H.H.; Morré, D.J.; Rowe, L.D. Alteration of intracellular traffic by monensin; mechanism, specificity and relationship to toxicity. *Biochim. Biophys. Acta BBA Rev. Biomembr.* **1990**, *1031*, 225–246. [CrossRef]

44. Przygodzki, T.; Sokal, A.; Bryszewska, M. Calcium ionophore A23187 action on cardiac myocytes is accompanied by enhanced production of reactive oxygen species. *Biochim. Biophys. Acta BBA Mol. Basis Dis.* **2005**, *1740*, 481–488. [CrossRef]

45. Olmsted, J.B.; Borisy, G.G. Ionic and nucleotide requirements for microtubule polymerization *in vitro*. *Biochemistry* **1975**, *14*, 2996–3005. [CrossRef] [PubMed]

46. Weisenberg, R.C. Microtubule Formation *in vitro* in Solutions Containing Low Calcium Concentrations. *Science* **1972**, *177*, 1104–1105. [CrossRef]

47. Kanje, M.; Edstro¨m, A.; Hanson, M. Inhibition of rapid axonal transport *in vitro* by the ionophores X-537 A and A 23187. *Brain Res.* **1981**, *204*, 43–50. [CrossRef]

48. Boehmerle, W.; Endres, M. Salinomycin induces calpain and cytochrome c-mediated neuronal cell death. *Cell Death Dis.* **2011**, *2*, e168. [CrossRef]

49. Duncan, C.; Smith, J.; Greenaway, H.C. Failure to protect frog skeletal muscle from ionophore-induced damage by the use of the protease inhibitor leupeptin. *Comp. Biochem. Physiol. Part C Comp. Pharmacol.* **1979**, *63*, 205–207. [CrossRef]

50. Mosmann, T. Rapid colorimetric assay for cellular growth and survival: Application to proliferation and cytotoxicity assays. *J. Immunol. Methods* **1983**, *65*, 55–63. [CrossRef]

51. Botha, C.J.; Venter, E.A.; Ferreira, G.C.; Phaswane, R.M.; Clift, S.J. Geigerin-induced disorganization of desmin, an intermediate filament of the cytoskeleton, in a murine myoblast cell line (C2C12). *Toxicon* **2019**, *167*, 162–167. [CrossRef]

52. Bankhead, P.; Loughrey, M.B.; Fernández, J.A.; Dombrowski, Y.; McArt, D.G.; Dunne, P.D.; McQuaid, S.; Gray, R.T.; Murray, L.J.; Coleman, H.G.; et al. QuPath: Open source software for digital pathology image analysis. *Sci. Rep.* **2017**, *7*, 16878. [CrossRef] [PubMed]

53. Schindelin, J.; Arganda-Carreras, I.; Frise, E.; Kaynig, V.; Longair, M.; Pietzsch, T.; Preibisch, S.; Rueden, C.; Saalfeld, S.; Schmid, B.; et al. Fiji: An open-source platform for biological-image analysis. *Nat. Methods* **2012**, *9*, 676–682. [CrossRef] [PubMed]

54. Dougherty, R. Extensions of DAMAS and Benefits and Limitations of Deconvolution in Beamforming. In Proceedings of the 11th AIAA/CEAS Aeroacoustics Conference, Monterey, CA, USA, 23–25 May 2005; p. 2961.

55. Alexander, B.; Browse, D.; Reading, S.; Benjamin, I. A simple and accurate mathematical method for calculation of the EC50. *J. Pharmacol. Toxicol. Methods* **1999**, *41*, 55–58. [CrossRef]